

Dissertation
Submitted to the
Combined Faculties for the Natural Sciences and for Mathematics
of the Ruperto-Carola University of Heidelberg, Germany
for the degree of
Doctor of Natural Science

Put forward by
Gu, Myojeong (MSc. Engineering)
Born in Busan, Republic of Korea

Oral examination: 17.01.2019

Long term trends of Stratospheric trace gases
from ground-based DOAS observations of
Kiruna, Sweden

Referee: Prof. Dr. Wagner, Thomas
Prof. Dr. Comba, Peter

ABSTRACT

This thesis provides analysis results of an extensive data set of stratospheric trace gases (NO_2 , BrO, OCIO) derived from ground based zenith sky DOAS measurements (1996 — 2016) at Kiruna, Sweden. Kiruna (67.84°N , 21.41°E) is located north of the polar circle and is thus well suited for the investigation of polar stratospheric ozone chemistry. The analysed trace gases are involved in the key-chemical reactions controlling stratospheric ozone. Thus their long-term monitoring is important for the independent control of the international CFC emission reduction agreements and to predict the future evolution of the ozone layer. The Kiruna zenith sky DOAS measurements are one of the longest records at polar regions and thus very well suited for these tasks. The thesis has three major parts. First, the whole set of raw spectra was re-analysed with consistent retrieval settings taking into account the most recent advances of the passive DOAS technique. The retrieval settings were further optimised by various sensitivity tests. Second, the derived data products were compared to several independent measurements, where overall very good agreement was found. Finally the long term data set was used to investigate the temporal variations on various scales and to relate them to stratospheric meteorological parameters. In particular the long term trends of NO_2 and BrO were determined. For NO_2 it was found that the amount has not significantly changed (a slight positive, but non-significant change of about $1.5 \pm 2\%$ /decade was found.). This is in good agreement with the trend of its precursor gas N_2O (2.3% /decade). For BrO a strong positive trend before 2001 and a negative trend after 2005 is found confirming the expected reduction of the emissions of the precursor gases. Here it should be noted that the results of this thesis extend the existing time records by several years. From the measured BrO amounts the total stratospheric bromine mixing ratio was estimated to about 20.7 ppt, and the contribution of very short lived bromine species to about 5 ppt.

ZUSAMMENFASSUNG

Diese Arbeit beschreibt die Analyse und Interpretation eines umfangreichen Datensatzes stratosphärischer Spurengase (NO_2 , BrO, OCIO), der aus bodengebundenen Zenith-DOAS-Messungen (1996–2016) in Kiruna, Schweden, gewonnen wurde. Kiruna (67.84°N , 21.41°E) liegt nördlich des Polarkreises und ist daher sehr geeignet für die Untersuchung der polaren stratosphärischen Ozonchemie. Die analysierten Spurenstoffe sind involviert in wesentlichen chemischen Reaktionen, die die Menge des stratosphärischen Ozons bestimmen. Daher ist ihre Langzeit-Messung wichtig, um die Einhaltung der internationalen FCKW-Emissionsreduktionsvereinbarungen zu kontrollieren sowie die zukünftige Entwicklung der Ozonschicht vorherzusagen. Die Zenith-DOAS-Messungen in Kiruna sind eine der längsten Messreihen in Polarregionen und daher bestens geeignet für diese Aufgaben. Die Arbeit hat drei wesentliche Teile: Zunächst wird der gesamte Satz an Roh-Spektren mit konsistenten Auswerteparametern ausgewertet, wobei die neuesten Entwicklungen der DOAS-Auswertetechnik berücksichtigt wurden. Die Auswerte-Parameter wurden dabei anhand vieler Sensitivitätsstudien weiter optimiert. Danach wurden die gewonnenen Datensätze mit

mehreren unabhängigen Messungen verglichen und insgesamt sehr gute Übereinstimmung gefunden. Letztlich wurden die gewonnenen Langzeit-Datensätze dazu genutzt, die zeitliche Variabilität auf verschiedenen Skalen zu untersuchen und in Bezug zu stratosphärischen meteorologischen Parametern zu setzen. Insbesondere wurden auch Langzeit-Trends von NO_2 und BrO bestimmt. Für NO_2 wurde ein leicht positiver, aber unsigifikanter Trend von $1.5 \pm 2\%$ pro Dekade gefunden. Dieser ist in guter Übereinstimmung mit dem Trend des Vorläufergases N_2O (2.3% pro Dekade). Für BrO wurde vor 2001 ein starker positiver Trend und nach 2005 ein negativer Trend gefunden, was die beobachtete Reduktion der Vorläufergase bestätigt. Hier sollte beachtet werden, dass die in dieser Arbeit gewonnenen Ergebnisse über die Zeiträume früherer Studien um mehrere Jahre hinausgehen. Von den BrO-Messungen konnte auch die Gesamtmenge an stratosphärischen Bromverbindungen zu 20.7 ppt und der potentielle Beitrag sehr kurzlebiger Vorläufergase zu 5 ppt abgeleitet werden.

CONTENTS

i INTRODUCTION	1
1 STRATOSPHERIC OZONE CHEMISTRY	5
1.1 Hydrogen Catalytic cycle	6
1.2 Nitrogen Catalytic Cycle	7
1.3 Halogen catalytic cycles	8
1.3.1 Bromine Chemistry	10
1.3.2 Chlorine Chemistry	13
1.3.3 Heterogeneous Halogen Chemistry	14
2 METHODOLOGY	17
2.1 Absorption spectroscopy	17
2.2 Differential Optical Absorption Spectroscopy (DOAS)	18
2.3 Passive differential optical absorption spectroscopy	19
2.3.1 Ground based zenith sky DOAS	20
2.3.2 Instrument History	21
ii RESULTS: STRATOSPHERIC TRACE GASES	25
3 NO₂	27
3.1 Analysis	27
3.1.1 Wavelength ranges and reference spectra	27
3.1.2 Langley plot method	29
3.1.3 Retrieval of vertical profiles	30
3.2 Results	33
3.2.1 Overview on the stratospheric NO ₂ variation	33
3.2.2 Temporal and vertical variability of stratospheric NO ₂	35
3.2.3 Statistical sensitivity test of the profile inversion	39
3.2.4 Comparison with other instruments	45
3.2.5 Trend analysis of stratospheric NO ₂	55
3.3 Summary	62
4 BRO	65
4.1 Analysis	65
4.1.1 Wavelength range and reference spectra	65
4.1.2 Taylor series approach	65
4.1.3 Dependence of the BrO results on the choice of the ozone cross section	67
4.1.4 Ring temperature dependence	69
4.1.5 Retrieval of vertical profiles	70
4.2 Results	71
4.2.1 Variation of stratospheric BrO concentration profiles	71
4.2.2 Dependence of the BrO profile inversion results on the sky condition	74
4.2.3 Time series of the vertical distribution	78
4.2.4 Comparison with other instruments	81
4.2.5 Trend analysis	86

4.2.6	Estimation of the total stratospheric Br _y , its temporal evolution, and the contribution of Very Short-lived substances	87
4.3	Summary	90
5	OCLO	93
5.1	Analysis	93
5.1.1	Choice of the wavelength range	94
5.1.2	Selection of the Fraunhofer reference spectrum	96
5.2	Results	101
5.2.1	General variability	101
5.2.2	Time series of OCIO over Kiruna	102
5.2.3	Comparison of the time series of OCIO with the time series of NO ₂ , BrO, and O ₃	111
5.2.4	Comparison of the zenith sky DOAS OCIO results with simultaneous measurements of the GOME-2 satellite instrument	113
5.3	Summary of the ground-based OCIO measurements	116
iii	RESULTS: TROPOSPHERIC TRACE GAS	119
6	VOLCANIC TRACE GASES	121
6.1	Analysis	122
6.2	Results	124
6.2.1	Enhanced SO ₂ during the volcanic episode	124
6.2.2	Enhanced BrO correlation with sky condition	125
iv	CONCLUSION AND OUTLOOK	131
7	CONCLUSION	133
c.1	NO ₂	133
c.2	BrO	135
c.3	OCIO	136
c.4	Volcanic Trace Gases	137
c.5	Outlook	137
v	APPENDIX	139
A.1	Appendix: Stratospheric NO ₂	141
A.1.1	Vertical distribution of stratospheric NO ₂	141
A.1.2	Trend analysis	144
A.2	Appendix: Stratospheric BrO	146
A.2.1	Analysis	146
A.2.2	Temporal and vertical distribution of stratospheric BrO at different SZA condition	147
A.2.3	Meteorology of polar winter periods	150
A.2.4	Vertical distribution of stratospheric BrO	153
A.2.5	Trend analysis	156
A.3	Appendix: Stratospheric OCIO	157
A.3.1	Analysis	157
A.4	Appendix: Tropospheric volcanic gas	158
	BIBLIOGRAPHY	161

LIST OF FIGURES

Figure 1.1	The stratospheric ozone profile according to the Chapman Mechanism, compared to observations.	6
Figure 1.2	The relative global mean ozone loss rates by chemical family and the global mean ozone profile	6
Figure 1.3	Changes in halogen source gases entering the stratosphere	9
Figure 1.4	Diurnal cycle of the relative contribution of the most abundant bromine species BrO, BrONO ₂ , HBr and BrCl in the lower stratosphere	12
Figure 2.1	Scheme of an experiment to measure trace gas absorptions in open air conditions	18
Figure 2.2	The principle of DOAS: I_0 and σ are separated by an adequate filtering process into a narrow (D' and σ' and broad band part I'_0 and σ_b	19
Figure 2.3	Geometry of a zenith sky DOAS measurement and radiation transport in the atmosphere assuming single scattering	20
Figure 2.4	Picture of the ground-based zenith sky DOAS at Kiruna, Sweden	21
Figure 2.5	Time series of different instrument quality parameters from 1997 to 2016	22
Figure 2.6	Sketch of the telescope settings (left) and the UV spectrograph. Modified version from Otten [1997]	23
Figure 2.7	The full image has been recorded on the 24th January 2013 as an example for the settings of the long term measurement. The black parts indicate areas with no light. This figure and a cation are adopted from Gottschalk [2013].	23
Figure 2.8	Raw spectrum output of the camera on the 29th January 2013 at 8:54 GMT. In addition the number of accumulations, the measuring temperature and the exposure time is shown as well. This figure and a cation are adopted from Gottschalk [2013].	24
Figure 3.1	Example of a NO ₂ analysis of a spectrum measured on 2015 Sep.14, 17:03 UTC (SZA at 89°).	28
Figure 3.2	The variation of the SZA in Kiruna. Red and blue lines indicate the seasonal variation of the maximum and minimum SZAs during the year.	28
Figure 3.3	Example to illustrate the Langley plot method.	29
Figure 3.4	The variation of NO ₂ slant columns with SZA for different NO ₂ profiles with the peak mixing ratio at different altitudes.	30
Figure 3.5	Typical examples of the retrieval of a stratospheric NO ₂ profile and the corresponding averaging kernels.	32
Figure 3.6	The trace of A as a function of the upper limit of the SZA, the measurement response indicating the sum of the rows of the averaging kernels at different heights and NO ₂ profiles retrieved for different SZA upper limit.	32
Figure 3.7	Diurnal variation of the measured stratospheric NO ₂ dSCDs depending on SZA for selected days during sunrise (A) and sunset (B).	33

Figure 3.8	Box and whisker plots for monthly stratospheric NO ₂ VCDs from 1997 to 2016 derived from the Langley plot method.	34
Figure 3.9	Stratospheric monthly mean profiles from ZS-DOAS observations from 1997 to 2016. Odd number-columns represent monthly means and the number of occurrences.	35
Figure 3.10	Curtain plots of the time series of the stratospheric NO ₂ vertical distribution measured in a.m.	36
Figure 3.11	Curtain plots of the time series of the stratospheric NO ₂ vertical distribution measured in p.m.	37
Figure 3.12	Temporal variation of different retrieved quantities from ZS-DOAS observations on a clear sky day and a cloudy sky day.	40
Figure 3.13	RMS and a trace of the averaging kernel matrix under different sky conditions categorised by the number of occurrences of each sky condition during the period used for the profile retrieval.	41
Figure 3.14	Vertical NO ₂ mean profiles derived from the ground-based measurements in a.m for 14 years depending on the sky conditions and season.	42
Figure 3.15	Vertical NO ₂ mean profiles derived from the ground-based measurements in p.m for 14 years depending on the sky conditions and season.	43
Figure 3.16	NO ₂ profiles (mixing ratios) as a function of time in a.m and p.m.	44
Figure 3.17	Absolute differences between the smoothed SCIAMACHY profiles and the ZS-DOAS profiles for different distances between the ZS-DOAS measurement site and the tangent point of the SCIAMACHY limb observations	46
Figure 3.18	Surface projection of the direction of the scanned air masses for ZS-DOAS and the 2D box air mass factors (AMF) as a function of altitude and distance from the instrument for measurements at a SZA of 90°.	47
Figure 3.19	Typical measurement sensitivities of SCIAMACHY and ZS-DOAS.	48
Figure 3.20	Comparison of coincident ZS-DOAS and SCIAMACHY profiles from 2002 to 2006.	48
Figure 3.21	Time series of NO ₂ VCDs (from ZS-DOAS using the Langley plot method) and partial column densities (19 – 37km) obtained from ZS-DOAS and SCIAMACHY in 2005 and 2006.	49
Figure 3.22	Comparison of stratospheric NO ₂ profiles derived from ZS-DOAS and SAOZ for different days.	50
Figure 3.23	Time series of stratospheric daily mean NO ₂ VCDs compared with three different satellite nadir observations.	54
Figure 3.24	Daily averaged stratospheric NO ₂ VCDs from satellite observations plotted against those derived from ZS-DOAS observations.	55
Figure 3.25	Box and whisker plots of the absolute and relative differences of the stratospheric NO ₂ VCDs between satellite and ZS-DOAS observations from 1997 to 2016.	56
Figure 3.26	Explanatory proxy parameters for the trend analysis from 1997 to 2015.	59
Figure 3.27	Trend analysis of monthly mean NO ₂ VCDs determined by the Langley plot method.	60
Figure 3.28	Trend analysis of monthly mean NO ₂ VCDs determined by the integrated profiles.	61

Figure 4.1	Example of a BrO analysis of a spectrum measured on 2016 Feb.26, 15:19 UTC (SZA at 89°)	66
Figure 4.2	Retrieved optical depth of BrO measured on Feb.18, 2014 (SZA 90° a.m).	67
Figure 4.3	Time series of BrO results for one year (2013).	68
Figure 4.4	Difference of the Ring spectra for a temperature change of 20K for different temperatures $T = 213, 233, 253, 273,$ and 293K	69
Figure 4.5	Typical example of a stratospheric BrO profile retrieval and the corresponding averaging kernels.	70
Figure 4.6	The trace of \mathbf{A} as a function of the upper limit of the SZA, measurement response and BrO profiles retrieved for different SZA upper limit conditions.	71
Figure 4.7	SZA dependence of the BrO VCDs measured and the retrieved BrO profiles and the retrieved BrO profiles at various SZA measured on Mar.15 of 2006.	72
Figure 4.8	Monthly mean BrO concentration profiles (February – October) from ZS-DOAS observations from 1997 to 2016.	73
Figure 4.9	Box and whisker plots of stratospheric BrO partial columns (15 – 27 km) from 1997 to 2016 derived from integrating the profiles retrieved with OEM.	74
Figure 4.10	Frequencies of different sky conditions derived from the zenith sky DOAS cloud classification scheme from 1997 to 2015 (except 2002)	74
Figure 4.11	RMS and the trace of the averaging kernel matrix (\mathbf{A}) which gives the number of independent pieces of information included in the measurement under different sky conditions.	75
Figure 4.12	Vertical mean BrO profiles derived from ground-based measurements in a.m for 14 years for different sky conditions and seasons.	76
Figure 4.13	Vertical mean BrO profiles derived from ground-based measurements in p.m for 14 years for different sky conditions and seasons.	77
Figure 4.14	Curtain plots of the time series of the stratospheric BrO vertical distribution measured in a.m.	79
Figure 4.15	Curtain plots of the time series of the stratospheric BrO vertical distribution measured in p.m.	80
Figure 4.16	Comparison of BrO profiles derived from ZS-DOAS and SAOZ (a-e) for different days.	82
Figure 4.17	Comparison of coincident ZS-DOAS and SCIAMACHY profiles from 2002 to 2006.	84
Figure 4.18	Time series of BrO partial column densities obtained from ZS-DOAS and SCIAMACHY in 2005 and 2006.	85
Figure 4.19	Trend analysis of stratospheric BrO partial columns derived from the ground based ZS-DOAS measurements.	87
Figure 4.20	Annual mean mixing ratio of total stratospheric inorganic bromine calculated from ground-based zenith sky DOAS measurements of stratospheric BrO at Kiruna (67°N)	89
Figure 5.1	Example of an OCIO analysis of a spectrum measured on 2016 Feb. 2, 13:54 UTC	94

Figure 5.2	Comparison of halogen lamp spectra recorded by the old (January 23rd,2013) and new detectors (January 24th, 2013)	96
Figure 5.3	Time series of daily OCIO DSCDs (at $90.5^\circ \leq \text{SZA} \leq 91.5^\circ$) observed by the zenith sky DOAS instrument during three winters 1996/97 to 1998/99	97
Figure 5.4	The time series of the SZA variation from October 2015 to April 2016	97
Figure 5.5	Time series of OCIO DSCDs, RMS, spectral shift and intensity offset for analyses using either a fixed or a daily Fraunhofer reference spectrum for the winter 2015/2016	99
Figure 5.6	A systematic periodic structure in a dark current spectrum measured on 25th January, 2000; DOAS fit results of residuals, O_4 , NO_2 , and (OCIO	99
Figure 5.7	The time series of OCIO DSCDs using original and modified spectra and an absolute difference between those two	100
Figure 5.8	Diurnal variation of OCIO DSCDs as a function of SZA for three selected days of January 2016	101
Figure 5.9	Potential vorticity maps over the northern hemisphere for three selected days of January 2016	101
Figure 5.10	The annual cycle and variability of the minimum temperatures at 50 hPa in the northern hemisphere denoted by NH ($50^\circ\text{N} - 90^\circ\text{N}$, left) and the southern hemisphere denoted by SH ($50^\circ\text{S} - 90^\circ\text{S}$, right) . . .	102
Figure 5.11	Time series of the OCIO DSCD over Kiruna as well as the stratospheric temperature at the 475K isosurface in 1996/1997, 1997/1998, and 1998/1999	103
Figure 5.12	Time series of the OCIO DSCD over Kiruna as well as the stratospheric temperature at the 475K isosurface in 1999/2000, 2000/2001, and 2001/2002	104
Figure 5.13	Time series of the OCIO DSCD over Kiruna as well as the stratospheric temperature at the 475K isosurface in 2002/2003, 2003/2004, and 2004/2005	105
Figure 5.14	Time series of the OCIO DSCD over Kiruna as well as the stratospheric temperature at the 475K isosurface in 2005/2006, 2008/2009, and 2012/2013	106
Figure 5.15	Time series of the OCIO DSCD over Kiruna as well as the stratospheric temperature at the 475K isosurface in 2013/2014, 2014/2015, and 2015/2016	107
Figure 5.16	Time evolutions of the minimum temperature at different altitudes during the winter 2000/2001	109
Figure 5.17	Polar vortex maps for selected days from February 27th to March 9th, 2001	109
Figure 5.18	Time series of OCIO, BrO, NO_2 DSCDs, the total column O_3 from the OMI OMDOAO ₃	111
Figure 5.19	PM/AM ratio of the OCIO DSCDs (SZA $90.5^\circ - 91.5^\circ$) from 96/97 to 15/16 winters	112
Figure 5.20	Example of the OCIO analysis of a spectrum measured on 2016 Jan. 10, 09:14 UTC (SZA at 91.42°)	115
Figure 5.21	Comparison of daily OCIO SCD measured over Kiruna by GOME-2A/B (GDP-4.8) and the ground based measurements	115

Figure 5.22	Comparison of OCIO SCDs obtained from Zenith Sky DOAS and satellite observations	116
Figure 6.1	SO ₂ vertical column densities derived from GOME-2 measurements in September 1, 2014	122
Figure 6.2	DSCDs of SO ₂ and O ₃ obtained from ground-based zenith sky DOAS measurements	123
Figure 6.3	Scheme of the SO ₂ background correction	123
Figure 6.4	SO ₂ vertical column density derived from GOME-2 on MetOp A & B for the selected eight days during the fissure eruption	125
Figure 6.5	SO ₂ and BrO dSCDs from Sep.4 to Sep.30	126
Figure 6.6	BrO DSCDs measured by the ground-based zenith sky DOAS on Sep.11, Sep.26, Sep.27, and Sep.29, 2014	127
Figure 6.7	MODIS-Terra & Aqua cloud top pressure and cloud optical thickness images on Sep.11 and Sep.26	128
Figure 6.8	BrO DSCDs measured by the ground-based zenith sky DOAS on Sep.06, Sep.11, Sep.13, and Sep.14, 2013	130
Figure A.1	Curtain plots of the time series of the stratospheric NO ₂ vertical distribution measured in a.m from 1997 to 2016	142
Figure A.2	Curtain plots of the time series of the stratospheric NO ₂ vertical distribution measured in p.m from 1997 to 2016	143
Figure A.3	Trend analysis of NO ₂ VCDs determined by the Langley plot method	144
Figure A.4	Trend analysis of NO ₂ VCDs determined by the integrated profiles	145
Figure A.5	Comparison for the different ozone cross sections	146
Figure A.6	Time series of BrO RMS of the residuals, and Taylor series O ₃ dSCDs measured on 2013, p.m	146
Figure A.7	Monthly mean BrO profiles from ZS-DOAS observations from 1997 to 2016 retrieved by SZA 80°	147
Figure A.8	Monthly mean BrO profile from ZS-DOAS observations from 1997 to 2016 retrieved by SZA 85°	148
Figure A.9	Box and whisker plots of time series of stratospheric BrO partial columns (15 – 27 km) from 1997 to 2016 derived from integrating retrieved profiles by the OEM method at SZA 80°	149
Figure A.10	Box and whisker plots of time series of stratospheric BrO partial columns (15 – 27 km) from 1997 to 2016 derived from integrating retrieved profiles by the OEM methods at SZA 85°	149
Figure A.11	The minimum temperature for the Arctic polar region on the 50hPa surface between 50°N and 90°N during the winter of 1998/1999 in comparison to the climatological mean of the years between 1978 and 2017	150
Figure A.12	The minimum temperature for the Arctic polar region on the 50hPa surface between 50°N and 90°N during the winter of 1999/2000 in comparison to the climatological mean of the years between 1978 and 2017	151

Figure A.13	The minimum temperature for the Arctic polar region on the 50hPa surface between 50°N and 90°N during the winter of 2013/2014 in comparison to the climatological mean of the years between 1978 and 2017	152
Figure A.14	Curtain plots of the time series of the stratospheric BrO vertical distribution measured in a.m from 1997 to 2016	154
Figure A.15	Curtain plots of the time series of the stratospheric BrO vertical distribution measured in p.m from 1997 to 2016	155
Figure A.16	Trend analysis of BrO VCDs determined from the integrated profiles	156
Figure A.17	Times series of (A) the RMS of the residuals, (B) intensity offsets, and (C) spectral shift using the original or modified spectra	157
Figure A.18	Time series of SO ₂ dSCDs from Sep.1, 2014 to Oct.5, 2014.	158
Figure A.19	MODIS-Terra & Aqua cloud top pressure and cloud optical thickness images on Sep.06 and Sep.11, Sep.13 and Sep.14	159

LIST OF TABLES

Table 1.1	Atmospheric life times, global emissions, ozone depletion potentials. anthropogenic and natural sources are included	10
Table 3.1	Specification for the ZS-DOAS spectrum evaluation for NO ₂	28
Table 3.2	Example for the potential vorticity thresholds for the polar vortex for the Arctic winter of 1994/1995.[Woyke, 1998; Raffalski et al., 2005] . .	35
Table 3.3	Overview of the SAOZ balloon flights chosen for comparison	51
Table 3.4	Comparison results of the NO ₂ partial columns derived from ground-based zenith sky DOAS and SAOZ balloon measurements.	52
Table 3.5	Summary of stratospheric NO ₂ trends reported in former studies measured at various sites. Asterisk(*) represents the trend observed in p.m.	58
Table 3.6	Derived absolute and relative trends of the stratospheric NO ₂ VCDs over Kiruna. Values in the bracket represent the trends performed from fits without QBO, solar activity and aerosol terms.	62
Table 4.1	Settings for the spectral analysis of BrO from the ground-based zenith sky DOAS measurements.	66
Table 4.2	Different O ₃ cross sections used for the BrO analysis.	68
Table 4.3	Comparison of BrO fit results during one year(2013).	69
Table 4.4	Overview of the SAOZ balloon flights chosen for comparison with the ZS-DOAS observations	81
Table 4.5	Comparison of the BrO partial columns derived from ground-based zenith sky DOAS and SAOZ balloon measurements.	83
Table 4.6	Summary of former studies investigating the stratospheric BrO trends measured at various sites.	86

Table 4.7	Derived absolute and relative trends of the partial columns of stratospheric BrO.	88
Table 4.8	Estimation of the contribution of very short-lived substances (Br _y VSLs) to total stratospheric inorganic bromine from BrO measurements	91
Table 5.1	Specification for the ground-based zenith sky DOAS spectrum evaluation for OCIO.	94
Table 5.2	Comparison of the OCIO analysis settings used in the previous sub-chapters and in the validation study of the satellite data in current subsection.	114
Table 6.1	Specification for the ground-based zenith sky DOAS spectrum evaluation settings for SO ₂ and BrO.	122
Table 6.2	Cloud classification results for four days in September.	128
Table A.1	Derived absolute trends of the stratospheric NO ₂ VCDs (molec·cm ² /year) and relative trends (%/decade) performed without semi-annual terms.	144
Table A.2	Derived absolute trends of the stratospheric BrO VCDs (molec·cm ² /year) and relative trends (%/year) performed without semi-annual terms. .	156

Part I

INTRODUCTION

Ozone exists only in small amounts in the atmosphere although it is essential to humans and other life forms outside the oceans. About 90% of atmospheric ozone is contained in the ozone layer around 25 km which absorbs harmful ultraviolet radiation from the sun. There has been already well established research about stratospheric ozone since the 1920s, first as fundamental research, and later because of the concern of the effect of a thinning ozone layer for humans and the environment. Such concerns arose after the discovery of the destructive effect of on the anthropogenic emissions of nitrogen and halogen compounds on the ozone layer [Molina and Rowland, 1974; Crutzen, 1970; Bates and Nicolet, 1950]. After these findings, many scientists and governments of the world made increased efforts to monitor the ozone layer in order to better understand ozone chemistry. In 1985 the so called ozone hole was discovered over Antarctica [Farman et al., 1985]. After this unexpected discovery the research efforts were further increased and finally the Montreal protocol with its amendments and adjustments was established. As a consequence, the ozone depleting substances have been strongly reduced. And very recent research reported even an indication of an ozone recovery [Solomon et al., 2016].

As mentioned above, stratospheric ozone research showed notable achievements but several scientific issues still remain unresolved. For example, most research focused on the Antarctic while the measurements were rarely performed at high latitude in the northern hemisphere. Arctic ozone depletion is mainly controlled by variations of temperature and dynamical processes and those meteorological conditions strongly vary from year to year in the northern hemisphere. Additionally, there has been a growing interest in the effects of climate change and the role of very short-lived halogenated species.

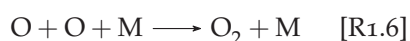
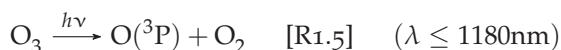
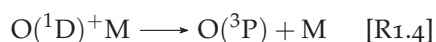
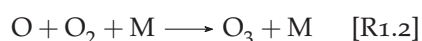
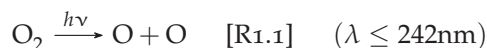
To better understand the chemical mechanisms of stratospheric trace gases involving ozone chemistry, long-period measurements of many atmospheric components are required. From such observations, the temporal and spatial variations can be determined, with particular focus on variations on different scales (diurnal, day to day, seasonal, year to year) as well as long term trends. Kiruna, Sweden is a good location for atmospheric research because dynamic variability above Kiruna is such that during winter, the measurement site is often located inside the polar vortex. From the results of this thesis an improvement of the detailed understanding of polar ozone processes, such as the relation between the polar vortex and vertical distributions of stratospheric trace gases is expected. The following points will be intensively discussed in this thesis based on the results of the Kiruna observations.

- What are the amounts of NO_2 , BrO, and OClO and how are those distributed above Kiruna?
- What is the relation between the enhanced frequency of occasional cold temperatures in the stratosphere and the variation of stratospheric trace gases?
- How well do the ground-based measurements in this work agree with other remote sensing instruments at Kiruna?
- How do stratospheric NO_2 and BrO vary in the long-term measurement data?
- What is the contribution of brominated very short-lived species (VSLS) to the total stratospheric inorganic bromine budgets?

This chapter gives a brief introduction of the chemical processes. It focuses on the stratospheric ozone layer and its formation and destruction process.

STRATOSPHERIC OZONE CHEMISTRY

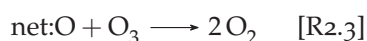
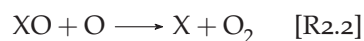
The Chapman cycle [Chapman, 1930] is a well-known theory for formation and destruction of stratospheric ozone.



Chapman proposed that the ozone layer originates from the photolysis of oxygen molecules. In the upper stratosphere there are high amounts of energetic UV light which is sufficient to photolyse the oxygen molecule. This is the initial process which forms two oxygen atoms (R1.1). The oxygen atoms combine rapidly with oxygen molecules to form ozone (R1.2). Also ozone is photolysed (but by photons of lower energy) and yield an oxygen molecule together with an excited atom (M denotes a third body molecule, likely O_2 , N_2).

To sum up, the above reactions lead to a steady state of ozone levels in the stratosphere. Because of the altitude dependencies of the air pressure and the penetration of solar radiation of different wavelengths, these processes also explains the vertical distribution of stratospheric ozone with maximum ozone concentration in the lower stratosphere. In the lower stratosphere and troposphere, the rate of O_2 photolysis becomes low. On the other hand, in the upper stratosphere the rate of recombination of $\text{O} + \text{O}_2$ becomes slow, since the concentration of third bodies reduces proportional to the atmospheric pressure. Thus, in spite of increasing UV radiation, the O_3 concentration decreases with altitude.

Figure 1.1 shows the comparison between measured ozone profiles and those obtained from the Chapman cycle. It clearly shows that the shape of the stratospheric ozone profile is qualitatively well described by the Chapman cycle, but the magnitude of the ozone concentration is systematically overestimated. This is an indication that stratospheric ozone is not only destroyed by photolysis or reaction with atomic oxygen but also by catalytic reactions involving other species e.g. hydrogen, nitrogen and halogen species. The following mechanism describes these additional ozone destruction cycles.



Here, X represents the species which is mentioned above.

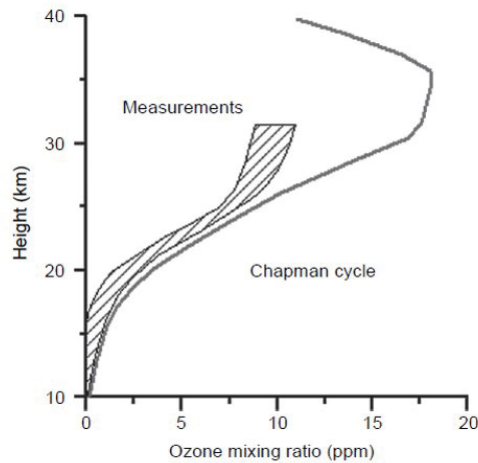


Figure 1.1: The stratospheric ozone profile according to the Chapman Mechanism, compared to observations. The figure and the caption are adopted from Platt and Stutz [2008].

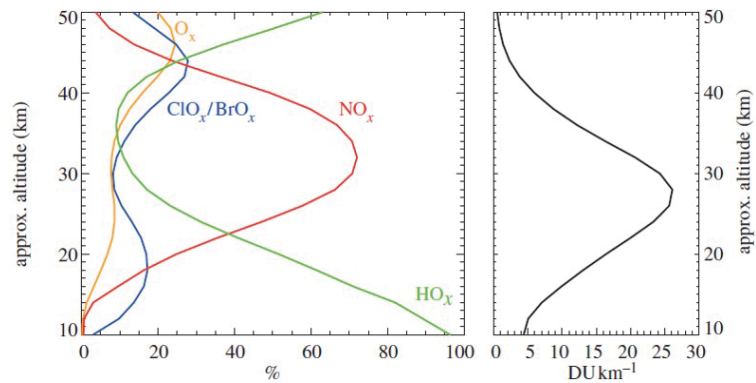
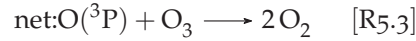
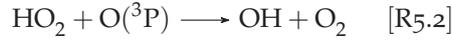
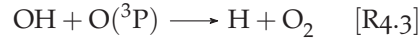
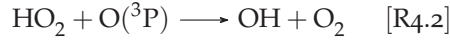
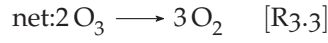


Figure 1.2: Left: The relative global mean ozone loss rates due to different catalytic destruction cycles computed for 2000 levels of source gases by the National Oceanic and Atmospheric Administration/National Center for Atmospheric Research (NOCAR) two-dimensional model; Right: The global mean ozone profile, which highlights the ozone layer maximum in the middle stratosphere. The figure and the caption are adopted from Portmann et al. [2012].

Figure 1.2 shows the global annual mean ozone loss rates by the contributions of each catalyst at different altitudes. Those catalytic destruction cycles explain the difference between measured and calculated O_3 profiles based only on the Chapman cycle. It clearly shows that the NO_x cycle mainly contributes in the middle stratosphere, HO_x does in the upper and lower stratosphere, and halogens (e.g. ClO_x and BrO_x) do in the upper and lower stratosphere.

1.1 HYDROGEN CATALYTIC CYCLE

The first catalytic ozone destruction cycle, the so-called HO_x cycle ($HO_x = OH + HO_2$) involves hydrogen species and was proposed by Bates and Nicolet [1950]. It is shown below in the groups of reactions $R_{3.x}$, $R_{4.x}$, and $R_{5.x}$. This cycle dominates in the lower stratosphere (e.g. 20 km).

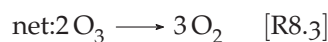
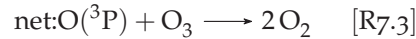
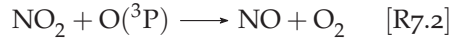


1.2 NITROGEN CATALYTIC CYCLE

Crutzen [1970] and Johnston [1971] introduced the role of the NO_x (NO + NO₂) radicals into the photochemical theory of stratospheric ozone. Stratospheric reactive NO_x mainly originates from Nitrous Oxide (N₂O) which is emitted from natural sources including ocean and soils (about 60 %), from anthropogenic sources such as biomass burning, fertilizer use, and from several industrial process (about 40 %).



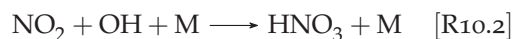
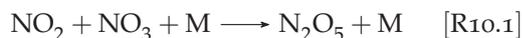
Because N₂O is stable in the troposphere, it can reach the stratosphere without significant loss. Another source of NO_x is downward transport from the mesosphere and thermosphere due to solar proton events and cosmic rays. But usually the contribution from this source is low. Major sink of stratospheric NO_y (NO_y=NO + NO₂ + NO₃ + 2N₂O₅ + HNO₃ + ClONO₂ + HO₂NO₂ + BrONO₂) is removal from the stratosphere by transport into the troposphere either in the gas phase or liquid or solid particles (HNO₃).



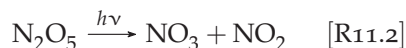
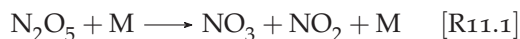
The reaction cycle 7.x dominates in the upper stratosphere where the concentration of oxygen atoms is highest, and the reaction cycle 8.x is most effective in the lower stratosphere.



Considering the diurnal variation, NO and NO₂ are in a photochemical steady state and the photodissociation of NO₂ through reaction R6, or the reaction cycles R7.x and R8.x happens during day time. The amount of NO₂ rapidly decreases early in the morning and increases during sunset due to the photolysis of NO₂. During night, dinitrogen pentoxide (N₂O₅) is formed and is photolysed under the sunlight. This leads to typically lower NO_x values in the morning than in the afternoon (except during polar night or polar day). The impact of the reactive nitrogen species on the ozone destruction is moderated by a number of three-body reactions which convert NO_x species into so-called reservoir species as shown in following chemical reactions.

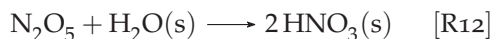


The fast photolysis of NO₂ together with the slow photolysis of N₂O₅ is responsible for the typical diurnal variation of NO₂. As a result, the increase of NO₂ during day time is shown to be almost linear.



From the reservoir species the reactive nitrogen compounds can be released by photolysis or by reaction with OH.

The conversion of NO_y into nitric acid in the liquid or solid phase (denoxification) is important in this cycle. The hydrolysis of N₂O₅ occurs on the surface of stratospheric aerosols such as aqueous sulfate aerosol or ice shown in reaction 12.



During polar winter, N₂O₅ is continuously converted into HNO₃ which is the dominant NO_y species. Some more important (heterogeneous) reactions not mentioned in this section will be discussed in Section 1.3.3.

1.3 HALOGEN CATALYTIC CYCLES

Reactive halogens in the stratosphere originate from halocarbon gases which are usually emitted from the earth surface and move to the stratosphere. In the stratosphere the halocarbon gases are converted to reactive halogens such as Cl and Br by photolysis or reactions with OH or O(¹D). The reactive halogens again react with ozone to form halogen oxides (ClO and BrO) which can be converted into other stratospheric inorganic halogen species.

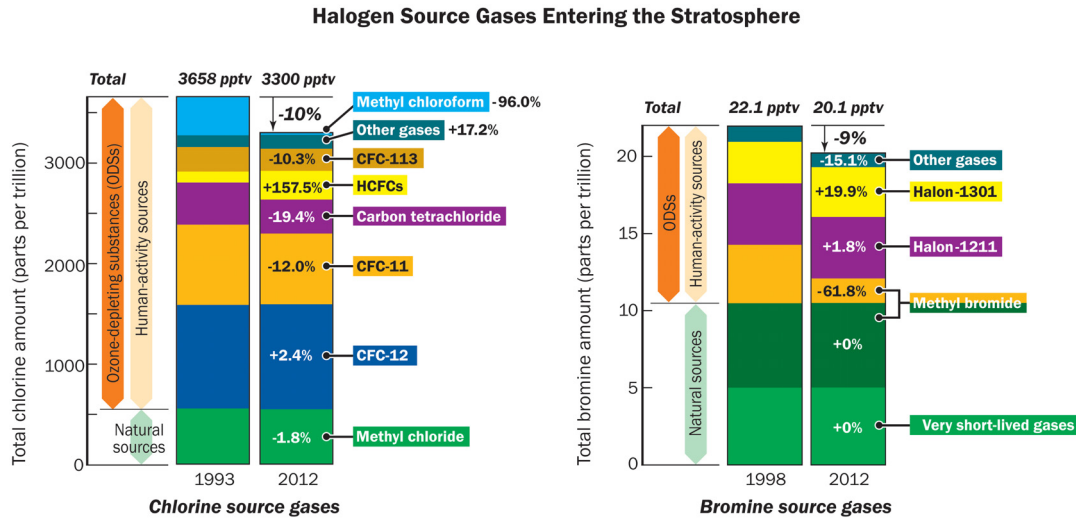


Figure 1.3: Changes in halogen source gases entering the stratosphere. The figure and the caption are adopted from Hegglin et al. [2015].

Figure 1.3 shows a summary of the change of the primary source gases of chlorine and bromine for the stratosphere from 1999 to 2012 [Hegglin et al., 2015]. The sources of chlorine in the stratosphere are classified as natural (mainly methyl chloride: CH_3Cl) and anthropogenic (chlorofluorocarbons: CFCs, along with carbon tetrachloride: CCl_4 , and methyl chloroform: CH_3CCl_3). The most critical sources are chlorofluorocarbons (CFCs) which have been industrially manufactured for a long time as a refrigerant but were banned by the Montreal protocol and its amendments. CFCs are stable in the lower atmosphere and insoluble in water. Thus the lifetime of CFCs is very long in the troposphere and they can reach to the stratosphere in which they are photolysed to release the reactive halogens by the following reactions.



Methyl bromine (CH_3Br) is the most abundant bromine source gas. It originates from both natural (oceanic and terrestrial ecosystems) and anthropogenic sources (fumigation for pest control in agriculture and disinfection of export shipping goods). As a result of the Montreal Protocol, human-made CH_3Br has significantly decreased (-61.8%) in 2012 compared to 1999. The second important source of bromine are halons (especially, Halon-1211, Halon-1301, and Halon-2402) which are emitted from human activities. Most of the main source gases of stratospheric bromine are transported from the surface to the stratosphere and are then converted into inorganic forms. The total inorganic stratospheric bromine ($\text{Br}_y = \text{BrO} + \text{HBr} + \text{Br} + \text{HOBr} + \text{BrONO}_2 + \text{BrCl}$) has decreased by $0.6 \pm 0.1\%$ /year since 2001. This decline is consistent with the decrease of the total tropospheric organic Br based on measurements of CH_3Br and the halons [Hegglin et al., 2015]. In the stratosphere, BrO is the only steadily observed bromine compound of the Br-family.

Therefore, it is important to quantify the budget of Br_y loading in the stratosphere. Several studies showed a discrepancy between the Br_y estimations derived from BrO measurements in combination with model calculations and from the expected contribution of (only) long-lived organic bromine source gases [Wamsley et al., 1998; Salawitch et al., 2005]. This finding

Table 1.1: Atmospheric life times, global emissions, ozone depletion potential of anthropogenic and natural halogen containing source gases. This table is adapted from Hegglin et al. [2015]

Halogen source gases	Atmospheric lifetime (years)	Global emissions in 2012(Kt/yr) ²	Ozone Depletion Potention(ODP)
Chlorine gasses			
CFC-11	52	46–68	1
CFC-12	102	16–64	0.73
CFC-113	93	0–7	0.81
Carbon tetrachloride (CCl ₄)	26	40–74	0.72
HCFCs	1–18	400–528	0.01–0.1
Methyl chloroform (CH ₃ CCL ₃)	5	0–5	0.14
Methyl chloride (CH ₃ Cl)	0.9	2708	0.015
Very short-lived Cl-containing gases	less than 0.5	^b	^b very low
Bromine gasses			
Halon-1301	72	1.4–2	15.2
Halon-1211	16	0.3–9.3	6.9
Methyl bromide (CH ₃ Br)	0.8	85	0.57
Very short lived Br-containing gases	less than 0.5	^b 260–1080	^b very low

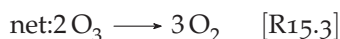
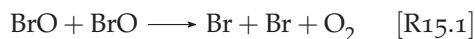
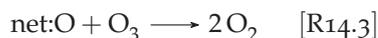
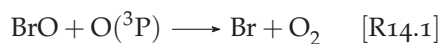
^a Includes both human activities and natural sources. 1 kilotonne =1000 metric tons =1Gg=10⁹ grams

^b Estimates are very uncertain for most species

indicates that there are probably other possible bromine compounds (e.g. so-called Very short lived species (VSLs)), which will be discussed in the result section of this thesis. Table 1.1 shows an overview of atmospheric lifetimes and ozone depletion potentials of the most important chlorine and bromine source gases [Hegglin et al., 2015].

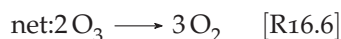
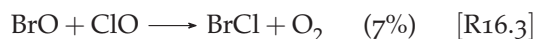
1.3.1 Bromine Chemistry

This section includes the bromine-catalysed destruction cycles of O₃ presented in Lary [1996]; Lary et al. [1996]; Molina and Rowland [1974]; Wofsy et al. [1975]



Here, the reaction cycle 14.x shows the 'classical' bromine catalysed O_3 destruction cycle while the cycle 15.x represents another bromine-catalysed ozone destruction cycle via the BrO-BrO self-reaction. However, the contribution of this additional cycle to ozone loss is very low due to the slow rate.

There exists also a combined bromine-chlorine cycle:



The reaction cycle 16 shows that the reaction of BrO with ClO has several channels, which is most important for the polar lower stratosphere. This is because bromine is most effective while chlorine is strongly activated inside the polar vortex, which can effectively destroy ozone.

The following reaction cycle shows the formation and destruction of bromine reservoir species. Here, the reaction 17.1 is not involved in catalytic ozone destruction. However, if BrONO_2 photolysis produces Br and NO_3 , then catalytic destruction of ozone can occur [Lary, 1996].

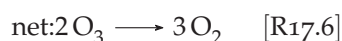
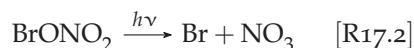


Figure 1.4 shows the modeled diurnal variation of the bromine partitioning in the lower stratosphere calculated by the SLIMCAT global 3D chemical transport model by Sinnhuber

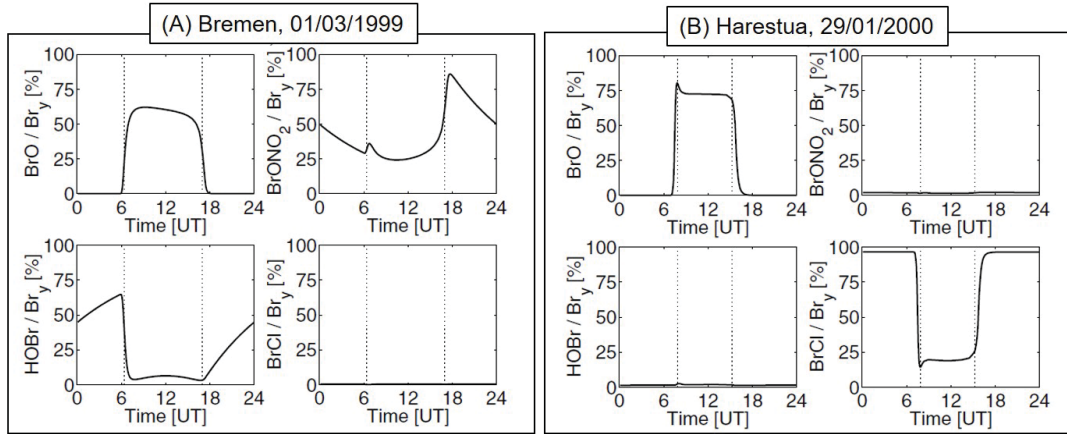


Figure 1.4: Diurnal cycle of the relative contribution of the most abundant bromine species BrO, BrONO₂, HOBr and BrCl in the lower stratosphere (480K isentropic level), calculated by a photochemical model. (A) shows the typical bromine partitioning at mid-latitudes (Bremen, 53°N), (B) shows the bromine partitioning for a situation of high chlorine activation (Harestua, 60°N). This figure and caption are adapted from Sinnhuber et al. [2002].

et al. [2002]. Figure 1.4(A) shows an example for Bremen on 1. March 1999 which represents a typical behavior at mid-latitudes. It shows that BrO is the major inorganic bromine species during day time and BrONO₂ is the most important bromine reservoir as shown in reactions below.



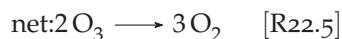
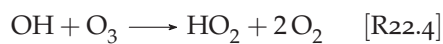
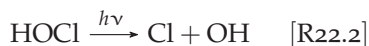
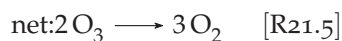
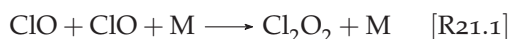
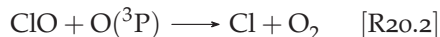
These reactions are not only important for the diurnal variation but also for the yearly variation of BrO. The BrONO₂ concentration mainly depends on the actinic flux, as well as the concentration of NO₂, and aerosols [Höpfner et al., 2009]. During polar winter, due to the denoxification and possible denitrification, the NO₂ concentration decreases. Thus also the formation of BrONO₂ decreases and the BrO concentration increases. In contrast, in summer BrO decreases due to an enhanced BrONO₂ abundance. The model also considered heterogeneous reactions, in particular that BrONO₂ is converted by hydrolysis on sulfate aerosols into HOBr during night (a major bromine reservoir before sunrise). [Hanson and Ravishankara, 1995; Hanson et al., 1996; Lary et al., 1996].



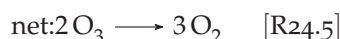
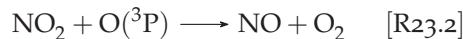
At sunrise, BrO rapidly increases due to the fast photolysis of HOBr. The hydrolysis of BrONO₂ is generally important as it influences the HOx and NOx abundances, and it is connected to the stratospheric ozone depletion. For the conditions of strong chlorine activation (see figure 1.4(B)), the reaction cycle 16 of BrO and ClO becomes important. These reactions are important for situations with small concentrations of NO₂ and large amount of reactive chlorine species. In such conditions, the concentrations of BrONO₂ and HOBr are very low and inorganic bromine is almost exclusively partitioned between BrO and BrCl.

1.3.2 Chlorine Chemistry

Molina and Rowland [1974] mentioned the impact of the CFCs on ozone. CFCs are photolysed in the stratosphere into inorganic chlorine compounds. These inorganic compounds are involved in the following reactions:



Here, Reactions 20.x show the chlorine-catalysed O_3 destruction cycle which is one of the most effective ozone loss cycles at 35 to 45 km. The self reaction of ClO in reaction 21.x (ClO-dimer cycle) is especially important in the polar regions during winter conditions, if polar stratospheric clouds (PSCs) are present. The reaction cycle 22.x is an important link between chlorine and odd-hydrogen chemistry. It is effective at the mid-latitude lower stratosphere and also plays a role in the sunlit polar lower stratosphere.



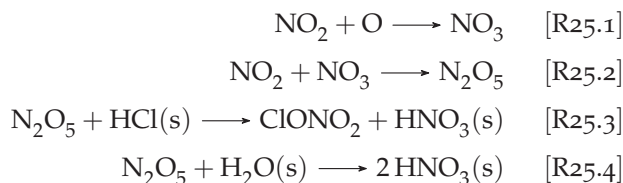
The reaction cycle 24.x shows the formation of the reservoir species of ClOx through the reactions of NO_2 .

1.3.3 *Heterogeneous Halogen Chemistry*

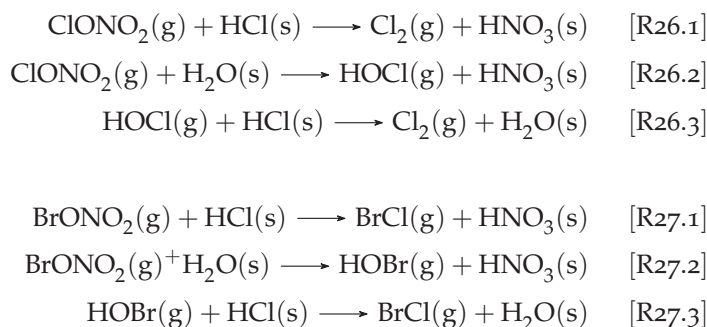
Farman et al. [1985] discovered the strong ozone depletion over Antarctica during polar spring. There was nearly complete ozone loss in the altitude range 14 – 24 km. This phenomenon could not be explained using only the gas-phase reactions mentioned above. The prerequisite for strong ozone destruction in the polar region is the formation of polar stratospheric clouds (PSCs). During polar night a polar vortex forms and blocks the external warmer airmasses from lower latitude. If the temperature falls below 195K, PSCs are formed. Water, nitric acid and sulfuric acid are the main constituents of PSCs. On the surface of the solid (s) PSC particles, heterogeneous reactions can occur.

PSCs are classified into three subtypes based on their composition and formation temperatures [Beyer et al., 1994; Carslaw et al., 1994, 1997; Luo et al., 1995]: The stratospheric sulfate aerosols take up water and nitric acid and form so-called supercooled ternary solutions (STS) ($\text{H}_2\text{SO}_4 \cdot \text{H}_2\text{O} \cdot \text{HNO}_3$). The STS droplet composition depends on the temperature. During the cooling of the STS, the fraction of HNO_3 increases in the droplet but H_2SO_4 decreases. Below the ice frost point where this mixture is frozen, nitric acid trihydrate (NAT) is formed. PSC Type 1a defines a solid NAT particle, and type 1b refers a liquid STS droplet. The last type (PSC type2) is mainly composed of ice particles and is formed in the stratosphere at very low temperature, below the ice frost point at approximately 188K.

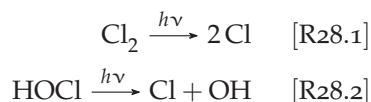
During polar night, the absence of sunlight changes the stratospheric chemistry, such that NO_x is converted into N_2O_5 and then further converted to HNO_3 (denoxification) as shown in the reaction below.



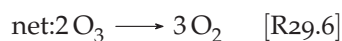
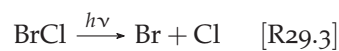
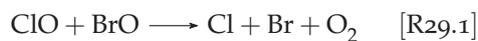
PSCs provide the surface for the heterogeneous reactions converting halogen reservoir species to more reactive species.



At the beginning of polar spring, photochemically unstable compounds rapidly photodissociate and release Cl atoms by the following reactions.



O_3 is destroyed by two gas-phase catalytic cycles, the first is the ClO-dimer cycle [Molina and Molina, 1987] (reaction cycle 21.x), which is responsible for the majority (70-80%) of the ozone depletion in the polar vortex in the late winter/early spring. The second is the ClO/BrO cycle [McElroy et al., 1986] described by the following reactions:



In contrast to the other catalytic ozone destruction cycles, these two cycles require sun light. Thus they can only occur after the end of the polar night. They explain most of the ozone loss observed in the Arctic and Antarctic stratosphere in the late winter/early spring season (when sunlight returns to the polar regions).

METHODOLOGY

This thesis includes the investigation of the temporal and spatial distributions of stratospheric NO_2 , BrO , and OCIO measured from a ground-based zenith sky DOAS instrument. These trace gases show distinctive narrow absorption structures in the visible and/or UV spectral ranges. Differential Optical Absorption Spectroscopy (DOAS) is a remote sensing technique which allows to detect and to analyse these atmospheric trace gases. This method was introduced by Perner et al. [1976] and Platt and Stutz [2008] and it has been improved over several decades. The following chapter describes the principle of the absorption spectroscopy and the DOAS technique mainly based on Platt and Stutz [2008].

2.1 ABSORPTION SPECTROSCOPY

When molecules absorb or emit photons, the energy state of molecules is changed. Photons of the UV/Vis wavelength ranges have high enough energy to cause electronic transitions of the absorbed molecule. Each molecule has its own characteristic absorption spectrum depending on its molecular structure, more specifically on the electronic, vibrational, and rotational states. Therefore, the absorber and its concentration can be identified from the type and the strength of its absorption. The specific absorption spectra of each molecule are the basis for the absorption spectroscopy technique.

The Lambert-Beer's law describes the relation between the absorption and the concentration of an absorber:

$$dI(\lambda) = -\sigma(\lambda)\rho(s)I(\lambda)ds, \quad (2.1)$$

where, $I(\lambda)$ represents the light intensity at a certain wavelength λ after passing through a very thin layer ds . $\rho(s)$ is the number density of an absorber and $\sigma(\lambda)$ stands for the absorption cross section at a given wavelength. Equation 2.1 can be re-written by partially integrating the number density of the absorber over distance L ,

$$I(\lambda, L) = I_0(\lambda)\exp\left(-\sigma(\lambda)\int_0^L \rho(s)ds\right). \quad (2.2)$$

After integration under the assumption of a homogeneous absorber concentration, Eqn. 2.2 becomes:

$$I(\lambda) = I_0(\lambda)\exp\left[-\sigma(\lambda)\rho L\right], \quad (2.3)$$

$$\ln \frac{I_0(\lambda)}{I(\lambda)} = \sigma(\lambda)\rho L, \quad (2.4)$$

$$\tau = \sigma(\lambda)\text{SCD}, \quad (2.5)$$

where τ is the optical density of the particular absorber and $\text{SCD}=\rho(\lambda)L$ is the integrated concentration along the light path (SCD: slant column density).

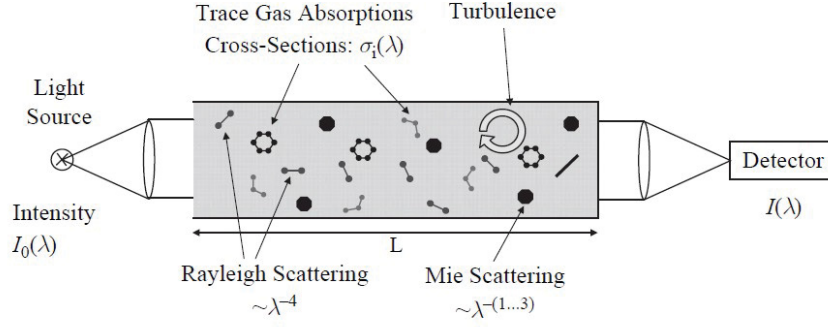


Figure 2.1: Scheme of an experiment to measure trace gas absorptions in open air conditions so-called long path DOAS. It represents the direct application of the Lambert-Beer law. Figure and caption adopted from Platt and Stutz [2008]

2.2 DIFFERENTIAL OPTICAL ABSORPTION SPECTROSCOPY (DOAS)

For the measurement of individual trace gases, the Lambert-Beer's law in Eqn. 2.2 cannot directly be applied to open atmospheric measurements because several processes occur simultaneously including absorption by trace gases and, aerosols as well as scattering on molecules and aerosols, as shown in Fig. 2.1. Also, turbulence and instrumental effects have to be taken into account.

Therefore, Eqn. 2.2 can be expanded to:

$$I(\lambda, L) = I_0(\lambda) \exp \left[- \int_0^L \cdot \sum_j (\sigma_j(\lambda) \cdot c_j(s)) + \epsilon_R(\lambda, s) + \epsilon_M(\lambda, s) \cdot ds \right] \cdot A(\lambda), \quad (2.6)$$

where, $\epsilon_R(\lambda)$ and $\epsilon_M(\lambda)$ represent the extinction coefficients for Rayleigh and Mie scattering, respectively. $A(\lambda)$ accounts for instrumental effects and the scattering efficiency of direct sun light into the line of sight of the instrument. To calculate the concentration of a certain trace gas it is necessary to quantify all other influencing factors which is not possible for the open atmospheric measurement. Differential Optical Absorption Spectroscopy (DOAS) solves this problem by using the fact that aerosol extinction, molecular scattering and the effect of turbulence show very broad or even smooth spectral characteristics, while many trace gases can be identified by their characterising narrow-band absorption structure.

Figure 2.2 shows the way of separation of broad and narrow band structures for an absorption band. The total absorption cross section consists of narrow and broad band structures:

$$\sigma_j(\lambda) = \sigma_{j0}(\lambda) + \sigma'_j(\lambda), \quad (2.7)$$

where, σ_{j0} denotes the broad-band contribution which is mainly caused by Rayleigh and Mie scattering. σ'_j refers to the narrow-band contributions which represent the-characteristic 'rapid' absorption features of a trace gas. Thus Eqn. 2.6 is re-written by taking these narrow- and broad band absorptions into account:

$$I(\lambda, L) = I_0(\lambda) \exp \left[- \int_0^L \cdot \left(\sum_j (\sigma'_j(\lambda) \cdot c_j(s)) \right) ds \right] \cdot \exp \left[- \int_0^L \cdot \left(\sum_j (\sigma_{j0}(\lambda) \cdot c_j(s)) + \epsilon_R(\lambda, s) + \epsilon_M(\lambda, s) \right) \cdot ds \right] \cdot A(\lambda). \quad (2.8)$$

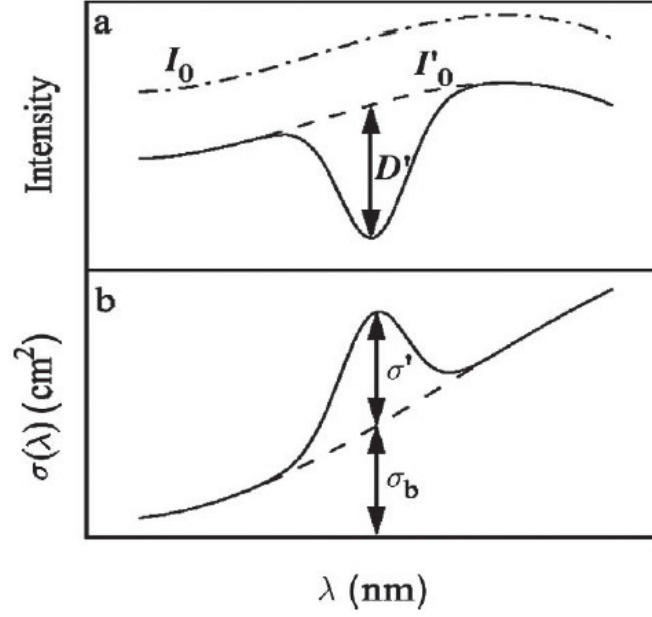


Figure 2.2: The principle of DOAS: I_0 and σ are separated by an adequate filtering process into a narrow (D' and σ' and broad band part I'_0 and σ_b). Figure and caption adopted from Platt and Stutz [2008]

Here, the first exponential term describes the narrow band absorptions by atmospheric trace gases and the second exponential term describes the broad-band caused by gas and aerosol absorptions as well as scattering processes. Now the modified initial intensity I'_0 can be defined:

$$I'_0(\lambda) = I_0(\lambda) \cdot \exp \left[- \int_0^L \cdot \left(\sum_j (\sigma_{j0}(\lambda) \cdot c_j(s)) + \epsilon_R(\lambda, s) + \epsilon_M(\lambda, s) \right) \cdot ds \right] \cdot A(\lambda). \quad (2.9)$$

In practice, the broad-band contribution of a measured spectrum is approximated by polynomial functions. The differential cross-sections σ'_j can be determined by a high-pass filtering of a trace gas measurement in the laboratory. If the initial light intensity and the effective light path are known, the mean concentration of the individual absorbers can be determined by Eqn. 2.9. Considering all above processes, the differential optical density (D') can be determined by:

$$D' = \ln \frac{I'_0(\lambda)}{I(\lambda)} = \int_0^L \cdot \left(\sum_j (\sigma'_j(\lambda) \cdot c_j(s)) \right) ds. \quad (2.10)$$

For the quantitative trace gas analysis, the measured spectra are fitted by the absorption spectra of different trace gases which show narrow absorption features in the respective spectral range and a polynomial function via a non-linear least square fitting algorithm. The detailed mathematical descriptions of the spectral fitting process can be found in Platt and Stutz [2008].

2.3 PASSIVE DIFFERENTIAL OPTICAL ABSORPTION SPECTROSCOPY

The DOAS measurements can be performed using artificial light sources (active DOAS) or natural light sources like the Sun, the Moon, and stars (passive DOAS). Passive DOAS is subdivided into direct and scattered light measurements. The scattered sunlight measurements

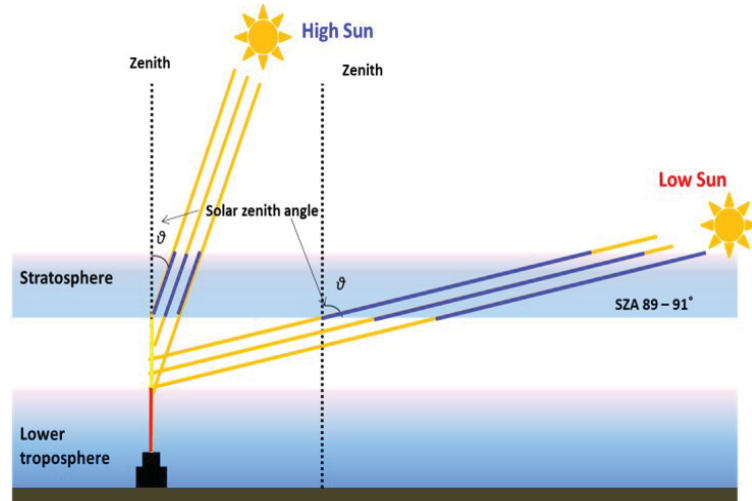


Figure 2.3: Geometry of a zenith sky DOAS measurement and radiation transport in the atmosphere assuming single scattering. This figure and caption are modified from Richter [2018].

are commonly used and have the advantage of a relatively simple experimental setup, which can be easily installed also in dangerous and remote areas. One important disadvantage of passive DOAS is that the quantitative interpretation is more difficult because the conversion of the observed slant column densities (SCDs) into vertical column densities (VCDs), or even concentration, profiles are big challenges. Because it is difficult to determine the atmospheric light path length when using the passive scattered light DOAS radiative transfer calculations are typically considered.

2.3.1 Ground based zenith sky DOAS

Since the observations in this thesis are based on a ground-based zenith sky DOAS instrument, a brief introduction of the instrument is presented in this section. The instrument detects scattered sun light at zenith direction (elevation angle of 90°). This is the earliest application of the passive DOAS which is useful for the observations of stratospheric trace gases and has largely contributed to the understanding of the stratospheric O_3 catalytic destruction cycles, (e.g NO_x , ClO_x , BrO_x etc) [Noxon, 1975; Noxon et al., 1979; Harrison, 1979; McKenzie and Johnston, 1982; Solomon et al., 1987; Fiedler et al., 1993; Pommereau and Piquard, 1994; Kreher et al., 1997]. Figure 2.3 shows the geometry of the zenith sky DOAS and how the scattered light travels to reach the detector. The observations of stratospheric trace gases are usually analysed during twilight periods (when the Sun is low, around SZA $89^\circ - 91^\circ$). Under these conditions, the sensitivity of the zenith sky DOAS for stratospheric trace gases is enhanced as a result of the long light paths in stratosphere. In Fig. 2.3, the light path in the troposphere (marked as red) is the same for measurements at high and low Sun. Because the slant column densities for stratospheric absorbers are much greater during twilight, this tropospheric effect will cancel out by comparing noon and twilight measurements of the same day.

As already mentioned it is a challenge to convert the SCD into VCD at large SZA, so usually radiative transfer model simulations are required. Platt et al. [1997] introduces various effects which might influence the accuracy of zenith sky DOAS measurements including overlapping spectra of different trace gases, the effect of spectral distortion,



Figure 2.4: Picture of the ground-based zenith sky DOAS at Kiruna, Sweden: (A) Outside on the roof, the arrow indicates the glass dome for the zenith sky DOAS measurements. (B) Image of the glass dome (C) Detector and spectrograph (inside the box), and (D) View of the inside of glass dome to prevent moisture

temperature dependence of absorption cross sections, stray light, signal dependent dark current, polarisation sensitivity of the spectrometer, Ring effect, the uncertainty of the air mass factor, scattering due to tropospheric and stratospheric clouds, etc. If those effects are properly considered the uncertainties of the calculated VCDs can reach below about 10%.

2.3.2 Instrument History

This part presents the history and the current state of the instrument used in this thesis. It contains two parts, one of which describes the history of the instrument and the other the instrumental setup.

2.3.2.1 Instrument History

The ground-based zenith sky DOAS (ZS-DOAS) instrument was installed at around 7 km east of Kiruna at the Institute for Rymdfysik (IRF) Kiruna (Sweden) in December 1996 and since then the instrument has operated continuously (but with several periods without measurement due to technical problems).

Since the ZS-DOAS observations used in this study are already described in detail in Bugarski [2003] and Gottschalk [2013], only a brief overview of the instrument is given here. At the beginning, the ZS-DOAS instrument consists of two spectrograph/detector systems for the UV and visible spectral ranges, covering the wavelength ranges 300 – 400 nm and 347 – 682 nm, respectively. Three years later (October 6th, 1999), the instruments were moved into the inside of the IRF institute building. Since then the air temperature was much more stable, which also lead to more stable instrument operation. This improvement can also be seen in the results of the BrO spectral analysis (Fig.2.5). It shows different quality

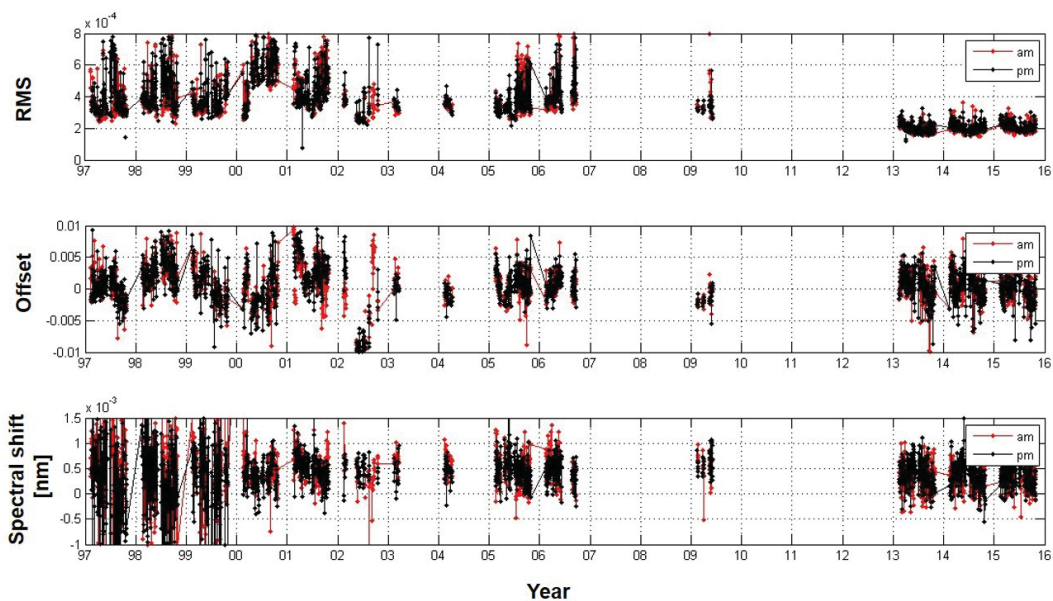


Figure 2.5: Time series of different instrument quality parameters from 1997 to 2016: Upper panel: RMS of the spectra residual, middle: fitted intensity offset, lower: spectral shift. Red and black lines denote measurements at a.m (sunrise) and p.m (sunset), respectively.

parameters, e.g. root mean square of the spectral residual (RMS), the fitted intensity offset, and the spectral shift. It is clearly seen that the spectral shift which is most sensitive to the temperature reduces significantly since 2000.

In addition, it indicates several technical problems, for example, in 2001 the spectrometer temperature controller had problems, and also the photo diode array (PDA) detector had an enhanced noise level. Since beginning of 2009, problems with the old PDA detector occurred. In particular it was not anymore compatible to state of the art computer systems (it only worked with an old window 98 computer). Thus the detector was replaced in 2012 by a CCD detector (Charge Coupled Device) to start again the monitoring. It can be seen in the figure that the new detector has a much lower noise level, which leads to significant reduced RMS values after 2013. The detailed setup information is reported by Gottschalk [2013].

2.3.2.2 Composition of the instrument

Figure 2.6 describes the installation of the zenith sky DOAS, which consists of two main parts, the telescope unit (the light receiving part) and the spectrograph part. In the light receiving part (fig. 2.6, left), scattered sunlight passes through the glass dome in the ceiling (fig. 2.4, B) and is collected by a focal lens on top of the telescope unit. The focused light passes an optical filter and falls into a fiber glass bundle. The UG-5 filter (product of Schott Glaswerke) reduces the incoming visible light (420 – 650 nm) in order to reduce the amount of spectral stray light. The light receiving part is connected via the glass fiber bundle to the UV spectrograph. It is developed by Heidelberg University in 1996, details of which are described in Otten [1997]; Bugarski [2003]. The spectrograph is covered with an aluminum box and polystyrene layers for insulation. It is connected with a CCD detector. The end of the glass fibre bundle is formed as a slit, and is attached to the entrance of the spectrograph. The incoming light is reflected by a spherical flat-filied grating and projected onto the detector.

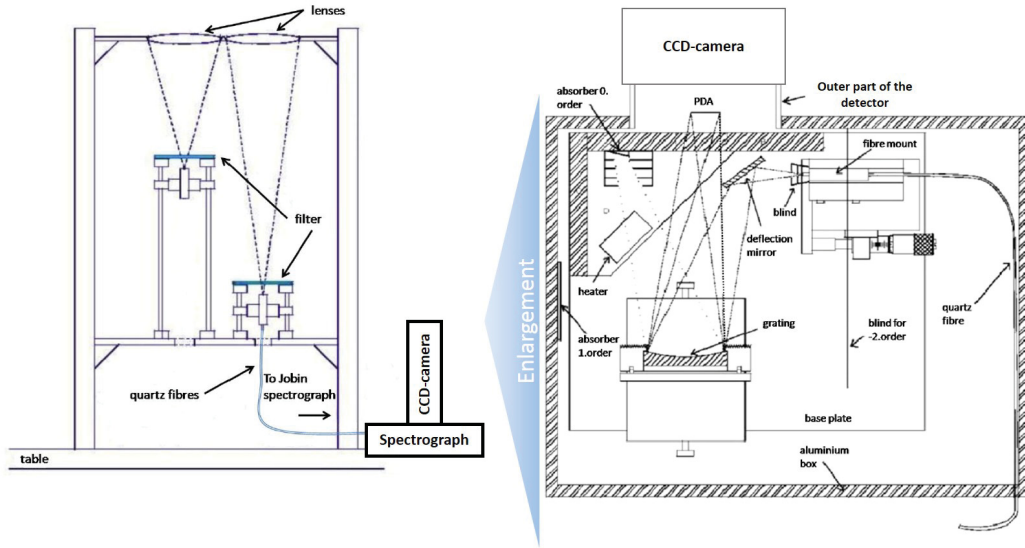


Figure 2.6: Sketch of the telescope settings (left) and the UV spectrograph. Modified version from Otten [1997]

From 1996 to beginning of 2013, a 1D photo diode array (PDA) was used. In January 23, 2013, a new detector with 2 dimensional CCD array was installed. One (vertical) dimension of the detector is binned, and the other (horizontal) dimension contains the spectral information. Here, Fig.2.7 and Fig.2.8 show examples of 2D CCD image and an extracted spectrum, respectively. Figure 2.7 shows the full image which is taken after the adjustment of the new detector on the January 24th, 2013. In the illuminated part, the Fraunhofer lines as dark vertical lines are clearly seen. And the horizontal lines indicate the different glass fibres which connect the telescope with the spectrograph. Figure 2.8 is taken from the measurement mode as full vertical binning and the duration time is set to approximately 300 s. To this measured spectrum offset, dark current correction and the wavelength calibration were already applied.

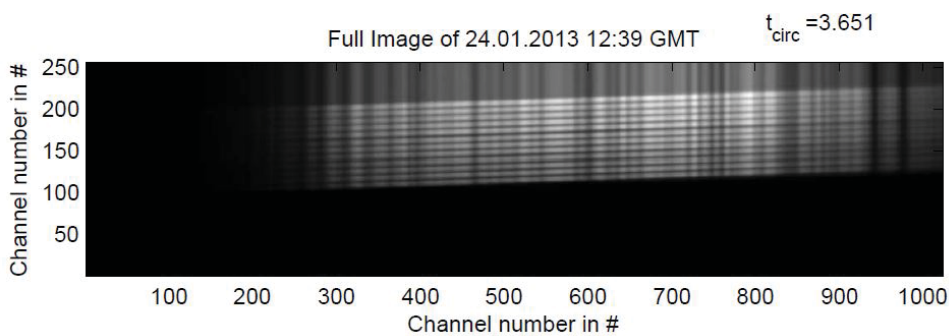


Figure 2.7: The full image has been recorded on the 24th January 2013 as an example for the settings of the long term measurement. The black parts indicate areas with no light. This figure and a cation are adopted from Gottschalk [2013].

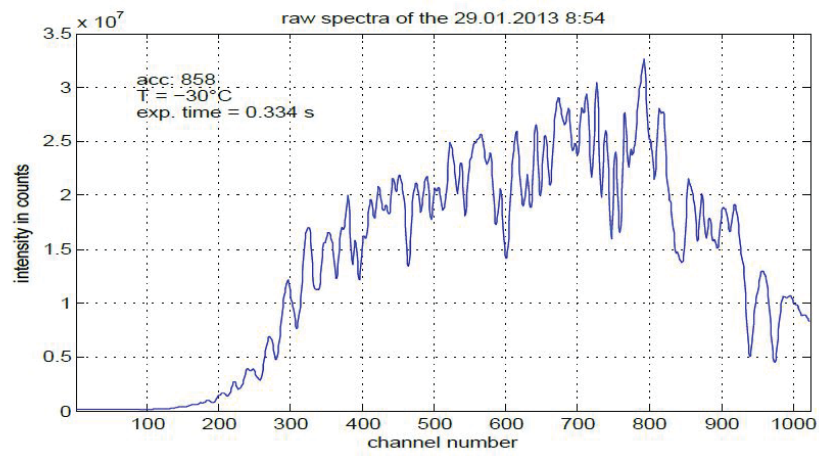


Figure 2.8: Raw spectrum output of the camera on the 29th January 2013 at 8:54 GMT. In addition the number of accumulations, the measuring temperature and the exposure time is shown as well. This figure and a cation are adopted from Gottschalk [2013].

Part II

RESULTS: STRATOSPHERIC TRACE GASES

Nitrogen oxides (NO_x=NO₂+NO) play an important role in the chemistry of both the stratosphere and the troposphere. Especially, stratospheric NO_x has been a long-lasting research topic since about 1970 with several observation techniques including ground-based remote sensing observations, balloon-borne measurements, air-borne measurements, and satellite observations [Brewer et al., 1973; Noxon, 1975; Noxon et al., 1979; Coffey et al., 1989; Otten et al., 1998; Mankin et al., 1990; Liley et al., 2000; Hendrick et al., 2004; Richter et al., 2005; Kühl et al., 2008]. NO_x acts as a buffer against halogen catalysed O₃ loss and also is involved in the O₃ destruction cycle depending on altitude. During the last decade, several studies have shown the spatial and temporal variation of stratospheric NO₂ for different locations and periods. Recent studies were often based on satellite observations and their comparison with the ground-based observations in order to validate the satellite observations and quantify potential discrepancies. At Kiruna the NO₂ observations can contain both stratospheric and tropospheric adsorptions. Since Kiruna is located at a high latitude it is relatively unpolluted and thus, it is usually dominated by stratospheric NO₂.

In this chapter, the results are divided into five parts. Overall, this chapter describes the retrieval of stratospheric NO₂ during the last nineteen years of measurements in Kiruna using the ground-based zenith sky DOAS (ZS-DOAS) instrument. The general temporal variation of stratospheric NO₂ is described in the first section. The second and third sections show the derived vertical distribution of stratospheric NO₂. The comparison results with other data sets are presented in the fourth section, and finally, a non-linear least squares model used for the trend study as well as the results of the trend analysis is presented.

3.1 ANALYSIS

3.1.1 Wavelength ranges and reference spectra

In this section, the analysis settings for stratospheric NO₂ are described in detail. First of all, UV spectra recorded by the ZS-DOAS are evaluated using the DOAS technique [Platt and Stutz, 2008]. For the NO₂ analysis the spectral range of 356 – 392 nm is chosen; further analysis details are summarised in Tab. 3.1 and Fig. 3.1.

Here, two daily reference spectra taken at a Solar Zenith Angle (SZA) of 80° in a.m and p.m are used for the spectral analysis of stratospheric NO₂. By using daily reference spectra, the fit residuals can be largely minimised. Figure 3.2 shows the variation of available SZA ranges above Kiruna. It clearly shows how the SZAs at the Kiruna vary with season. Since Kiruna is located at high latitude in the winter solstice the minimum SZA stays above 90°. While it is often located below the polar vortex, the period outside the polar night is longer than for many other polar measurement sites (e.g Eureka (80°N), NyAlesund (79°N)). Nevertheless, it is very challenging to get retrievals of vertical profiles and VCDs in winter and summer solstice periods because during these periods the variations of the SZA in

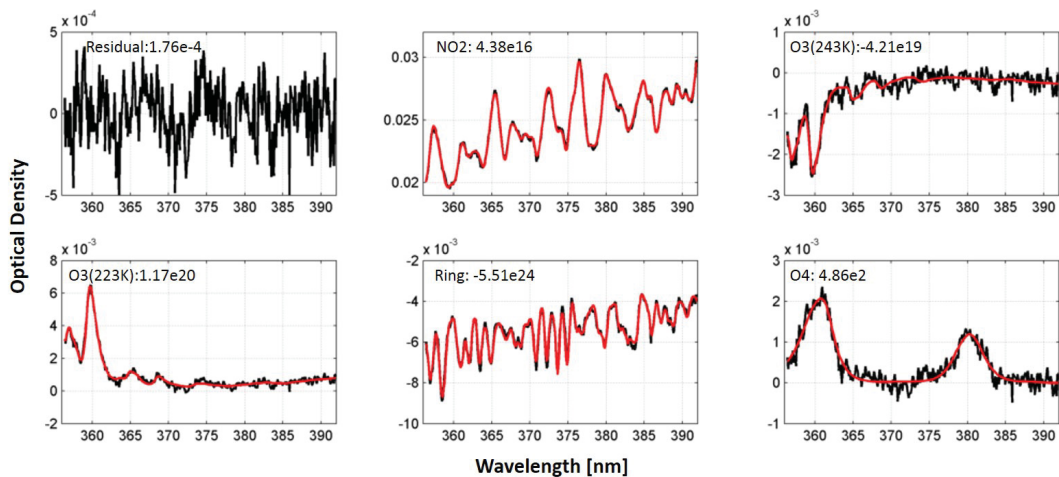


Figure 3.1: Example of a NO₂ analysis of a spectrum measured on 2015 Sep.14, 17:03 UTC (SZA at 89°). The red lines indicate the different reference spectra scaled to the respective absorptions retrieved from the measured spectrum (black lines).

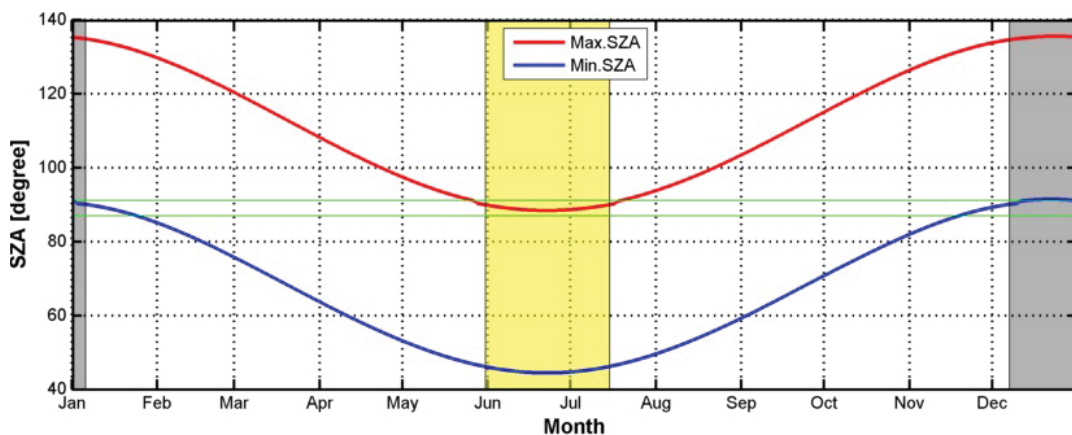


Figure 3.2: The variation of SZA in Kiruna. Red and blue lines indicate the seasonal variation of the maximum and minimum SZAs during the year. The grey shaded area represents the period of the polar night when the sun does not rise above the horizon, while the yellow shaded area indicates when the sun is never below the horizon. The green lines indicate SZA 87° and 91°, respectively.

sunset and sunrise are rather small. Strategies to deal with this challenge will be discussed in Sec.3.1.3 in detail.

Table 3.1: Specification for the ZS-DOAS spectrum evaluation for NO₂.

Fitted Spectra	Reference
NO ₂	Vandaele et al. [1998] 220K
O ₃	Bogumil et al. [2003] 223K, 243K
O ₄	Greenblatt et al. [1990] 273K
Ring	Kraus [2006]; Wagner et al. [2009]
Polynomial order	5th

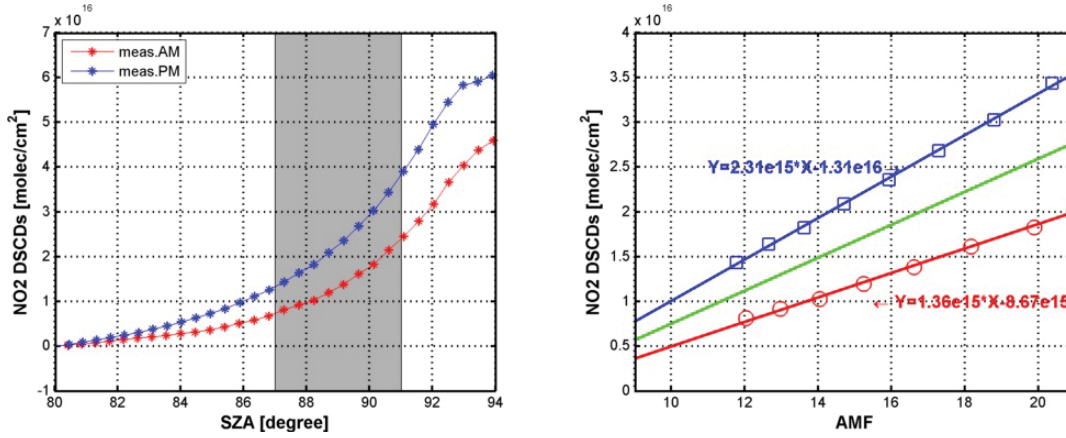


Figure 3.3: Example to illustrate the Langley plot method. Left: NO₂ dSCDs measured on 20 March 2015. Red and blue lines indicate the values during a.m and p.m twilight. The grey shaded area represents the range of SZA 87°–91° used for the Langley-plot. Right: Langley plot for SZA 87°–91° on that day. The green line represents the mean values between a.m and p.m.

3.1.2 Langley plot method

In this study, daily based reference spectra are used when the SZA is around 80° during twilight. The reason of this choice is that a SZA of 80° occurs during most days of the year, see Fig. 3.2 (between end of October and mid of February reference spectra at higher SZA are used). The first output from the analysis is the differential slant column density (DSCD) which represents the difference of the slant column densities of the measured spectrum and the Fraunhofer reference spectrum:

$$\text{DSCD} = \text{SCD}_{\text{ref}} - \text{SCD}_{\text{meas}}, \quad (3.1)$$

where SCD_{ref} indicates the slant column density (SCD) of the Fraunhofer reference spectrum and SCD_{meas} the SCD of the measurement of interest. The SCD represents the integrated NO₂ concentration along the atmospheric light path. Like for direct light observations, also for scattered sunlight measurements, the SCDs depend on the SZA. Therefore, the SCD is converted to the vertical column density (VCD) using an air mass factors (AMF), which is derived from radiative transfer simulations [Platt and Stutz, 2008].

$$\text{AMF} = \frac{\text{SCD}}{\text{VCD}}, \quad (3.2)$$

However, because SCD_{ref} (for the Fraunhofer reference spectrum) is usually not known, it has to be determined before the VCDs can be calculated from the dSCDs. One widely used method for the determination of the SCD_{ref} is the so-called Langley plot method, which is derived by combining Eqns. 3.1 and 3.2:

$$\text{dSCD} = \text{AMF} \times \text{VCD} - \text{SCD}_{\text{ref}}, \quad (3.3)$$

The measured dSCDs are plotted against the corresponding AMFs and then a linear fit is applied. Figure 3.3 shows an example of the Langley plot method using data measured on 2015. Mar. 20. The VCD is determined the slope of the fitted regression line. Typically, this method works correctly for species with very slowly changing concentrations with time,

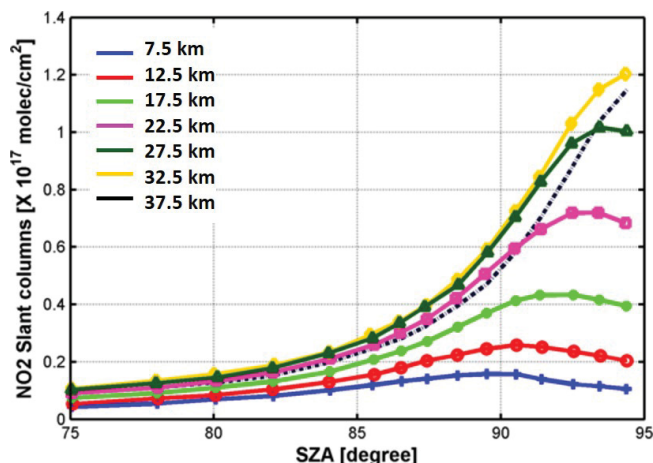


Figure 3.4: The variation of NO₂ slant columns with SZA for NO₂ profiles with the peak mixing ratio at different altitudes. These results are derived from a photo-chemical model coupled with a radiative transfer model. This figure is taken from Preston et al. [1998]

for example O₃. However, stratospheric NO₂ is rapidly photolysed during day time from NO₂ to NO, and it also varies due to conversion processes from and to its reservoir species N₂O₅. Both reaction cycles are highly dependent on the amount of sun light. Therefore, this study employs a photo-chemically modified Langley plot method using the NDACC Look-up table (LUT) of NO₂ AMFs [Van Roozendael and Hendrick, 2012]. This NDACC climatology NO₂ LUT is based on the harmonic climatology of stratospheric NO₂ profiles derived from several satellites and balloon observations (UARS HALOE v19, SPOT POAM3, and SAOZ balloon measurements) and a global monthly climatology of the surface albedo derived from GOME observations. The AMFs are calculated with the UVSPEC/DISORT radiative transfer model [Mayer and Kylling, 2005].

3.1.3 Retrieval of vertical profiles

In this chapter, the profiling inversion algorithm based on the optimal estimation method (OEM)[Preston et al., 1997, 1998; Rodgers, 2000; Schofield et al., 2004] is described which enables the profile retrieval for stratospheric trace gases as well as the corresponding stratospheric VCDs. For this study, the IASB-BIRA profiling tool [Hendrick et al., 2004] is adapted. The OEM used in this algorithm allows the inversion of the measured SCDs into a vertical concentration distribution. The basic principle of the profile inversion method is introduced by Preston et al. [1997]. The slant columns increase with SZA due to the increase of the stratospheric light path length. Moreover, with increasing SZA also the altitude of the first scattering event of the solar photons in the atmosphere increases. Thus the measured SCDs taken at different SZA provide information on the concentrations at different altitudes, which is illustrated in Fig. 3.4.

Since during twilight usually the concentration of NO₂ changes rapidly, in the inversion process also the effects of photochemistry have to be considered for NO₂. In the IASB-BIRA profiling tools, this inverse retrieval problem is solved based on the pioneering work by Rodger [Rodgers, 2000], and the photochemical reactions are considered. The inversion

method is shown by an equation which simply states that the measurements are related to the vertical profile by a forward model F , [Rodgers, 1990]:

$$\mathbf{y} = F(\mathbf{x}, \mathbf{b}) + \epsilon_y, \quad (3.4)$$

where \mathbf{y} indicates the set of measured SCDs, \mathbf{x} indicates the NO_2 profile at a selected SZA, \mathbf{b} represents additional parameters of the forward model, and ϵ_y represents the retrieval error. On important limitation of this method is that different atmospheric profiles, could fit to the same \mathbf{y} .

This problem can be addressed by introducing the weighting function matrix \mathbf{K} to select the optimum value from a number of possible solutions. The weighting functions are derived by $\mathbf{K} = \partial \mathbf{y} / \partial \mathbf{x}$ and each row of the matrix \mathbf{K} represents the SZA of a measurement. The weighting function contains information about the dependence of the dSCDs on the vertical profile at each SZA. By considering also the error covariance, the relation between the measured dSCDs and the vertical profile follows [Hendrick et al., 2004]:

$$\bar{\mathbf{x}} = \mathbf{x}_a + (\mathbf{K}^T \mathbf{S}_\epsilon^{-1} + \mathbf{S}_a^{-1})^{-1} \mathbf{K}^T \mathbf{S}_\epsilon^{-1} (\mathbf{y} - \mathbf{K} \mathbf{x}_a), \quad (3.5)$$

where $\bar{\mathbf{x}}$ is the retrieved profile, \mathbf{x}_a is a given a priori profile, \mathbf{y} is the measurement vector, and \mathbf{K} is the weighting function matrix. \mathbf{S}_a and \mathbf{S}_ϵ are their respective a priori and measurement uncertainty covariance matrices. \mathbf{x}_a and \mathbf{K} are derived from the Forward model.

Forward model

In this study, a forward model which is a combination of a photochemical model and a radiative transfer model is used to derive the weighting functions. The photochemical model is a stacked box photochemical model PSCBOX [Errera and Fonteyn, 2001] that is usually utilised to reproduce the diurnal variation of NO_2 SCDs for defined a priori profiles. The photochemical correction is applied in this profiling tool based on climatological model runs. The UVspec/DISORT radiative transfer model [Mayer and Kylling, 2005] calculates the intensity weighted average of the paths of scattered light through the atmosphere. These path lengths are combined with the retrieved NO_2 concentrations from the photochemical model to derive the NO_2 slant columns.

Information contents

To characterise the sensitivity of the retrieved NO_2 profile, the following equation is used:

$$\mathbf{A} = \frac{\partial \bar{\mathbf{x}}}{\partial \mathbf{x}}, \quad (3.6)$$

where \mathbf{A} represents the averaging kernel which is derived from the algorithm depending on the input parameters and the measured NO_2 SCDs. The averaging kernel indicates the sensitivity of the retrieved profile with respect to the true atmospheric state and it shows how the retrieval smoothes the true profile. Each averaging kernel is related to a retrieval altitude. Averaging kernels close to unity indicate retrieval results which are dominated by the measurement (high sensitivity). Averaging kernels close to zero indicate results which are dominated by the a priori profile (low sensitivity). Figure 3.5 shows an example of averaging kernels for the ground-based NO_2 observations on 20 March 2015. The trace of \mathbf{A} provides the information about the degree of freedom of the retrieval.

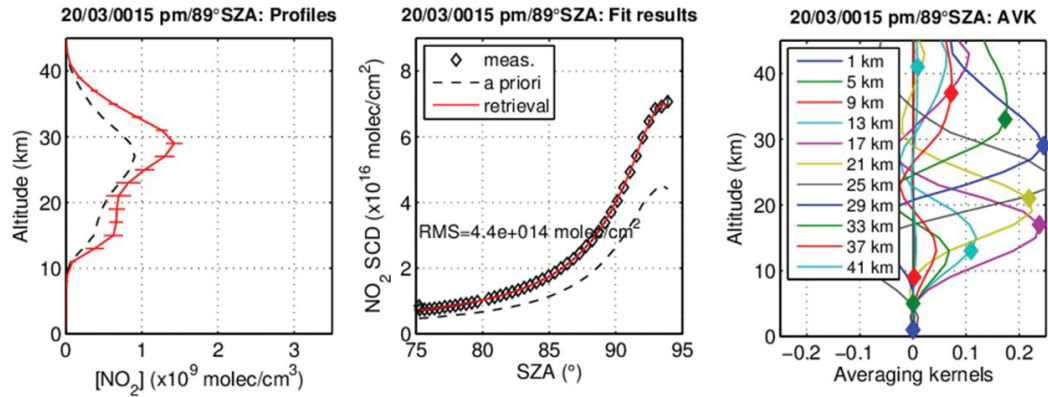


Figure 3.5: Typical examples of the retrieval of a stratospheric NO_2 profile and the corresponding averaging kernels. Left: retrieved stratospheric NO_2 profile (red), a priori profile (black), and the corresponding error bars indicating the standard deviations. Middle: measured NO_2 SCDs as a function of the SZA. Here, the black open diamonds and the red line represent the measured and simulated NO_2 SCDs, respectively. The dashed line indicates the SCDs corresponding to the a priori profile. Right: averaging kernels calculated by the algorithm. The closed diamonds indicate the altitude for which the averaging kernels are representative.

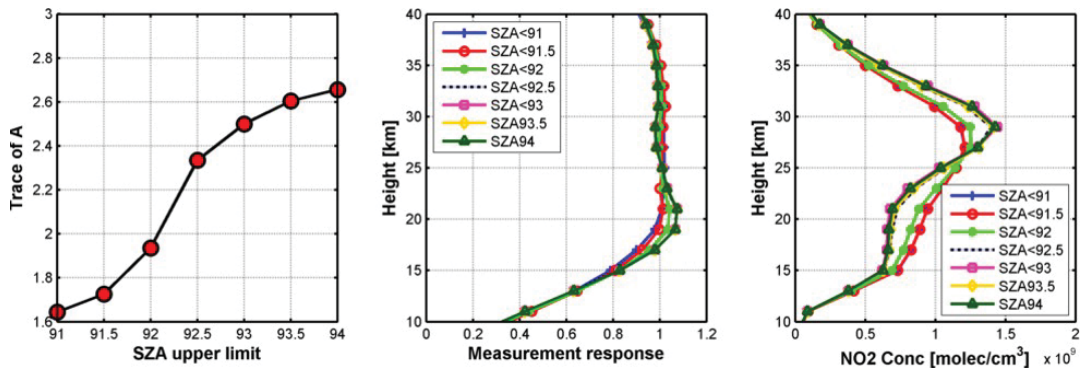


Figure 3.6: Left: The trace of **A** as a function of the upper limit of SZA. Middle: The measurement response indicating the sum of the rows of the averaging kernels at different heights. Right: NO_2 profiles retrieved for different SZA upper limits.

One of the critical points which has to be considered is the choice of the SZA upper limit of the observations. The number of independent pieces of information is determined by the trace of **A** where **A** depends on the SZA upper limit. To check the sensitivity, the SZA upper limit is varied between 91° and 94° . Figure 3.6 shows retrieval results for a typical profile using measurements from 20 March 2015 at SZA 89° . The left figure shows the dependence of the trace of **A** for different SZA upper limits showing a systematic increase with an increasing SZA as expected. The figure in the center shows the sum of the rows of **A** (averaging kernel) where each line represents a different SZA upper limit. The right figure shows the retrieved NO_2 profiles for different SZA upper limits which are significantly different. The largest differences are found for SZA upper limits between 92° and 93° as already mentioned in Fig.3.2, during the period indicated by the yellow and grey areas (before middle of February, middle of May to end of July, and after the end of October), when not the whole SZA is covered. Therefore, data in those measurement periods are

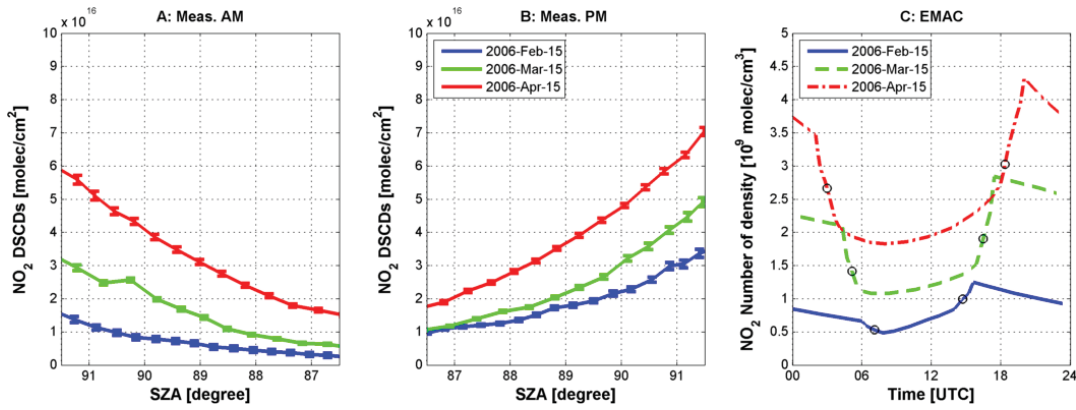


Figure 3.7: Diurnal variations of the measured stratospheric NO_2 dSCD depending on SZA for selected days (Feb.15, Mar.16, and Apr.15, 2006) during sunrise (A) and sunset (B). (C) shows the diurnal variation of the simulated NO_2 concentration on those days.

ignored. And the measured data which was observed at $75^\circ \leq \text{SZA} < 91^\circ$ for the vertical inversion was finally chosen.

3.2 RESULTS

3.2.1 Overview on the stratospheric NO_2 variation

3.2.1.1 Diurnal variation

Figure 3.7 shows the diurnal variations of the stratospheric NO_2 dSCDs for three selected days (Feb. 15th (blue), Mar. 15th (green), and Apr. 15th of 2006 (red)). The SZA range between 87° and 91° is chosen to show the variation during twilight. The observed SZA dependence is different for the different months indicating (a) the different relationship between SZA and time, and (b) the different chemical partitioning of the nitrogen compounds. To understand the stratospheric NO_2 photochemical behavior during day, the diurnal variations of the NO_2 number density simulated by the ECHAM5/MESy Atmospheric Chemistry (EMAC) simulations [Jöckel et al., 2006, 2010] is shown in Fig. 3.7(C). The amount of NO_2 rapidly decreases early in the morning and rapidly increases during sunset due to the photolysis of NO_2 . During the day an almost linear increase is found due to the photolysis of N_2O_5 . During night N_2O_5 is accumulated and is photolysed by sunlight. In this graph, the black open-circles denote SZA of 90° which allows to compare the simulated model results with the measurements in Figs. 3.7(A) and (B). One can see that as the sunlit time increases from February to April the NO_2 number density (and also the measured NO_2 dSCDs) increases. In addition, also the rate of change of NO_2 with SZA increases from February to April. The difference of the NO_2 variations between a.m and p.m can also be understood by the photolysis of NO_2 .

3.2.1.2 Multi-year monthly averages: 1997 to 2016

In this section, the seasonal variation of stratospheric NO_2 is investigated. In Fig. 3.8 the box and whisker plots of the multi-year monthly average of stratospheric NO_2 VCDs derived from the Langley plot method from 1997 to 2016 are shown (except for January, November, and December due to the limited SZA range). The red crosses are outliers defined as data

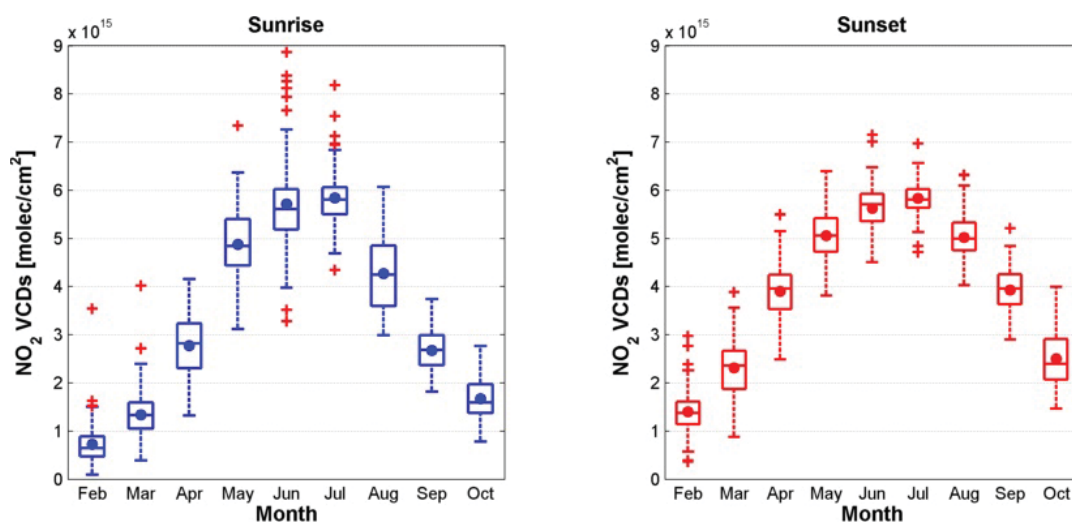


Figure 3.8: Box and whisker plots of time series of stratospheric NO₂ VCDs from 1997 to 2016 derived from the Langley plot method. Left and right panels represent measurements during sunrise and sunset, respectively. The box edges denote 25 and 75% of the measured NO₂ VCDs, and the center line indicates the median. The mean values are denoted by dots inside of the box. Red cross indicates outliers.

points higher or lower than 1.5 times of the inter-quartile range, and the whiskers show the maximum and minimum values excluding the outliers. Here, the stratospheric NO₂ VCDs measured during sunrise and sunset show a strong seasonal variation with maximum values in summer and minimum values in winter. Mean annual values are 3.2×10^{15} and 3.8×10^{15} molec/cm² for sunrise and sunset, respectively. It is also interesting that (except during polar day and polar night) values measured during sunset are larger than during sunrise which is related to the photolysis of N₂O₅. Furthermore, the year-to-year variation during sunrise is larger indicated by a higher number of outliers. This can be understood by the fact that rapidly decreasing NO₂ is caused by the increase of sunlight during sunrise.

In addition to the stratospheric NO₂ VCDs, also the monthly mean NO₂ profiles (for 14.5 years), obtained from the OEM inversion algorithm are calculated. The monthly mean vertical profiles for 14.5 years are shown in Fig. 3.9 and the spring data for selected ten years are additionally provided in the next sub-section. The NO₂ vertical distributions generally show a strong annual cycle and there is a high variability observed below 30 km. After the end of the polar night the recovery of NO₂ is clearly seen, and the NO₂ concentrations continue to increase towards the summer (the largest amount of NO₂ of about 3.3×10^9 molec/cm³ is found at the altitude of 26 km). After summer the values decrease again. Except for the summer and winter months, the NO₂ concentrations measured in p.m are systematically larger than in a.m. The mean differences in the profiles from April to August show an oscillatory structure with largest differences between 15 and 25 km, while the mean differences during the other months shows one primary negative peak. The mean differences during the period from winter to summer have larger values than from summer to winter. The standard deviation of the twilight profiles is the largest between 26 km and 30 km. Regarding the profiles measured in p.m a larger variability of NO₂ is found between about 15 km and 25 km with a strong bimodal distribution especially in April and May. The reason for this finding will be discussed in the next section 3.2.3.

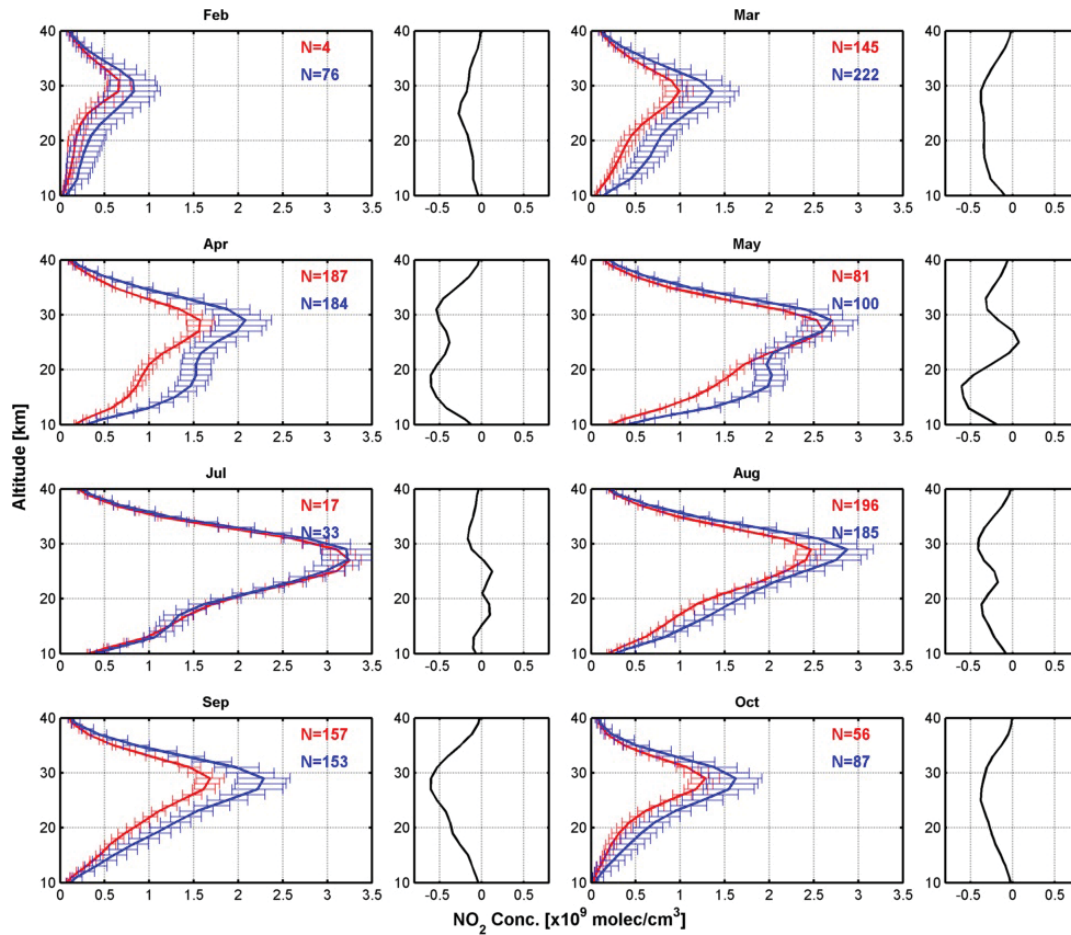


Figure 3.9: Stratospheric monthly mean profiles from ZS-DOAS observations from 1997 to 2016. Odd number-columns represent monthly means and the number of occurrences; the error bars indicate the 1σ standard deviation. In these graphs, red and blue lines indicate mean profiles measured during a.m and p.m, respectively. The number of occurrences for each observation is written in the legend. Also the mean differences between profiles in a.m and p.m are shown. The x -axis and y -axis represent the concentration and altitude from 10 km to 40 km, respectively.

3.2.2 Temporal and vertical variability of stratospheric NO_2

This section shows the temporal (day to day) variation of the stratospheric NO_2 vertical distribution during spring for individual years which can help to understand the connection of the stratospheric NO_2 chemistry to atmospheric dynamics (e.g the polar vortex) and temperature. The results are retrieved from the OEM profiling algorithm described above. Due to the seasonal variation of the SZA, data before mid February are missing. There are additional data gaps due to instrumental problems.

Table 3.2: Example for the potential vorticity thresholds for the polar vortex for the Arctic winter of 1994/1995.[Woyke, 1998; Raffalski et al., 2005]

Θ in K	435	475	500	550	575	600	635	675	950
PV in PVU	22	35	45	75	100	120	160	220	975

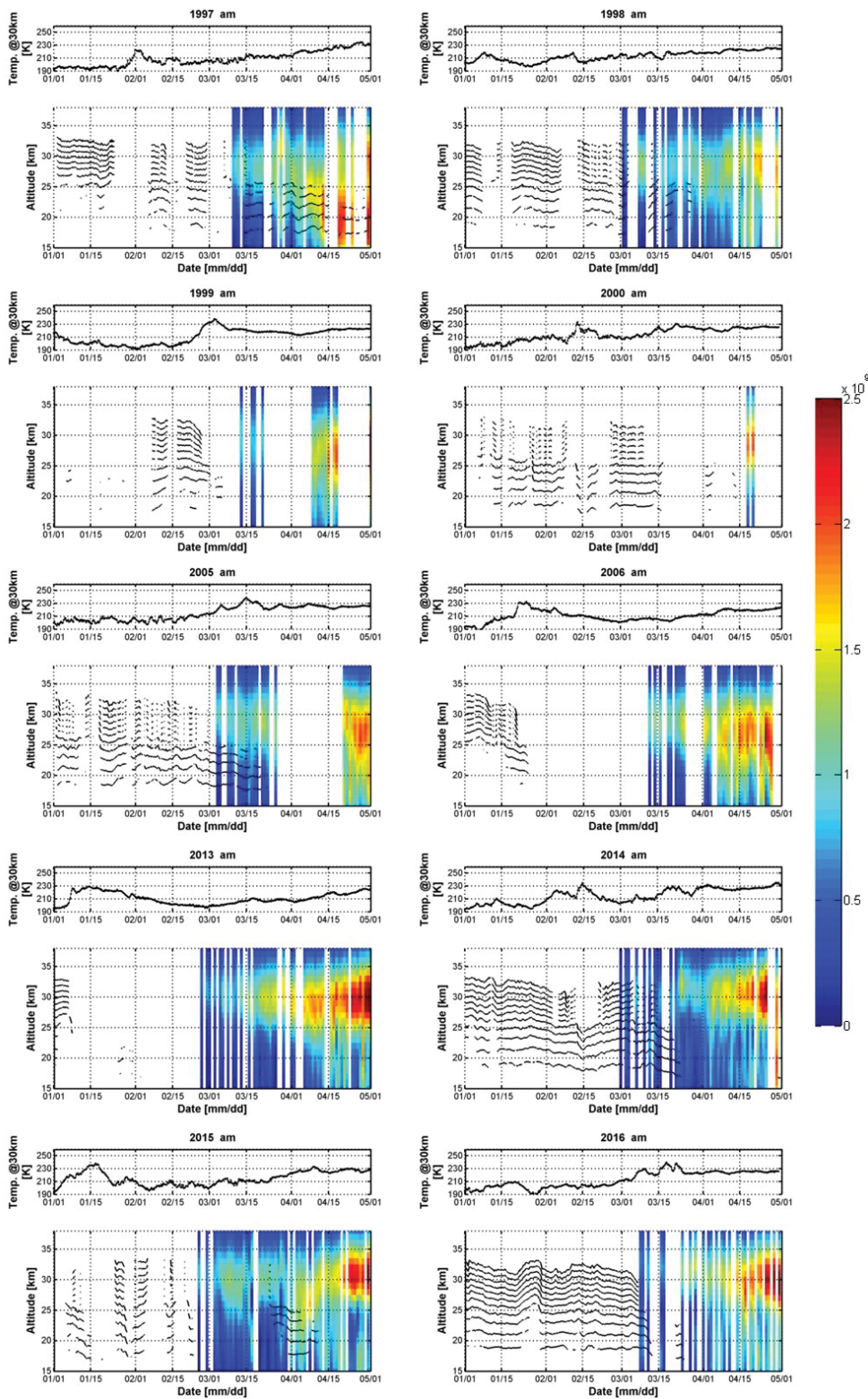


Figure 3.10: Curtain plots of the time series of the stratospheric NO₂ vertical distribution measured in a.m. Black contour dots indicate the polar vortex barrier at each potential temperature level. x - and y -axes indicate time and altitude, respectively. The altitude covers the altitude range from 15 km to 38km. And additionally, the subplots above the curtain plots show the temperature around 30 km.

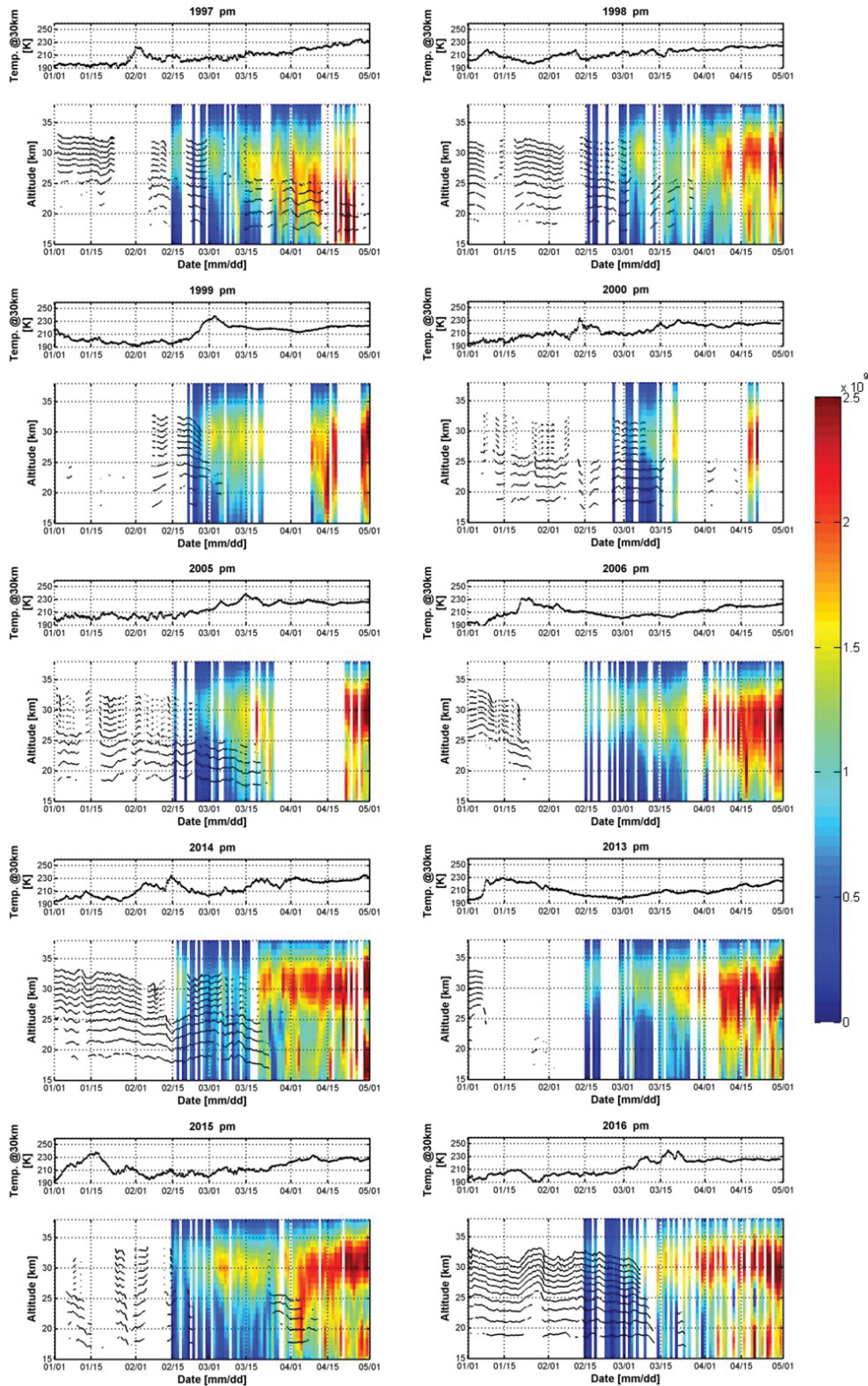


Figure 3.11: Curtain plots of the time series of the stratospheric NO₂ vertical distribution measured in p.m. Black contour dots indicate the polar vortex barrier at each potential temperature level. x - and y -axes indicate time and altitude, respectively. The altitude covers the altitude range from 15 km to 38 km. And additionally, the subplots above the curtain plots show the temperature around 30 km.

Figures 3.10 and 3.11 show curtain plots of the NO₂ vertical distributions and overlaid black dots which indicate whether the polar vortex was located above Kiruna or not. The information is given for different potential temperature levels (for the potential vorticity thresholds see Tab. 3.2). This information is very helpful to understand the horizontal distribution of NO₂ above Kiruna as well as to know how the daily position of the polar vortex influences the NO₂ concentrations. These plots have data gaps in the beginning due to the limitations of the profiling algorithm in polar night. And additionally, the subplots above the curtain plots show the temperature around 30 km. To indicate how the evolution of the polar vortex affects the NO₂ variation, the plots cover the entire period from January 1st. to May 1st. Here, eight different winters are chosen: 1997, 1998, 1999, 2000, 2005, 2006, 2013, 2014, 2015, and 2016 because those show less data gaps than other winters. Four winters (1997, 2005, 2014, and 2016) are very cold winters and show relatively large ozone losses with 25, 23, 21 and 27 %, respectively [Goutail et al., 2017]. The other four years are warmer, and the ozone loss is less than for the four cold years. All of these figures clearly show the general feature of the NO₂ reformation when the sun returns in early spring. The stratospheric NO₂ has its maximum around 30 km but during the spring period increased values also appear towards the tropopause.

For the cold winters in 1997, 2005, 2014 and 2016, a clear difference of the shape and timing of the NO₂ vertical distribution is found when Kiruna is located below the polar vortex. While the NO₂ reformation starts in the middle of February during warm winters, very low NO₂ values are still found in the same period during cold winters, especially in 2014 and 2016. In 2016, a vertically extended polar vortex stays stable over Kiruna until the beginning of March. This winter is known as one of the coldest winters during the observation period which results in a late reformation of NO₂. In 2014, a strong and vertically extended polar vortex is found from mid to end of February. However, after the first week of March a stable vortex is only found below about 25km. Enhanced NO₂ values appear late in this winter, after about 15 March.

The winters in 1998, 2006, 2013, and 2015 can be categorised as warm winters. A sudden stratospheric warming (SSW) in January is observed especially in the winters of 2006 and 2013, which leads to a sporadic increase of the temperature. During the major warming periods, the lower stratospheric temperature usually rises rapidly above the threshold for PSC formation and thus no further conversion of chlorine to active compounds occurs. Consequently, major SSWs in early winter are associated with a minimum O₃ loss.

The 1997 winter is also interesting. In this period, the polar vortex is unusually expanded in the beginning of April towards lower altitudes (15–25km), and an NO₂ enhancement is simultaneously observed. The NO₂ enhancement in this period can be explained by a couple of ways. The first is that it might be related to the stable vortex at low altitudes. During the 96/97 winter, the vertically-developed and very strong vortex contains abundant NO₂ reservoir species until the beginning of April, might be photolysed to form the NO₂ enhancement after the sun is returning which inside of the polar vortex. Secondly, it might be either originated from heating up air due to air parcels descending or being transported from other regions.

3.2.3 Statistical sensitivity test of the profile inversion

To clarify the reason of the bimodal distribution of the NO_2 profiles during the late spring periods, the effect of clouds could be considered as a possible reason. In particular, Hendrick et al. [2007] mentioned that a wrong surface albedo or an inappropriate treatment of low clouds can cause an increasing uncertainty. This section investigates the cloud effects on the profile inversion. Wagner et al. [2014] described that zenith sky measurements are appropriate for cloud detection. Such measurements are independent from the solar azimuth angle and can thus be directly compared with clear sky reference spectra. As well, the zenith sky instrument can continuously measure spectra during the whole day, thus it can better capture the temporal variability of clouds.

Here, the cloud classification scheme developed by Wagner et al. [2014, 2016] and Wang et al. [2015] is applied to separate the observation data depending on the different sky conditions. The basic idea of the classification scheme is the same as of the original algorithm, but there are also small changes introduced: For example the discrimination of different aerosol loads is omitted, because for this classification also non-zenith elevation angles are needed. Moreover, the modified scheme is only based on the colour index, which simplifies its application, but also has the limitation that no optically thick clouds can be distinguished from optically thin clouds.

With the modified version still four different sky conditions including clear sky, cloud holes, broken clouds and continuous clouds can be distinguished. The cloud classification results show that overall 42% of all measurements are made under clear sky conditions, 20% under cloud holes, 15% under broken clouds, and 23% under continuous clouds from 1997 to 2015 (except for 2002). To clarify whether this scheme works well for this study or not, the cloud classification results on two selected days are shown in Fig.3.12 (left panel: Aug. 31st, 2014; right panel: Sep. 29th, 2015). On the first day, the sky was clear, and on the second day the sky was cloudy, as can also be seen in the satellite images. In the upper part of the figure, the cloud classification results are shown. Below, the quantities retrieved from the measured spectra (O_4 , Ring, CI, and the normalised radiance) are shown. For clear sky conditions, they show smooth variations, while for the cloudy skies they show rapid variations, which are caused by the effect of clouds on the atmospheric light paths. The CI value for clear sky is higher than that in the cloudy sky, and the presence of clouds (measured in the afternoon of the second day) results in small CI values. The O_4 absorption and the Ring effect are especially sensitive to changes of the atmospheric radiative transport [Wagner et al., 1998, 2014]. From this graph, it is clearly shown that the results of the cloud classification are well consistent with the retrieved quantities obtained from the Zenith measurement and the satellite images. Therefore, this cloud classification scheme is well suited to be applied to the Kiruna measurements.

To investigate the potential influence of clouds on the profile retrieval, the sky condition during the measurement period considered for the profile retrieval is categorised by counting the relative frequency of occurrences of each sky condition during this period. Here it should be noted that the classification method is only applied to SZA below 90° , while the SZA range of the profile retrieval in this study is from 75° to 94° . Thus the cloud classification results are not perfectly consistent with the profile retrievals. Nevertheless, in general the associated errors should be small. The cloud classification results can be directly compared with the retrieved NO_2 profiles and the quality indicators of the profile retrieval. One quality indicator is the root mean square (RMS) between the simulated and measured absolute

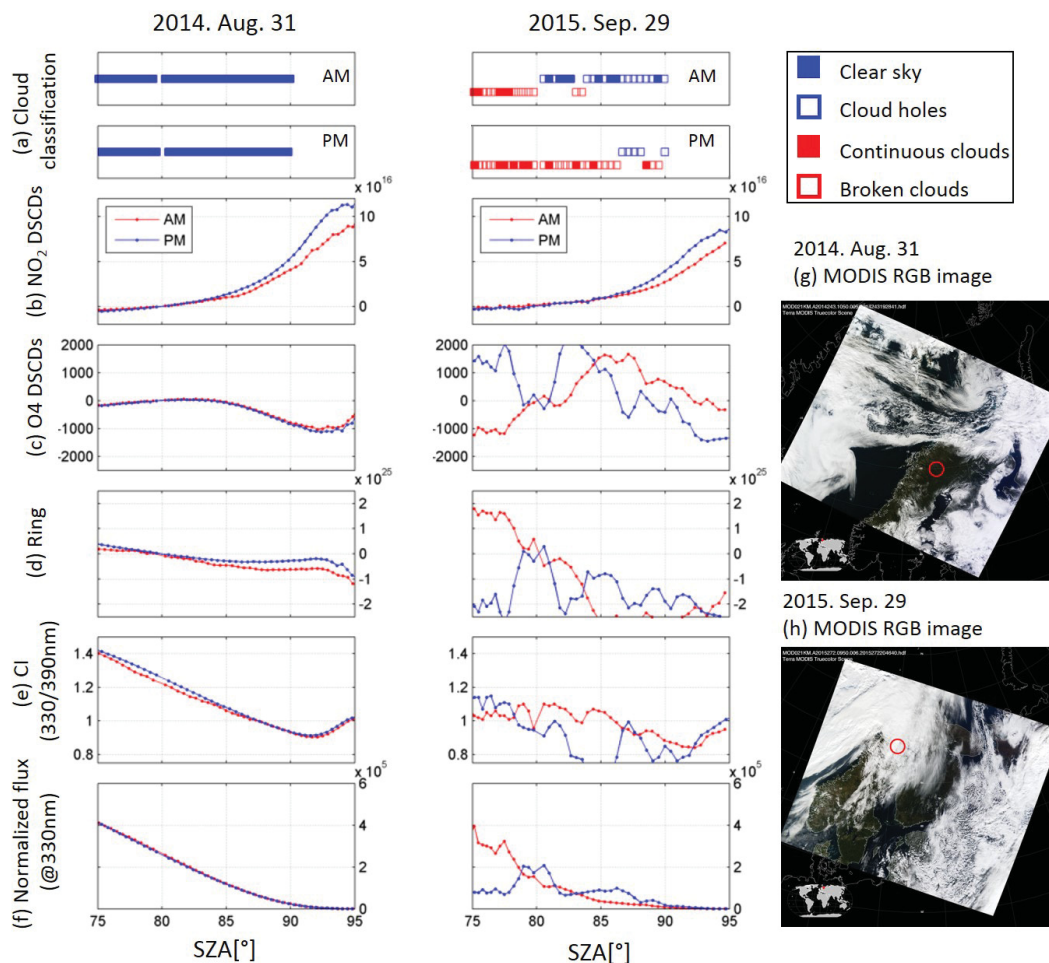


Figure 3.12: Temporal variation of different retrieved quantities from ZS-DOAS observations on a clear sky day (Aug. 31st, 2014, left) and a cloudy sky day (Sep. 29th, 2015, center): (a) the results of cloud classification scheme at a.m (upper panels) and p.m (lower panels), (b) NO₂ DSCDs, (c) O₄ DSCDs, (d) Ring effect, (e) color index (330/390), and (f) normalised radiances measured at 330 nm. Figures (g) and (h) show cloud images from satellite (MODIS RGB images) on both selected days. The red circles indicate the observation site (Kiruna, Sweden).

slant column densities (SCDs). Another quality indicator is the trace of \mathbf{A} derived from the profile retrieval.

Figure 3.13 shows quality indicators including RMS and a trace of the averaging kernel matrix (\mathbf{A}) which represents the number of independent pieces of information included in the measurement observed in a.m and p.m. The bar graphs are plotted as a function of the sky condition, and each sky condition is represented by the frequency range at which the condition occurs during the period of interest. For example, a blue bar represent average values of RMS or trace of \mathbf{A} obtained for days on which the relative frequency of observations of the specific sky conditions is more than 80%. In this graph, a small RMS (and a high trace of \mathbf{A}) means that the retrieved profile is very well consistent with the measurements. First, better RMS fit results are clearly found under clear sky than cloudy sky conditions, while large RMS are obtained under broken or continuous clouds conditions. The trace of \mathbf{A} results indicate that there is no significant difference for the different sky

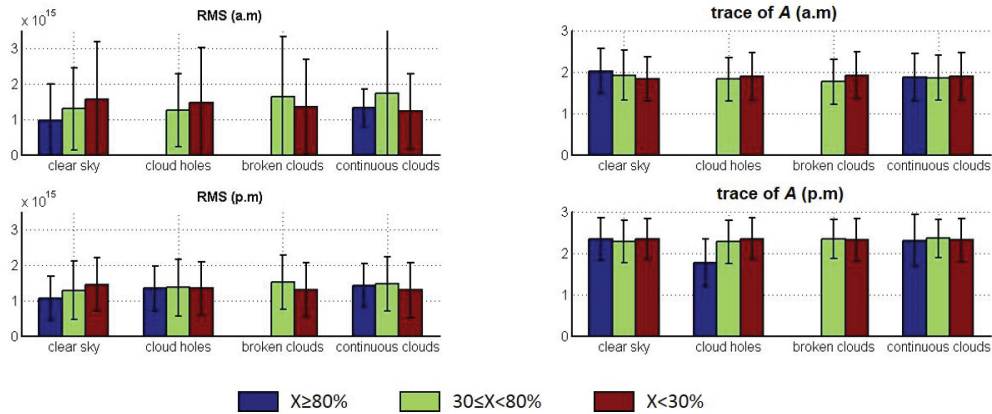


Figure 3.13: (Left) RMS and (Right) trace of the averaging kernel matrix under different sky conditions categorised by the number of occurrences of each sky condition during the period used for the profile retrieval. Each color represents the relative frequency of the different sky conditions. For example, the blue bars indicate values under which the sky condition of interest occurs more than 80% during the measurement period. Green and red bars represent relative frequencies between 30% and 80%, and smaller than 30%, respectively. The error bar represents standard deviation.

conditions. This finding can be explained by the fact that clouds are below the height, for which the profiles are retrieved. However, slight discrepancies are still found, which might be related to the fact that the algorithm is based on a Climatology, whereas the meteorological conditions might also vary from day to day. It should also be noted that for some sky conditions the number of measurements is limited.

Figures 3.14 and 3.15 show the stratospheric NO_2 mean vertical profiles depending on the sky conditions at each season. Due to the high latitude of the measurement site and also the retrieval algorithm acceptance criteria, there is no data in January, June, November and December. Thus the winter data only include measurements made in February as mentioned above. Each graph includes four mean NO_2 profiles which denote different sky conditions: the blue line represents clear sky condition, the red, green, and black lines represent the three different cloudy conditions.

At first, data obtained in a.m and p.m are compared in the category of which the frequency of each sky condition is larger than 80% (1st row). For the a.m measurements, only two sky conditions, clear sky (blue line) and continuous clouds (black line), are observed. One can see negligible differences during winter and summer, while in spring and autumn the NO_2 profiles for clear sky conditions are systematically smaller. Especially during spring, these differences are large at altitudes below 28 km. Compared to the a.m data, the NO_2 mean profiles in p.m show larger discrepancies depending on the sky conditions, especially in spring, summer, and autumn as shown in Fig. 3.15. The results during spring are very similar with the a.m results, in which strongly enhanced NO_2 concentrations below 25km are observed. For measurements under ‘cloud holes’ the NO_2 concentration shows systematically smaller values at low altitudes for summer and autumn than for clear sky and continuous clouds. Overall, the shape of the p.m. profiles show large discrepancies compared to the a.m profiles, especially a bimodal distribution under continuous clouds is observed in MAM and SON. For cases with less clear assignments to a specific cloud

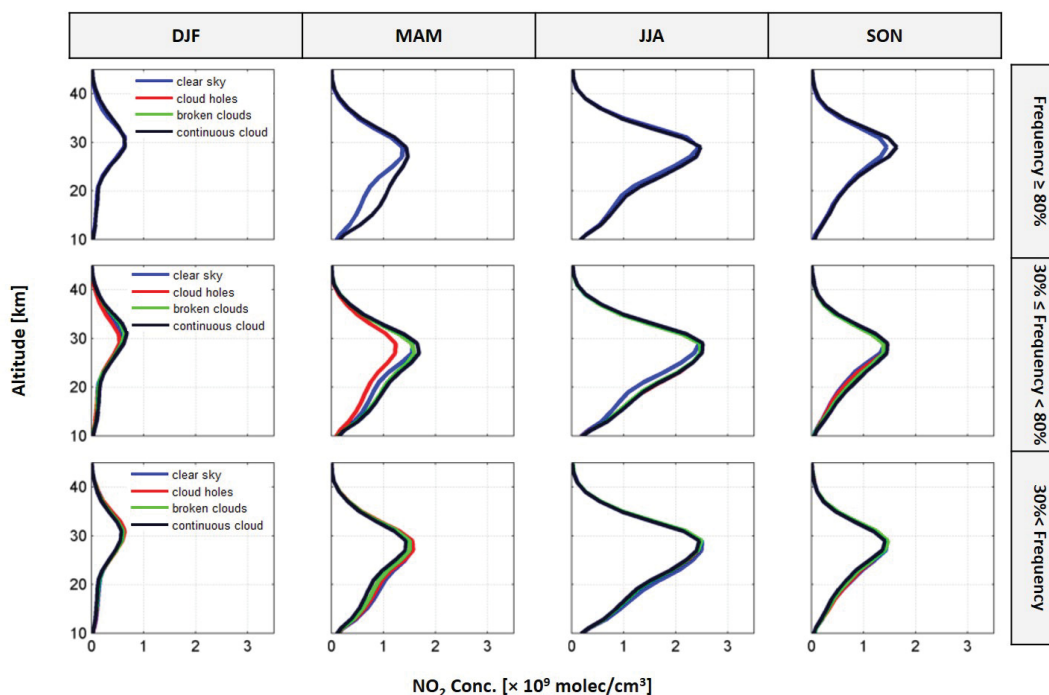


Figure 3.14: Vertical NO₂ mean profiles derived from the ground-based measurements in a.m for 14 years depending on the sky conditions and season. Each column indicates measurements during different seasons (DJF: winter, MAM: spring, JJA: summer, SON: autumn) and each row represents the relative frequency of the sky conditions. Different sky conditions are represented by different colors (blue: clear sky, red: cloud holes, green: broken clouds, and black: continuous clouds).

condition (second and third row in Fig.3.14 and Fig. 3.15 much smaller differences are found.)

There are several possible reasons which might be responsible for the differences between clear and cloudy sky conditions:

- The actinic flux increases when clouds enhance the effective albedo
- Clouds have a strong effect on the radiative transfer in the tropopause
- Clouds can also have an effect on the radiative transfer in the stratosphere
- Clouds are typically connected to weather systems, which also have an influence on the height of the tropopause

The first reason is most likely not playing an important role, because an enhanced actinic flux would result in an enhanced photolysis rate of NO₂ and thus a decreased NO₂ concentration. However, typically higher NO₂ concentrations are found for cloudy sky conditions. The second reason could in principle have a strong effect on the retrieved total NO₂ DSCD. However, it should in first order affect all measurements during the whole period in a similar way and thus mainly cancel out. Moreover, measurements during a.m and p.m should be affected in the same way, which is not observed. The third reason also can not explain the differences between clear and cloudy sky conditions. Radiative transfer simulations were performed for different cloud properties, but the effect on the stratospheric NO₂ AMF was found to be negligible. The fourth reason might explain the observed differences because

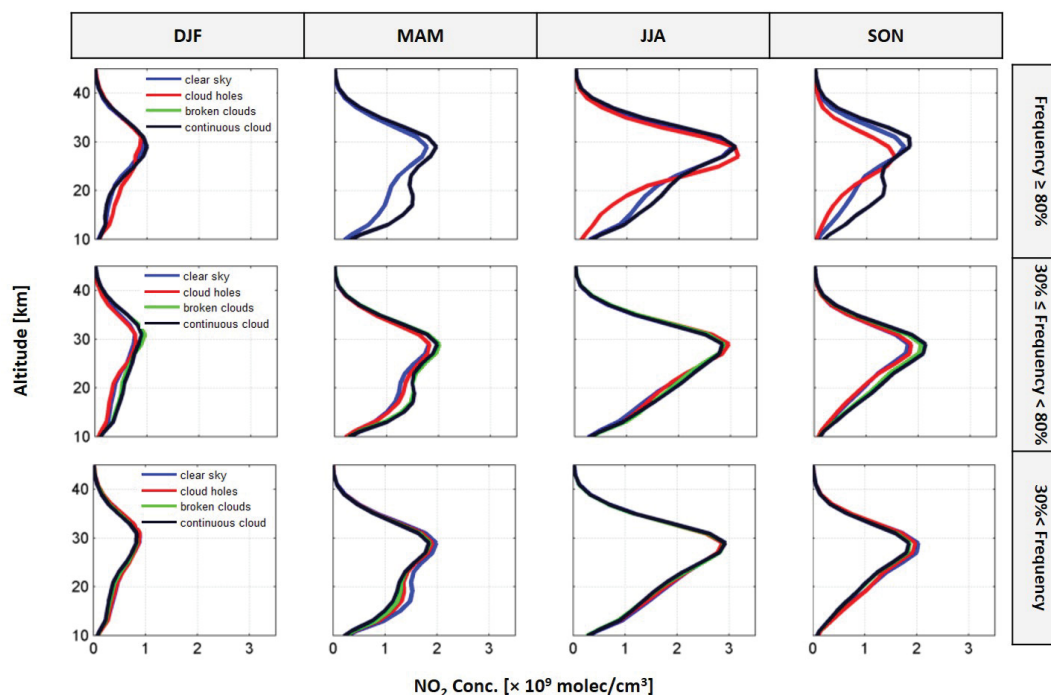


Figure 3.15: Vertical NO_2 mean profiles derived from the ground-based measurements in p.m for 14 years depending on the sky conditions and season. Each column indicates measurements during different seasons (DJF: winter, MAM: spring, JJA: summer, SON: autumn) and each row represents the relative frequency of the sky conditions. Different sky conditions are represented by different colors (blue: clear sky, red: cloud holes, green: broken clouds, and black: continuous clouds).

clouds typically occur during low pressure conditions. However, this effect can not (easily) explain why the differences mainly occur during pm.

To conclude, at the moment no clear reason for the observed discrepancies between clear and cloudy sky conditions is identified. However, if it is assumed that the mean profile measured in clear sky condition is true, according to the second category the difference under the different sky conditions is less than 12%. This category covers an intermediate range and most measurements are included in this category. Therefore, except for the extreme sky conditions, the NO_2 profiles do not show a big difference under different sky conditions.

Artifact from the profiling tool

It was already mentioned that a photochemical correction is applied in the profiling tool, which is based on climatological model runs. Thus it is possible that for some days, the model output does not well characterise the real chemical and meteorological conditions in the stratosphere above Kiruna. The calculation of the photochemistry in near-real-time for the exact location of the station would, however, be too computationally demanding. Thus in this work, the influence of the photochemical correction is tested for a selected time period in 2014 (see Fig. 3.16). The profile inversion was repeated using not the photochemical results for exactly that day, but for a fixed day (4 May 2014). For a.m and p.m completely different results are found: for the a.m profiles, in May improved profiles are obtained compared to

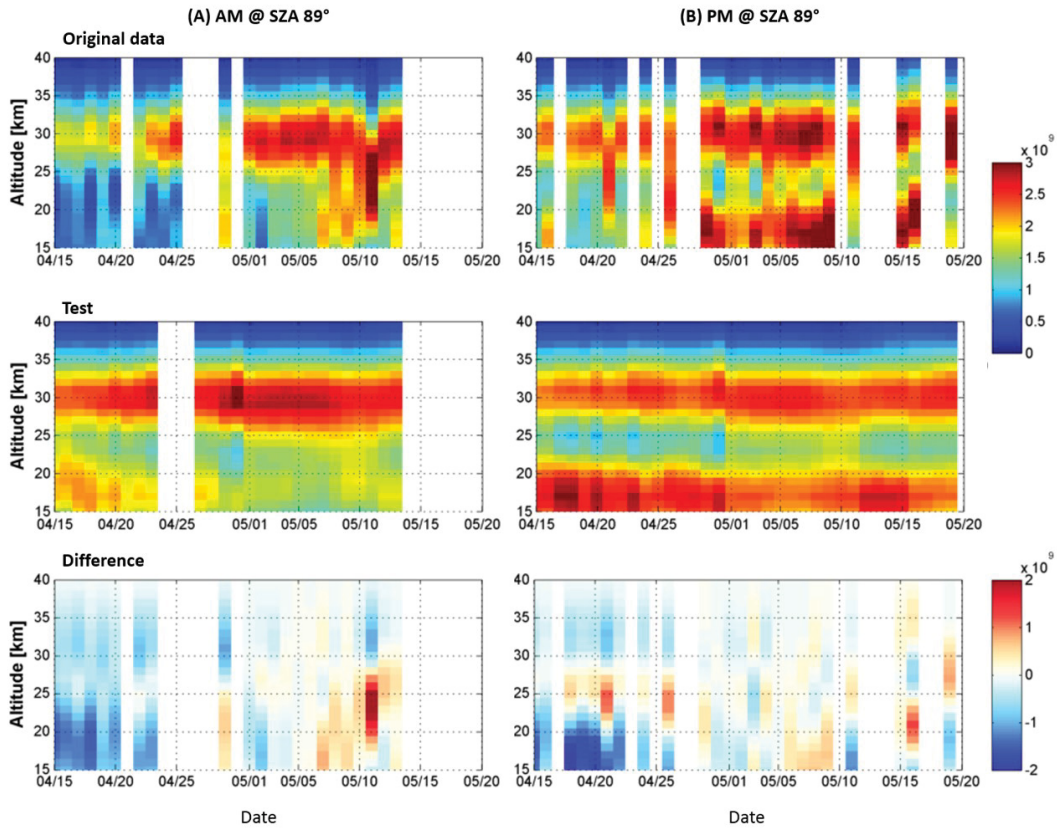


Figure 3.16: NO₂ profiles (mixing ratios) as a function of time in a.m. (left) and p.m. (right), respectively. Figures on top and in the middle show the original profiles and those derived with the ‘fixed’ photochemistry (see text), respectively. On the bottom, the absolute difference between the original results and test results is shown.

the original inversion for measurements in May: in particular, the double peak disappears during that time. However, for the measurements in April a double peak appears, which was not there in the original inversion. For the p.m. measurements, a double peak is always found, even for measurements, which did not show a double peak in the original inversion.

The result indicate that possible deficiencies of the photochemical model are the most probable reason for our findings because the effect of changing photochemistry is largest at p.m., for which also most of the profiles with double peaks were found in the original inversion. In general we find that during the period after April, the derived profiles are rather sensitive to the description of the photochemistry. It seems that it is especially difficult to correctly simulate the photochemistry for the transition period between days of a clear day/night separation and polar day. Also, SZA close to 90° occur for long periods, thus possible errors of the calculation of the actinic flux for such SZA have a strong influence of the profile results. To conclude, the bimodal distributions are found especially in spring and in summer. Thus the results for these periods should be treated with caution. They can not be well explained by the effects of clouds, but are most likely an artifact from the photochemical description in the profiling tool.

3.2.4 Comparison with other instruments

In the previous section, the vertical distributions of NO_2 retrieved from ZS-DOAS from 1997 to 2016 was presented. It is quite important to validate the quality of these retrieval results by comparing them with results obtained from other instruments, which is the main purpose of this section. Here, the retrieved profiles are compared to partial columns and profiles retrieved from satellite and balloon measurements. The comparisons are made using limb observations from the satellite instrument SCIAMACHY (SCanning Imaging Absorption spectroMeter for Atmospheric Chartography), from the Systeme d'Analyse Par Observation Zenithale (SAOZ) Balloon-borne measurements and also Nadir mode observations from three different satellites measurements.

3.2.4.1 Comparison with Satellite observations

This section contains the profile comparison results between the SCIAMACHY limb observations and the ZS-DOAS. The satellite profiles are obtained using a two-dimensional (2-D) retrieval approach (SCIA)[Kühl et al., 2008; Pukite et al., 2008].

Before the comparison with the ZS-DOAS profiles, the SCIAMACHY profiles are smoothed by the averaging kernels of the ZS-DOAS observations according to the following formula [Connor et al., 1994; Hendrick et al., 2004; Butz et al., 2006]:

$$\mathbf{x}_{\text{smoothed SCIA}} = \mathbf{x}_a + \mathbf{A}(\mathbf{x}_{\text{SCIA}} - \mathbf{x}_a), \quad (3.7)$$

where \mathbf{A} and \mathbf{x}_a are the averaging kernel matrix and a priori profile derived from ZS-DOAS observations, respectively. \mathbf{x}_{SCIA} is the original SCIAMACHY profile and $\mathbf{x}_{\text{smoothed SCIA}}$ is the smoothed SCIAMACHY profile.

Coincidence criteria

For a meaningful comparison it is important that both ZS-DOAS and SCIAMACHY measurements observe the same air masses at the same time. Thus it is important to define collocation criteria between SCIAMACHY and ZS-DOAS measurements. Several tests have been made to select such coincidence criteria. It is found that only measurements at the same (both a.m and p.m) day and the same SZA ($\pm 1^\circ$) should be selected. The third criterion is to select a proper distance between the tangent point of the SCIAMACHY observations and the ZS-DOAS measurement site. For the last condition, Fig. 3.17 shows the differences between the profiles from ZS-DOAS and SCIAMACHY depending on the distance. Different distances between the tangent point and Kiruna are chosen for each season (winter: DJF, spring: MAM, summer: JJA, autumn: SON). The five representing distance conditions which are used for this test are following:

$$\begin{aligned} d &< 300\text{km}, \\ 300 &< d \leq 450\text{km}, \\ 450 &< d \leq 600\text{km}, \\ 600 &< d \leq 750\text{km}, \\ 750 &< d \leq 1000\text{km}. \end{aligned}$$

From the profiles shown in Figure 3.17 it can be concluded that for most cases the smallest differences are found for small distances (<300km). Another important finding is that the

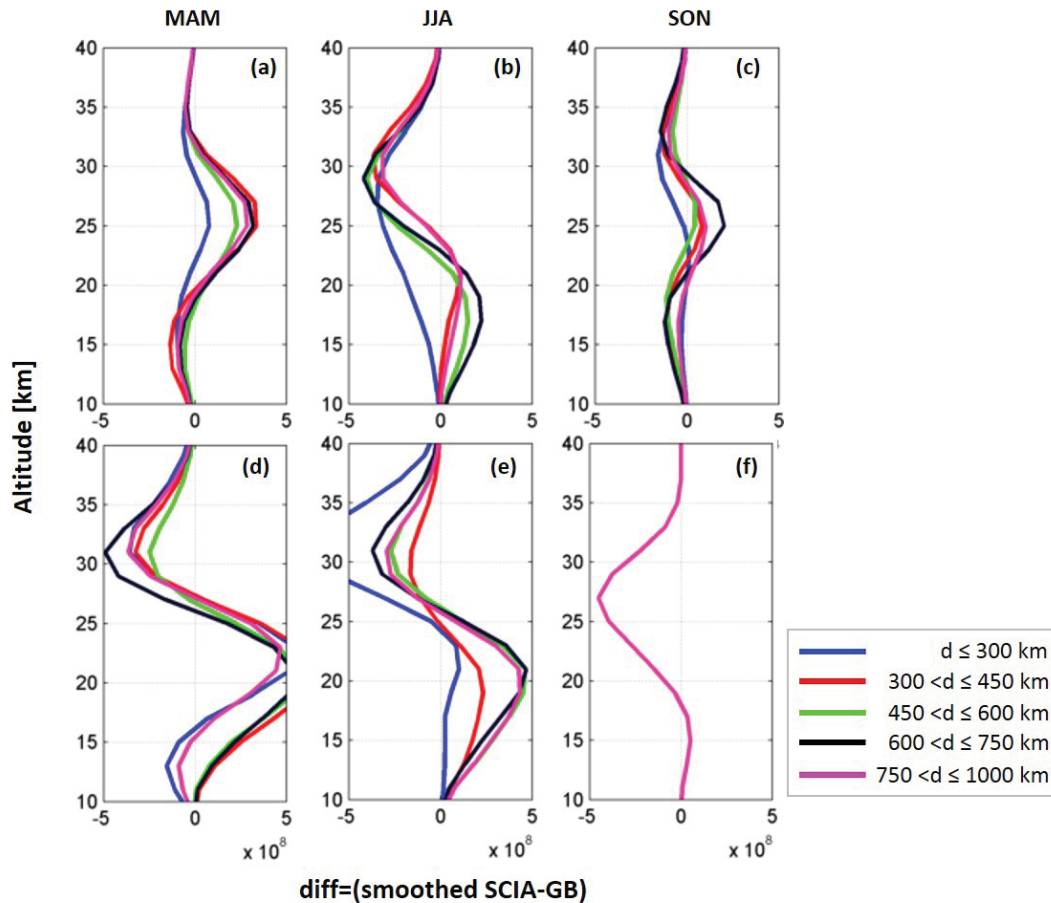


Figure 3.17: Absolute differences between the smoothed SCIAMACHY profiles and the ZS-DOAS profiles for different distances (indicated by the different colours) between the ZS-DOAS measurement site and the tangent point of the SCIAMACHY limb observations. Upper, (a, b, c) and lower figures (d, e, f) represent results for a.m and p.m, respectively.

differences can be classified into two cases depending on the variability of the difference in the profile shape: The first case shows differences only in one layer corresponding to Figs. 3.17(a), (c), and (f). In this case, the difference with respect to the distance criteria is mainly observed around 25 to 27 km, but the profiles look similar with each other regardless of the distance criteria. The second case represents largely varying differences at different altitudes (Figures 3.17(b), (d), and (e)). For these cases below 25 km, the values of the smoothed SCIA profiles are larger than the ZS-DOAS profiles, and above 25 km *vice versa*. One interesting observation here is that the shorter the distance criterion is, the smaller the differences are below 25 km. Above 25 km, however, no dependence of the differences on the criterion is shown. Here it is interesting to note that for the ZS-DOAS the ‘double peak profiles’ were mainly found during p.m, and that the photochemical correction had a stronger effect during pm (see Fig. 2.16). Thus results shown in Fig. 3.17 are another indication for a possibly insufficient photochemical correction of the ZS-DOAS profile algorithm. While in general better agreement is found for smaller distances, for the p.m profiles this is not always the case, especially above 25km. Also this finding can be seen as an indication for problems of the ZS-DOAS profiles during p.m.

Overall it should be noted that no perfect agreement can be expected because of the differences between both observational methods. SCIAMACHY limb observations represent

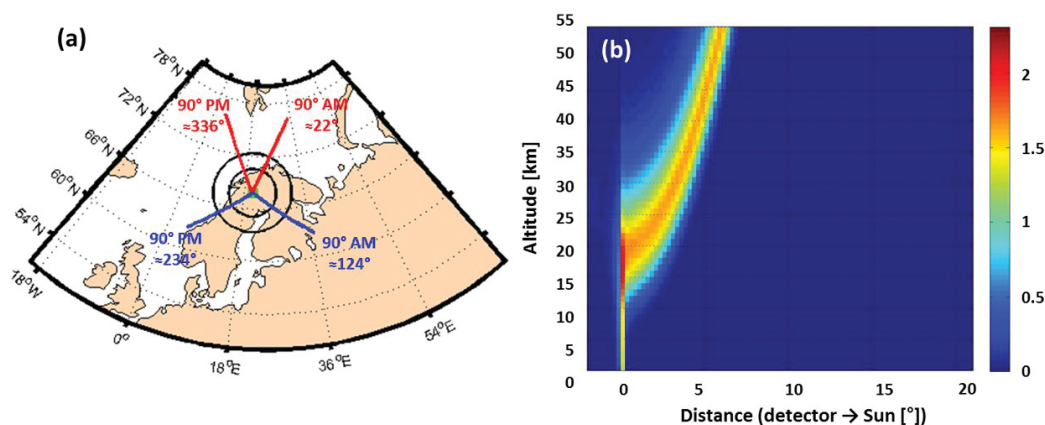


Figure 3.18: (a) Surface projection of the direction of the scanned air masses for ZS-DOAS. The green dots indicate Kiruna, and the blue and red lines represent the azimuth angles of the probed air masses for a SZA at 90° on Feb.13 (Oct.26) and May.19 (Jul.22), respectively. The two rings indicate distances of 300 km and 500 km around Kiruna, respectively. (b) 2D box air mass factors (AMF) as a function of altitude and distance from the instrument for measurements at an SZA of 90° . High values of the box AMF indicate air masses for which the instrument has an increased sensitivity. Here, a horizontal distance of 1° corresponds to around 110 km. The y axis indicates the altitude.

averages for a whole limb swath whose width is around 940 km. Also the different altitudes are not scanned simultaneously, but sequentially while the satellite travels from north to south. Thus the SCIAMACHY values at different altitudes do represent air masses at different distances from the Kiruna site. Another complication is that the air mass probed by the ZS-DOAS instrument is also not located directly above the measurement site, and its distance also varies with SZA. Therefore, an additional test, not with respect to the location of the instrument itself, but with respect to the location showing the largest sensitivity of the Kiruna instrument was performed.

Figure 3.18(a) shows the surface projection of the scanned air masses for ZS-DOAS measurements on Feb.13 (Oct.26) and May.19 (Jul.22). In part (b) of Fig. 3.18 the altitude of the probed air masses as a function of the distance from the instrument is shown. It is found that for an altitude of 25 km, where typically most of the NO_2 exists, the highest sensitivity is found at a distance of about 300 km. Therefore, SCIAMACHY observations with tangent points within a 300 to 500 km radius from Kiruna are selected for comparison with the ground-based measurements in the following.

Profile comparison

The sensitivities of SCIAMACHY and ZS-DOAS observations as function of altitude are plotted in Fig.3.19. In this study the altitude range from 19 km to 37 km is chosen, where both instruments show high sensitivity.

Figure 3.20 shows the comparison of coincident ZS-DOAS and SCIAMACHY profiles from 2002 to 2006 after the coincidence criteria are applied as mentioned above. Here, it should be noted that due to the collocation criteria no coincident data are found in some seasons. For example for data measured in p.m, in September to November no coincident events with SCIAMACHY were found. In this figure, the seasonal mean profiles are shown

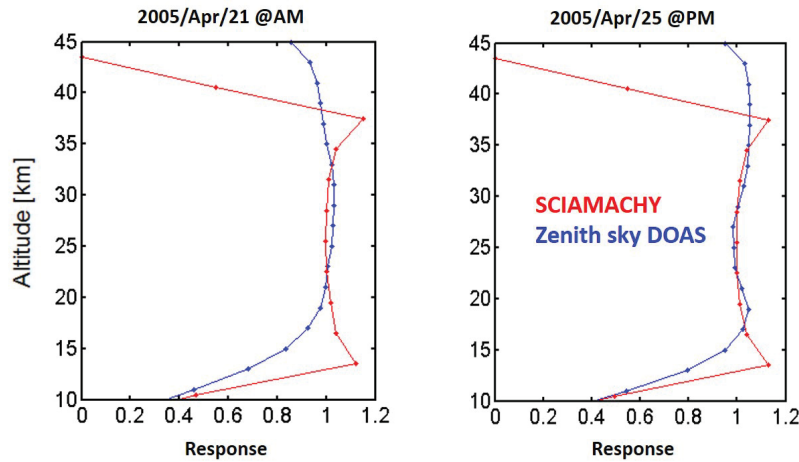


Figure 3.19: Typical measurement sensitivities of SCIAMACHY and ZS-DOAS. The sensitivity is defined as the sum of the rows of the averaging kernels.

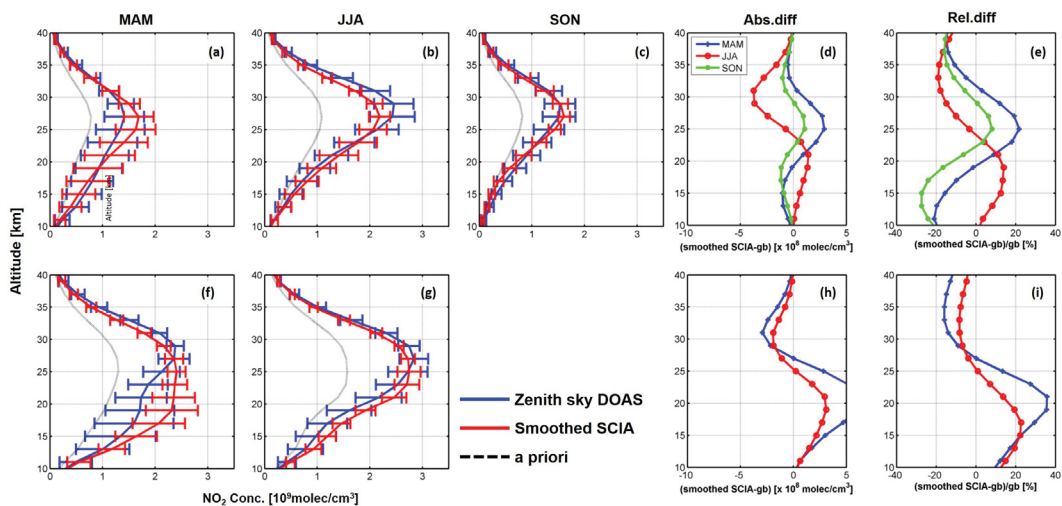


Figure 3.20: Comparison of coincident ZS-DOAS and SCIAMACHY profiles from 2002 to 2006. Figures (a, b, c) and (f, g) represent the seasonal mean profiles measured in a.m and p.m, respectively (blue ZS-DOAS, red: SCIAMACHY). Figures (d, h), and Figs. (e, i) show the corresponding absolute and relative differences. The black dotted lines represent the a priori profiles used for the ZS-DOAS profile inversion.

separately for a.m and p.m. In general, both instruments show good agreement with each other where the relative difference between both profiles is around $\pm 20\%$ in a.m and $-40 - 20\%$ in p.m. The largest absolute differences are observed above 25 km in a.m. The results in MAM and SON show similar profile shapes and the largest relative difference is found around 25 km. For JJA the smoothed SCIAMACHY profile seems to be slightly larger than the ZS-DOAS profile around 30 km (but slightly smaller below 25 km for the pm profiles). Overall the agreement in JJA and SON is better than in MAM with relative differences smaller than 18 % from 25 to 35 km.

Partial column comparison

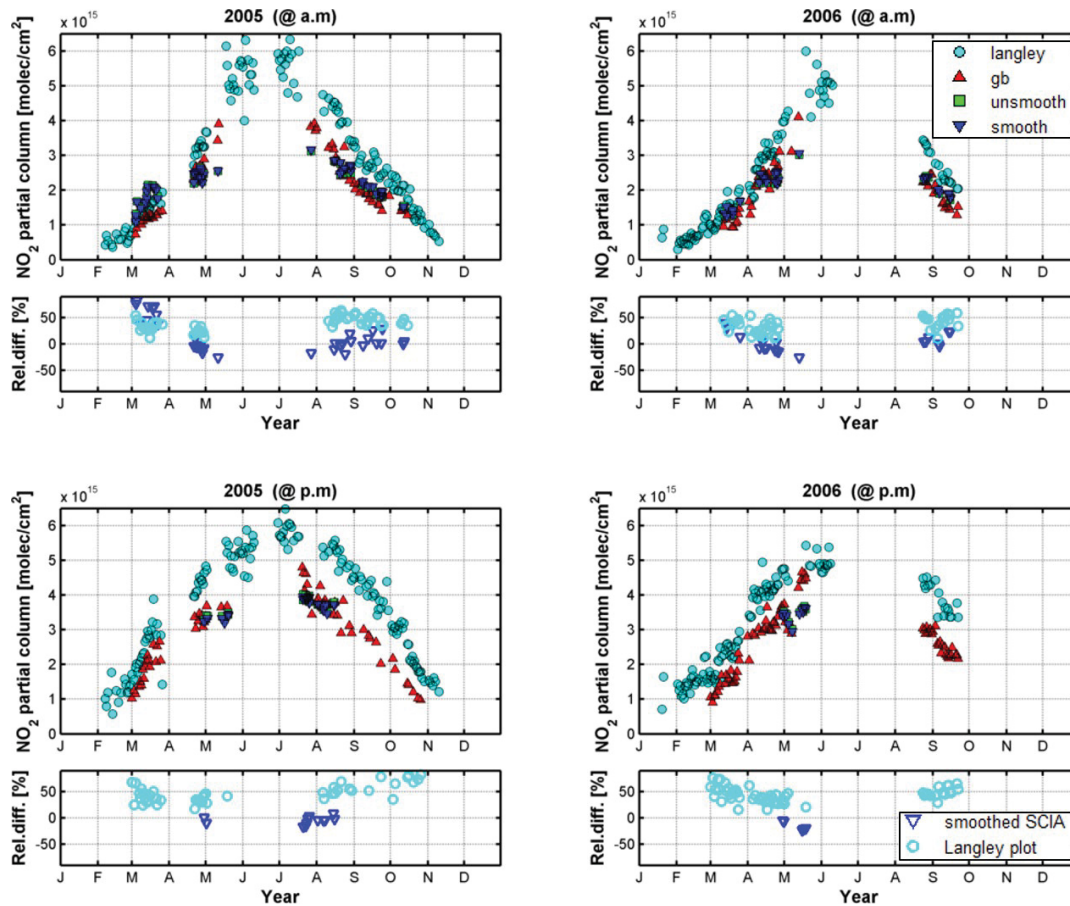


Figure 3.21: Time series of NO_2 VCDs (from ZS-DOAS using the Langley plot method) and partial column densities (19 – 37km) obtained from ZS-DOAS and SCIAMACHY in 2005 (left) and 2006 (right). Data for a.m. are plotted in the upper graphs and for p.m. in the lower graphs. x - and y -axes indicate the time and the monthly averaged (partial) column density (molec/cm^2), respectively. In all figures, cyan dots indicate NO_2 VCDs derived from the Langley plot method (LP), red triangles represent the integrated profiles (19 – 37km) obtained from the ZS-DOAS (IGB), green squares represent unsmoothed integrated SCIAMACHY profiles (US-SCIA) and blue triangles represent smoothed integrated SCIAMACHY profiles (S-SCIA). The lower figures show the relative differences of smoothed integrated SCIA profiles (S-SCIA) and Langley plot method using ZS-DOAS (LP) with respect to integrated profiles obtained from the ZS-DOAS (IGB).

Figure 3.21 shows time series of NO_2 VCDs and partial VCDs (19 – 37 km) obtained from different data sets. The reason for the choice of the altitude range (19 – 37 km) is that both instruments show good measurement responses in this range (see Fig.3.19). Since only few data from 2002 to 2004 exist because technical problems of the instrument, this study focuses on the period from 2005 to 2006. In this graph, NO_2 VCDs obtained from the Langley plot method using ZS-DOAS (abbreviated in the following by LP), integrated ZS-DOAS profiles (IGB), unsmoothed integrated (US-SCIA) and smoothed integrated SCIA profiles (S-SCIA) are shown. In general, the NO_2 column densities obtained from the different data sets show a remarkable agreement. Especially, the partial VCDs obtained from the profiles (IGB, US-SCIA, S-SCIA) are well consistent. LP results show some high outliers and thus a slightly poorer agreement. In both years, large variations in the spring period are observed which are clearly seen in the left and right graphs of Fig. 3.21. At the beginning of the year, the

NO₂ VCDs are small and the relative differences are quite large, but the absolute differences are still small. The relative differences for the LP results are up to 50 %, while those of the profile inversion results (IGB, US-SCIA, S-SCIA) are around $\pm 20\%$. The larger deviations of the LP results are probably caused by two reasons: first, here the total VCD is retrieved, including also altitudes below 19km and above 37 km. Second, since this method is not corrected for the effects of photochemistry, the slope of the Langley plot (which represents the VCD) is systematically overestimated, which was discussed in Sec. 3.1.2.

3.2.4.2 Comparison with Balloon measurements

In this section, the stratospheric NO₂ profiles retrieved from the ZS-DOAS observations and balloon-borne measurements are discussed. For the comparison, this study selects the Systeme d'Analyse Par Observation Zenithale (SAOZ) balloon measurements launched at Kiruna, Sweden. The SAOZ balloon measurement is a lightweight UV-Visible spectrometer carried by balloons designed by Centre National de la Recherche Scientifique (CNRS). A detailed description of the instrument can be found in Pommereau et al. [1990] and Pundt et al. [2002]. As the balloon ascends in the afternoon and floats in the beginning of sunset, it measures NO₂ during twilight. All flights used in this study are such ascent measurements. Thus a photochemical correction is not necessary.

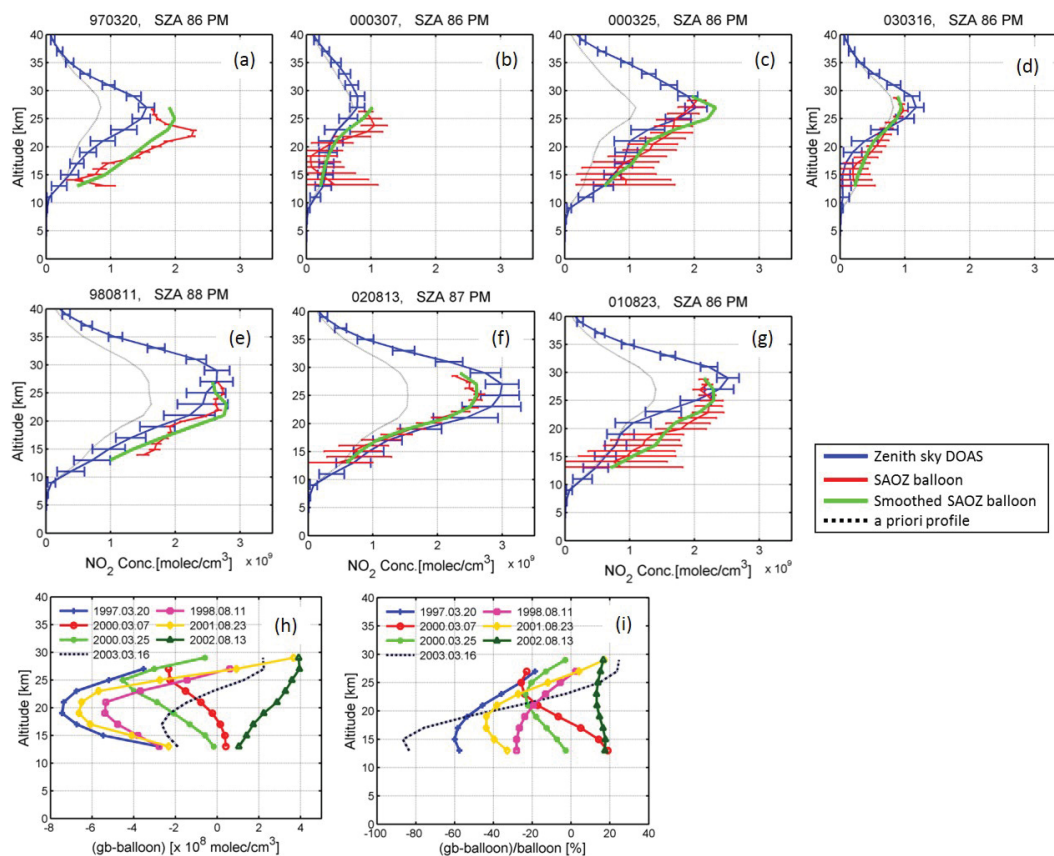


Figure 3.22: Comparison of stratospheric NO₂ profiles derived from ZS-DOAS and SAOZ (a–g) for different days (see Tab. 3.3). Each graph includes four different profiles. Blue lines indicate the results from ZS-DOAS, red and green lines denote unsmoothed and smoothed SAOZ measurements, respectively. Black dotted lines indicate the a priori profile used for the inversion of the ZS-DOAS measurements. (h) and (i) show absolute and relative differences between ZS-DOAS and SAOZ measurements, respectively.

Figure 3.22 shows the comparison of stratospheric NO₂ profiles measured by the ZS-DOAS and the SAOZ balloon (SAOZ) instruments. For this study, seven coincidence events are found (see table 3.3), four in spring (a)–(d), and three in summer (e)–(g). The absolute differences between ZS-DOAS and SAOZ are shown in Fig. (h). Figure (i) represents relative differences calculated from absolute difference by division by the SAOZ values are shown for altitudes from 13 km to 29 km since information from the SAOZ balloon measurements is only available in this altitude range.

As for the comparison with the SCIAMACHY limb measurements, also here both instruments have different vertical resolution (the resolution of ZS-DOAS is coarser compared to SAOZ). Therefore, the SAOZ measurements are smoothed using the averaging kernels from the ZS-DOAS profiles. However, there is another aspect which has to be considered: SAOZ only offers limited altitude information. Thus this study adopts the method of Rodgers and Connor [2003]; Hendrick et al. [2004]; Ryan et al. [2016]. The information of the altitude not covered by SAOZ are generated using a scaled a priori profile. Here, the term "scaled" means that the SAOZ profile is scaled to the a priori profile at the lower and upper altitude limits.

In general (except 20 March 1997), very good agreement between the profiles from ZS-DOAS and SAOZ is found. Maximum NO₂ concentrations are obtained around 27–30 km in spring, and around 25 km in summer. In spring, significant differences are observed on one day (20 March 1997). On this day the vortex edge has moved above Kiruna. Thus both instruments probably observe different air masses.

Observations in summer are shown in Fig. 3.22(e)–(g). Here it should be noted that for the comparison shown in Fig. 3.22(f), we used the balloon data which was obtained one day before the retrieval of the ZS-DOAS profile since there was no balloon-borne measurement on August 13. However, in summer, the dynamic of the stratosphere is more stable than in winter, and thus the atmospheric conditions did probably not vary much during these two days. In all these summer observations, the maximum peak altitude is around 25 km. Except for Fig. 3.22(g), the thickness of the NO₂ layer seems to be broader than for the spring observations. Figure 3.22(g) shows less enhanced NO₂ below 20 km. Figures 3.22(e) and (f) are measured at the beginning of August and (g) at the end of August. NO₂ shows maximum values around early August, and starts to slightly decrease until the end of August. A steady decrease of NO₂ at lower altitudes was already discussed in Fig.3.9. Another

Table 3.3: Overview of the SAOZ balloon flights chosen for comparison

Balloon flight date	Measurement location 20 km	Time(UT) and SZA 20 km
20 Mar 1997	67.5N, 21.8E	16h, 86.3
11 Aug 1998	67.8N, 20.9E	19h, 87.7
07 Mar 2000	67.6N, 21.4E	15.2h, 85.8
25 Mar 2000	67.6N, 21.8E	16.4h, 86.5
23 Aug 2001	67.7N, 22.1E	17.8h, 86.2
12 Aug 2002	67.7N, 21.7E	18.7h, 87.3
16 Mar 2003	67.6N, 22.0E	15.8h, 86.4

possible explanation of the difference between both data sets might be the cloud effect. In Sec. 3.2.3, it was shown that broken and continuous clouds might influence the NO₂ profiles at lower altitudes. For the case of Fig.3.22(e), the results of the cloud classification algorithm indicate a rather cloudy day, while for Fig. (g), the sky was mostly clear.

Table 3.4 shows the NO₂ partial columns calculated by integrating each profile. Here, relative differences are calculated with respect to the SAOZ results. Depending on the balloon floating range, the altitude range varies between 13 km – 29 km and 13 km – 27 km. The second column in this table shows whether the polar vortex is located above Kiruna or not. For most of the cases the partial VCDs from SAOZ are larger than those from ZS-DOAS, but the relative differences are less than 22%, except for Mar.20, 1997, when the vortex edge was above Kiruna.

To conclude this section, it is found that in most cases ZS-DOAS NO₂ shows somewhat lower NO₂ number densities than SAOZ, but the magnitude and peak altitudes show in general good agreement. The relative difference show large variations below 20km, but more consistent results within about 20% are found around 25 km.

3.2.4.3 Comparison with Satellite Nadir observations

This section contains the comparison between ZS-DOAS observations and satellite nadir mode (SAT) observations. Three data sets in different time frames obtained from SAT are used for the comparison. Stratospheric daily mean NO₂ VCDs from ZS-DOAS have been compared to stratospheric NO₂ VCDs from GOME (ERS-2), SCIAMACHY (ENVISAT), and GOME2-A (MetOp) retrieved with scientific algorithms developed at IUP Bremen [Richter et al., 2005, 2011]. All those products show daily averaged VCDs of NO₂ for measurements within a 200 km radius around Kiruna. To minimise any possible bias induced by clouds, only measurements with a cloud fraction below 0.1 are utilised.

The NO₂ SCDs are retrieved in a spectral windows of 425 – 450 nm (for GOME and SCIAMACHY) and 425 – 497 nm (for GOME2-A) using a DOAS algorithm. The SCDs are converted to stratospheric NO₂ vertical columns (VCDs) using a static AMF based on the US standard atmosphere profile. This AMF is derived based on the assumption of zero NO₂ concentrations in the troposphere while in reality there might be slightly enhanced

Table 3.4: Comparison results of the NO₂ partial columns derived from ground-based zenith sky DOAS and SAOZ balloon measurements.

Date	Kiruna within/out the polar vortex	Altitude [km]	ZS-DOAS [10 ¹⁵ molec/cm ²]	SAOZ [10 ¹⁵ molec/cm ²]	Rel.diff [%]
20 Mar 1997(a)	edge	13-27	1.19	2.03	-42
07 Mar 2000(b)	inside	13-27	0.59	0.71	-15
25 Mar 2000(c)	outside	13-29	1.98	2.36	-16
16 Mar 2003(d)	inside	13-29	0.82	0.93	-11
11 Aug 1998(e)	-	13-27	2.56	3.07	-17
13 Aug 2002(f)	-	13-29	3.37	2.94	15
23 Aug 2001(g)	-	13-29	2.15	2.75	-22

tropospheric values over the Kiruna site. Such a presence of a non-zero tropospheric NO₂ concentration will lead to a slight underestimation of the true stratospheric AMF. But this effect is probably overcompensated by the fact that the derived NO₂ SCD is larger than the stratospheric NO₂ SCD because it also contains the tropospheric NO₂ partial column. Finally, the stratospheric NO₂ profile varies systematically with season. Thus the static AMF might slightly over- or underestimate the true stratospheric AMF in different seasons, respectively.

Figure 3.23 shows the temporal variation of the stratospheric daily NO₂ VCDs measured from ZS-DOAS with the Langely plot method (LP) and integrated profiles (IGB), together with the results from satellite observations for individual years from 1997 to April 2016. In general, all data sets show a similar seasonality, with minima in winter and maxima in summer. Note that in some years two satellite data sets are shown in one figure: during the overlap period between GOME and SCIAMACHY (2002 – 2003), and SCIAMACHY and GOME2 (2009). Here it is interesting to note that a systematic difference between GOME and SCIAMACHY observations is obtained during the overlap period of these two sensors. The mean relative difference between LP and GOME in 2003 is 34%, while between LP and SCIAMACHY is 4.9 %. Such an inconsistency was found also in comparison results of other ground-based measurement stations e.g. Andoya and Sondankyla. It is known that this difference is induced by a technical problem of the so-called diffusor plate in GOME which was used for irradiance measurements [Gil et al., 2008]. Different AMFs used for the different satellite instruments also might cause the difference.

Figure 3.24 shows daily averaged stratospheric NO₂ VCDs from GOME, SCIAMACHY, and GOME2-A plotted versus the coincident ground-based ZS-DOAS results. A linear regression is applied to all data. The derived slopes of the fitted lines are systematically smaller than unity indicating that the Satellite data are systematically lower than the ZS-DOAS measurements for high values (in spring, summer and autumn). This is probably related to the difference of the satellite overpass time from the times of the ZS measurements. Especially in summer, during polar day, the NO₂ / NO ratio is probably smaller during the time of the satellite overpass leading to smaller values of the satellite observations. But also deviations of the applied stratospheric AMF from the true AMF might play a role. Smallest differences are found in winter (except for GOME). In general the agreement of SCIAMACHY and GOME2-A observations with ZS-DOAS is better than that with GOME. Interestingly, a much larger *y*-intercept is found for GOME than for the other instruments, which is probably related to the errors introduced by the diffuser plate as mentioned above. Also a larger scatter during spring is observed for GOME. The correlation results versus the IGB data (Figs. 3.24(d)-(f)) show less data points due to the filters applied to the ZS profile data, but in general very similar results as for the comparison with the LP data are found.

In Fig. 3.25, box and whisker plots of absolute and relative differences between the satellite and ZS-DOS observations (1997 – 2016) derived from LP and IGB are shown. Here, the absolute difference is calculated by subtracting the ZS-DOAS data from the satellite results, and the relative difference represents the absolute difference divided by the ZS-DOAS value. Results between January and December are missing in this figure because no ZS-DOAS measurement data is available. In general, the absolute and the relative differences show similar seasonal variations. For the absolute differences the smallest values are found in spring and autumn, while in summer large negative deviations occur. For the relative differences, the largest (positive) deviations are found for spring and autumns. The relative differences are largest for the comparison to GOME, which is most probably related to the

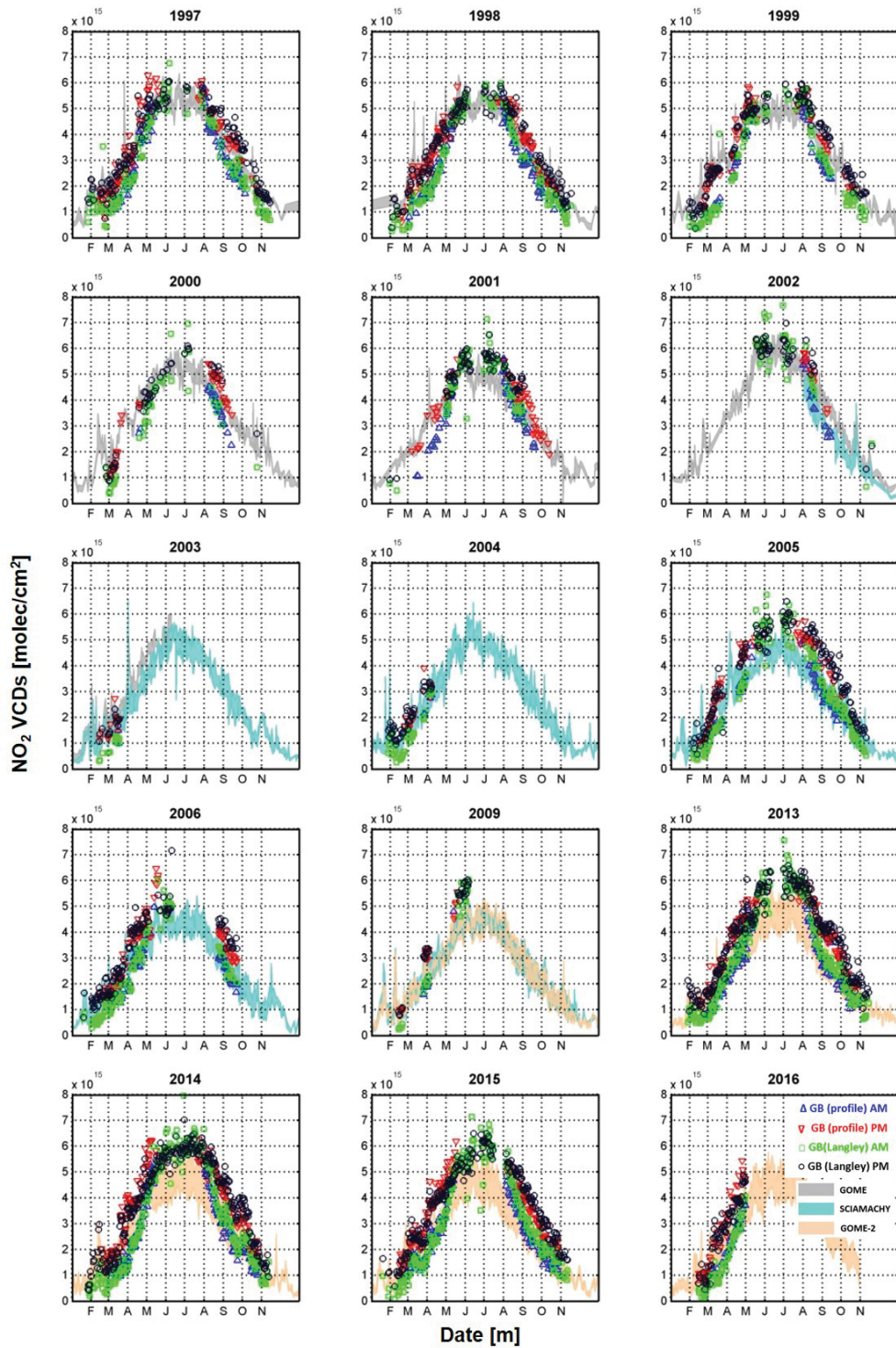


Figure 3.23: Time series of stratospheric daily mean NO₂ VCDs compared with three different satellite nadir observations: GOME (1997 – 2002), SCIAMACHY (2002 – 2009), and GOME2-A (2009–2015). Green squares and black dots indicate the VCDs obtained from the ground based observations by the Langley plot method (LP) at a.m and p.m, respectively. Blue and red triangles indicate the VCDs derived from the integrated stratospheric profiles at a.m and p.m. The shaded areas represent satellite nadir mode observations indicating daily minimum and maximum NO₂ VCDs.

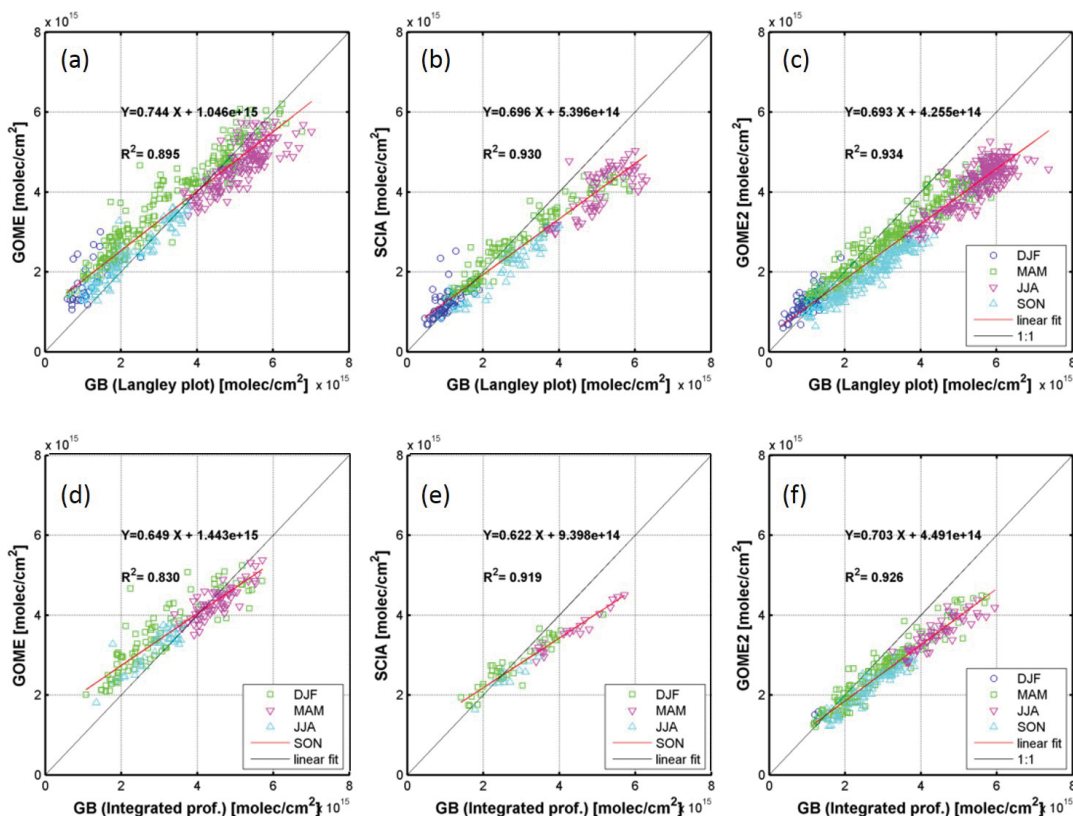


Figure 3.24: Daily averaged stratospheric NO_2 VCDs from satellite observations plotted against those derived from ZS-DOAS observations. Different colors indicate different seasons (winter: DJF, spring: MAM, summer: JJA, autumn: SON). Figures (a)–(c) present comparisons to ZS-DOAS measurements derived using the Langley plot method and (d)–(e) show the corresponding comparisons to the integrated profiles from ZS-DOAS. Each column indicates results for a different satellite instrument.

offset caused by the diffuser plate problem (see above). Part of the deviations might be related to the conversion process of SCDs to VCDs in which the satellite products use static AMFs. Since the vertical distribution of stratospheric NO_2 above Kiruna varies depending on the season as already shown in Fig.3.9, the use of a static AMF probably leads to systematic differences depending on season. Another possible contribution to the differences is a spatial resolution of the satellite ground pixel. GOME has a lower resolution with a larger ground-pixels size ($320 \times 40\text{km}$) than SCIAMACHY ($60 \times 30\text{ km}$) and GOME2-A ($80 \times 40\text{km}$). It is interesting to note that the comparison to the IGB data shows rather similar results as the comparison to the ZS-DOAS measurements.

3.2.5 Trend analysis of stratospheric NO_2

Stratospheric NO_2 is formed from nitrous oxide (N_2O) which is emitted from natural sources including oceans and soils (about 60 %), and also from anthropogenic sources such as biomass burning, fertilizer use, and from several industrial processes (about 40 %). Because N_2O is stable in the troposphere, it can reach the stratosphere without significant

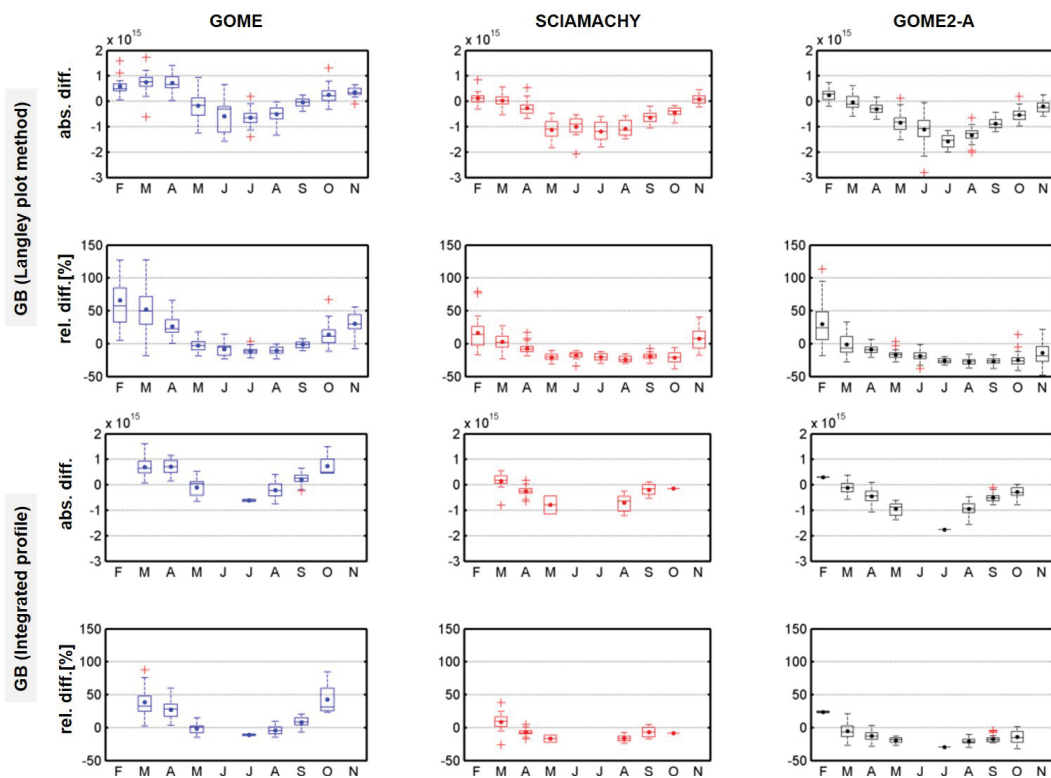
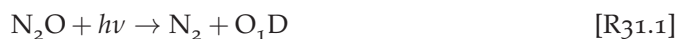


Figure 3.25: Box and whisker plots of the absolute and relative differences of the stratospheric NO₂ VCDs between satellite and ZS-DOAS observations from 1997 to 2016. Each column indicates a different satellite instrument. The results in the 1st and 2nd rows are for comparison to the ZS-DOAS LP data, those in the 3rd and 4th rows are for the comparisons to the ZS-DOAS IGB data. In each box, red crosses indicate outliers defined as data points higher and lower than 1.5 times of the inter-quartile range, and the whiskers show the maximum and minimum values excluding the outliers. The horizontal lines and the dots indicate median and mean of the differences, respectively.

loss. In the middle stratosphere, 90% of N₂O is photolysed by UV radiations according to the following chemical reactions:



These reactions lead to the production of NO which is one of the reactive nitrogen oxide species and is involved in the ozone depleting catalytic cycle [Crutzen, 1970]. NO reacts quickly with O₃ to form NO₂. The equilibrium between NO and NO₂ is determined between the O₃ concentration and the amount of solar radiation.

The latest observation from the WMO Global Atmosphere Watch (GAW) program showed that the globally averaged N₂O has increased by 4.4 % between 1991 and 2010 [WMO, 2016] due to the growth of fertilizer use in agriculture, increasing industrial processes and increasing release of N₂O from soils. Here the growth in the period between 1991 and 2010 was chosen, because it corresponds to the stratospheric trends between 1997 and 2016 taking into account the age of air of stratospheric air above Kiruna of about 5.7 years. Several studies have shown that increasing stratospheric NO₂ is related to the increasing N₂O emissions. Nevertheless, both gases are intricately correlated by photochemical reactions

depending on the measurement site, observation period, aerosol amount, atmospheric dynamics, the NO₂ partitioning and the stratospheric temperature. Thus investigating the correlation between NO₂ and N₂O is highly demanded.

Several efforts have been made to investigate the trend of stratospheric NO₂ using satellite and ground-based measurements aided by computational models, but those have mainly focused on mid-latitudes and the southern hemisphere as shown in Tab. 3.5. Gruzdev [2009] showed the latitudinal distribution of stratospheric NO₂ trends from 23 different NDACC stations. This study also included data from the Kiruna and Harestua measurement sites. Harestua is located in Norway rather close to Kiruna, but a few hundred kilometers to the South. Here, it should be noted that the trends at Kiruna were derived from measurements of the DOAS instrument operated by NIWA. Gruzdev [2009] found a positive trend of NO₂ in the southern hemisphere but no significant trend in northern latitudes. Liley et al. [2000] and Dirksen et al. [2011] observed a strong positive trend during three decades at Lauder, New Zealand. Cook and Roscoe [2009] investigated the stratospheric NO₂ trend in Antarctica between 1990 and 2007 and showed that it has changed from a positive to a negative trend with a maximum NO₂ concentrations around the year 2000. Those studies also mentioned that the increase of the stratospheric aerosol loading due to the Pinatubo volcano eruption (1991) has led to a decline of stratospheric NO₂. Hendrick et al. [2012] showed a negative trend at Jungfraujoch in contrast to Robles-Gonzalez et al. [2016] who found a strong positive trend at Izana. Summing up all these former studies, stratospheric NO₂ trends strongly depend on the investigated time period and measurement site. Also, some of the reported trends are not consistent with each other. In this study, the trend of stratospheric NO₂ using long-term observations (1997 to 2015) from ground-based zenith sky DOAS at Kiruna (located at a high latitude inside of the Arctic circle) is analysed and discussed.

3.2.5.1 Trend analysis method

In order to determine the linear trend of the stratospheric NO₂ measured by ground-based zenith sky DOAS, a nonlinear least-squares algorithm (the python LMFit module by Newville et al. [2014]) is utilised [Marquardt, 1963; Beirle et al., 2013]. The NO₂ time series (of monthly mean values) is modeled by various explanatory variables: the annual cycle, the semi-annual cycle, the quasi-biennial oscillation (QBO), the solar flux, stratospheric aerosol, as well as a constant and a linear term.

The general form of the model function used in the least square fit model is represented by the following equation:

$$y(t) = b + mt + \sum_{n=1}^2 (a_n \cos(n\omega t) + c_n \sin(n\omega t)) + D \cdot \text{QBO}_{30}(t) + E \cdot \text{QBO}_{50}(t) + F \cdot \text{Solarflux}(t) + G \cdot \text{Aerosol}(t), \quad (3.8)$$

where b is an additive constant and m describes the linear trend. Annual and semi-annual cycles are considered by the 1st and 2nd order Fourier terms. In addition, two QBO(t) terms, a Solarflux(t) term and a stratospheric aerosol(t) term are considered. $y(t)$ represents the time series of monthly mean values of the stratospheric NO₂ VCD at Kiruna. b , m , a_n , c_n , D , E , F and G are fitting parameters determined from the least squares regression.

Table 3.5: Summary of stratospheric NO₂ trends reported in former studies measured at various sites. Asterisk(*) represents the trend observed in p.m.

	Covered period	Site	Instrument	Trend (%/decade)
Liley et al., (2000)	1981-1991	Lauder (45°S, 170°E)	ZS-DOAS	+5
Cook & Roscoe (2009)	1990-1995	Faraday (65.25°S, 64.27°W)	ZS-DOAS	9±4/11±4* : (1990-2000, excluding 1991-1992)
	1996-2007	Rothera (67.57°S, 68.13°W)		-21±6/-22±6* relative to value in 2000: (2000-2007)
Gruzdev et al., (2009)	1991-2006	Kiruna (67.8°N, 20.4°E)	ZS-DOAS	-0.3±4/-2.3±3*
	1994-2007	Harestua (60.2°N, 10.8°E)	ZS-DOAS	1.7±5.5/0.5±4.2*
Dirksen et al., (2011)	1981-2010	Lauder (45°S, 170°E)	ZS-DOAS	+5.2±0.5
Hendrick et al., (2012)	1991-2009	Jungfauioch (46.5°N, 8.0°E)	ZS-DOAS UV-visible(SAOZ)	-3.7±1.1
			FTIR	-3.6±0.9
Robles-Gonzalez et al., (2011)	2000-2012	Izaña (28.3°N, 16.5°E)	DOAS	+13.5

The quasi-Biennial-Oscillation (QBO) term

The QBO characterises the equatorial stratospheric wind which strongly influences the distribution of stratospheric O₃ depending on the easterly and westerly winds averaged during a period of 27 months. Although the QBO is a tropical phenomenon, it influences the stratospheric flow from the tropics to the poles [Baldwin et al., 2001]. There are also substantial QBO signals in many short-lived chemical constituents. Through the modulation of the extratropical wave propagation, the QBO has also an effect on the breakdown of the stratospheric polar vortices at the end of polar winter and thus on the high-latitude ozone depletion. In order to account for the QBO periodic oscillations in the stratosphere, zonal winds measured at Singapore at 30 hPa and 50 hPa are taken. The data are obtained freely from the website. (<http://www.geo.fu-berlin.de/en/met/ag/strat/produkte/qbo/index.html>).

The Solar flux term

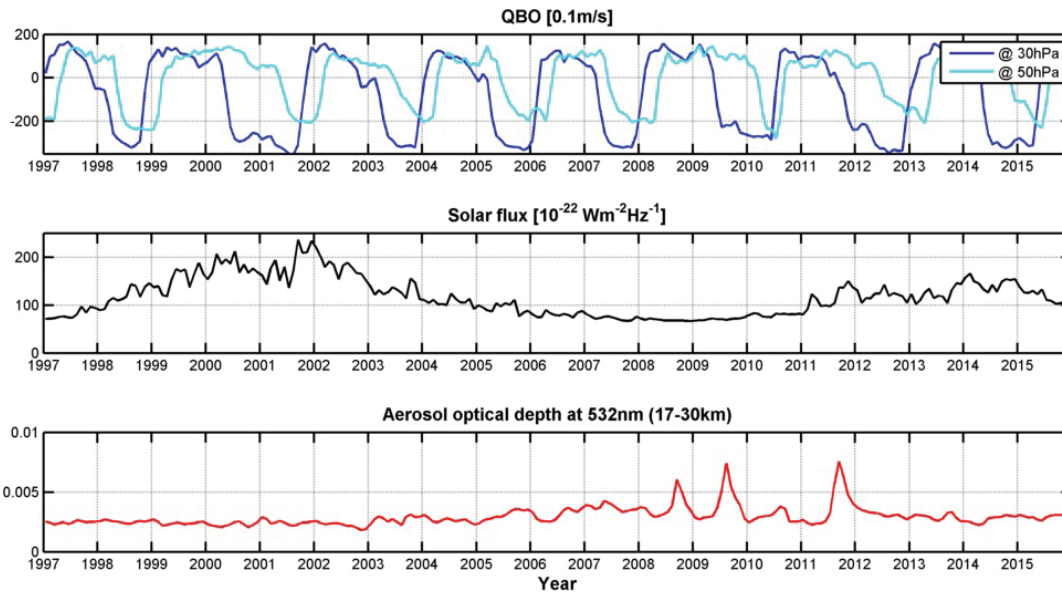


Figure 3.26: Explanatory proxy parameters for the trend analysis from 1997 to 2015. The upper figure represents the QBO at 30 hPa (colored blue) and 50 hPa (colored cyan), the middle figure shows the monthly averaged radio emission from the Sun at a wavelength of 10.7 cm. And the lower figure shows the time series of monthly mean AOD (17–30 km) from OHP lidar observations.

Several studies have shown that a change of the solar variability influences the stratospheric ozone in different ways [Shindell, 1999; WMO, 2002; Hood et al., 2010]. For example, variations in the UV flux caused by the solar variability can directly affect the polar stratospheric O_3 . In addition, the precipitation of energetic particles into the atmosphere at high latitude is well known [Randall et al., 2005; Sinnhuber et al., 2006]. Callis and Lambeth [1998] showed that the precipitation of energetic particles can affect the formation of NO_y . Sinnhuber et al. [2006] proved that negative O_3 anomalies are strongly correlated with the flux of energetic electrons. To account for these effects, the solar radio flux at 10.7 cm is used as an indicator of the solar activity. This data can be freely obtained from the National Research Council of Canada [Tapping, 2013].

The stratospheric aerosol term

Stratospheric aerosols provide a surface on which heterogeneous chemical reactions take place. They also affect the stratospheric photochemistry and in particular the partitioning of reactive nitrogen, NO_y species [Coffey, 1996]. Several studies have measured a significant decrease in total column of NO_2 after large volcanic eruptions, for example, El Chichon (1982) and Pinatubo (1991) as studied by Koike et al. [1993]; Van Roozendaal et al. [1994, 1997]. Stratospheric aerosol particles also reflect the short wave solar radiation, and thus cool the atmosphere [Humphreys, 1940]. Therefore, in this study, the stratospheric aerosol optical depth (AOD) has also been included as a proxy parameter in the model function. The chosen data set is the monthly averaged stratospheric AODs between 17 and 30 km altitude obtained by a differential absorption lidar system (referred to as LiO₃S) at the French Observatoire de Haute-Provence (OHP, 44°N) [Khaykin et al., 2017]. This dataset covers a period from 1994 to 2015 and is largely consistent with results from several satellite

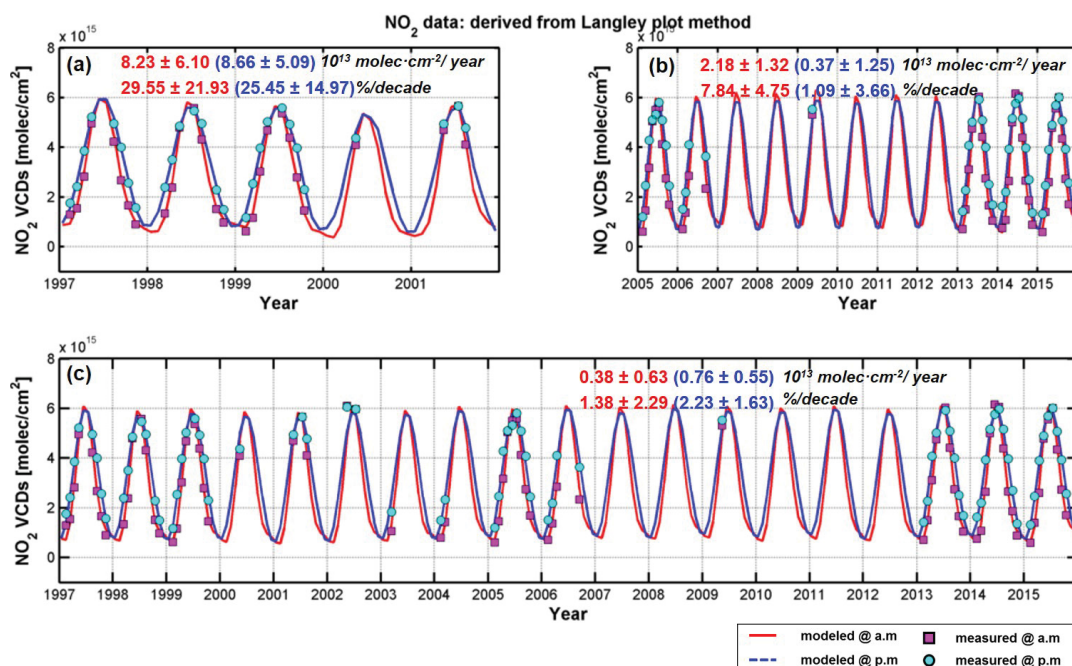


Figure 3.27: Trend analysis of monthly mean NO₂ VCDs determined by the Langley plot method. Magenta squares and cyan dots represent measured data at a.m. and p.m., respectively. Red and blue continuous lines indicate the corresponding fit results. Figures (a) to (c) show the results for the different time periods. The derived absolute (upper) and relative (lower) trends at a.m. (red) and p.m. (blue) are shown in each figure.

aerosol sounders (e.g. SAGE2, GOMOS, OSIRIS, CALIOP and OMPS) where the difference is $-1.0 \pm 2.0\%$ with 0.96 of correlation.

Figure 3.26 shows all explanatory variables discussed in this sub section.

3.2.5.2 Results of the trend analyses

The stratospheric NO₂ trends are determined separately for the two NO₂ data sets, derived either by the Langley plot method or from the integration of the derived profiles. The corresponding results are shown in Fig. 3.27 and 3.28. Three time periods are chosen for the trend analysis (a) 1997–2001, (b) 2005–2015, and (c) 1997–2015 (according to the data gaps caused by the technical problems of the instrument). This separation also helps to test how strong the derived trends depend on the chosen time period. Table 3.6 summarises the results of the trend analyses. To quantitatively compare the trend results, absolute trends as well as relative trends per decade for the different periods are calculated. Here, the relative trends are calculated with respect to the average of the NO₂ VCD for the whole period (1997–2015).

In general, no strong and significant trends are found for the periods under consideration. Especially, if only short periods are selected, the derived trends differ strongly depending on the chosen data set (Langley-plot VCDs or stratospheric profiles) or whether the time series of QBO, solar flux, and aerosol were considered or not. There are also different trends observed for a.m. and p.m. These findings indicate that there are no strong (significant) trends and/or that the chosen periods are too short to determine meaningful trends of stratospheric NO₂. In contrast, for the whole time period (1997–2015) more consistent and

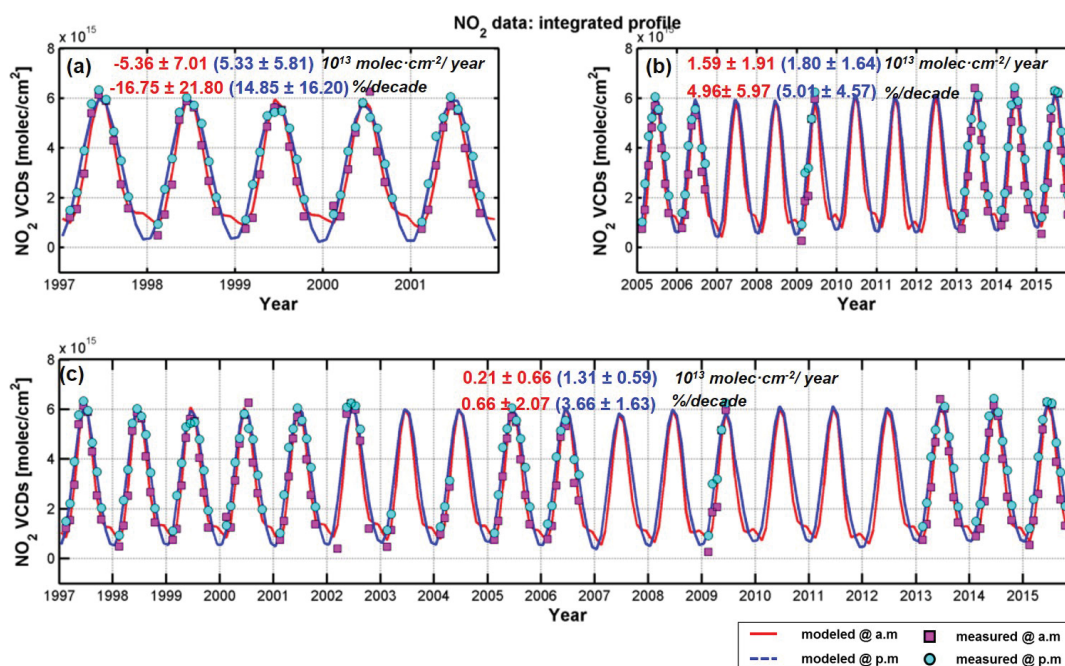


Figure 3.28: Trend analysis of monthly mean NO₂ VCDs determined by the integrated profiles. Magenta squares and cyan dots represent measured data at a.m and p.m, respectively. Red and blue continuous lines indicate the corresponding fit results. Figures (a) to (c) show the results for the different time periods. The derived absolute (upper) and relative (lower) trends at a.m (red) and p.m (blue) are shown in each figure.

slightly positive trends are obtained (with significant positive trends only in p.m). For the long time period for most cases also similar trends are obtained regardless of whether the time series of QBO, solar flux, and aerosol are included or not. The fitted model functions (Figs.3.27 and 3.28) indicate that the seasonal cycle is the dominant contributor to the overall variability. Here, it should be noted that a strange feature for a.m in winter is obtained which is caused by the missing observation data during winter. However, the results for the whole period do not dramatically change if the semi-annual term is excluded from the fit, which is shown in Appendix (Figs. A.3 and A.4). Overall, the trend results indicate that the stratospheric NO₂ over Kiruna did not strongly change within the last two decades. As mentioned in Seidel et al. [2016], also the trend of stratospheric temperature is most pronounced in mid latitudes, but not significant at high latitudes.

Our NO₂ trend results reasonably agree with N₂O which has shown a positive trend during the last 20 years (about 4.4 %, [WMO, 2016]). However, it is also interesting to note that the NO₂ trend derived in this study seems to be not consistent with NO₂ trends reported in former studies measured at mid latitudes. Besides possible measurement errors, this finding indicates that stratospheric NO₂ trends strongly depend on the measurement site and the selected period. Further research including the use of atmospheric chemistry models is needed to better understand the trends of stratospheric NO₂.

Table 3.6: Derived absolute and relative trends of the stratospheric NO₂ VCDs over Kiruna. Values in the bracket represent the trends performed from fits without QBO, solar activity and aerosol terms.

Method	Period	molec· cm ² /year		% /decade	
		a.m (×10 ¹³)	p.m (×10 ¹³)	a.m	p.m
Langly Method	(a) 1997-2001	8.23±6.10 (-6.07±3.89)	8.66±5.09 (-6.03±3.39)	29.55±21.93 (-22.46±14.39)	25.45±14.97 (-18.95±10.66)
	(b) 2005-2015	2.18±1.32 (0.31±0.86)	0.37±1.25 (0.34±0.75)	7.84±4.75 (1.17±3.19)	1.09±3.66 (1.08±2.38)
	(c) 1997-2015	0.38±0.63 (0.38±0.48)	0.76±0.55 (0.63±0.42)	1.38±2.29 (1.40±1.76)	2.23±1.63 (1.98±1.31)
Integrated Profile	(a) 1997-2001	-5.36±7.01 (-3.05±2.90)	5.33±5.81 (-2.30±2.52)	-16.75±21.90 (-10.93±10.38)	14.85±16.20 (-7.53±8.25)
	(b) 2005-2015	1.59±1.91 (1.63±1.20)	1.80±1.64 (1.94±1.03)	4.96±5.97 (5.83±4.28)	5.01±4.57 (6.35±3.38)
	(c) 1997-2015	0.21±0.66 (-0.31±0.52)	1.31±0.59 (0.73±0.46)	0.66±2.07 (-1.10±1.87)	3.66±1.63 (2.41±1.50)

3.3 SUMMARY

In this chapter, the temporal and spatial variation of stratospheric NO₂ above Kiruna, Sweden is investigated by using ground-based zenith sky DOAS measurements. The following general points summarise the main findings derived from this chapter:

- NO₂ VCDs derived using the Langely plot method show multi-year monthly mean variations from 1997 to 2015, in which year-to-year variabilities in spring and autumn are proven to be very large and a strong seasonal variation is generally shown. Moreover, the retrieved NO₂ vertical distributions based on the optimal estimation method show monthly and daily based NO₂ profiles and how NO₂ is reformed and declines depending on the meteorological conditions. To understand the unexpected bimodal structure in these profiles, cloud effects are investigated for the first time in this study. Cloud effects are found to be small, but an artifact from the photochemical modeling tool can strongly influence the derived profiles.
- In order to confirm the data obtained from ground-based zenith sky DOAS, they are compared with other measurements including SCIAMACHY limb observations, SAOZ balloon-borne measurements and three different satellite nadir observations. Comparison with the SCIAMACHY limb observation are shown to be well consistent with the DOAS observation. The seasonal variability of NO₂ profile shape is clearly provided in this comparison. The balloon measurements in which seven coincident events are selected show also a good agreement with the DOAS measurements and the influence of the polar vortex condition on the NO₂ profile is proven. The comparison between daily averaged stratospheric NO₂ VCDs from GOME, SCIAMACHY, and GOME-2A versus the coincident ground-based zenith sky DOAS shows in general,

good agreement but the satellite nadir observations are systematically lower than the ground-based observations which is mainly related to the use of a static AMF for the satellite data.

- In order to see the long term variability of stratospheric NO_2 , a trend analysis is performed using a nonlinear least-squares algorithm. In this study, two different NO_2 data sets, NO_2 VCDs derived from the Langley plot method, and from the integration of the profile inversion are utilised. Relative trend values of 1.38 ± 2.29 ($0.66 \pm 2.07^*$)/decade in a.m, and 2.23 ± 1.63 ($3.36 \pm 1.63^*$)/decade in p.m for 1997 – 2015 are obtained (the asterisk indicates the trend derived from integrating the profile inversion data.). This obtained trend is consistent with the positive trend (2.3%/decade) of N_2O observed from 1991 to 2010 (year of stratospheric entry).

In addition to stratospheric chlorine compounds, also bromine compounds contribute to ozone loss. Bromine compounds are much less abundant than chlorine compounds but their ozone depletion efficiency is roughly 45 times larger than chlorine's [Dorf et al., 2006a]. Among inorganic bromine species, BrO is the most abundant inorganic bromine species (around 70% of Br_y [Stachnik et al., 2013]), and it is the only chemical compound which can be measured in the Br_y family by UV/Vis remote sensing measurements. The Montreal Protocol has regulated the emission of the sources of bromine, which results in a decline of the total bromine loads in the stratosphere by 1% per a year. However, the evolution of BrO concentration in the stratosphere is still worth to be investigated due to the lack of knowledge for the bromine releasing mechanisms and chemical recycling processes.

The main objective of this chapter is to quantify the stratospheric BrO abundance and to observe its temporal and vertical variability in the northern polar region under different atmospheric conditions, based on long-term observations from ground-based instrument at Kiruna. In the first section, detailed information for the optimisation of the settings of the spectral analysis is provided. The general temporal variation of stratospheric BrO is described in the second section. The derived vertical distribution of stratospheric BrO is shown in the third section and is compared with results obtained from other measurement methods in the fourth section. The results of a trend analysis are presented in the final section.

4.1 ANALYSIS

4.1.1 Wavelength range and reference spectra

In this section the analysis settings for stratospheric BrO are described in detail. For the BrO analysis the spectral range of 342 – 357 nm is chosen using daily based noon reference spectra; further analysis details are summarised in Tab. 4.1 and Fig. 4.1.

The BrO absorption of typical measurement spectra is smaller than 0.1% and thus the BrO results can be significantly affected by interference with the much stronger absorption bands of ozone in the same wavelength range [Theys et al., 2007b]. To minimise these possible interferences, in this work, several sensitivity tests are performed to choose the optimal BrO analysis settings as discussed in the following.

4.1.2 Taylor series approach

First, the so-called Taylor series approach is implemented to analyse BrO SCDs. This approach was first introduced by Pukite et al. [2010] and it contributed greatly to an improvement of the BrO spectral analysis. It considers the spectral dependency of the SCDs

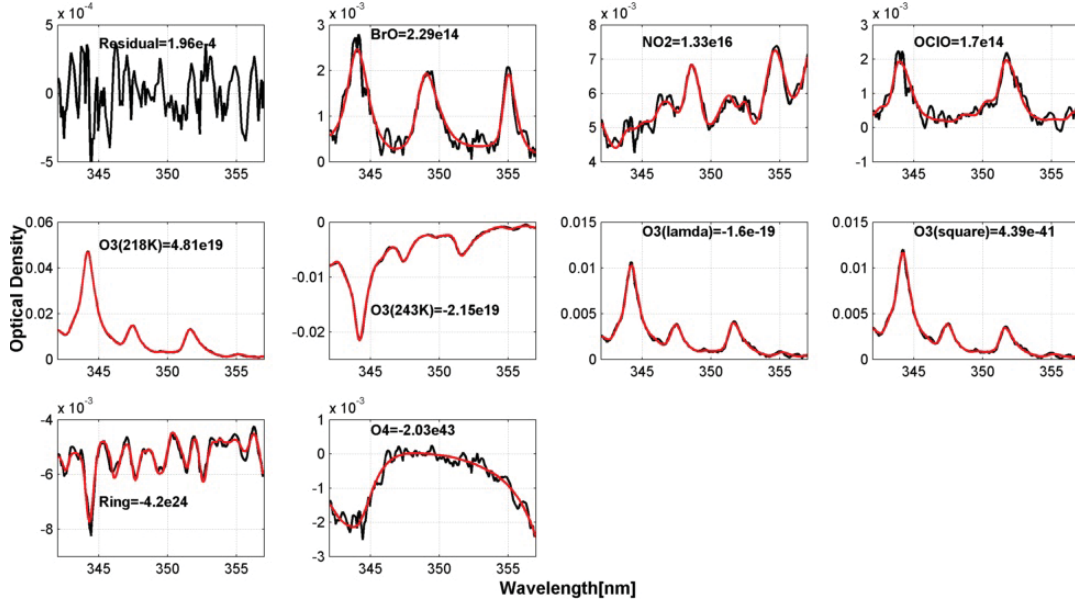


Figure 4.1: Example of a BrO analysis of a spectrum measured on 2016 Feb.26, 15:19 UTC (SZA at 89°). The red lines indicate the different reference spectra scaled to the respective absorptions retrieved from the measured spectra (black lines).

or AMFs on the wavelength in the DOAS fit to minimise the associated retrieval error. In the standard DOAS approach the BrO DSCD is calculated by the following equation,

$$\ln \frac{I_0}{I} = S_{O_3} \sigma_{O_3} + S_{NO_2} \sigma_{NO_2} + S_{BrO} \sigma_{BrO} + P, \quad (4.1)$$

where S_X and σ_X are a slant column and absorption cross sections of a chemical species X , respectively. P represents the broadband features e.g due to Mie and Rayleigh scattering by a polynomial function. In the considered UV spectral range the absorption by ozone dominates. Taking the first order Taylor series expansion for O_3 into account, the DOAS equation can be re-written as follows,

$$\ln \frac{I_0}{I} = \left(S_{0,O_3}^* \sigma_{O_3} + S_{\lambda,O_3} \lambda \sigma_{O_3} + S_{O_3,O_3} \sigma_{O_3}^2 \right) + S_{NO_2} \sigma_{NO_2} + S_{BrO} \sigma_{BrO} + P, \quad (4.2)$$

Table 4.1: Settings for the spectral analysis of BrO from the ground-based zenith sky DOAS measurements.

Fitted Spectra	Reference
BrO	Wilmouth et al. [1999] 228K
O_3	Daumont et al. [1992]; Malicet et al. [1995] 218K, 243K
O_4	Thalman and Volkamer [2013] 273K
NO_2	Vandaele et al. [1998] 220K
OCIO	Kromminga et al. [2003] 213K
Ring	Kraus [2006]; Wagner et al. [2009]
Polynomial order	4th

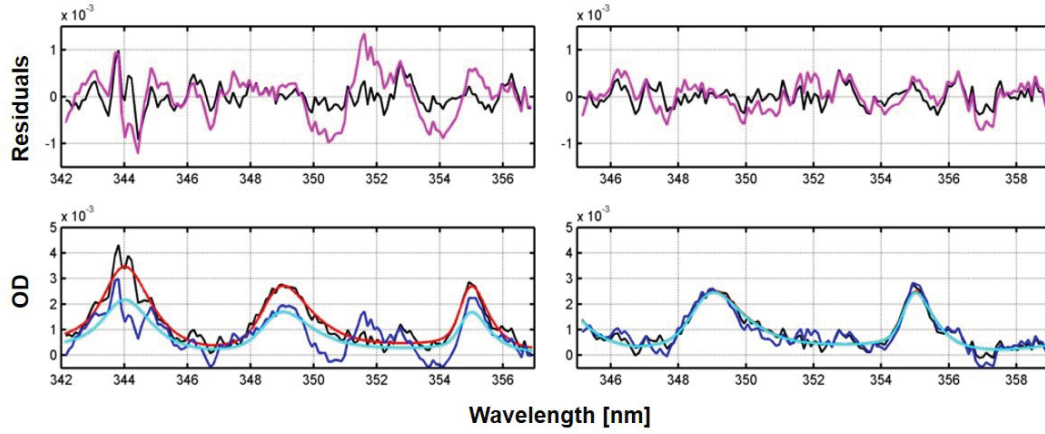


Figure 4.2: Retrieved optical depth of BrO measured on Feb.18, 2014 (SZA 90° a.m). Upper panels show residuals where black and magenta lines represent the results from the Taylor series approach and standard DOAS method, respectively. Lower panels show the retrieved BrO optical depth, in which the black and red lines are the results from the Taylor series approach, and the blue and cyan lines are from the standard DOAS approach. Left and right columns show results for the wavelength ranges : 342 – 357 nm and 345 – 359 nm, respectively.

where S_{0,O_3}^* , S_{λ,O_3} and S_{O_3,O_3} are fit parameters representing the wavelength-dependent SCD of ozone. Here, the three terms in parenthesis represent the Taylor series expansions. In general the DOAS fit minimises the difference between the left and right sides of Eqn. 4.1 for all wavelengths. Pukite et al. [2010] showed that using the standard method leads to an overestimation of BrO and strong residual structures. In contrast, the Taylor series approach reduces the residual structures as well as the fit-errors.

This study also quantitatively compares these two methods as shown in Fig. 4.2. In the wavelength range of 342 – 357 nm (left panel), the residual structures are largely reduced for the Taylor series approach by about one order of magnitude, and a significantly improved BrO fit is obtained. In the 345 – 359 nm wavelength range (right panel), in contrast, the difference of both methods is negligible due to much weaker O_3 absorption. To keep consistent conditions with the fitting window used in former studies, this study uses a wavelength range 342–357 nm with the Taylor series approach.

4.1.3 Dependence of the BrO results on the choice of the ozone cross section

This section describes the way to find the optimal O_3 cross sections to be used in the BrO fit window. Different O_3 cross sections are summarised in Tab.4.2. The comparison of the different ozone cross sections is provided in Appendix A.5. In this graph, different absolute values for different wavelengths as well as small discrepancies between the positions of the absorption peak depending on the O_3 cross sections are observed.

Figure 4.3 shows results of the BrO analysis during one year (2013) measured at SZAs around 90°, a.m (There is no significant difference between a.m and p.m results). The p.m data is shown in Appendix A.6. Each subplot includes four different data sets which represent the results obtained for the different O_3 cross sections. Clear differences of the results for the different O_3 cross sections are obtained.

Table 4.2: Different O_3 cross sections used for the BrO analysis. ‘Abbr.’ indicates the abbreviation used in the following, and T indicates the temperature.

Reference	Abbr.	Cold T	Warm T
Brion-team Daumont et al. [1992] & Malicet et al. [1995]	BR	218 K	243 K
Bogumil et al. [2003]	BO	223 K	243 K
Serdyuchenko et al. [2014]	SC1	213 K	243 K
	SC2	223 K	243 K

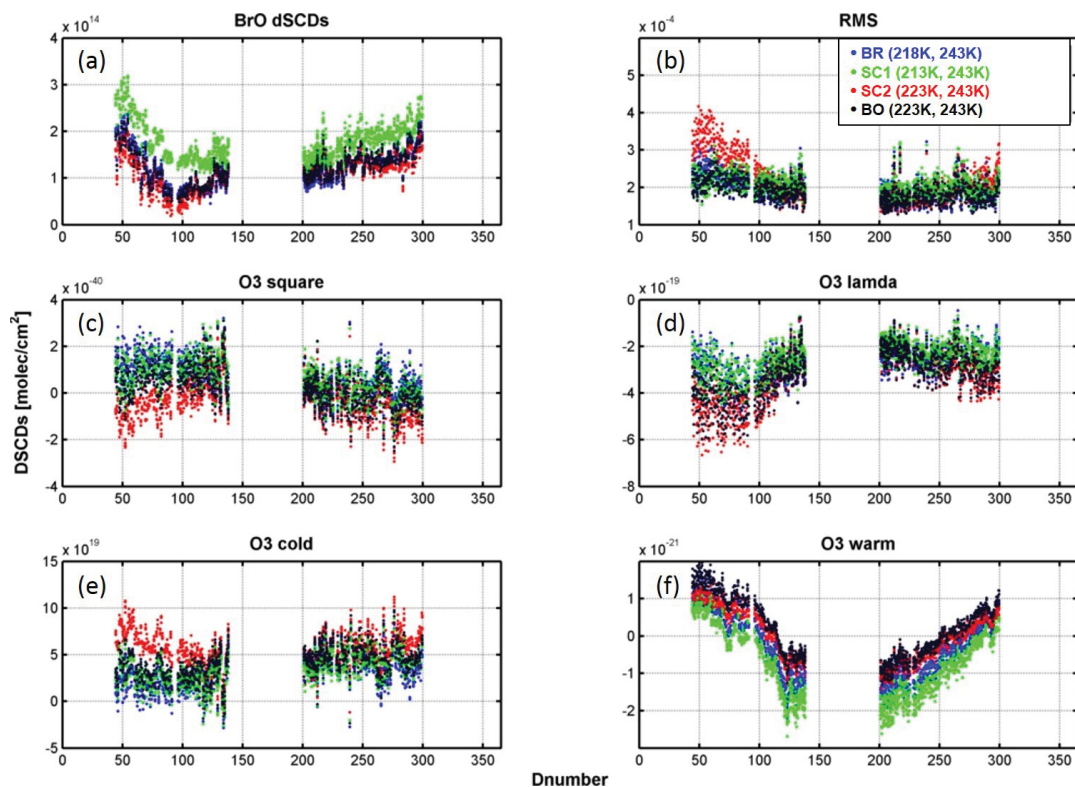


Figure 4.3: Time series of BrO results for one year (2013). (a) BrO dSCDs; (b) RMS of the fit residuals; (c)-(f) Fit coefficients of the different O_3 terms. Each subplot includes four different colored-dots indicating the results obtained for the different O_3 cross sections. Blue indicates BR, red SC2, green SC1, and black BO (see Table 4.2).

Especially the results for SC1 and SC2 are different from the others: the largest RMS is obtained for SC2, while for SC1 the largest deviations of the derived BrO dSCDs is found. Currently the reason for these discrepancies is not known, but it seems that they are related to possible problems of the Serdyuchenko et al. [2014] cross sections. Based on these results, and to keep the consistency with other studies for this study the 218K, 243K cross sections of the Brion-team (BR) [Daumont et al., 1992; Malicet et al., 1995] are selected.

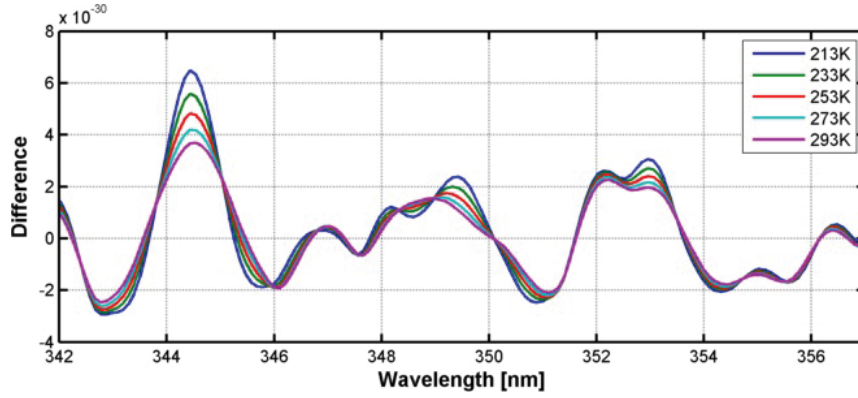


Figure 4.4: Difference of the Ring spectra for a temperature change of 20K for different temperatures $T = 213, 233, 253, 273,$ and 293K .

4.1.4 Ring temperature dependence

The effect of rotational Raman scattering is considered by including a Ring spectrum. This study also considers the temperature dependence of the Ring effect. For the measurements at high SZA considered here the bulk of the elastic and inelastic scattering events happens at high altitudes, mostly in the stratosphere. Thus, the variation of the stratospheric temperature changes the intensity of Stokes and anti-Stokes lines. This study follows the method in Lampel et al. [2017] which includes two Ring spectra representing two different temperatures in the fits. This method is especially important for absorbers with small optical depths like BrO. To test the effect of the temperature dependence of the Ring effect on the BrO retrievals, the BrO dSCDs are derived using different Ring temperature setting (Tab.4.3, 1st column). Either a Ring spectrum for $T = 213, 233, 253, 273, 293\text{K}$ or a combination of two Ring spectra (250K and 213K, one is orthogonalised to the other) is used. The resulting BrO dSCDs are compared to the BrO dSCDs obtained for the default temperature (250 K).

Figure 4.4 shows the difference of Ring spectra for different temperatures (with a temperature difference of 20 K). The magnitude and the spectral shape depend systematically on the temperature. Table 4.3 summarises the results of BrO dSCDs using different Ring temperature setting during one year (2013) measured at SZAs around 90° . Only small

Table 4.3: Comparison of BrO fit results during one year(2013) obtained for Ring spectra at different temperatures T (mean values, standard deviations, and variations of BrO dSCDs).

T	a.m.			p.m.		
	Mean(10^{14})	Std(10^{14})	Variance	Mean(10^{14})	Std(10^{14})	Variance
213K	1.129	0.346	1.195	1.223	0.334	1.118
233K	1.151	0.349	1.221	1.245	0.338	1.143
253K	1.173	0.354	1.255	1.267	0.344	1.180
273K	1.196	0.360	1.297	1.290	0.351	1.231
293K	1.220	0.367	1.350	1.314	0.360	1.296
250K and 213K	1.194	0.329	1.083	1.263	0.339	1.150
250K (default)	1.169	0.353	1.249	1.264	0.343	1.175

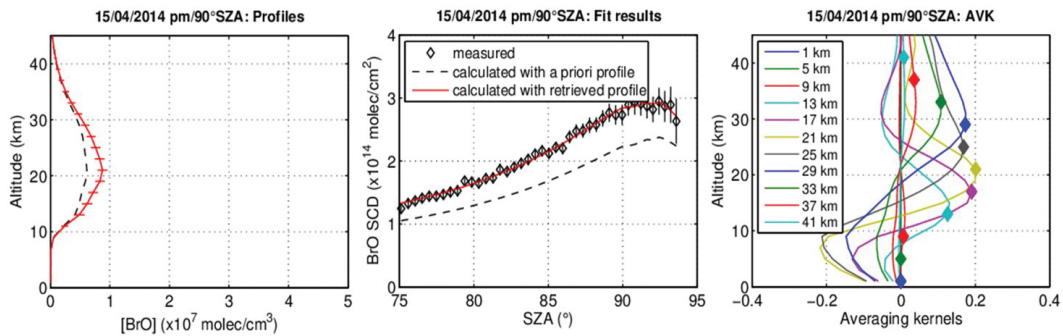


Figure 4.5: Typical example of a stratospheric BrO profile retrieval and the corresponding averaging kernels. Left: retrieved stratospheric BrO profile (red), a prior profile (black), and the corresponding error bars indicate the standard deviation. Middle: measured BrO SCDs as a function of the SZA. Here, the black opened diamonds and the red line represent the measured and simulated BrO SCDs, respectively. The dashed line indicates the SCDs corresponding to the a priori profile. Right: averaging kernels calculated by the algorithm. The closed diamonds indicate the altitude for which averaging kernels are representative.

differences are found for the different settings with a slightly increasing standard deviation of BrO dSCDs with increasing temperatures. Therefore, we selected the lowest temperature 213K for the generation of the Ring spectrum. Here, it should be noticed that Kiruna is often located inside of polar vortex, thus it might be interesting to further investigate the temperature dependence of the Ring effect in future studies.

4.1.5 Retrieval of vertical profiles

This section describes the conversion of the measured BrO dSCDs into vertical profiles using a profiling inversion algorithm based on Optimal Estimation Method (OEM). As for the NO_2 profiling algorithm in subsection (3.1.3), the IASB-BIRA profiling tool [Hendrick et al., 2004, 2007, 2009a] is adopted. Detailed information on this algorithm can be found in subsection 3.1.3 and Hendrick et al. [2007, 2009a]. Thus only the important details are briefly described here. This method enables one to convert the measured BrO dSCDs into concentration profiles (from which also to the corresponding stratospheric partial columns can be derived). The BrO dSCDs derived from the spectral analysis are directly used as input for the retrieval algorithm. Unlike the method of Hendrick et al. [2007] in which the residual amount of BrO in the reference spectrum is calculated prior to the profiling step this study adopts the option that the residual amount of BrO in the reference spectrum is fitted by the algorithm. This option can be used because this study uses a noon reference spectra, not a fixed one which was used in Hendrick et al. [2007]. As shown in Eqn. 3.5, the retrieved BrO profile is calculated from the observed BrO dSCDs for different SZA based on an a priori profile from a forward model, and assumed errors. The forward model used here is a UVspec/DISORT RTM model coupled with a PCSBOX photochemical model. Such a procedure is necessary because, like NO_2 , the BrO concentration systematically changes with SZA during twilight. Figure 4.5 shows a typical example of a stratospheric BrO profile retrieval and the corresponding averaging kernels.

The retrieval procedure simulates the BrO concentration at each altitude for each SZA value. Therefore, the SZA range of the considered measurement has to be set. Also the

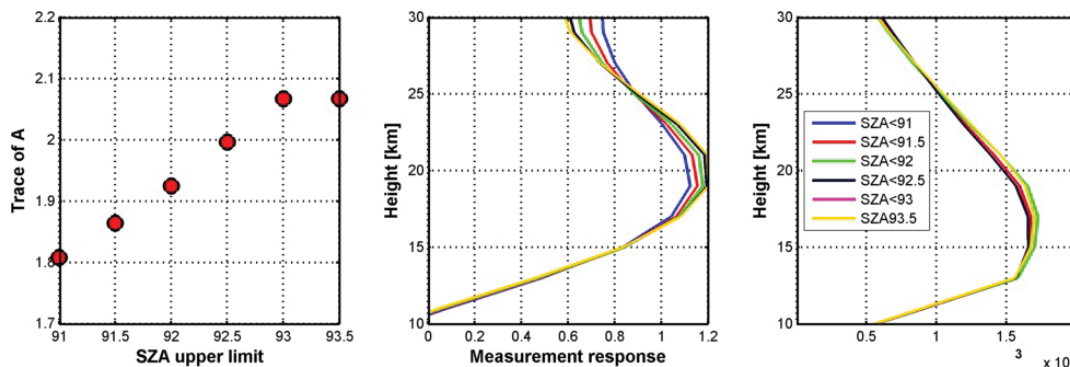


Figure 4.6: Left: The trace of \mathbf{A} as a function of the upper limit of SZA, center: measurement response and right: BrO profiles retrieved for different SZA upper limit conditions.

number of independent pieces of information which is described by the trace of \mathbf{A} depends on the SZA range, and in particular on the upper limit. To determine the optimum SZA range, the SZA upper limit is varied (below SZA of 94°) by steps of 0.5° . Figure 4.6 (left) shows the dependence of the trace of \mathbf{A} for different SZA upper limits (measurements from April 26, 2015 in p.m). The trace of \mathbf{A} increases systematically with an increasing SZA up to SZA 93° . Interestingly, the measurement sensitivity (sum of the rows of \mathbf{A} , center of Fig. 4.6) hardly depends on the chosen upper limit. This is different from the NO_2 profile retrieval in Fig. 3.6, which strongly depends on the upper SZA limit. These differences are caused by the different effects of the photochemistry on NO_2 and BrO: the NO_2 concentration strongly increases for $\text{SZA} > 90^\circ$, while the BrO strongly decreases for $\text{SZA} > 90^\circ$. A small dependence of the measurement response for the BrO inversion on the upper SZA limit is still found with a narrower peak with increasing SZA. Therefore, the measured data which was observed at $75^\circ \leq \text{SZA} < 92.5^\circ$ for the vertical inversion was finally chosen.

4.2 RESULTS

In this study, BrO SCDs are not directly converted to VCDs using the Langley-plot method as it was done for NO_2 . This is because the relative change of the BrO concentration during twilight is even stronger than for NO_2 . Instead, BrO dSCDs are analysed first and then used for the inversion of a vertical profile of BrO. Finally, partial columns of stratospheric BrO are calculated by integrating the derived BrO concentration profiles.

4.2.1 Variation of stratospheric BrO concentration profiles

4.2.1.1 Diurnal variations

Figure 4.7 shows the diurnal variation (SZA dependence) of the BrO VCDs measured on Mar. 15 of 2006 as well as the retrieved BrO profiles. All of these results are photochemically corrected by the profile inversion algorithm. Correspondingly, strong diurnal variations as a results of photochemical reaction between BrO and its nighttime reservoir species (HOBr , BrONO_2) are found. BrO VCDs derived in p.m are slightly higher than in a.m. This finding is typical for all measurements. For SZA higher than 86° the BrO concentrations (and VCDs) strongly decrease indicating the strong influence of the photochemistry during twilight. As the SZA increases, also the difference between the concentrations (and VCDs) in a.m and

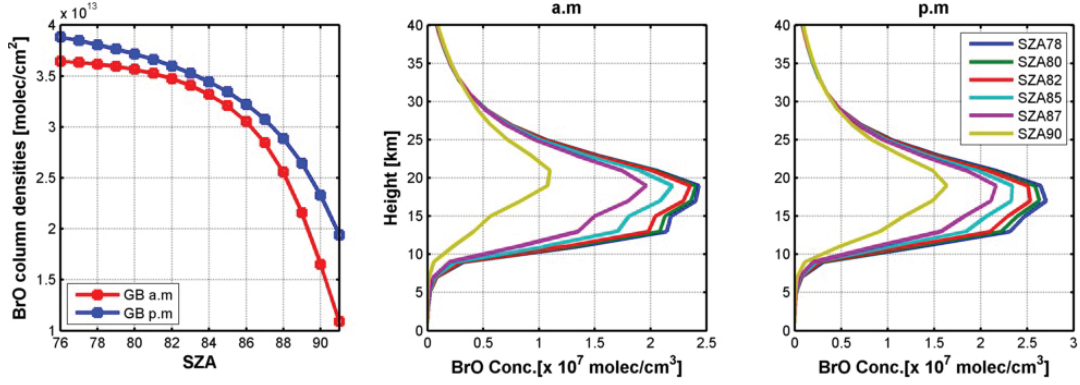


Figure 4.7: Left: SZA dependence of the BrO VCDs (red and blue dots indicate a.m and p.m, respectively); Middle and right: The retrieved BrO profiles at various SZA (at a.m and p.m) derived from measurements on Mar.15 of 2006.

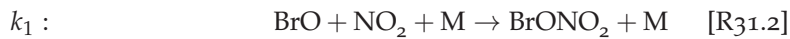
p.m increases. This is related to the termolecular reaction between BrO, NO₂ and M. This reaction is explicitly considered in the BrO profiling algorithm.

4.2.1.2 Multi-year monthly mean variation (1997 – 2016)

Figure 4.8 shows the monthly mean BrO profiles retrieved from the OEM inversion algorithm (February – October) for all years from 1997 – 2016. The results shown here represent the profiles for SZA at 90°, the results for other SZA values (80° and 85°) can be found in the Appendix A.7 and A.8. The BrO vertical distributions show a strong seasonal variations like NO₂, and a high variability below 20 km. The largest concentrations are found in the early spring with values around 2.5×10^7 molec/cm³ around 19 km. The minimum concentration, less than 1×10^7 molec/cm³ is observed during summer.

This seasonal variation of the BrO profiles is a result of photochemical reactions and it depends in particular on the concentration of NO₂ because the reaction with NO₂ is a source of the reservoir species (BrONO₂). The BrONO₂ concentration mainly depends on the actinic flux, as well as the concentration of NO₂, and aerosols [Höpfner et al., 2009]. During polar winter, due to the denoxification (and possibly denitrification), the NO₂ concentration decreases. Thus also the formation of BrONO₂ is decreased and the BrO concentration is enhanced. In contrast, in summer BrO decreases due to high concentrations of NO₂ and low SZA (thus BrONO₂ becomes abundant). For details of the relevant photochemical reactions see also the Introduction Section 1.3.1.

$$[\text{BrONO}_2] = \frac{k_1[\text{NO}_2][\text{BrO}]}{j_1 + j_2} \quad [\text{R31.1}]$$



During daytime, BrONO₂ is rapidly photolysed, but is simultaneously produced by the termolecular reaction between BrO, NO₂, and another collision partner [Lary, 1996]. Based on these reactions the differences of the profile shape measured in a.m and p.m during spring and autumn can be understood by the following argument. During summer, the sun stays above or close to the terminator for the whole day. Thus no nighttime reservoir species

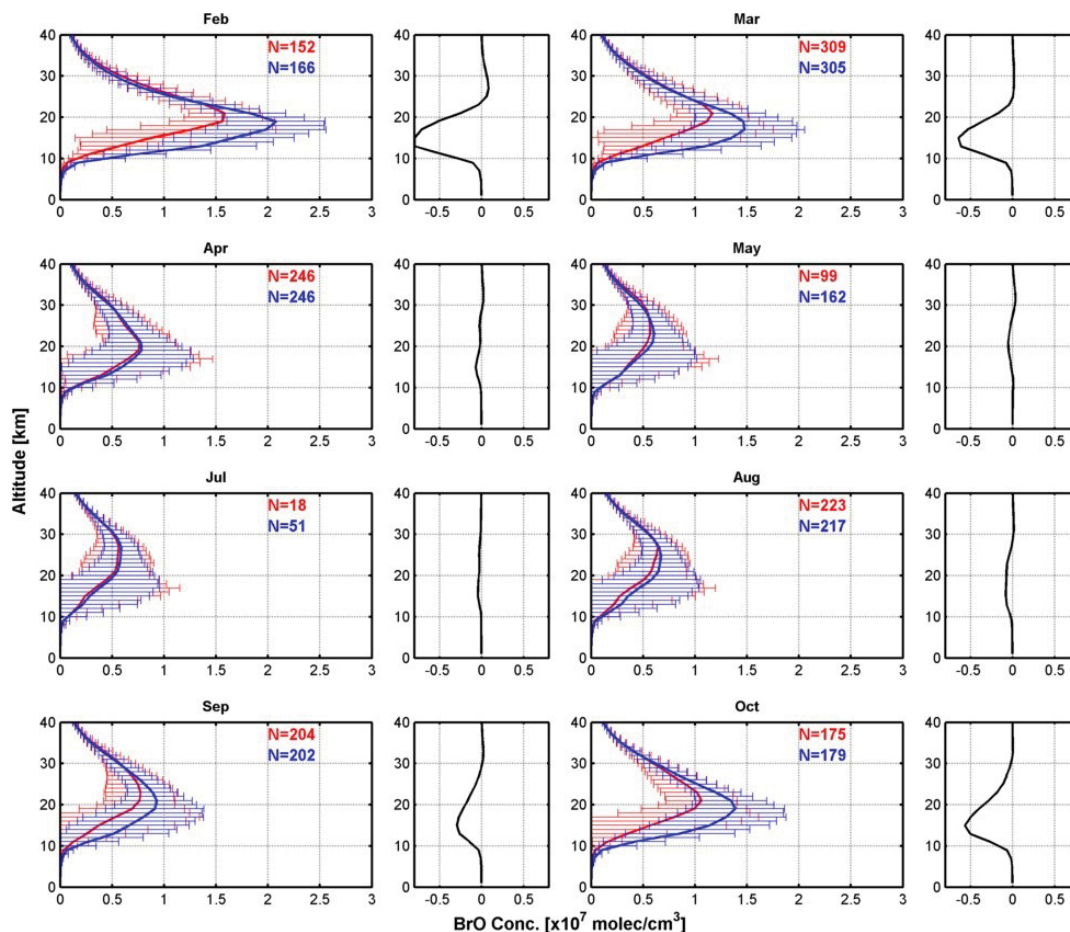


Figure 4.8: Monthly mean BrO concentration profiles (February – October) from ZS-DOAS observations from 1997 to 2016 (red and blue lines indicate mean profiles measured during a.m and p.m, respectively). Odd number-columns represent monthly means and number of occurrences; the error bars indicate the 1σ standard deviation. All retrieval results are representative for SZA of 90° . Also the mean differences between the profiles in a.m and p.m are shown. The x -axis and y -axis represent the concentration and altitude from 10 km to 40 km, respectively.

can build up. As a consequence the concentration of BrO strongly changes during daytime according to the SZA, but the concentrations during a.m and p.m are very similar. On the other hand, during spring and autumn, NO_2 concentrations are lower than in summer.

During the night, BrONO_2 becomes more abundant while BrO decreases rapidly. During daytime, $[\text{R}_{31.3}]$ reaction is faster than the others and also the restricted availability of NO_2 influences the difference. It is also interesting to note that in spring and autumn the peak in the profile measured in a.m is higher than in p.m and this differences can be found mainly below 20 km. These differences are not observed for lower SZA (Appendix A.9 and A.10). This finding indicates that the reactions causing the asymmetries are most important around sunset and sunrise. This result is well consistent with the BrO variation as a function of SZA shown in Fig. 4.7.

Figure 4.9 shows box and whisker plots of the multi-year monthly mean values of the partial columns of BrO from 15 to 27 km. This figure represents BrO column densities at a SZA of 90° from 1997 to April of 2016 (the partial columns at other SZAs (80° and 85°) are shown in Appendix. A.9 and A.10). The red crosses represent outliers defined as data

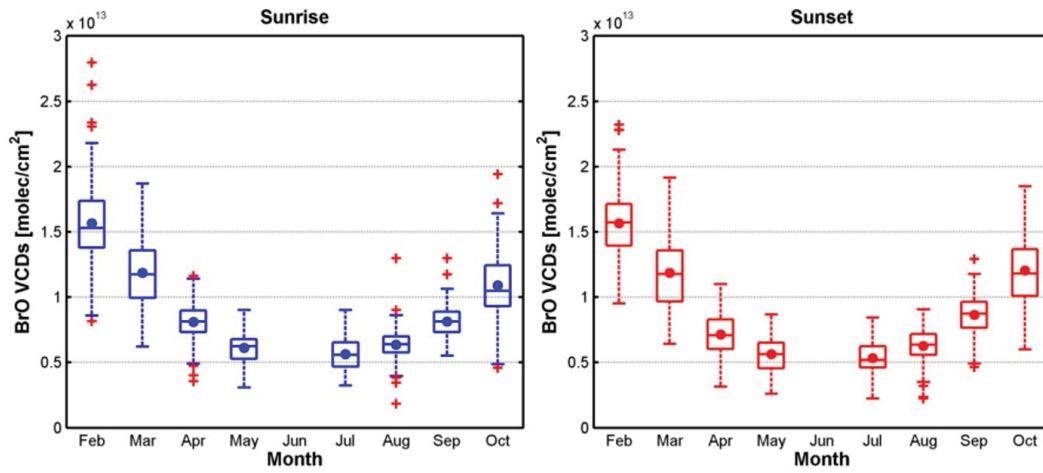


Figure 4.9: Box and whisker plots of stratospheric BrO partial columns (15 – 27 km) from 1997 to 2016 derived from integrating the profiles retrieved with OEM. The left and right panels represent measurements during sunrise and sunset, respectively. The box edges denote 25 and 75 % of the BrO partial columns and the center lines and dots indicate the medians and means, respectively. Red crosses indicate outliers.

points higher or lower than 1.5 times of the inter-quartile range, and the whiskers show the maximum and minimum values excluding the outliers. The BrO column densities show strong seasonal variations with maxima in spring and minima in summer. In summer the year-to-year variability is smaller than in spring and autumn. The partial columns measured in sunset are slightly larger than measured in sunrise, which was already discussed above. In contrast, at SZA of 80° the partial columns are larger in a.m. than in p.m. The profiling inversion model taking the termolecular reactions (R_{31.2}) into account can explain this observation. During day time, BrO decreases due to the increasing stratospheric NO₂.

4.2.2 Dependence of the BrO profile inversion results on the sky condition

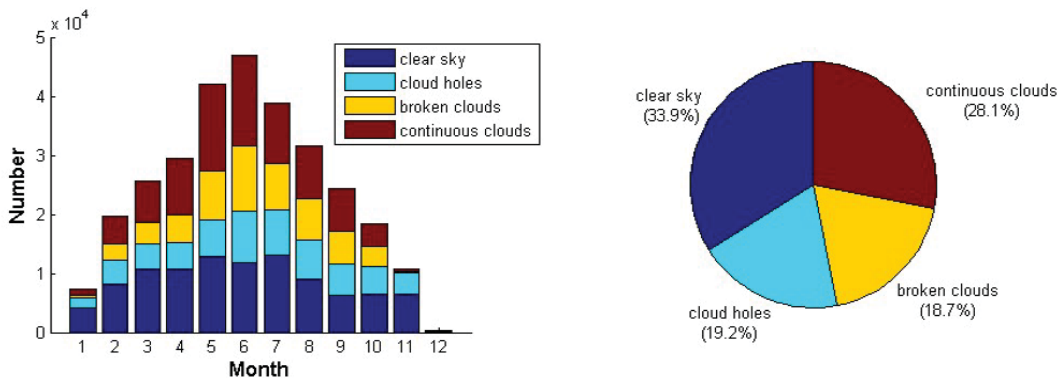


Figure 4.10: Frequencies of different sky conditions derived from the zenith sky DOAS cloud classification scheme from 1997 to 2015 (except 2002). Left: Results for individual months, Right: Yearly averaged relative frequencies. The different colors represent different sky conditions: blue: clear sky; cyan: cloud holes; yellow: broken clouds; brown: continuous clouds.

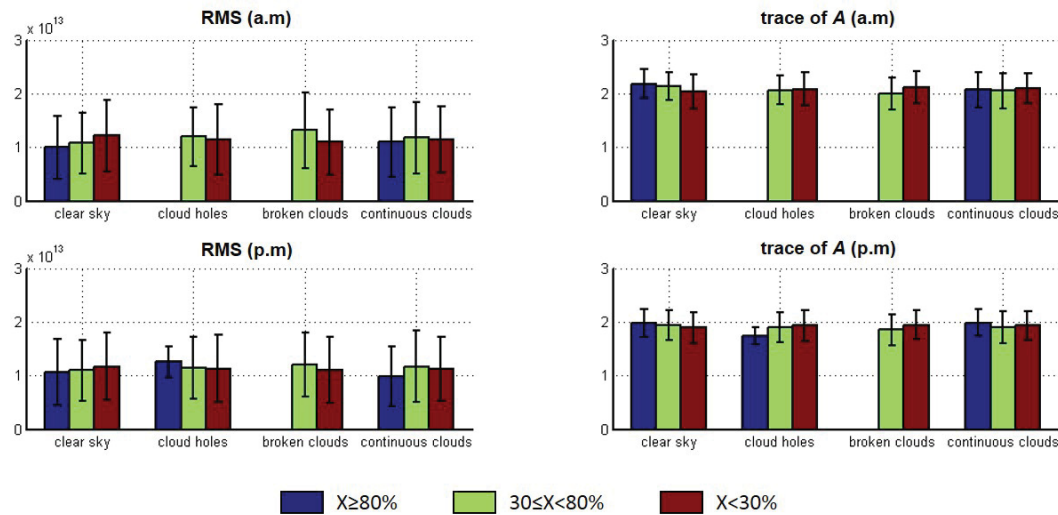


Figure 4.11: RMS (left) and the trace of the averaging kernel matrix (**A**) which gives the number of independent pieces of information (right) under different sky conditions. For each sky condition three results are shown indicating the relative frequency of the respective sky condition (X). The blue bars indicate results for which the sky condition of interest occurs more than 80% during the measurement period. Green and red bars represent the results for relative frequencies of the respective condition between 30% and 80%, and smaller than 30%, respectively. The error bars represent the standard deviation.

As already mentioned in Section 3.2.3 a wrong surface albedo or an inappropriate treatment of low clouds could cause increasing uncertainties in the retrieved profiles. For example, the correlation between BrO and O_4 in the spectral retrieval process has been noticeable. Moreover, the O_4 absorption and the Ring effect are especially sensitive to changes of the atmospheric radiative transport [Wagner et al., 1998, 2014]. Therefore, it is worth to study the variation of the BrO results for different cloud conditions. To investigate the cloud effects on the BrO profile inversion, the results of a cloud classification scheme are used, which was already described in Sec. 3.2.3. Figure 4.10 shows the sky conditions derived from the zenith sky DOAS cloud classification scheme from 1997 to 2015 (except 2002). It is obvious in the left panel that the accumulated number of observations in summer is larger than in winter because of the longer measurement time of the day. The right panel shows the relative fraction of occurrences of the different sky conditions for the whole measurement periods. From 1997 to 2015, the fraction of clear sky conditions is 33.9 % indicating that cloudy sky conditions (including cloud holes, broken clouds and continuous clouds) are dominant.

The cloud classification results can be used to study the dependence of retrieved BrO profiles and the quality indicators on the sky condition. One of the quality indicators is the root mean square (RMS) between the simulated and measured absolute slant column densities (SCDs), another is the trace of **A** derived from the profile retrieval. Figure 4.11 shows those quality indicators observed in a.m. and p.m. In this graph, a small RMS (and a high trace of **A**) means that the retrieved profile is very well consistent with the measurements. Here, quite similar results as for the NO_2 profile inversions are found. One can also see that better RMS fits are obtained under clear sky conditions compared to broken clouds and continuous clouds conditions. In contrast, the trace of **A** results show no significant difference under different sky conditions. Slight differences are also found

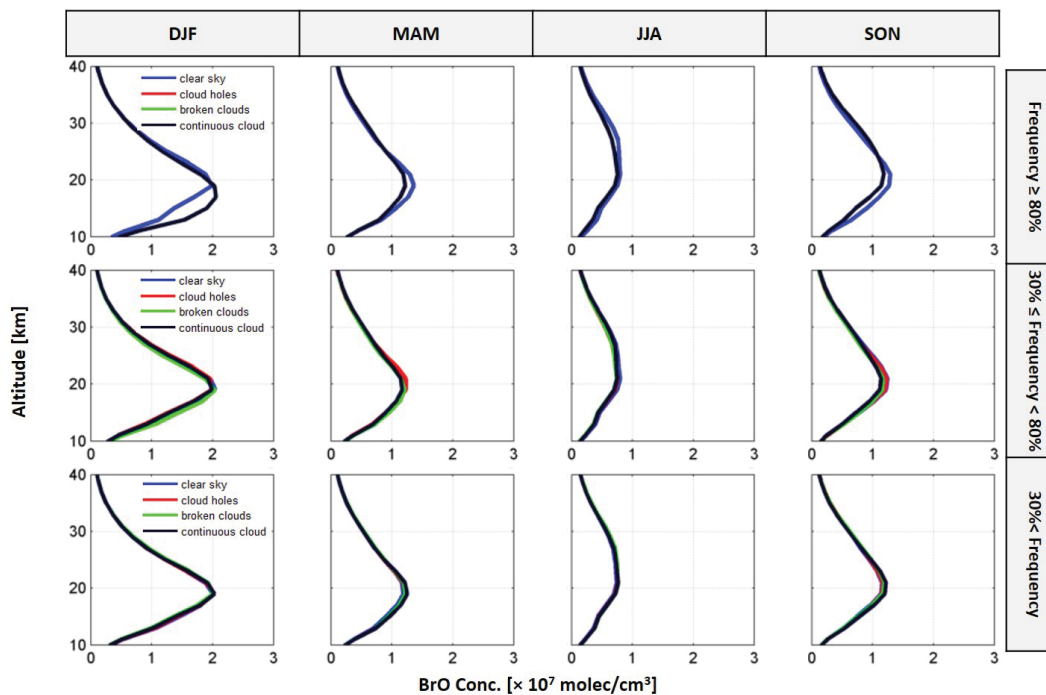


Figure 4.12: Vertical mean BrO profiles derived from ground-based measurements in a.m for 14 years for different sky conditions and seasons. Each column shows the results for different seasons (DJF: winter, MAM: spring, JJA: summer, SON: autumn), and each row represents the relative frequency of the sky conditions. Different sky conditions are represented by different colors (blue: clear sky, red: cloud holes, green: broken clouds, and black: continuous clouds).

indicating remaining small effects of clouds on the measurement sensitivity for stratospheric trace gas absorptions.

Figure 4.12 and Figure 4.13 show the seasonal mean BrO vertical profiles under different sky conditions measured in a.m and p.m, respectively. Because of the high latitude of the measurement site and the retrieval algorithm criteria, there is no data in January, June, November, and December. Each subfigure includes four mean BrO profiles, each of which represents results for different sky conditions.

First, the BrO profiles in a.m and p.m are compared for the categories for which the frequency of the respective sky condition is larger than 80 % (1st row). During a.m only results for two sky conditions, clear sky (blue line) and continuous clouds (black line) are observed and the differences between these two are negligible except for winter, which is different to the NO_2 results. While the NO_2 concentrations under continuous clouds are higher than under clear sky, the BrO results show an opposite tendency but with very small differences. In winter the BrO profiles for clear sky show smaller values than under continuous clouds, and the difference becomes larger at altitudes below 20 km. Compared to the a.m data, the BrO mean profiles in p.m show larger discrepancies depending on the sky conditions except for spring as shown in Fig. 4.13. However, this difference is probably also related to the only few data points compared with other seasons.

Assuming that the BrO profiles under the clear sky conditions represent the true stratospheric state, the enhancement under cloudy conditions (including broken clouds, cloud holes and the continuous clouds) can be interpreted as an artifact caused by the clouds. The

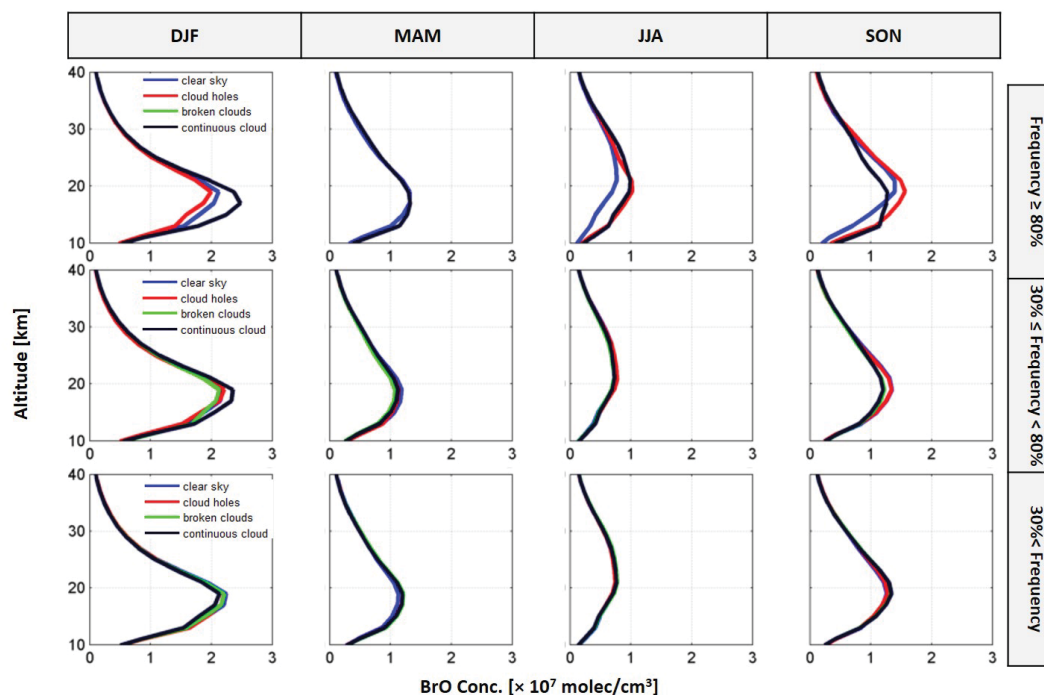


Figure 4.13: Vertical mean BrO profiles derived from ground-based measurements in p.m for 14 years for different sky conditions and seasons. Each column shows the results for different seasons (DJF: winter, MAM: spring, JJA: summer, SON: autumn), and each row represents the relative frequency of the sky conditions. Different sky conditions are represented by different colors (blue: clear sky, red: cloud holes, green: broken clouds, and black: continuous clouds).

results during winter and autumn show larger discrepancies compared to a.m, especially the maximum peak height of the profile is changed under the cloudy conditions. In the second and third rows in Fig. 4.12 and Fig. 4.13, much smaller differences for the different cloud conditions are obtained than for the results for the more strict cloud classification in the 1st row.

As mentioned in Sec. 3.2.3, there are four possible reasons for the differences between clear and cloudy sky condition. For the BrO profiles, the most important factor influencing the profile is that the cloud has a substantial effect not only on the radiative transfer in the troposphere, but also in the stratosphere because the BrO is located at lower altitude than NO_2 . Furthermore, previous studies have reported simultaneously enhanced BrO and O_4 absorptions in the free troposphere. Frieß et al. [2004] mentioned that multiple Mie scattering on atmospheric particles e.g clouds can strongly enhance the observed BrO dSCDs for tropospheric BrO concentrations. Such an effect might also occur at Kiruna, which is close to polar regions, where enhanced tropospheric BrO is often observed. The simultaneous enhancement of BrO and O_4 will be discussed in detail in Chapter 6.

To conclude, a bimodal distribution as found for NO_2 is not observed for BrO, but some small discrepancies under the extreme sky conditions are found. However, the second sky category ($30\% \leq \text{frequency} < 80\%$) includes most of the data and the BrO profiles in this category show only very small differences under different sky conditions which indicates that the BrO profile retrieval yields stable and reliable results.

4.2.3 Time series of the vertical distribution

This subsection shows the day to day variation of the stratospheric BrO vertical distribution during spring for individual years which can help to understand the connection of the stratospheric halogen chemistry to atmospheric dynamics (e.g the location and strength of the polar vortex) and temperature. The retrieved profiles are derived from the OEM profiling algorithm described above. Figures 4.14 and 4.15 show curtain plots of the BrO vertical distribution. The overlaid black dots indicate whether the polar vortex was located above Kiruna or not. The information is given for different potential temperature levels (for the potential vorticity thresholds see Tab.3.2 and additional 380 K and 400 K potential vorticity values are plotted). All results are obtained by the same method as explained in Sec. 3.2.2. Each subplot above the curtain plot shows the temperature around 19 km. To understand the evolution of the polar vortex and polar stratospheric clouds (PSCs) affecting the BrO variation, the plots cover the entire period from January 1st. For the direct comparison with the vertical distributions of NO₂ and BrO, ten different winters are chosen: 1997, 1998, 1999, 2000, 2005, 2006, 2013, 2014, 2015, and 2016.

In general, all of these figures clearly show that BrO concentrations increase in spring and decay from the beginning of March during the whole measured period (until May). The main BrO layer develops at around 20 km, the maximum in spring is found around 2.5×10^7 molec/cm³ and the minimum is found in summer. This variation seems anti-correlated with NO₂ for which the NO₂ layer is located around 30 km, and the minima and maxima are observed in spring and summer, respectively.

Here, both figures show that a large year to year variation of BrO exists during the spring periods. And especially, a strong BrO enhancement is typically found under polar vortex conditions. BrO profiles in p.m show a larger and broader BrO layer (see also subsection 4.2.1.1). The BrO enhancement under polar vortex conditions is related to the photochemical reactions (R₃₁) which strongly depend on the NO₂ concentrations. During polar winter, NO₂ was converted into reservoir species and in cold winters even partly removed from the stratosphere (denitrification). During spring the reservoir species are (slowly) converted back to NO₂.

For the cold winters in 1997, 2000, 2005, 2014 and 2016, a strong BrO enhancement under the polar vortex condition is clearly found. Interesting events of strong bromine activation above Kiruna are found less frequently during a.m. (2000 and 2014) than during p.m. (1998, 2000, 2005, 2006, 2014, and 2016).

The vertical distribution of BrO in those winters shows that high BrO concentrations are to be found when temperature drops below or near the threshold for the formation of PSCs. The temperatures at 19 km in 2000 and 2014 are close to T_{NAT} or slightly higher than T_{NAT} . However, these temperatures are representative for the stratosphere above Kiruna. In order to see the general tendency of the temperature variations, the minimum temperatures at 50 hPa in the northern hemisphere (50° – 90°) are shown in the Appendix (A.11, A.12 and A.13). According to those figures, the minimum temperature falls below the threshold for formation of PSCs type 1 between Feb.25 and Mar.5 in 2000. In case of 2014 between Jan.21 and Jan.31, the minimum temperature was 188 K which is cold enough to form the PSCs type 2, therefore it is probably that activated airmasses inside the polar vortex were transported above Kiruna.

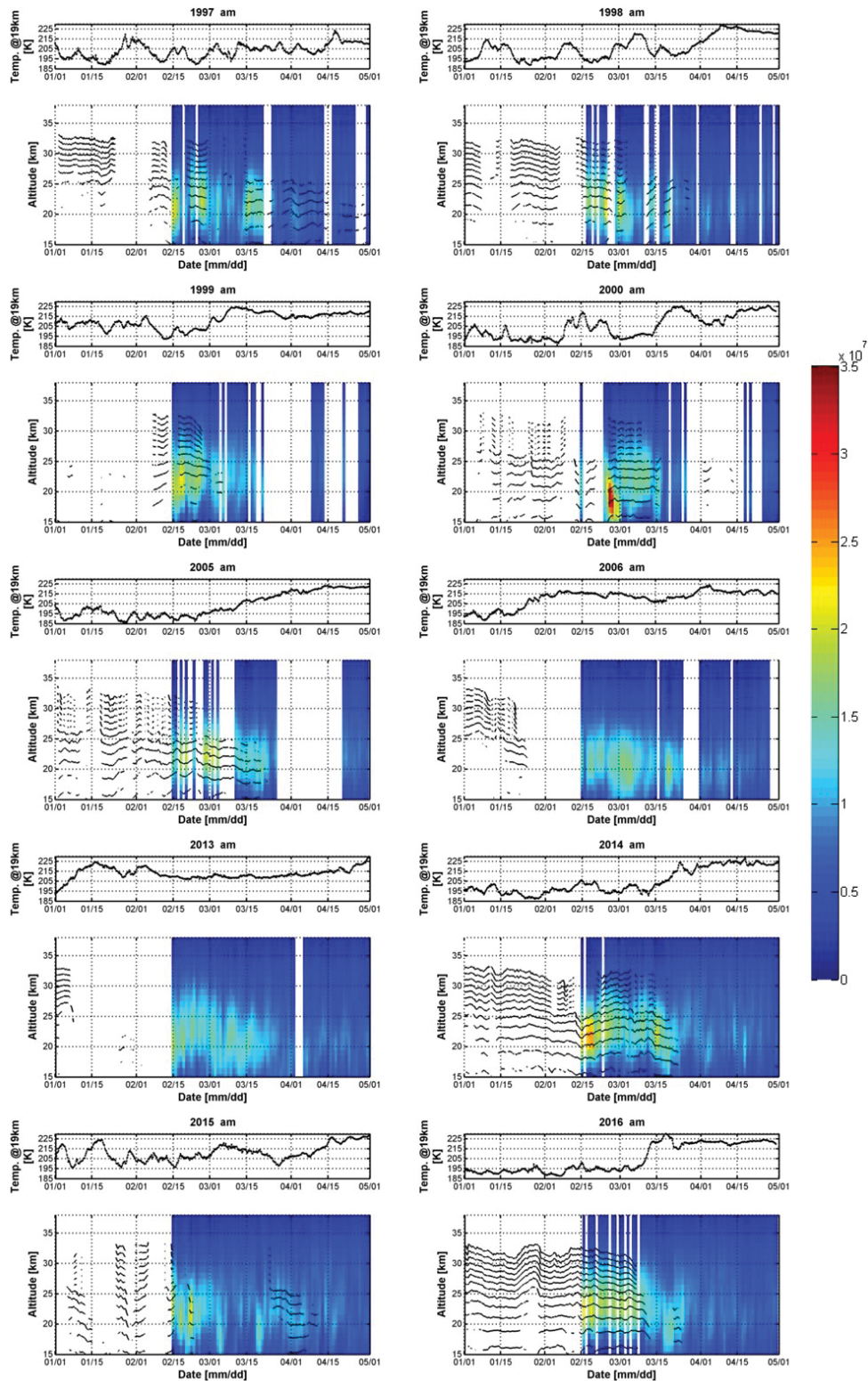


Figure 4.14: Curtain plots of the time series of the stratospheric BrO vertical distribution measured in a.m. Black contour dots indicate the polar vortex barrier at each potential temperature level. x - and y -axes indicate time and altitude, respectively. The altitude covers a range from 15 km to 38 km. And additionally, the subplots above the curtain plots show the temperature around 19 km.

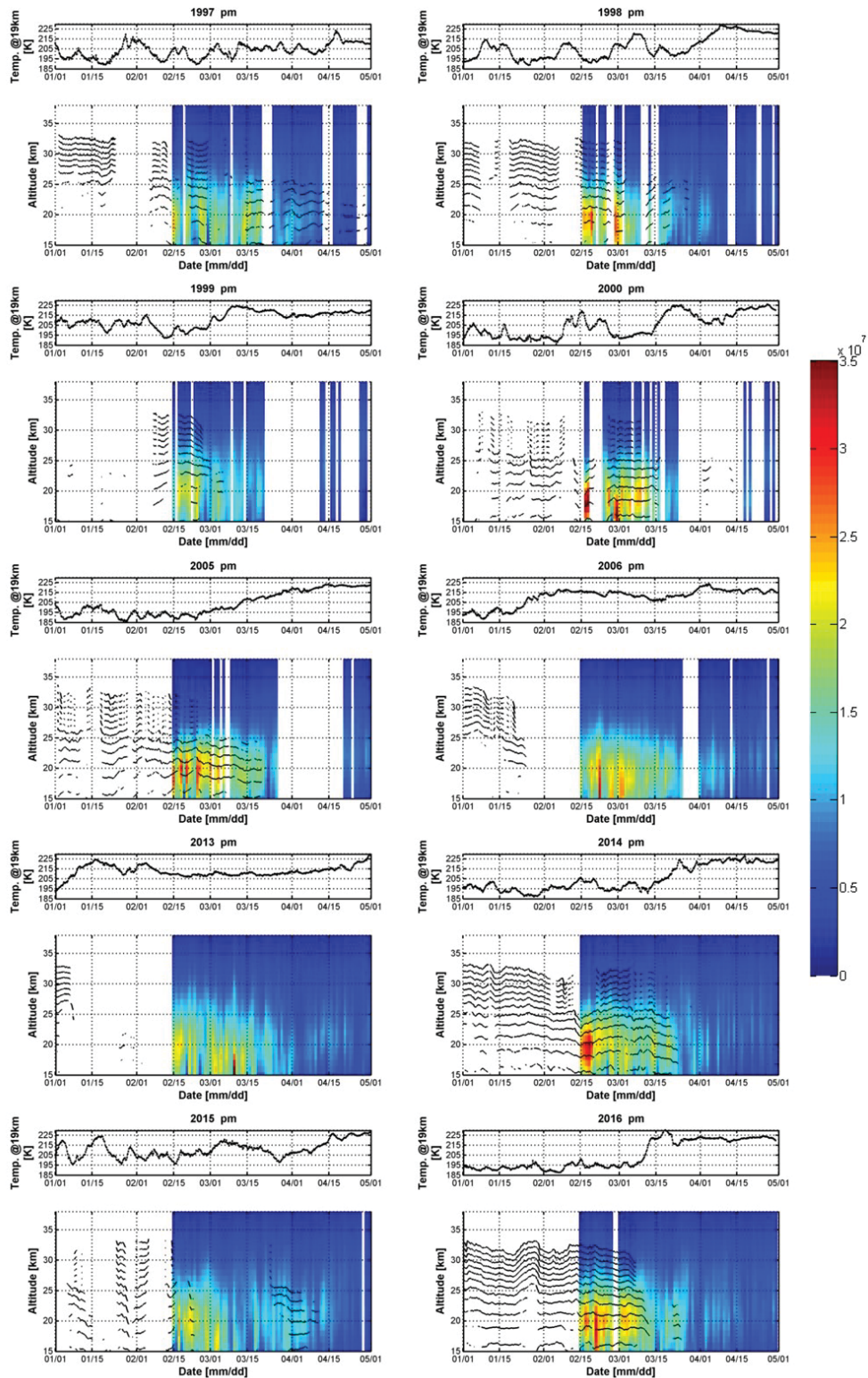


Figure 4.15: Curtain plots of the time series of the stratospheric BrO vertical distribution measured in p.m. Black contour dots indicate the polar vortex barrier at each potential temperature level. x - and y -axes indicate time and altitude, respectively. The altitude covers a range from 15 km to 38 km. And additionally, the subplots above the curtain plots show the temperature around 19 km.

4.2.4 Comparison with other instruments

This section shows the comparison of the BrO results with other measurements to verify the BrO profile retrieval. In particular, the retrieved profiles are compared to partial columns and profiles retrieved from satellite and balloon-borne measurements. The Kiruna ZS-DOAS results are compared to limb observations from the satellite instrument SCIAMACHY and from the balloon-borne SAOZ measurements.

4.2.4.1 Comparison with Balloon measurements

In this part, BrO profiles retrieved from the ZS-DOAS observations and balloon-borne measurements are compared. SAOZ balloon measurements were launched by the Centre-National de la Recherche Scientifique (CNRS, France) at Kiruna, Sweden. The SAOZ balloon experiment measures spectra during the afternoon ascent at SZA below 90° and during float at about 30 km (SZA $92^\circ - 93^\circ$). The measured spectra are analysed using the DOAS method. More details about the instrument and the retrieval algorithm are provided in Pundt et al. [2002] and Dorf et al. [2006a]. All flights used in this comparison study are ascent measurements.

Figure 4.16 shows the comparison of BrO profiles measured from ZS-DOAS and the SAOZ balloon (SAOZ) instruments. For the present comparisons, five flight events are selected (see Tab. 4.4), three in spring (a)-(c) and two in summer (d)-(e). The SZA range of the SAOZ measurements was also chosen for the ZS-DOAS measurement. Figures 4.16 (f and g) show the absolute and relative differences between ZS-DOAS and SAOZ. The relative differences are calculated with respect to the SAOZ results. These differences are restricted to the altitude range 13 km to 27 km for which SAOZ balloon measurements are available. To allow a meaningful comparison, the SAOZ measurements are smoothed using averaging kernels from the ZS-DOAS profiles since the resolution of ZS-DOAS is coarser compared to the SAOZ measurements. A detailed description of the smoothing procedure can be found in Sec. 3.2.4.2.

Overall, the profiles from ZS-DOAS and SAOZ show very good agreement. Maximum BrO concentrations are obtained around 15 — 20 km in spring, and minimum in summer. Except (e), the relative difference of the vertical distributions are around 20 %, and the observed differences are within the error bars of the ZS-DOAS profiles in most cases. In Figs. 4.16 (a)-(c), the comparison is carried out for different meteorological conditions: in

Table 4.4: Overview of the SAOZ balloon flights chosen for comparison with the ZS-DOAS observations

Balloon flight date	Measurement location 20 km	Time(UT) and SZA 20 km
09 Feb 2000	67.8N, 21.0E	14h, 89.6
07 Mar 2000	67.6N, 21.4E	15.2h, 85.8
16 Mar 2003	67.5N, 22.0E	15.8h, 86.4
11 Aug 1998	67.8N, 20.9E	19.0h, 87.7
12 Aug 2002	67.7N, 21.7E	18.7h, 87.3

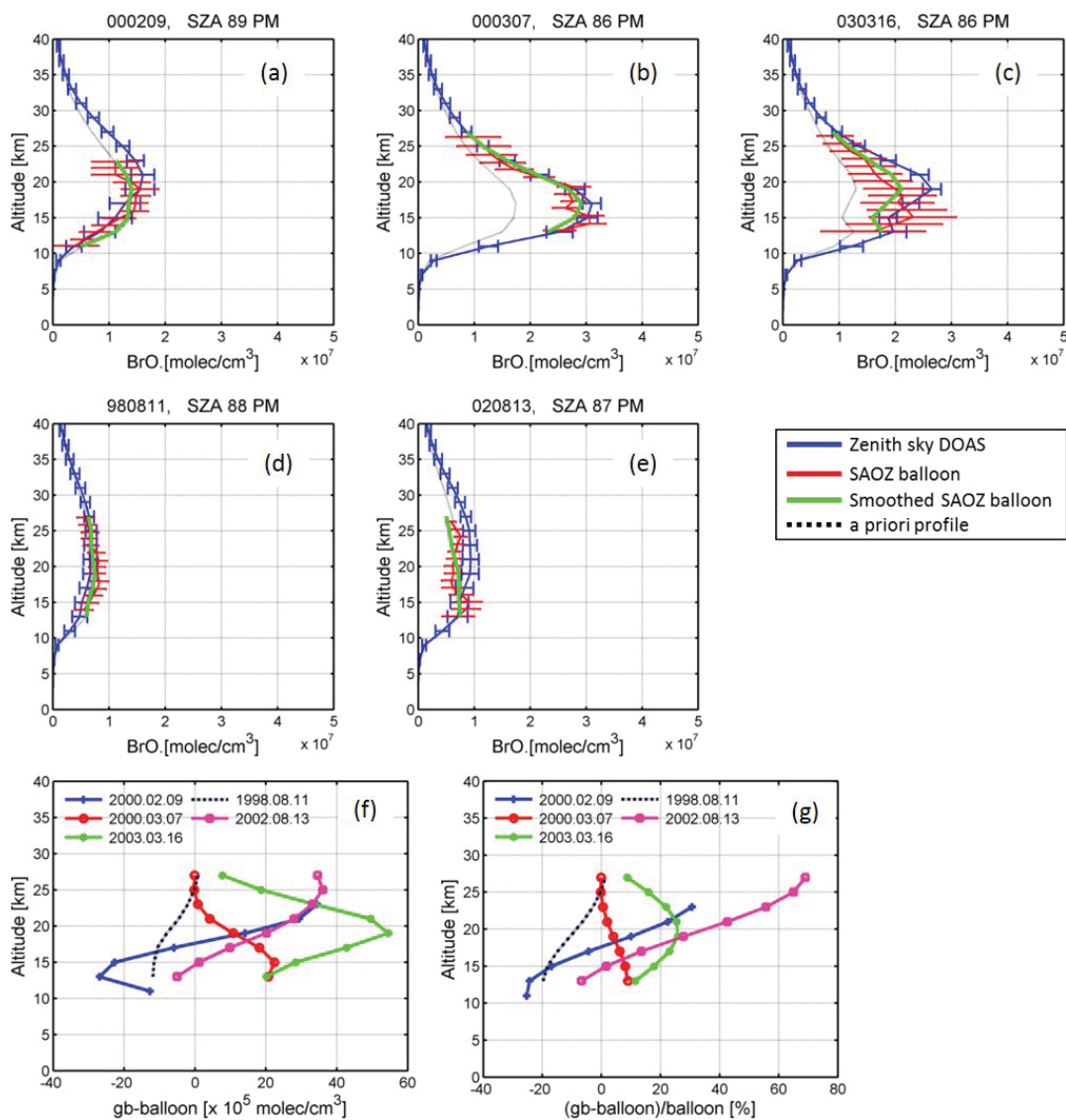


Figure 4.16: Comparison of BrO profiles derived from ZS-DOAS and SAOZ (a-e) for different days. Each graph includes four different profiles. Blue lines indicate the results from ZS-DOAS, red and green lines indicate unsmoothed and smoothed SAOZ measurements, respectively. Black dots denote the a priori profile used for the inversion of ZS-DOAS measurements. (f) and (g) show absolute and relative differences between ZS-DOAS and SAOZ (smoothed) measurements, respectively.

case (a) Kiruna is outside the polar vortex with the vortex edge located at the northern Scandinavian Peninsula; in cases (b) and (c) Kiruna was inside the polar vortex. However, in (b) the polar vortex covers the whole Scandinavian Peninsula while in (c) it starts to split and becomes weak. According to these different meteorological conditions slightly different results are found. The BrO concentration is larger if Kiruna is inside the polar vortex most probably due to the effects of denitrification and denoxification. As mentioned in the Introduction of the BrO Chemistry (Sec. 1.3.3), a long-continuous cold winter *e.g.* 1999/2000 allows the formation of PSCs. PSCs provide surfaces for heterogeneous reactions, which help to convert inactive halogen reservoir species (*e.g.* HBr, HCl, BrONO₂, and ClONO₂) into less photostable halogen compounds (Cl₂, HOCl, BrCl, and HOBr). These less stable halogen compounds are then converted to reactive halogen compounds (BrOx, ClOx) after

the polar sunrise. Compared to outside the polar vortex, in the polar vortex less photostable halogen compounds exist during polar winter and those are converted to the reactive forms in spring, which in general leads to the larger amounts of BrO inside the polar vortex.

Comparison results for summer are shown in Fig.4.16 (d)-(e). Here, it should be noted that the balloon measurement in Fig.4.16(e) is launched (12.Aug.2002) one day before the retrieval of the ZS-DOAS profile (13.Aug.2002) due to the lack of ground-based measurements on 12.Aug. 2002. However, in summer the dynamics of the stratosphere is more stable than in winter, thus the atmospheric conditions are assumed not to vary significantly during these two days. Because of the high NO₂ concentrations and the high actinic flux, rather low BrO concentrations and little vertical variations of the BrO concentrations are found.

Table 4.5 shows the BrO partial columns calculated by integrating each profile over the altitude range covered by the SAOZ measurements (11–23 km and 13–27 km). The relative difference is calculated with respect to the SAOZ results. The second column in the table shows the relative location of the measurement site with respect to the polar vortex. Except 16 Mar 2003(c) and 12 Aug 2002(e), the relative differences of the partial BrO columns are less than 10 %, and in most cases the partial columns from ZS-DOAS are larger than those from SAOZ, which is opposite to the NO₂ results. For case (c), the measurement site is inside of the polar vortex, but the vortex already started to split. Since the measurements were made in the middle of March, it is highly possible that air masses from outside and inside the polar vortex already started to mix. Case (e) has to be treated carefully as the measurements are not made at the same day. Nevertheless, the absolute difference is in the same range as shown for the other days because day-to-day variability is rather small during summer.

4.2.4.2 Comparison with Satellite observations (Limb geometry)

This section contains the profile comparison between the Satellite observations and ZS-DOAS. As for the NO₂ analysis, the satellite data are retrieved from SCIAMACHY limb observations. To derive vertical profiles of BrO from SCIAMACHY limb measurements, an algorithm developed by Kühl [2005]; Pukite et al. [2006]; Kühl et al. [2008] is employed, details of which can be found in Pukite et al. [2010]. In brief, the spectral analysis settings described in Kühl et al. [2008] are used for the SCD retrieval and the Taylor series approach is implemented.

Table 4.5: Comparison of the BrO partial columns derived from ground-based zenith sky DOAS and SAOZ balloon measurements.

Date	Kiruna within/out the polar vortex	Altitude range [km]	ZS-DOAS [10 ¹³ molec/cm ²]	SAOZ [10 ¹³ molec/cm ²]	Rel.diff [%]
09 Feb 2000(a)	outside	11-23	1.46	1.46	-0.2
07 Mar 2000(b)	inside	13-27	3.11	2.97	4.5
16 Mar 2003(c)	inside	13-27	2.79	2.31	20.9
11 Aug 1998(d)	-	13-27	0.87	0.96	-8.8
13 Aug 2002(e)	-	13-27	1.21	0.93	31.0

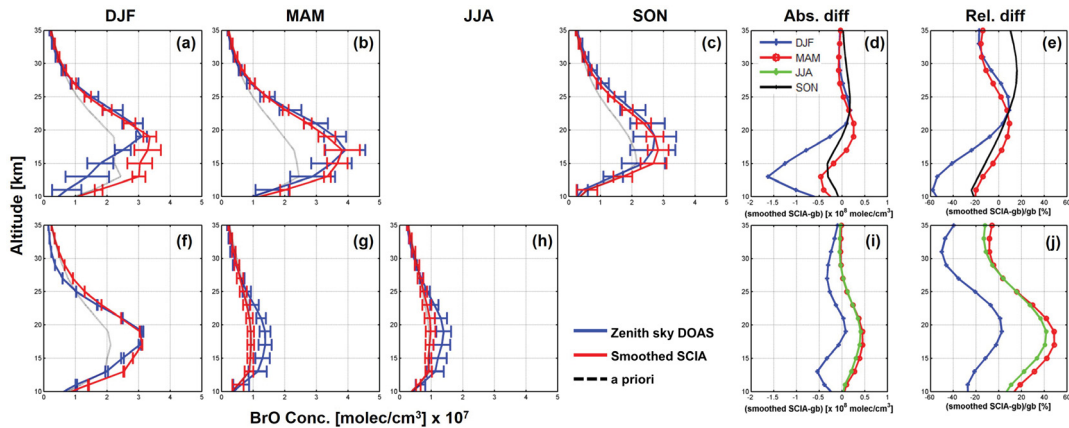


Figure 4.17: Comparison of coincident ZS-DOAS and SCIAMACHY profiles from 2002 to 2006. Figures (a,b,c) and (f,g,h) represent the seasonal mean profiles measured in a.m and p.m, respectively (blue: ZS-DOAS, red: SCIAMACHY). The black dotted lines represent the a priori profiles used for the ZS-DOAS profile inversion. Figures (d,e,i, and j) show the corresponding absolute and relative differences.

Coincidence criteria for comparison

The coincidence criteria used here are similar with those mentioned in Section 3.2.4. For the comparison data of the same day at the same SZA ($\pm 1^\circ$) taken from SCIAMACHY and ground-based observations are selected. Both ascending and descending parts of SCIAMACHY limb observations are used. After some sensitivity tests measurements are selected for which the distance between the tangent point of SCIAMACHY observations and the ZS-DOAS measurement is within 300 to 500 km.

Profile comparison

In Fig. 4.17 the BrO profiles retrieved by ZS-DOAS observations are compared with SCIAMACHY limb observations for different seasons from 2002 to 2006. The altitude range for the comparison is chosen from 15 km to 27 km as the best sensitivity for both measurements is found in that range. Due to the collocation criteria no coincident data are found in some seasons. For most seasons the agreement between both instruments is good, but for a.m observations in winter (DJF) larger discrepancies especially below 20 km are found (with differences up to 60 %). Large relative differences are also found for the p.m. profiles in summer, but here it should be noted that the absolute values of the BrO concentration are much lower compared to the other seasons. Interestingly, the differences are in general larger for p.m. than for a.m. (with larger ground based values in p.m.), which can be explained by the fact that the SCIAMACHY measurements are closer in time to the a.m. measurements.

Partial column comparison

Figure 4.18 shows the time series of BrO partial columns (15 km to 27 km) obtained from ZS-DOAS and SCIAMACHY limb observations. The altitude range is chosen as the range where both instruments show a good measurement response. Due to technical problems of the ZS-DOAS instrument from 2002 to 2004 and from 2007 to 2012, this study focuses on

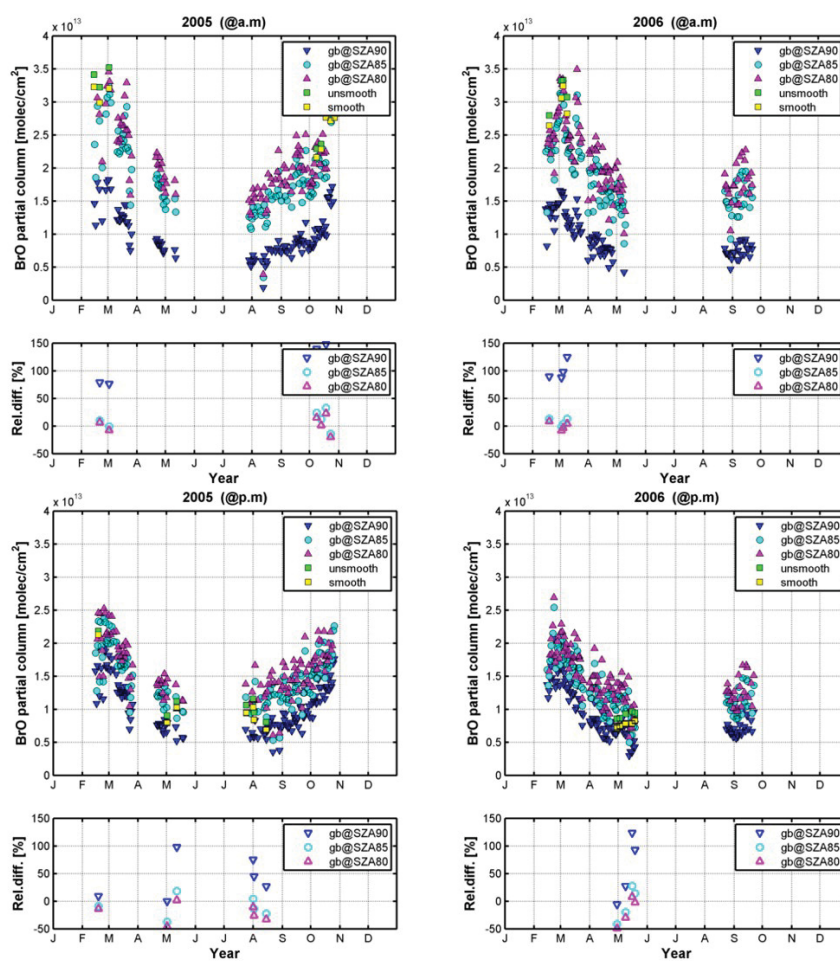


Figure 4.18: Time series of BrO partial column densities (15 - 27 km) obtained from ZS-DOAS and SCIAMACHY in 2005 (left) and 2006 (right). Data for a.m. are plotted in the upper graphs and for p.m. are in lower graphs. x - and y -axes indicate the time and the monthly averaged partial column densities ($molec/cm^2$), respectively. In all figures, blue, cyan, and magenta markers represent the integrated profiles obtained from the ZS-DOAS (IGB) at different SZA. Green and yellow squares represent unsmoothed integrated SCIAMACHY profiles (US-SCIA) and smoothed integrated SCIAMACHY profiles (S-SCIA), respectively. The relative differences between the smoothed integrated SCIAMACHY profiles and the BrO partial column obtained from ZS-DOAS at different SZA conditions are shown in separate figures.

the years 2005 and 2006. In this graph, BrO partial columns (PCs) obtained from integrated ZS-DOAS (IGB) are shown for three different SZA (at 80° , 85° , and 90°). For SCIAMACHY, unsmoothed (US-SCIA) as well as smoothed integrated SCIA profiles (S-SCIA) are shown. Here, it should be noted that the SZA at tangent point for the different season is DJF (81° – 87°), MAM (74.5° – 86°), JJA (79° – 85°), and SON (75° – 81.5°). The BrO column densities obtained from both measurements show a clear seasonal variation with high values in winter and low values in summer. During spring, larger day to day variations are found than in summer. Due to the strong variation of the BrO concentration during twilight, the best agreement between both data sets is found for ZS-DOAS results for SZA of 80° and 85° . For SZA of 90° much lower values are found. In general (except for SZA of 90°) a remarkably good agreement between both data sets is obtained.

4.2.5 Trend analysis

BrO is the most abundant inorganic bromine species (Br_y) in the stratosphere and it represents 70% of the total amount of Br_y . The main sources of Br_y in the stratosphere are natural (about 48 %) and anthropogenic (about 52%) bromine-containing source gases transported from the troposphere into the stratosphere. According to WMO, the Br_y loading of the stratosphere has declined by $-0.6\%/year$ between 2001 and 2013 as a consequence of the controlled anthropogenic bromine-containing sources [WMO, 2014]. A decreasing trend was also reported from several studies based on ground-based observations, balloon-borne observations and also satellite observations [Dorf et al., 2006b; Hendrick et al., 2008, 2009b].

An overview on the results of these studies is given in Table 4.6. However, these studies do not cover the most recent time period after 2009. The only trend study extending to 2013 is obtained from ground-based measurements at Harestua (update shown in WMO [2014]). The slightly negative trend between 2001 and 2013 of $-0.6\%/year$ is rather uncertain. Also it is not clear how representative it is for the rest of the world.

This section deals with the determination of the trend of stratospheric BrO using the long-term (1997 – 2015) observations from the ground-based zenith sky DOAS at Kiruna. For the BrO trends the same method is used as for NO_2 (See Sec. 3.2.5).

Table 4.6: Summary of former studies investigating the stratospheric BrO trends measured at various sites.

	Covered period	Site	Instrument	Trend (%/year)
Hendrick et al., (2008)	1995-2001	Harestua (60°N)	GB-DOAS	2.5 ± 0.5
	2001-2005			-0.9 ± 0.4
	1995-2001	Lauder (45°S)	GB-DOAS	2.2 ± 0.2
	2001-2005			-1.3 ± 0.3
Hendrick et al., (2009)	2002-2008	Harestua (60°N)	Satellite	-0.6 ± 0.3
		OHP (44°N)		-1.6 ± 0.4
		Lauder (45°S)		-1.2 ± 0.3
		Izana (22°S)		-2.1 ± 0.4

Results for the BrO trend analysis

Figure 4.19 shows time series of monthly averaged stratospheric BrO partial columns derived by integrating the inverted profiles according to Eqn. 3.8. In order to follow the influence of the Montreal Protocol and to see the consistency with other studies, trends are determined for different time periods: (a) 1997–2001, (b) 2005–2015, and (c) 1997–2015. The results are listed in Tab. 4.7.

In all cases of Fig.4.19, a strong seasonality is detected at a glance as in the NO_2 trend analysis, but with a phase shift of 6 months. This finding provides a rather remarkable

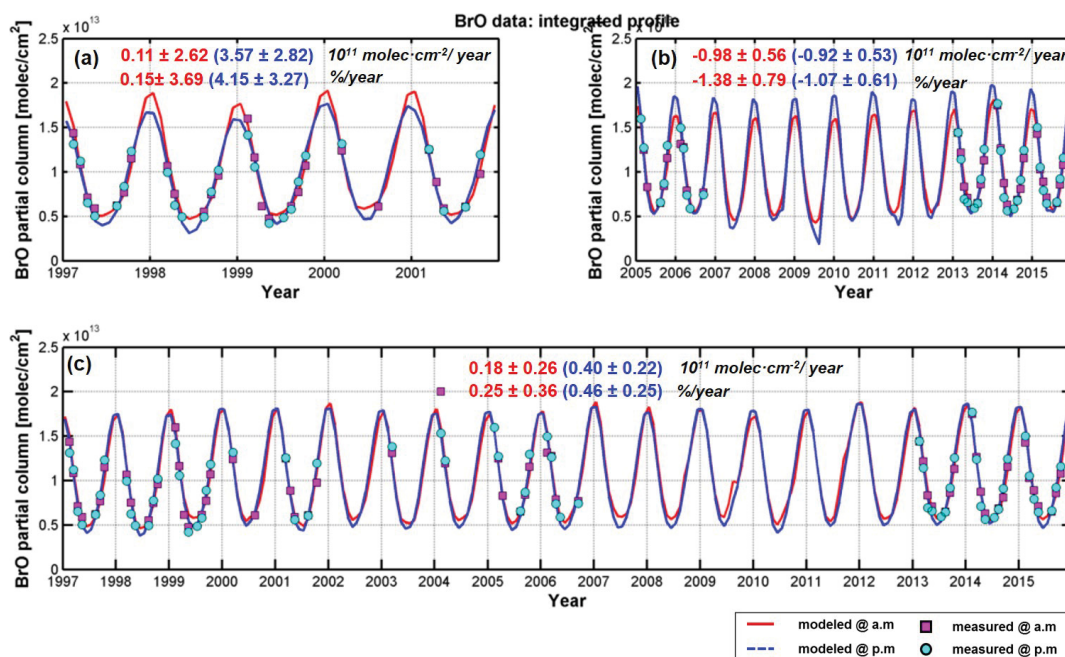


Figure 4.19: Trend analysis of stratospheric BrO partial columns (15 – 27km) derived from the ground based ZS-DOAS measurements. Magenta squares and cyan dots represent measurements in a.m and p.m, respectively. The continuous lines and the dashed lines indicate the corresponding fitted BrO VCDs. Figures (a) to (c) show the results for different period. Absolute and relative trends for a.m (red) and p.m (blue) are shown in each figure.

evidence for the strong anti-correlation between BrO and NO₂. The trend analysis is performed either by including the terms for QBO, solar cycle, and aerosol or by excluding these terms. The results without considering these terms are shown in brackets in Tab. 4.7. It is found that the contribution of the terms of QBO, solar cycles and aerosol is small (around 1%/year). Nevertheless, they can still have a strong effect on the derived trends for the short periods. In particular for the period 1997 – 2001 different trends are found for a.m and p.m. These findings also indicate that the trend results for the short periods should be treated with caution. Another point which should be mentioned is that the trend analysis by excluding the semi-annual term from the fit as shown in the Appendix (Fig. A.16). All trend results are summarised also in Appendix (Tab. A.2).

Before 2001 (a), one can clearly see increasing BrO, in particular, a significant positive trend in p.m. In contrast, after 2001 (b) negative trends (or an insignificant positive trend) are detected. These findings are in general agreement with previous studies, but the Kiruna measurements also cover the years after 2013. For the whole period (1997 to 2015) the relative trends in a.m and p.m are slightly positive ($0.25 \pm 0.36\%/year$ and $0.46 \pm 0.25\%/year$, respectively.), which is mainly related to the rather strong increase during the years before 2001.

4.2.6 Estimation of the total stratospheric Br_y, its temporal evolution, and the contribution of Very Short-lived substances

In this section the total stratospheric bromine mixing ratio is estimated from the measured BrO profiles. It is then compared to other measurements and to estimates of the stratospheric

Table 4.7: Derived absolute and relative trends of the partial columns of stratospheric BrO. Values in bracket indicate the trends performed without including the terms for QBO, solar activity and aerosols.

Method	Period	molec· cm ² /year		% /year	
		a.m (×10 ¹¹)	p.m (×10 ¹¹)	a.m	p.m
Integrated profile	(a)1997–2001	0.11±2.62 (1.56±1.01)	3.57±2.82 (3.09±1.24)	0.15±3.69 (1.52±0.99)	4.15±3.27 (3.06±1.23)
	(b)2005–2015	-0.98±0.56 (0.25±0.40)	-0.92±0.53 (-0.09±0.36)	-1.38±0.79 (0.24±0.40)	-1.07±0.61 (-0.09±0.35)
	(c)1997–2015	0.18±0.26 (0.44±0.20)	0.40±0.22 (0.53±0.17)	0.25±0.36 (0.43±0.19)	0.46±0.25 (0.52±0.17)

inorganic bromine mixing ratio based on long lived precursor compounds. From the difference, the potential contribution from Very Short-Lived Substances (VSLs) can be estimated. Oram et al. [2017] mentioned that the role of VSLs on the total stratospheric BrO amount is still uncertain. Recent studies have derived the total inorganic stratospheric bromine which has decreased by 0.6 ± 0.1 %/year from 2001 to 2012 [WMO, 2014].

Most of the stratospheric Br_y comes from long-lived bromine compounds containing organic gases which are transported from the surface to the stratosphere contributing to the stratospheric Br_y loading by about 16 – 17 ppt [Montzka et al., 2003a]. Meanwhile, several studies based on ground-based remote sensing measurements of BrO have estimated a total inorganic bromine loading of 18 – 25 ppt [Sinnhuber et al., 2002; Schofield et al., 2004; Hendrick et al., 2007; Theys et al., 2007a]. To bring both estimates into agreement, an additional source of bromine compounds is needed, and most studies suggested that this source might be very short lived species (VSLs) as mentioned above. Therefore, the stratospheric inorganic bromine mixing ratio, and from that the contribution of Br_y-VSLs is estimated from the BrO profiles obtained in this thesis using the same assumptions as in previous studies (see also Theys et al. [2007a]; Hendrick et al. [2007, 2008]).

- First the mixing ratio of BrO [molec/cm³] at 21 km is calculated from the retrieved BrO concentration profile using the ideal gas law by assuming that the temperature and pressure at 21 km are 217K and 55 hPa (US standard atmosphere) [Sissenwine et al., 1962]. It is also assumed that at this altitude (and above) bromine exists mostly in its inorganic form.
- To correct for the seasonal variation, the average seasonal cycle of BrO is determined using Fourier series fitting. Then, the ratio ('Seasonal factor') between the fitted seasonal cycle and the annual average is determined for the individual months. Then this factor is applied to the individual data points (monthly mean values) for the whole time period. Finally the yearly averaged BrO mixing ratios are calculated from the corrected monthly mean values.
- BrO is the most abundant inorganic species during day time. This study uses a ratio of BrO/Br_y (for day time) of 0.6. This ratio was calculated by the stacked box photochemical model PSCBOX (using measured data at 60°N, 10:30 LT) [Chipperfield,

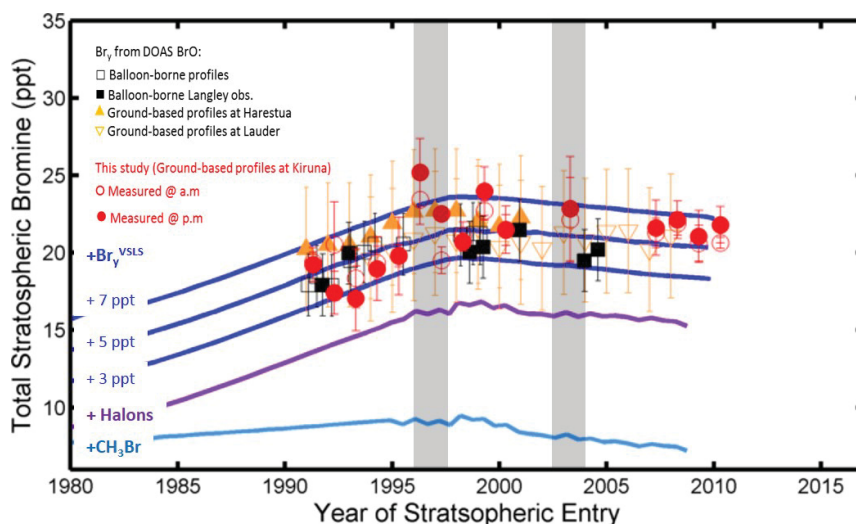


Figure 4.20: Annual mean mixing ratio of total stratospheric inorganic bromine calculated from ground-based zenith sky DOAS measurements of stratospheric BrO at Kiruna (67°N) (open and closed red dots). Here, error bars indicate the 1σ standard deviation of the monthly mean values of the respective year. Grey shaded areas indicate periods with technical problems of the ground-based instrument. Other data are adapted from WMO [2014] (Assessment Chapter 1, figure 1-20, see also Dorf et al. [2006a] and Hendrick et al. [2007, 2008]). For these data, the error bars correspond to the total uncertainties (Details are described in those papers and in the Assessment report.) The cyan line shows the global tropospheric bromine mixing ratio of methyl bromide as measured in firn air (Butler et al. [1999]) and ambient air (after 1995; Montzka et al. [2003b]) with no correction for tropospheric CH_3Br loss. The purple line shows the sum of methyl bromide plus halons (Butler et al. [1999] and Fraser et al. [1999] through 1995; and Montzka et al. [2003b] thereafter). The blue lines show bromine from CH_3Br and halons after bromine from VSLs organic compounds with different mixing ratios (of 3, 5, 7 ppt) was added. (Murphy and Thomson [2000]; Dorf et al. [2006a]). An assumed contribution of about 5 ppt matches best to the measurements. Note that for stratospheric data based on DOAS measurements in Kiruna, Lauder and Harestua, the corresponding times represent the measurement times minus the estimated mean age of the stratospheric air (about 4 to 5 years, see text).

2006; Feng et al., 2007; Hendrick et al., 2007; Theys et al., 2007a] and is assumed to be representative for an altitude of about 21 km. The yearly averaged BrO mixing ratios are divided by 0.6 to derive the corresponding total inorganic stratospheric bromine mixing ratios.

Figure 4.20 shows the calculated annual mean inorganic bromine mixing ratio from ground-based zenith sky DOAS measurements of stratospheric BrO measured at Kiruna together with results from other studies. Here, the x -axis indicates the time at which the air has been transferred from the troposphere to the stratosphere. For this correction, this study uses the mean age of stratospheric air over Kiruna which is around 5.7 years. This value is estimated using the correlation between the volume mixing ratio of the tracer N_2O and the mean age of air [Engel et al., 2002]. The mean age of air over Harestua and Lauder is 4.2 ± 1.0 years and 3.9 ± 1.0 years, respectively, which is slightly less than for Kiruna. In spite of the simple estimation with a few assumptions, Br_y derived in this thesis agrees well within the respective uncertainties with most of the previous estimations. The mean values

of stratospheric Br_y except 2002 are 20.6 ± 1.2 ppt at sunrise and 20.8 ± 1.9 ppt at sunset, respectively, which are in agreement with studies from Pfeilsticker et al. [2000] (21.5 ± 3 ppt in 1999, 68°N), Theys et al. [2007a] (23 ppt in 2005, 20.9°S), Millán et al. [2012] (20.3 ± 4.5 ppt in 2005, 50°S – 50°N), Hendrick et al. [2008] (22.5 ± 4 ppt in 2008, 60°N), Dorf et al. [2008] (19.5 ± 2.5 ppt, 2008, 5°S). Thus the estimate derived in this thesis confirms the hypothesis that about 5–6 ppt of stratospheric inorganic bromine are probably caused by VSLs. Another interesting finding is that the stratospheric BrO observed at Kiruna gradually increases until 2001 and declines from 2002 to 2012 (year of stratospheric entry). The decay is related to the decline of the tropospheric CH_3Br and Halons after 1997 considering the mean air age.

Yang et al. [2014] mentioned that a quarter of the current stratospheric Br_y is probably caused by naturally produced VSLs. Accordingly, the VSLs contribution to stratospheric bromine derived from BrO measurements at Kiruna is estimated to around 5.1 ± 0.5 ppt at Sunrise 5.2 ± 0.1 ppt at sunset, and this estimated contribution is consistent with the difference mentioned above, and most published estimations so far, see Table 4.8.

Despite the large uncertainties of the derived estimates of total inorganic bromine, these results are helpful in quantifying the contribution of brominated-VSLs to the stratospheric Br_y and also the temporal evolution. Because Kiruna is located at higher latitudes, it is affected by a more pronounced seasonal cycle, which might cause larger uncertainties of the partitioning ratios between BrO and Br_y and also more data gaps during polar night and polar day than measurement, at other locations.

An important advantage of our measurements is that it extends the existing time series of ground based measurements by several years. Such long term data at high latitude are rare compared to the data at mid latitudes. Thus it would be particularly worthwhile to compare the observational data with results from chemistry models in the future.

4.3 SUMMARY

In this chapter, the spatio-temporal variation of stratospheric BrO above Kiruna, Sweden, is investigated by using ground-based zenith sky DOAS measurements. The following general points summarise the main findings derived from this chapter:

- BrO profiles retrieved using the Optimal Estimation Method inversion algorithm yielded multi-year time series (19 years with gaps) of monthly mean BrO stratospheric partial columns (15 – 27 km). The derived data show a strong seasonal variation which is anti-correlated with stratospheric NO_2 .
- The day to day variation of stratospheric BrO often depends on the stratospheric temperature and the relative position of Kiruna to the polar vortex.
- The BrO data obtained from ground-based zenith sky DOAS is compared with other measurements including SCIAMACHY limb observations and SAOZ balloon-borne measurements. The balloon measurements show good agreement with the DOAS measurements. For the comparison with the SCIAMACHY observations very good agreement is found.
- Using a nonlinear least-squares algorithm, a trend analysis of stratospheric BrO is performed. BrO VCDs derived from the integration of the obtained profiles are utilised. Before 2001, a strong positive trend is found. In contrast, after 2001, a slightly negative

(or an insignificant positive trend) is detected. These findings are in good general agreement with previous studies. For the whole period (1997 – 2015) slightly positive relative trends are found (0.25 ± 0.36 %/year measured in a.m, and 0.46 ± 0.25 %/year in p.m).

- The total amount of inorganic stratospheric bromine and the contribution of Br_y-VLS is estimated based on the Kiruna measurements. From 1997 to 2016, the mean of total

Table 4.8: Estimation of from the contribution of very short-lived substances (Br_y VLS) to total stratospheric inorganic bromine from BrO measurements. by satellite, ground-based, and balloon-borne instruments. Adapted from WMO [2010] Tables 1-14 and Millán et al. [2012], Stachnik et al. [2013].

Data source	Br _y VLS Central Value(ppt)	Br _y VLS Range (ppt)	Reference
Ground-based BrO Kiruna, Sweden(67°N)	5.1 5.2	4.9-5.5 4.7-5.7	This Study
Ground-based BrO 11-sites, 78°S–79°N	5	1–9	Sinnhuber et al. [2002]
Ground-based BrO Lauder, New Zealand, 45°S	6	3–9	Schofield et al. [2004]
Ground-based BrO Arrival Heigts, Antarctica, 78°S	6	3–9	Schofield et al. [2006]
DOAS balloon BrO profile 5°S – 68°N, 0–35km	4.1	1.6–6.6	Dorf et al. [2006b]
Aircraft & balloon BrO 22°S–35°N, 17–32km and 45°S	7	4–10	Salawitch et al. [2005]
SCIAMACHY satellite BrO 80°S–80°N, 15–28km	8.4	6.4–10.4	Sioris et al. [2006]
SCIAMACHY satellite BrO 80°S–80°N	3	0–6	Sinnhuber et al. [2005]
Ground-based BrO Harestua (60°N) and Lauder (45°S)	6	2–10	Hendrick et al. [2008]
Ground-based BrO Reunion Island (21°S,56°E)	7	3–11	Theys et al. [2007a]
MLS satellite BrO 55°S–55°N, 10–4.6hPa	6.5	1–12	Kovalenko et al. [2007]
OSIRIS satellite BrO 80°S–80°N, 20–34km	5	0–10	McLinden et al. [2010]
OMI total column BrO and aircraft tropospheric BrO Arctic spring	7	5–10	Salawitch et al. [2010]
MLS satellite BrO 50°S–50°N, 10–4.6hPa	5	1.5-9.5	Millán et al. [2012]
Ballooon-borne BrO with submillimeterwave radiometer 16km Ft. Sumner, New Mexico(34°N)	6	4–8	Stachnik et al. [2013]

stratospheric Br_y except 2002 are 20.6 ± 1.2 ppt at sunrise and 20.8 ± 1.9 ppt at sunset, respectively. From these results, the contribution from VSLs to the stratospheric Br_y are estimated to be 4.7 to 5.7 ppt. The total amount of inorganic stratospheric bromine is in good agreement with previous studies. However, based on the Kiruna measurements the time series could be extended by several years.

After the Montreal protocol and amendments, the production of CFCs was strongly reduced. Since then scientists have steadily made efforts to monitor the amount of chlorine compounds which are mainly responsible for the destruction of ozone in the stratosphere. Although very recent research of stratospheric ozone indicates an ozone recovery [Solomon et al., 2016], ozone depletion is still observed in the polar spring and is expected to last for about another 70 years according to the WMO. Therefore, continuous observations and analysis of the stratospheric ozone as well as other stratospheric trace gases are highly demanded. Several previous studies have investigated OCIO which is an indicator for stratospheric chlorine activation using satellite, ground-based, and balloon remote sensing measurements [Solomon, 1988; Schiller et al., 1990; Fiedler et al., 1993; Gil et al., 1996; Kreher et al., 1996; Otten et al., 1998; Miller Jr. et al., 1999; Wagner et al., 2001; Richter et al., 2005; Kühl et al., 2006].

In this chapter, long-term time series of OCIO DSCDs above Kiruna, Sweden by using the ground-based zenith sky DOAS measurements are investigated. Since the measurements are performed at a fixed site, for the interpretation also the relative position of the polar vortex has to be considered. The long-term data obtained during about 15 years (from 1997 to 2016 except 2007, 2008, 2010, and 2011) allows to classify the dependence of the OCIO amount on various meteorological conditions.

Compared to satellite measurements, ground-based measurements have several advantages. Basically, satellite observations have a rather low signal to noise ratio due to the short exposure time. Especially, the relatively weak absorption of OCIO makes it difficult to obtain good quality data from satellite. In contrast, ground-based measurements have better sensitivity than the satellite measurement because of the longer exposure time. Ground-based observations also cover the whole diurnal cycle, while satellite observations are usually restricted to one overpass per day.

Therefore, in this study, the variation of OCIO is presented using long-term observations from ground-based measurements at Kiruna under different stratospheric conditions. This chapter is organised as follows. The optimisation of the analysis settings including wavelength range and reference spectra is explained in the first section. In the following, results of the temporal variation of OCIO DSCDs over Kiruna for 15 years are provided in detail.

5.1 ANALYSIS

In this section, the optimisation of the analysis setting for OCIO is shown. The analyses of OCIO are done by the DOAS method. The wavelength range of 372–392 nm is used which covers several absorption bands of OCIO. The analysis settings are summarised in Tab. 5.1. Fig. 5.1 also shows a typical example of the fitting process based on the analysis settings of Tab. 5.1. In this section, information on how these analysis settings were obtained is provided.

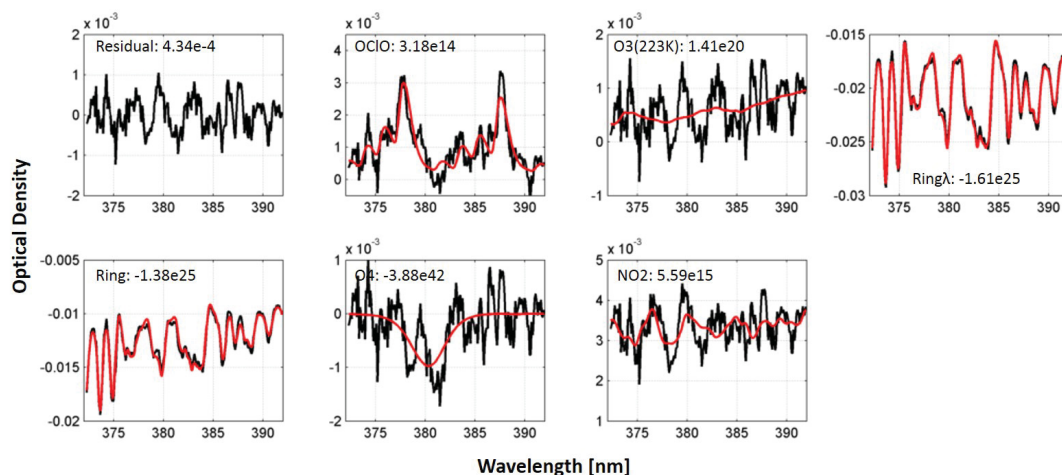


Figure 5.1: Example of an OCIO analysis of a spectrum measured on 2016 Feb. 2, 13:54 UTC (SZA at 90.94°). The red lines indicate the different reference spectra scaled to the respective absorptions retrieved from the measured spectrum (black lines).

Here, it should be noticed that for OCIO usually not the VCDs, but SCDs are provided. Normally, the SCDs are converted into vertical column densities (VCDs) by dividing the measured SCDs by an airmass factor ($AMF = SCD/VCD$) derived from radiative transport modelling. However, while the airmass factors can be well calculated for trace gases with constant vertical profiles, it is hardly possible for OCIO because of its rapid photolysis, especially under large SZA conditions.

5.1.1 Choice of the wavelength range

For the OCIO analysis the spectral range of 372–392 nm is chosen. This spectral range is somewhat narrower (only two absorption bands) than used in other studies (three absorption bands) [Wagner et al., 2001; Frieß et al., 2005] but it still clearly shows the OCIO absorption features. The reason for the choice of this spectral range is that the detector has been replaced since 23rd of January 2013 (see Sec. 2.3.2.1), and the spectra obtained before and after the replacement have different qualities. For measured spectra before 2013, a strong spectral structure is found in the fit residuals if the wide spectral range of 363 – 392 nm

Table 5.1: Specification for the ground-based zenith sky DOAS spectrum evaluation for OCIO.

Fitted Spectra	Reference
OCIO	Kromminga et al. [2003], 213K
O ₃	Bogumil et al. [2003], 223K
O ₄	Thalman and Volkamer [2013], 273K
NO ₂	Vandaele et al. [1998], 220K
Ring	Kraus [2006]; Wagner et al. [2009]
Ring·λ ⁴	-
Polynomial order	5th

is used. This structure can be explained by the Fabry-Perot Etalon effect. The Fabry-Perot Etalon effect was observed during DOAS measurements already and is discussed in several studies [Stutz and Platt, 1996; Hönninger et al., 2004]. It is an interference effect which is caused by multiple reflections on the parallel planes in the optical path. As the spectrograph cools down to -33°C , water vapor generates a thin layer of ice on the PDA surface. (See Fig. 2.6) The resulting of Etalon effect has a typical spectral shape as shown in the halogen lamp spectrum in Fig. 5.2. Two lamp measurements are shown, one with the new detector (colored blue) on January 24th, the other with the old detector (green) on January 23rd, 2013. Here, the Etalon effect is clearly obvious in the measurements with the old detector (green line). In contrast no significant Etalon effect is seen in the lamp spectrum obtained by the new detector (blue line).

In principle the Etalon effect cancels out if a measured spectrum is analysed versus a Fraunhofer reference spectrum, since both spectra are affected by the same Etalon structure. However, this expectation is only fulfilled for short time periods. For larger time differences (more than several days) between the measured spectrum and the Fraunhofer reference spectrum changes of the ice layer on the detector lead to changes of the etalon structures, which show up as systematic residual structures in the spectral analysis as depicted in Figs. 5.2 (B)–(D). These figures results for present data measured on February 24th 1997, and show a typical residual structure resembling the green line in Fig. 5.2(A). This residual structure also affects the spectral analysis of OCIO. In order to correct this interference, previous studies have employed the method that measured spectra are divided by lamp spectra [Bugalski 2001], which are regularly recorded during night. However, for long periods of the Kiruna measurements, lamp spectra are not available due to the absence of personnel, which could replace broken halogen lamps.

Therefore, in this work a different approach by including a halogen lamp spectrum as an additional reference spectrum in the fitting process is applied. The test of this correction procedure is performed in two different wavelength ranges, a narrow range (372–392nm), and a wide spectral range (363–392nm) used in other studies including three OCIO absorption bands. One additional condition for whether a lamp spectrum is included or not ('lamp on' or 'lamp off') is considered.

Figure 5.3 shows time series of OCIO DSCDs during three winters (96/97 to 98/99) using the four different analysis conditions described above. The results are obtained using fixed Fraunhofer reference spectra recorded at a SZA of 80° outside the period of stratospheric chlorine activation (8 March, 1997, 25 October 1997, and 25 October 1998). The results in this figure indicate that all results capture the same general features, in particular, the positions of peaks are very similar. However, the absolute values of the different analyses differ significantly.

From this figure, it is also found that the use of a lamp spectrum slightly improves the consistency of the OCIO analysis especially in late winter and early spring, but cannot compensate all effects of a changing Etalon structure. In contrast, the choice of the wavelength range induces a big difference which can be explained by the fact that in the wide wavelength range the Etalon effect strongly interferes with the OCIO absorption.

While in some years, the results for including or not including the lamp spectra are very similar, in other years large differences occur. There is no obvious reason for the different behavior in different years, but they might be related to different variations of the Etalon structure in different years. Based on these results it was decided to use the narrow window for the analysis as well as including the lamp spectrum in the fit for a

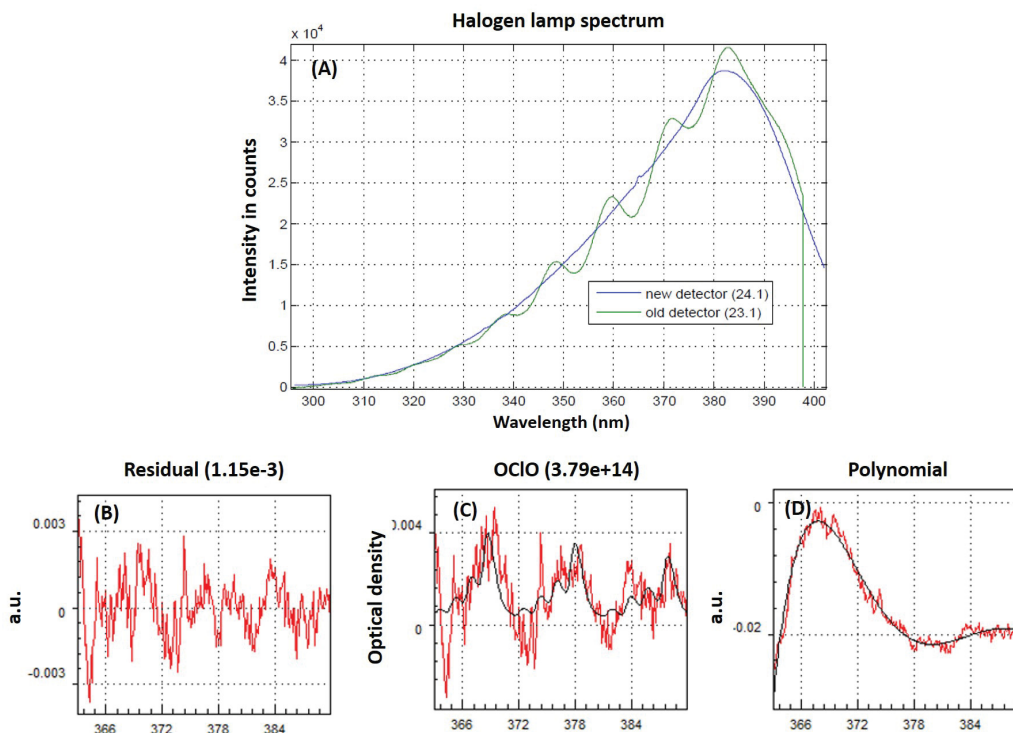


Figure 5.2: (A) Comparison of halogen lamp spectra recorded by the old (January 23rd, 2013) and new detectors (January 24th, 2013). This figure is taken from [Gottschalk, 2013]. Figures (B) to (D) show OCIO fit results which are affected by changes of the Etalon structure (observations from February 24th, 1997; solar zenith angle is 90.2°). The red lines indicate the different reference spectra scaled to the respective absorptions retrieved from the measured spectrum (black lines). While most of the Etalon structure is covered by the polynomial (D), the OCIO results are probably still affected by the remaining residual structures.

first order correction. Unfortunately the lamp spectrum can not be employed in the whole measurement period due to technical problems of the instrument. Thus, even for the use of the narrow spectral range, part of the OCIO results might be affected by remaining spectral interferences. However, based on the comparison studies, we conclude that these effects are small compared to the natural variation of the atmospheric OCIO absorption.

5.1.2 Selection of the Fraunhofer reference spectrum

The atmospheric absorption of OCIO is rather weak like that of BrO. In order to minimise the fit residuals as much as possible, a daily reference spectrum taken at SZA 80° during each twilight period can be used for the spectral analysis. Because the measurement site, Kiruna is located at high latitude, the SZA does not reach 80° from October 27th to February 15th. Figure 5.4 shows a time series of the SZA variation from October 2015 to April 2016. In this figure, magenta dots indicate the SZA of all spectra recorded during this period, and black dots represent the SZA of the daily reference spectra (taken either at a SZA of 80° or at the minimum SZA of the respective day). As can be seen in Fig.5.4, owing to the polar night, the daily minimum SZA is above SZA 90° in the middle of the winter. Thus

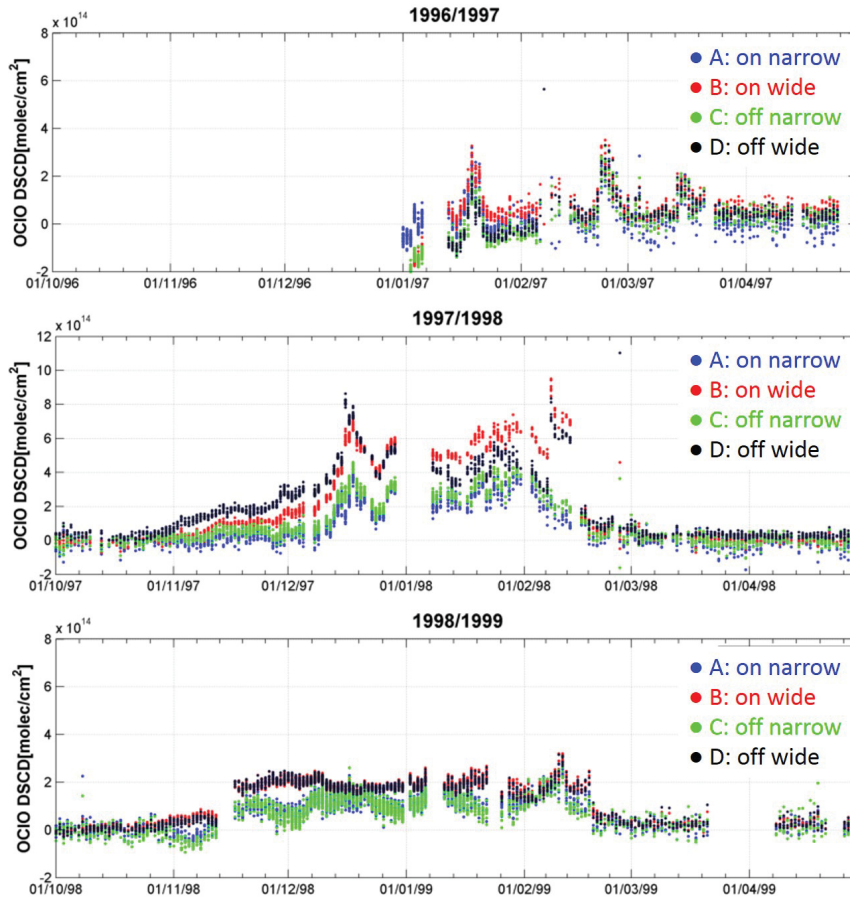


Figure 5.3: Time series of daily OCIO DSCDs (at $90.5^\circ \leq \text{SZA} \leq 91.5^\circ$) observed by the zenith sky DOAS instrument during three winters 1996/97 to 1998/99. The colors indicate A (blue: narrow spectral range, lamp spectrum included), B (red: wide spectral range, lamp spectrum included), C (green: narrow spectral range, no lamp spectrum included), and D (black: wide spectral range, no lamp spectrum included).

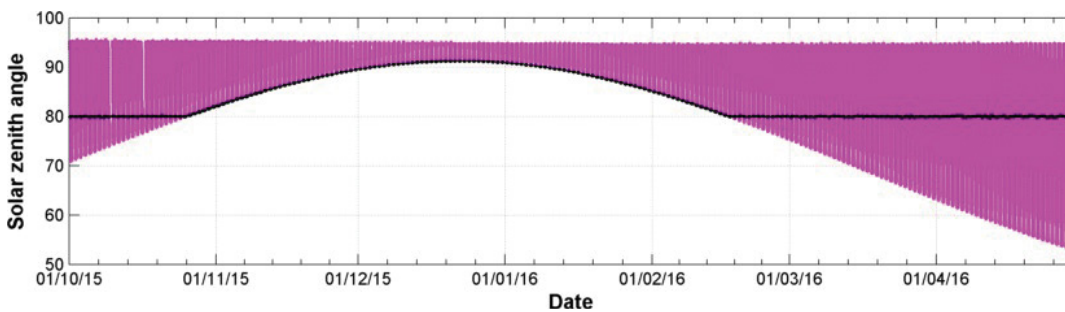


Figure 5.4: The time series of the SZA variation from October 2015 to April 2016. Magenta and black dots indicate SZAs of all recorded spectra and those of daily Fraunhofer reference spectra, respectively.

there is a high probability that the reference spectrum already includes a substantial OCIO absorption.

Therefore, a test analysis using a fixed reference spectrum taken in October around SZA 80° for the 2015/16 winter is performed. However, usually the error of the spectral analysis increases with increasing time distance between the measurement and the Fraunhofer reference spectrum. Thus it is not clear whether a meaningful OCIO analysis is still possible

with a fixed Fraunhofer reference spectrum in mid-winter. Figure 5.5 shows the comparison results of the time series of OCIO DSCDs as well as different quality parameters (RMS, spectral shift, and Offset) for the analyses with either daily or fixed Fraunhofer reference spectra. Blue and red lines indicate the results obtained by using fixed and daily references, respectively. Here, a fixed reference spectrum is measured on October 26th, 2015. In the first panel in Fig.5.5, it can be seen that especially in mid-winter the OCIO DSCDs of the analyses with different Fraunhofer reference spectra are largely different. Especially, the strong enhancement of OCIO on December 12th and 24th is only found for the analysis with the fixed Fraunhofer reference spectrum. These findings indicate that indeed the daily Fraunhofer reference spectra in mid-winter included substantial OCIO absorptions. Outside the polar night, there is almost no difference between both analyses.

The time series of the different quality indicators are provided in the second to fourth panels of Fig. 5.5. They are similar regardless of the two different reference conditions, but small differences are also found. For example, RMSs are about $2 - 4 \times 10^{-4}$ and $1 - 3 \times 10^{-4}$ for the analysis with the fixed and daily reference spectrum, respectively. The spectral shifts are $-8 - 4 \times 10^{-3}$ nm and $\pm 1 \times 10^{-4}$ nm, for the analysis with the fixed and daily reference spectrum, respectively. The intensity offsets are $\pm 4 \times 10^{-3}$ and $-4 - 1 \times 10^{-3}$, for the analysis with the fixed and daily reference spectrum, respectively. The most important conclusion of these findings is that the analysis using a fixed reference spectrum is possible without substantially increased uncertainties during mid-winter. Thus we apply two Fraunhofer reference settings for the retrieval of the OCIO DSCD: A fixed reference spectrum taken in October which is not affected by OCIO around SZA 80° is used for the analysis during the polar night period. For the periods before and after, daily Fraunhofer reference spectra are employed.

5.1.2.1 *Specific instrumental problems in the years 1999 to 2001 and their impact on the OCIO results*

During the almost two decades of operation, several technical problems occurred for the instrument. One of these problem was identified as an unknown systematic structure in the fit residuals for spectra measured from 1999 to February 2001 that is shown in Fig.5.6(A). A previous study [Bugalski 2003] has reported that frequent breakdowns of the measurement system happened during this period. Thus, it is expected that the problem might be related to problems of the electronic components of the controller unit. In Fig. 5.6, the structure is shown; it is characterised by spike features which are repeated in regular intervals. Unfortunately, the positions of the peaks vary. The structures are easy to notice in measured spectra taken at high SZA, but also in offset, dark-current, and lamp spectra. Moreover, this structure also clearly shows up in the fit residuals as shown in Fig.5.6(B)–(E). Those show DOAS fit results of residuals, O_4 , NO_2 , and OCIO. The red lines indicate absorptions of the retrieved trace gases in the measured spectra, and the black lines indicate the respective absorption cross section scaled to the absorption in the measured spectrum. Although the magnitude of the residual (B) is still relatively small, strong artificial structures can be seen in each DOAS fit.

To quantify the influence of this artificial structure on the OCIO retrieval results, a simple correction approach is tested by adding the structure (extracted on January 25th, 2000) to all measured spectra in the winter 2015/16 winter which is not influenced by the artificial structure. Figure 5.7 shows the obtained OCIO DSCDs results from either the original or the

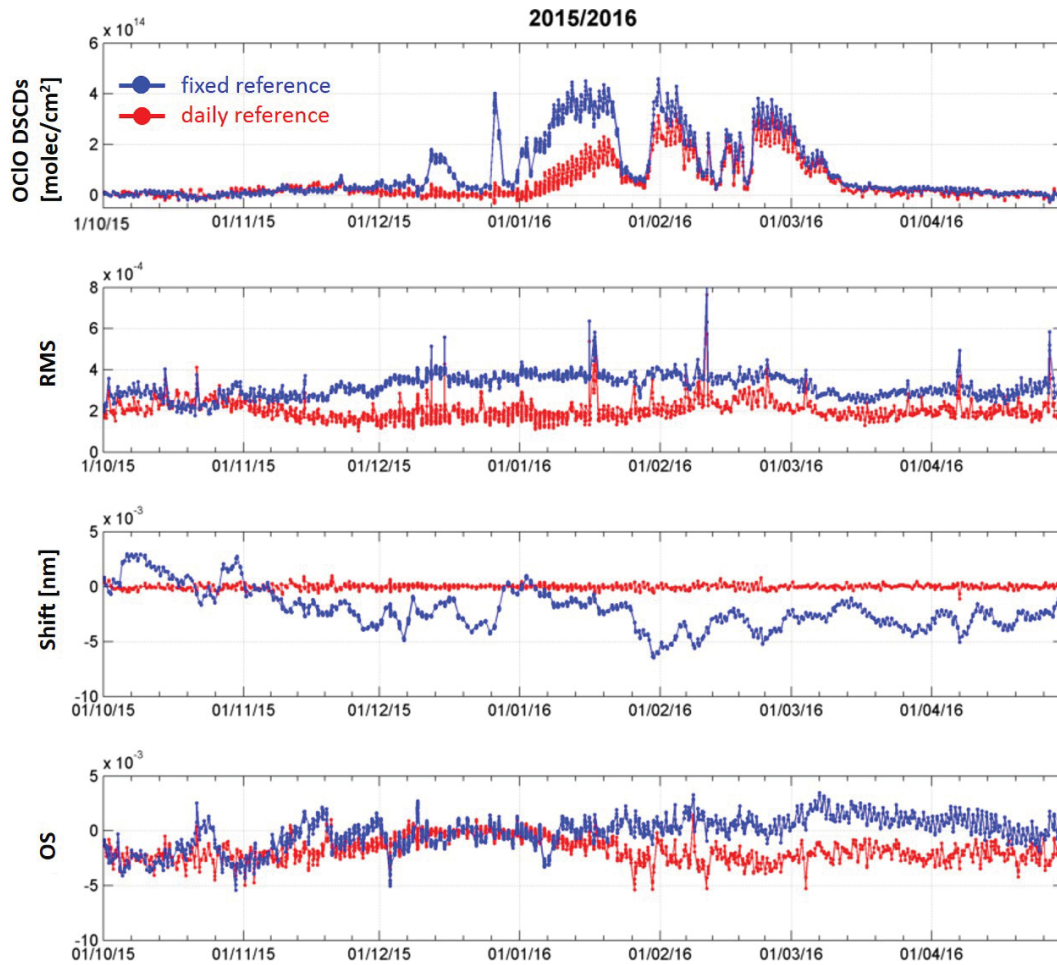


Figure 5.5: Time series of OCIO DSCDs (first panel), RMS (second), spectral shift (third) and intensity offset (fourth) for analyses using either a fixed (blue) or daily (red) Fraunhofer reference spectrum for the winter 2015/2016.

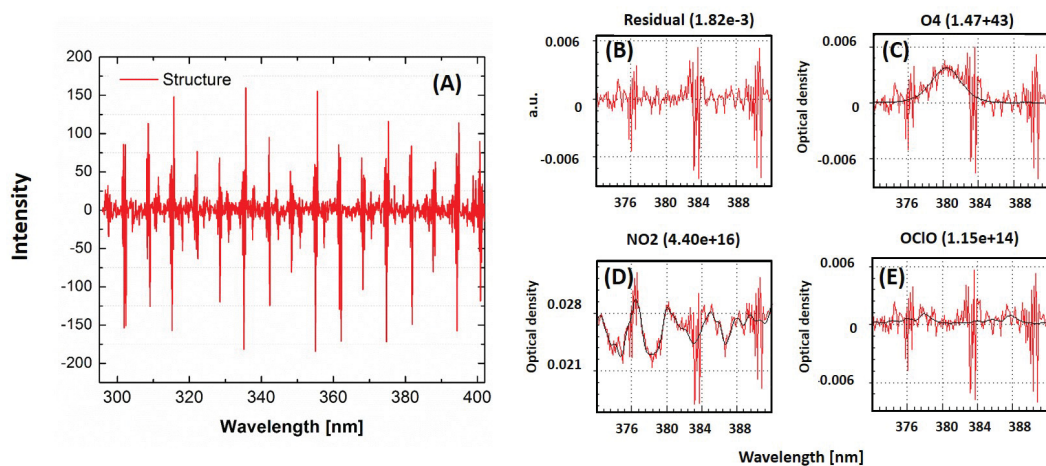


Figure 5.6: Figure (A) shows a systematic periodic structure in a dark current spectrum measured on 25th January, 2000; (B) DOAS fit results of residuals, (C) O_4 , (D) NO_2 , and (E) OCIO are also shown. Black lines in (C)–(E) indicate the fitted cross sections.

modified spectra. Also the absolute difference between both results is shown. It is found that the time series of OCIO DSCDs are almost similar to each other but the analysis of

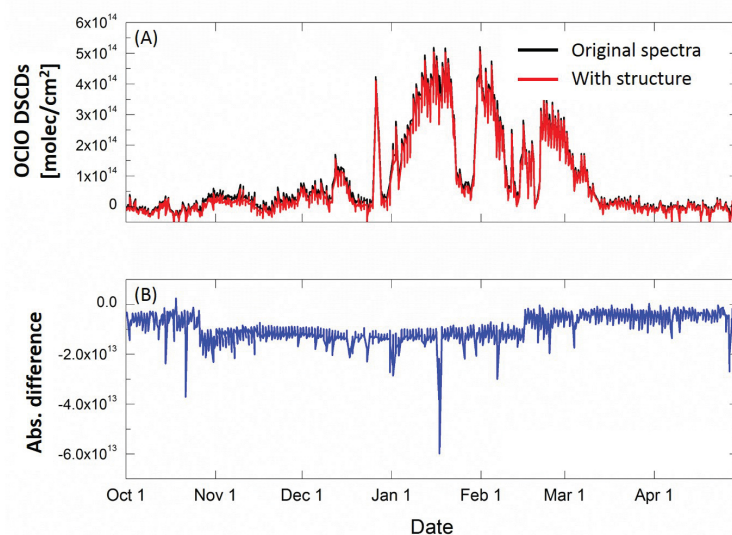


Figure 5.7: (A) The time series of OCIO DSCDs using original and modified spectra and (B) an absolute difference between those two. These results are analysed by using the spectra measured in the 15/16 winter.

the spectra with the added structure seem to be slightly more scattered than the original ones. Also the OCIO DSCDs of the modified spectra are slightly smaller than those of the original spectra. However, the absolute differences between them shown in Fig. 5.7(B) are only around -2×10^{13} to -0.8×10^{13} (typically $<3\%$). Compared to other uncertainties, these errors are negligible. It is important to note that these structures are also found in the DOAS fit results (see Fig. 5.7) where the residual is increased by 36%, and the OCIO DSCDs are decreased by 3.5%. The temporal variations of the three quality parameters (RMS of the residuals, intensity offset, and spectral shift) are also compared as shown in Appendix, Fig. A.17. The RMS of the residual is mainly affected by the artificial structure, while the intensity offset only slightly changes and the spectral shift is almost identical.

From these findings we conclude that the overall effect of the artificial structure on the OCIO results is rather small, especially when compared to other uncertainties. In particular the problems caused by the artificial structure do not affect the interpretation of the OCIO results with respect to stratospheric chlorine activation.

5.2 RESULTS

In this section, the interpretation of the OCIO DSCDs obtained for the measurements at Kiruna from 1997 to 2016 with respect to the meteorological condition is provided.

5.2.1 General variability

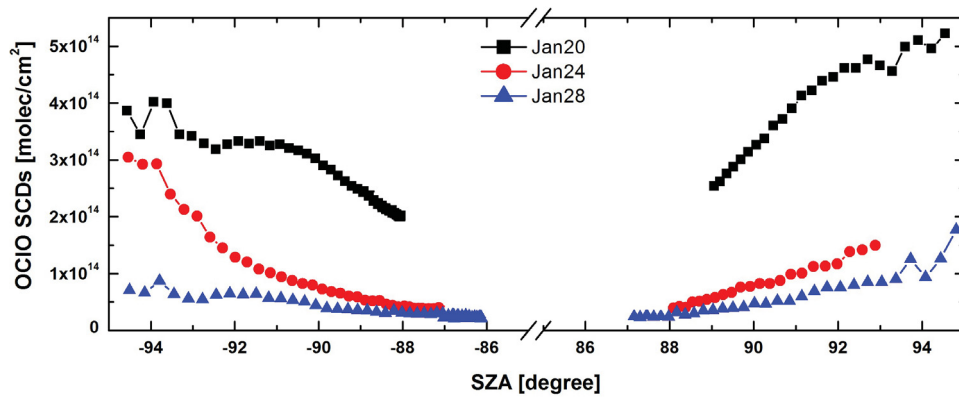


Figure 5.8: Diurnal variation of OCIO DSCDs as a function of SZA for three selected days of January 2016 (black: 20th, red: 24th, and blue: 28th). Negative SZA indicate results during sunrise.

Here, three days are chosen to illustrate how OCIO changes under different polar vortex conditions. In Fig. 5.8, results of OCIO DSCDs for the selected days of January 2016 (20th, 24th and 28th) are shown as a function of the SZA. Figure 5.9 illustrates the potential vorticity at the 475K isentropic level for the same days. The isentropic level of 475K is commonly used as reference altitude to decide whether a measurement location is inside or outside the polar vortex. The variation of the OCIO DSCDs in these three days is clearly related to the location of the polar vortex with respect to the measurement site: Kiruna is either located inside, at the edge or outside the polar vortex, respectively. The largest amount of OCIO is detected on 20th of January when Kiruna is located inside the polar vortex. It should be noticed that the OCIO DSCDs in the evening are larger than in the

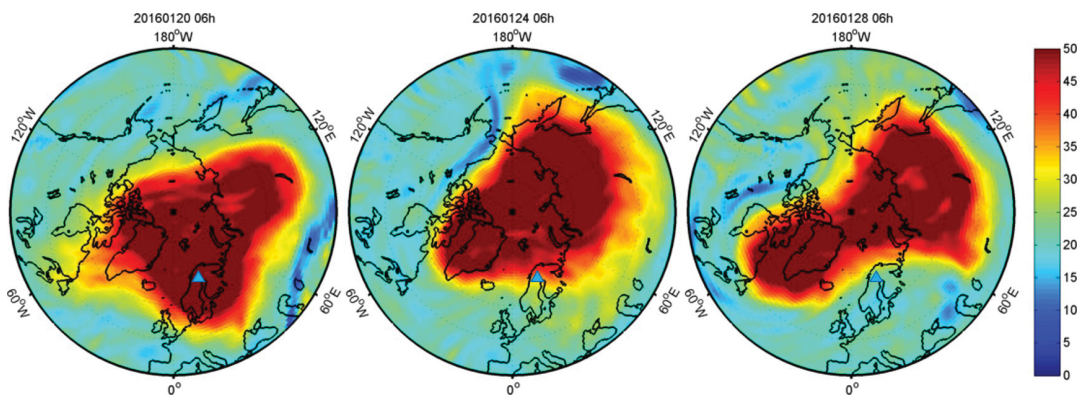


Figure 5.9: Potential vorticity maps over the northern hemisphere for three selected days of January 2016 (see Fig. 5.8). Colors indicate the potential vorticity on the 475K potential temperature level; the blue triangle is the location of the measurement site, Kiruna, Sweden.

morning indicating that the OCIO concentration in the western direction of Kiruna is higher than in the eastern direction. On 24th, the vortex edge is located above Kiruna, which results in much lower OCIO DSCDs than on 20 January. On the last day, 28th January, the smallest OCIO DSCDs are detected indicating almost no chlorine activation outside the polar vortex.

5.2.2 Time series of OCIO over Kiruna

In this section, the meteorological factors which influence the measured OCIO DSCDs are investigated in more detail. In order to explain the advantage of Kiruna as a good measurement site, the time series of the stratospheric temperatures in both the northern and southern hemisphere are illustrated in Fig.5.10. In this figure, it is clearly observed that the year-to-year variability of the stratospheric temperatures in the northern hemisphere is much larger than that in the southern hemisphere. Moreover, the temperatures during northern hemispheric winter are systematically higher than in the southern hemisphere. These differences can be explained by the different topographic conditions in both hemispheres: while in the northern hemisphere several mountain ridges in North-South direction exist, the Antarctica is surrounded by the open ocean. This causes a higher stability of the polar vortex in the southern hemisphere.

In addition, due to the higher surface elevation the temperatures in the southern hemisphere are smaller than in the northern hemisphere, which further leads to a higher stability of the polar vortex. Under these conditions, Kiruna is a good measurement site for observing both the day to day variability and the long-term temporal evolution of OCIO. Also the stratospheric temperatures differ largely from year to year which allows to investigate the temperature dependence of the OCIO DSCDs, and also their relation to other gases.

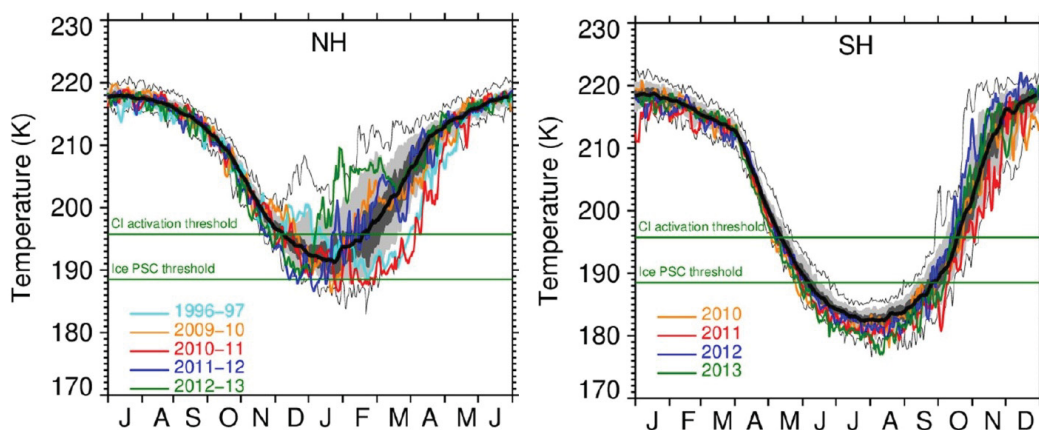


Figure 5.10: The annual cycle and variability of the minimum temperatures at 50 hPa in the northern hemisphere denoted by NH ($50^{\circ}\text{N} - 90^{\circ}\text{N}$, left) and the southern hemisphere denoted by SH ($50^{\circ}\text{S} - 90^{\circ}\text{S}$, right). The data sets are obtained from MERRA reanalysis data [Rienecker et al., 2011] (Figure adopted from WMO [2014] fig.3-1.). In both graphs, the temperatures of the different years are depicted in different colors. Upper and lower green horizontal lines represent thresholds for the chlorine activation and the formation of ice PSC, respectively.

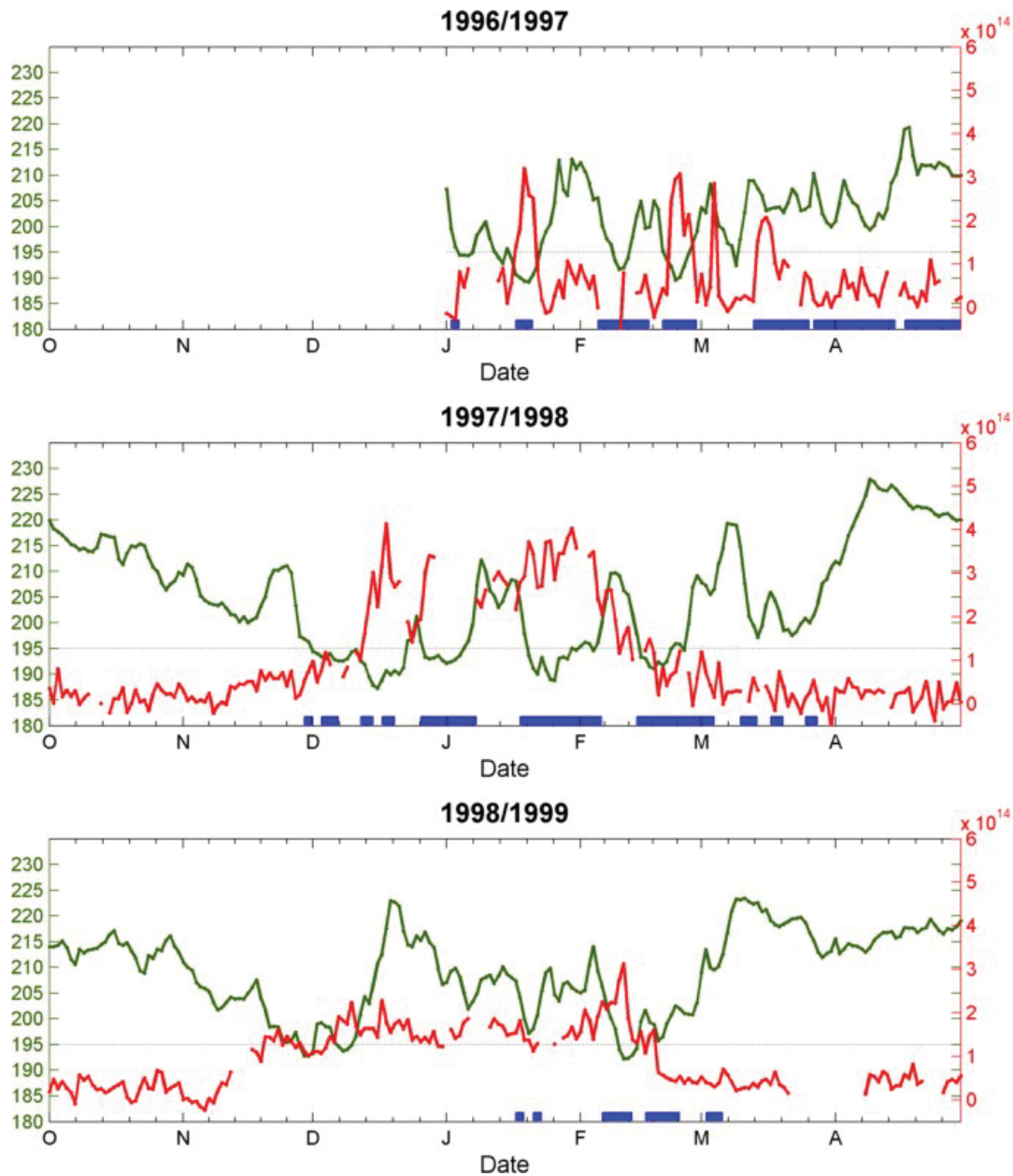


Figure 5.11: Time series of the OCIO DSCD (for SZA between 90.5° and 91.5°) over Kiruna (red line, right axis) as well as the stratospheric temperature at the 475K isosurface (green line, left axis) in 1996/1997 (top), 1997/1998 (middle), and 1998/1999 (bottom). Blue shaded areas at the bottom indicate periods with the potential vorticity above Kiruna larger than 35 PVU.

Figures 5.11–5.15 show time series of daily maximum OCIO DSCDs (for SZA between 90.5° and 91.5°) as well as daily minimum stratospheric temperatures at an isosurface of 475K above Kiruna (European Centre for Medium-Range Weather Forecasts:ECMWF, [Dee et al., 2011]). The dashed line indicates the threshold for PSCs formation and the blue square dots at the bottom indicate periods for which the potential vorticity above Kiruna was larger than 35 PVU. This value can be used as a rough threshold to decide whether Kiruna was in or outside the polar vortex.

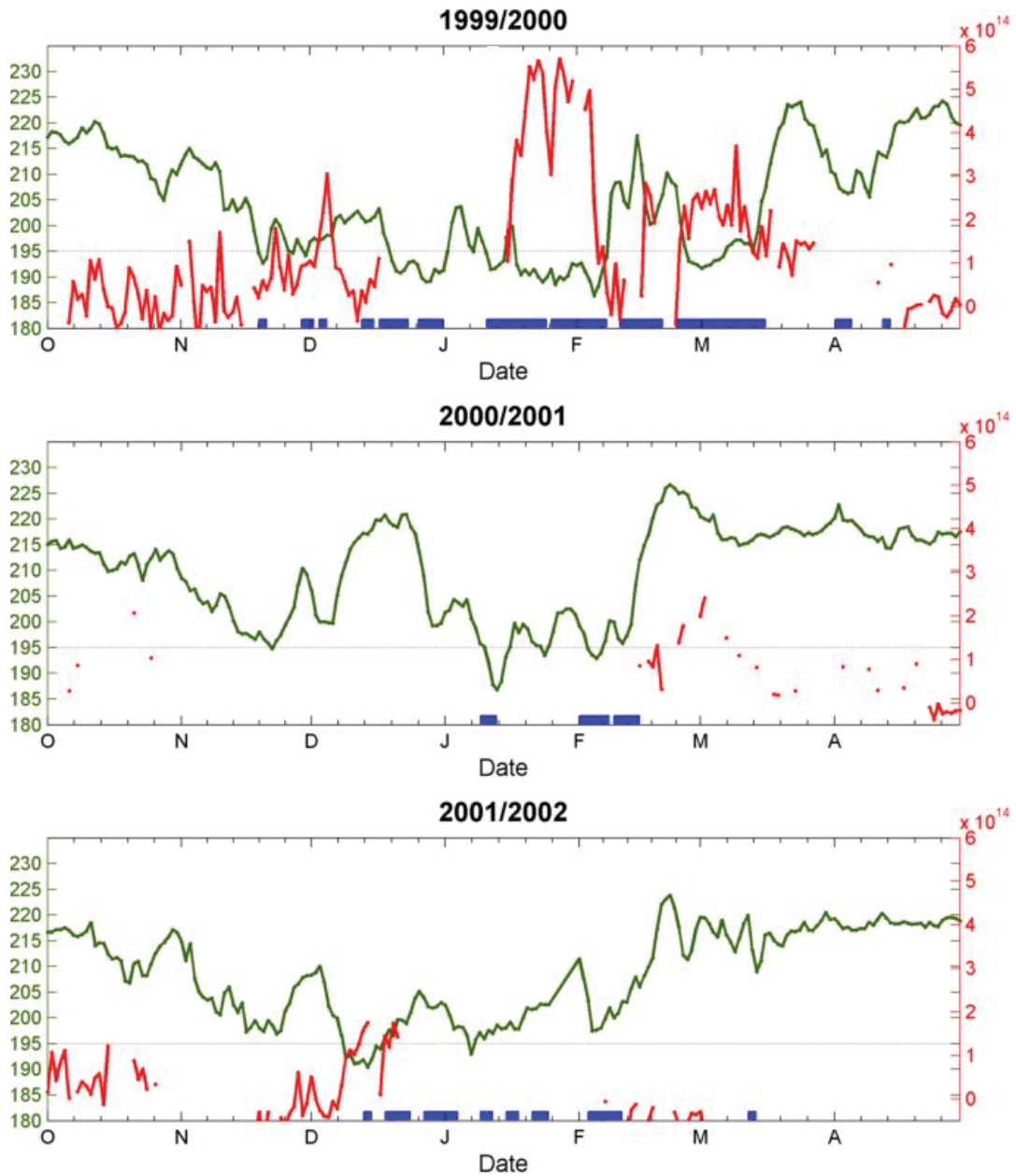


Figure 5.12: Time series of the OCIO DSCD (for SZA between 90.5° and 91.5°) over Kiruna (red line, right axis) as well as the stratospheric temperature at the 475K isosurface (green line, left axis) in 1999/2000 (top), 2000/2001 (middle), and 2001/2002 (bottom). Blue shaded areas at the bottom indicate periods with the potential vorticity above Kiruna larger than 35 PVU.

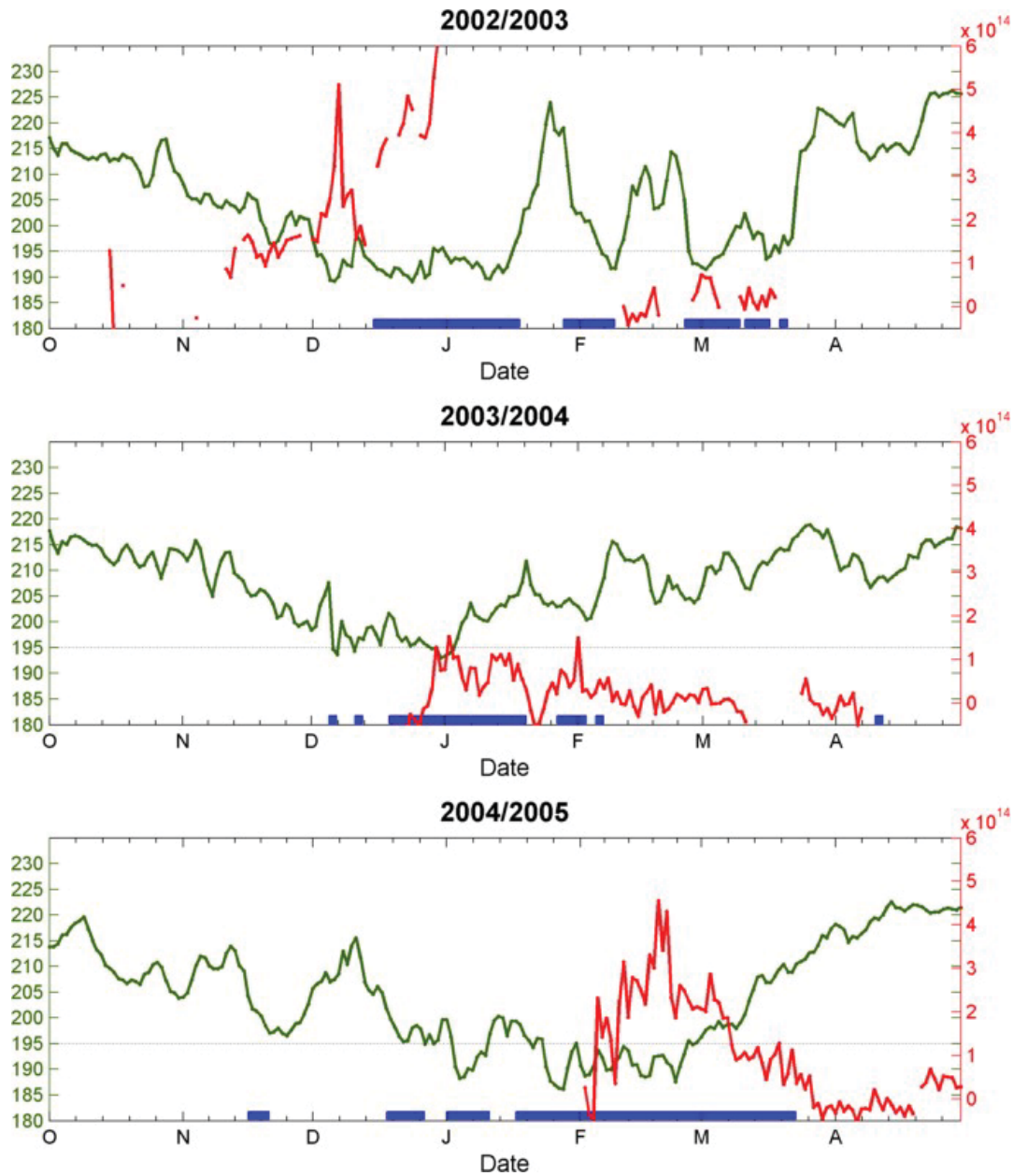


Figure 5.13: Time series of the OCIO DSCD (for SZA between 90.5° and 91.5°) over Kiruna (red line, right axis) as well as the stratospheric temperature at the 475K isosurface (green line, left axis) in 2002/2003 (top), 2003/2004 (middle), and 2004/2005 (bottom). Blue shaded areas at the bottom indicate periods with the potential vorticity above Kiruna larger than 35 PVU.

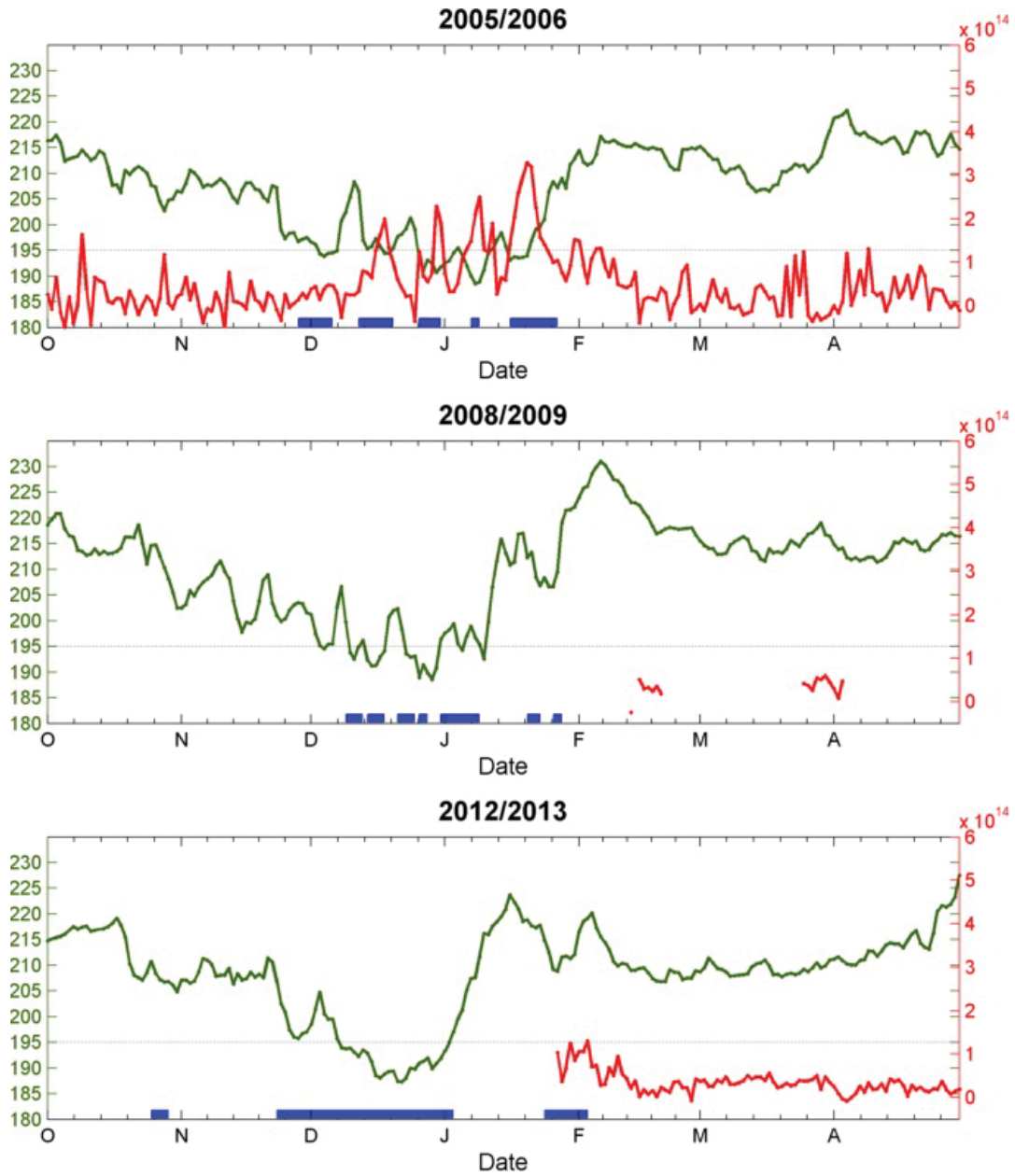


Figure 5.14: Time series of the OCIO DSCD (for SZA between 90.5° and 91.5°) over Kiruna (red line, right axis) as well as the stratospheric temperature at the 475K isosurface (green line, left axis) in 2005/2006 (top), 2008/2009 (middle), and 2012/2013 (bottom). Blue shaded areas at the bottom indicate periods with the potential vorticity above Kiruna larger than 35 PVU.

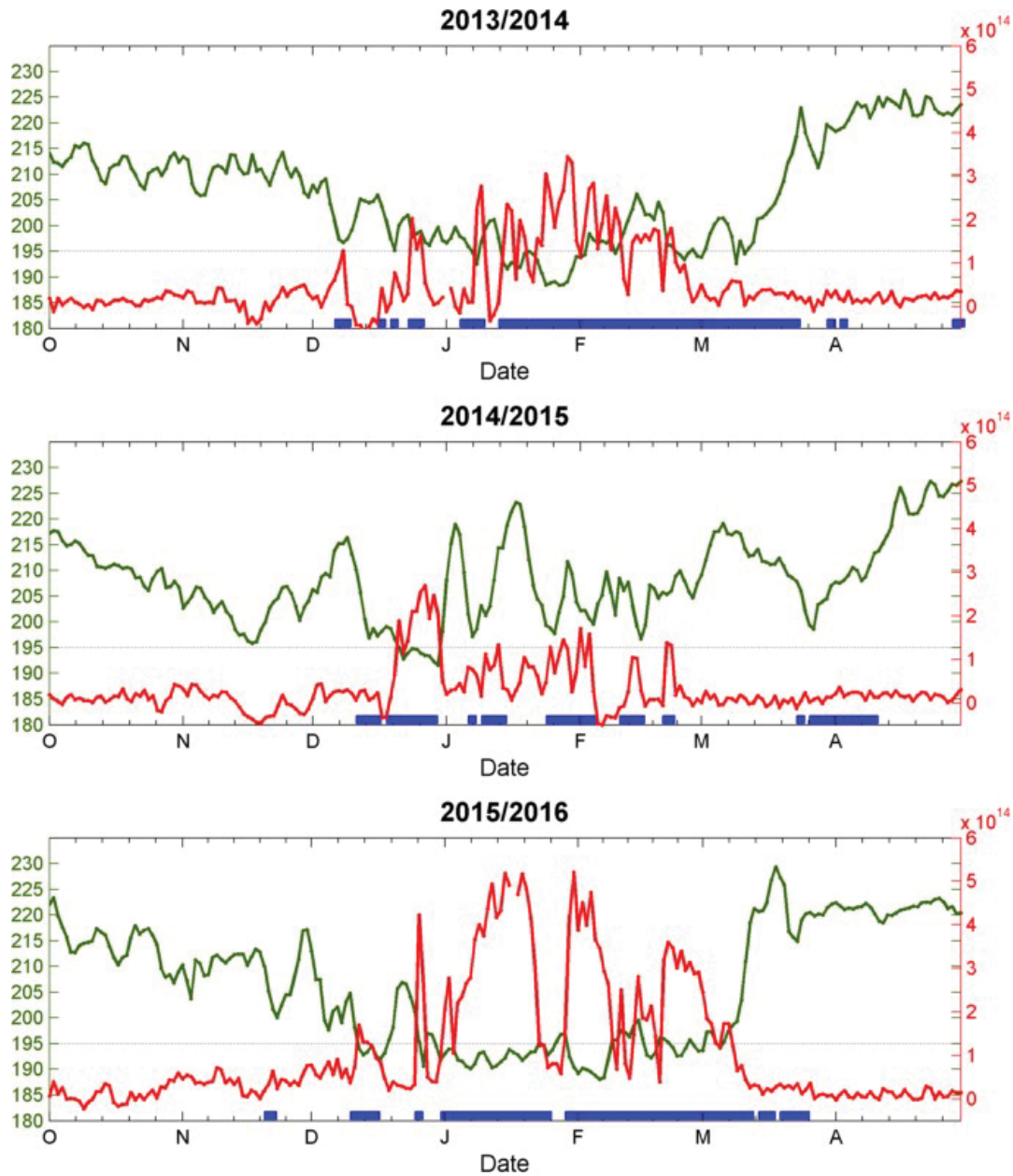


Figure 5.15: Time series of the OCIO DSCD (for SZA between 90.5° and 91.5°) over Kiruna (red line, right axis) as well as the stratospheric temperature at the 475K isosurface (green line, left axis) in 2013/2014 (top), 2014/2015 (middle), and 2015/2016 (bottom). Blue shaded areas at the bottom indicate periods with the potential vorticity above Kiruna larger than 35 PVU.

During the whole measurement period, four different characteristic meteorological conditions can be categorised:

- Long continuous cold winters: 97/98, 99/00, 04/05, 13/14 and 15/16,
- Enhanced OCIO during late period in spring: 96/97, 99/00, 00/01, 04/05, and 15/16,
- Warm winters: 98/99, 01/02 and 03/04,
- Half cold-half warm winters: 05/06, 08/09 and 12/13.

Long continuous cold winters occurred in 97/98, 99/00, 04/05, 13/14, and 15/16. In all of these winters, the stratospheric temperature dropped below 195K, which is the threshold temperature for the formation of PSCs. The cold temperatures held for around 2–3 months from December to March and the polar vortex was often located over Kiruna. These meteorological conditions are prerequisites for a strong chlorine activation, in agreement with the observation of large amounts of OCIO in these years.

The highest OCIO DSCDs are found in the cold winters 99/00 and 15/16. The temperature variation in these two years indicates long periods of temperatures below the PSC formation threshold in mid-winter. The cold temperatures extend into March, but are followed by a strong warming after which the OCIO DSCDs rapidly decrease. Although the results in late 2004 and early 2005 are missing due to technical problems of the instrument, strongly enhanced OCIO DSCDs are observed from February to the end of March in 2005. The enhancement of OCIO in 97/98 begins in mid-December which is earlier than in the other four winters mentioned above. The common feature of these five winters is that if Kiruna is out of the polar vortex, the amount of OCIO rapidly decreases, and *vice versa*. In the middle of the winter period, when Kiruna is inside the polar vortex, the OCIO amount is 8–10 times larger than when Kiruna is outside the polar vortex (OCIO varies from 0.5×10^{14} to 5.0×10^{14} molec/cm² in the 15/16 winter and from 0.6×10^{14} to 4.0×10^{14} molec/cm² in the 97/98 winter.)

The second category describes winters, in which enhanced OCIO DSCDs are observed until late spring. Such conditions occur in the five winters of 96/97, 99/00, 00/01, 04/05, and 15/16. In particular, the 99/00, 04/05, 15/16 winters show a much longer duration of chlorine activation than other years. While chlorine activation is often observed until early February, in these three years large OCIO DSCDs are found until March because the temperature stays below 195K and also the measurement site is inside the polar vortex. It is important to note that chlorine activation lasting until March seriously affects on the ozone concentration. This is because photochemical reactions of activated chlorine are catalysed by solar radiation after the end of the polar night leading to effective destruction of ozone. Especially, in the 99/00, 04/05, and 15/16 winters 4 – 5 times higher ozone destruction is observed compared to warm winter (ozone reduction (%): 23%, 23%, and 27%, respectively [Goutail et al., 2017]).

One more interesting finding in this category is that significantly enhanced OCIO DSCDs are found in late spring in the winters 96/97 and 00/01 in spite of high stratospheric temperatures. During that period in 00/01, the temperature is even around 215K above Kiruna, i.e. about 20K above the PSC threshold temperature. During that period OCIO DSCDs still reach values up to 2.6×10^{14} molec/cm². It is interesting that the 00/01 winter shows a distinguished weather condition in which the polar vortex already started to split in the middle of February and the temperature suddenly increased up to 225 K, which is about 30K above the threshold temperature for the formation of PSCs. Therefore, it was first suspected that while temperatures at the 475 K potential temperature level are high, low temperatures might still exist at other altitudes. To verify this hypothesis, a time series of

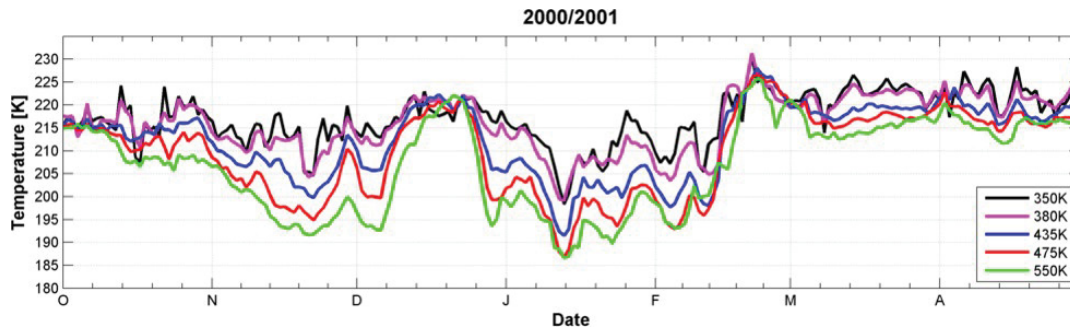


Figure 5.16: Time evolutions of the minimum temperature at different altitudes during the winter 2000/2001.[Harder et. al. 1999] Each color indicates different potential temperatures.

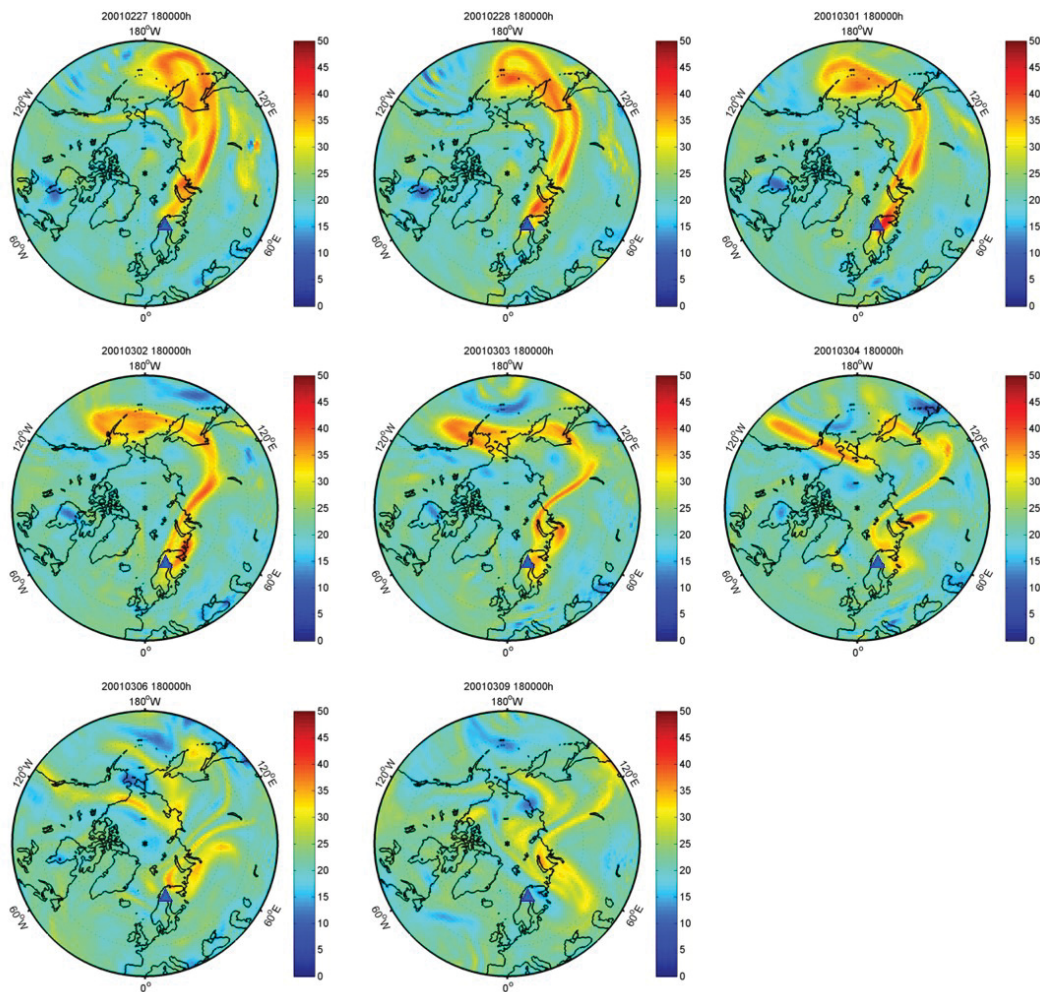


Figure 5.17: Polar vortex maps for selected days from February 27th (left, top) to March 9th (center, bottom), 2001. Colors indicate the potential vorticity at the 475K potential temperature level; the blue triangle is the location of the measurement site, Kiruna

the synoptic temperatures for the 00/01 winter at different potential temperature levels is shown in Fig. 5.16. From this figure, however, it can be concluded that a similar temperature increase happened at all altitudes. Thus the first hypothesis for the explanation of the enhanced OCIO DSCDs is not confirmed by this observations. Another possible explanation

for the observation is that in spite of enhanced temperatures, the deactivation of chlorine compounds does not occur directly after the evaporation of the PSCs, but is subject to some delay. This second hypothesis is tested by inspecting the evolution of the polar vortex. Figure 5.17 shows potential vorticity maps for different selected days from February 27th to March 9th, 2001. This figure shows that the polar vortex starts to split at the end of February, and parts of it remain as a tail shape. It is clearly observed that this tail passes over Kiruna on 6 days. Even though this vortex already gets weaker, it is probable that enhanced OCIO concentrations remained in the tail of the polar vortex and cause the relatively large amount of OCIO observed in the late spring. From Feb.28 to Mar.4, the enhanced OCIO absorption signature in measured spectra is clearly identified.

The third category describes the warm winters in 98/99, 03/04, and 01/02. Especially the temperature of the winter in 98/99 is record-breaking warm. Except for the short period in early December and mid February, the temperature is above 195K during most of the winter period, which results in the minimum OCIO DSCDs.

The last category describes winters which contain both cold and warm periods, which occur in 05/06, 08/09, and 12/13. These three years represent a 'Sudden Stratospheric Warming' (SSW). The temperature of one month, either in December, January, or February is very low (even below 195K), and after that period the temperature rapidly increases by about 30K. Unfortunately, a lot of data especially for the first half of 08/09 and 12/13 are lost due to technical problems of the instrument, but the temporal evolution of the OCIO DSCDs in such winters can be exemplarily explained by the results obtained in the winter 05/06, because the temperature variation in these years is very similar with each other. High variation of the temperature from late December to the beginning of January is often related to the fact that the position of the polar vortex over Kiruna rapidly changes. The results shown in the graph of the winter 05/06 indicate that the temperature rapidly increases during ten days from January 18th with decreasing OCIO amount while the polar vortex stays above Kiruna.

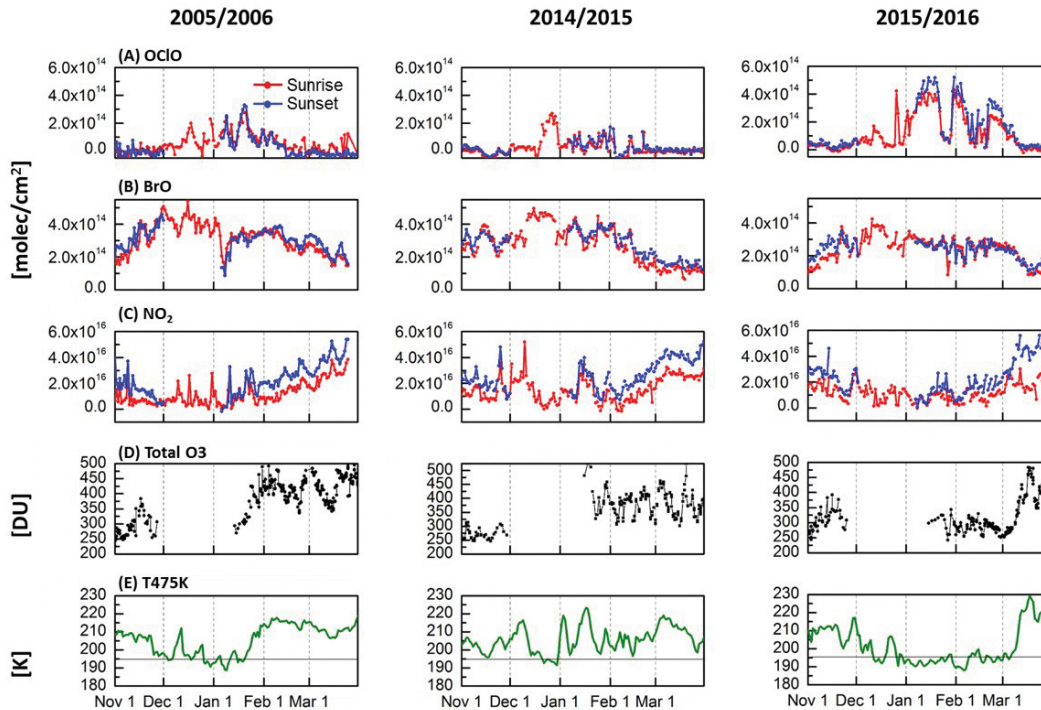


Figure 5.18: Time series of (A) OCIO, (B) BrO, (C) NO₂ DSCDs, (D) the total column O₃ from the OMI OMDOAO₃ v.1.2.3.1 product [Veefkind et al., 2006], and (E) the daily minimum temperature on the 475K level in two selected winters of 2005/2006, 2014/2015 and 2015/2016. In (A–C), red and blue lines represent the results measured during sunrise and sunset, respectively. In (E), the threshold temperature of PSC formation, 195K, is depicted by the black horizontal line.

5.2.3 Comparison of the time series of OCIO with the time series of NO₂, BrO, and O₃

The comparison of the temporal evolutions of different trace gases and the stratospheric temperature is helpful to gain insight into ozone chemistry in the stratosphere. In this section, therefore, OCIO, BrO, and NO₂ DSCDs retrieved from the zenith sky DOAS measurements for three selected winters, 05/06, 14/15 and 15/16 are presented and discussed. The 05/06 winter is a warm winter and experiences a sudden stratospheric warming (SSW), the 15/16 winter is one of the coldest winters during the whole measurement period and the 14/15 winter is the warmest winter with large fluctuations of the temperature. For the analysis of the BrO and NO₂ DSCDs, a fixed Fraunhofer reference spectrum is used for the analysis of the measurements from December to January; a daily reference spectrum at 80° of SZA is used for the remaining periods (see Sec. 5.1.2). Moreover, for the total column of O₃, the OMI OMDOAO₃ v.1.2.3.1 product is used [Veefkind et al., 2006], which is distributed freely by the Tropospheric Emission Monitoring Internet Service (TEMIS) via <http://www.temis.nl>. Figure 5.18 includes five panels: (A) OCIO DSCDs, (B) BrO DSCDs, (C) NO₂ DSCDs, (D) the total column of O₃, and (E) the 475K isosurface temperature. The first three panels (A–C) show the time evolution of the daily maximum amounts of each trace gas from November 1st to the end of March. In this figure, red and blue lines indicate the values observed in sunrise and sunset periods, respectively. From December to beginning of January, only an average value from sunrise and sunset is shown.

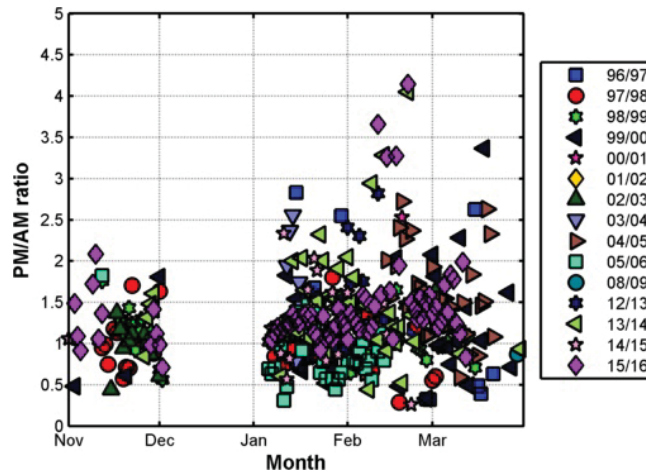


Figure 5.19: PM/AM ratio of the OCIO DSCDs (SZA $90.5^{\circ} - 91.5^{\circ}$) from 96/97 to 15/16 winters. The x -axis represents period from November to March of the next year.

The highest OCIO DSCDs are observed in the 15/16 winter, while only a very weak enhancement of the OCIO DSCDs is found in the 14/15 winter except for the second half of December (Fig.5.18 (A)). In 05/06, a slight OCIO enhancement is found before the sudden warming begins. In 15/16, enhanced OCIO DSCDs are found until the middle of March. Interestingly, in these periods the OCIO DSCDs during sunset are significantly larger than during sunrise. Sessler et al. [1995], Tørnkvist et al. [2002], and Otten et al. [1998] mentioned that the PM/AM ratio depends on the ClO_x concentrations. Figure 5.19 shows the ratio of the OCIO DSCDs measured in a.m and p.m from 96/97 to 15/16 winters to verify the asymmetry for other cold winters, where in general, a large variability of the ratio is observed. Especially, high values of the ratio are found for very cold winters e.g 99/00, 13/14, and 15/16 confirming the hypothesis of the studies mentioned before.

In the panel (E) of Fig.5.18, the time series of the total column of O_3 can be approximated as the amount of O_3 in the stratosphere because the stratospheric O_3 is known to be dominant in the total amount of O_3 . In this graph, the amounts of O_3 in three selected winters seem to be different with each other. In 05/06, strongly increased O_3 in the middle of January is observed, which is around 400 DU from February to March. In 14/15, the O_3 column is approximately constant around 350 DU except for November. During November, the low amount of O_3 around 230 DU is observed but it suddenly raises within one week from November 28th to December 6th. Compared to the preceding winter, the amount of O_3 is around 300 DU in the 15/16 winter. In the beginning of March it drops to approximately 240 DU and again strongly increases. Therefore, an obvious contrast is found in O_3 variations observed between cold and warm winters. Interestingly, there is a high correlation between the O_3 VCD and the stratospheric temperature indicating the strong influence of stratospheric dynamics (and tropopause height) on the altitude profile of O_3 .

The variation of NO_2 DSCDs is shown in Fig.5.18(C). Like O_3 , those are also highly correlated with the temperature for three winters. Under the polar vortex condition, NO_2 is converted into HNO_3 on PSC surfaces (denoxification). Therefore, when the temperature drops below 195K, the minimum NO_2 DSCDs are observed. In addition, also the stratospheric dynamics influence the vertical profile of NO_2 . For those years also a big discrepancy between sunrise and sunset (except during polar night) is observed indicating the effect of the N_2O_5 photolysis discussed in Chap. 3 (stratospheric NO_2).

During most periods in the 15/16 winter, the BrO DSCDs (Fig. 5.18(D)) are lower than in 05/06 and 14/15, especially during the periods with enhanced OCIO SCDs in the winter 2015/16. This finding is probably related to the consumption of BrO in the formation reaction for OCIO.

One more interesting finding in the result of the 15/16 winter is the anti-correlations between OCIO and O_3 , and BrO and O_3 at the end of the winter. It is clearly observed that OCIO and BrO start to decrease from the beginning of March, while the total column of O_3 rapidly increases in the same period. This finding is probably related to the mixing of air from inside and outside the polar vortex after the breakdown of the polar vortex.

5.2.4 *Comparison of the zenith sky DOAS OCIO results with simultaneous measurements of the GOME-2 satellite instrument*

One of the advantages of satellite observation is that they monitor simultaneously the temporal and spatial evolution of chlorine activation in both hemispheres. However, usually the satellite observations have a limited temporal coverage with typically one observation per day at a given location. In recent years, several groups have analysed OCIO SCDs from observations of difference space borne instruments, including GOME-1, SCIAMACHY, OSIRIS, and GOMOS [Wagner et al., 2001; Richter et al., 2005; Köhl et al., 2006; Oetjen et al., 2011]. In 2007, the GOME-2 instrument on board the MetOp satellite has started its observations. Usually the signal to noise ratio of satellite observations is much lower compared to ground based observations due to the rather short integration times of satellite observations. Thus OCIO SCDs obtained from satellite have to be validated by comparison with OCIO SCDs measured simultaneously from ground-based instruments.

The validation of stratospheric OCIO products at high latitude during winter is a very challenging task because not only the daily maximum elevation of the sun is quite low leading to large uncertainties, but also the photochemical destruction of OCIO at high SZA is very fast.

The instrument in Kiruna is involved in NDACC (Network for the Detection of Atmospheric Composition Change, not yet fully certified), which includes several remote sensing stations. The purpose of this network is to monitor the long term changes of stratospheric trace gas concentrations and their influence on the ozone layer, to detect trends in the overall atmospheric composition, and to understand their impacts on the stratosphere and troposphere. Besides these applications, our data are also useful to validate satellite observations. In this section, GOME-2 A and B satellite data products are compared with the zenith sky DOAS products. The GOME-2 A and B OCIO products are provided from BIRA and these results contribute to O₃SAF project.

In this section different analysis settings compared to those used in the previous sections are used. The settings are chosen in order to be as similar as possible to the analysis settings of the GOME-2A (launched on 2007) and GOME-2B (on 2012) instruments. In the previous sections we explained that for the OCIO analysis, two Fraunhofer reference settings are used. One of them is a fixed reference spectrum taken in October or March which is not affected by OCIO around a SZA of 80° for the measurements during the polar night period, while for the rest of the period daily reference spectra are used. However, for the validation exercise described in this section, a single Fraunhofer reference spectrum recorded at minimum SZA conditions on those days outside of the polar vortex is chosen. The results obtained

from narrow and wide fit window give in general similar results, but in October of 2015, a discrepancy was observed. The reason for the discrepancies are not fully understood at the moment, but in other years no similar discrepancies were found. We applied the modified fit setting only to the data obtained after 2013, when the new detector was installed because the measurements using the old detector were systematically affected by the rapid change of Etalon effect. The table 5.2 shows the summarised analysis setting.

Along the validation procedure of the GOME-2 instrument, there is a further step needed to ensure that the same air masses are measured by both instruments, ground-based DOAS and GOME-2. Here, in order to find the coincidence events, several criteria are used. An individual measurement of GOME-2 has a very short exposure time, therefore the measured data from the GOME-2 instrument over a 200 km radius around Kiruna are extracted and data measured with SZA between 85° and 95° are averaged to improve the signal to noise ratio. It is assumed that the OCIO SCDs measured by the satellite in nadir mode and those from the ground-based zenith sky light path are comparable at large SZA. In this section OCIO SCDs from both platforms are compared (instead of VCDs), because the OCIO photolysis at large SZA occurs rapidly, and under these conditions the calculation of an AMF is subject to very large uncertainties. [Richter et al., 2005; Oetjen et al., 2011].

Figure 5.21 shows time series of daily OCIO SCDs from GOME-2A (left) and GOME-2B (right) compared with those from ground-based DOAS (black). The satellite and ground based data sets show a consistent behavior of the day-to-day variability of OCIO. Figure 5.22

Table 5.2: Comparison of the OCIO analysis settings used in the previous subchapters and in the validation study of the satellite data in current subsection.

	Previous section sec.5.1	Current section (for validation)
Window	372-392	347.7-390
Polynomial	5	5
OCIO	Kromminga et al. [2003], 213K	Kromminga et al. [2003], 213K
O ₃	Bogumil et al. [2003], 223K	Bogumil et al. [2003], 223K, 243K
O ₄	Thalman and Volkamer [2013], 273K	Thalman and Volkamer [2013], 273K
NO ₂	Vandaele et al. [1998], 220K	Vandaele et al. [1998] 220K
Ring	Kraus [2006]; Wagner et al. [2009]	Kraus [2006]; Wagner et al. [2009]
Ring· λ^4		
BrO	-	Wilmouth et al. [1999] 228K
Fraunhofer reference spectrum	Fixed and daily refer- ence spectra used de- pending on the different time periods	Using a single reference spectrum taken at inter- mediate solar elevation outside of the activated periods

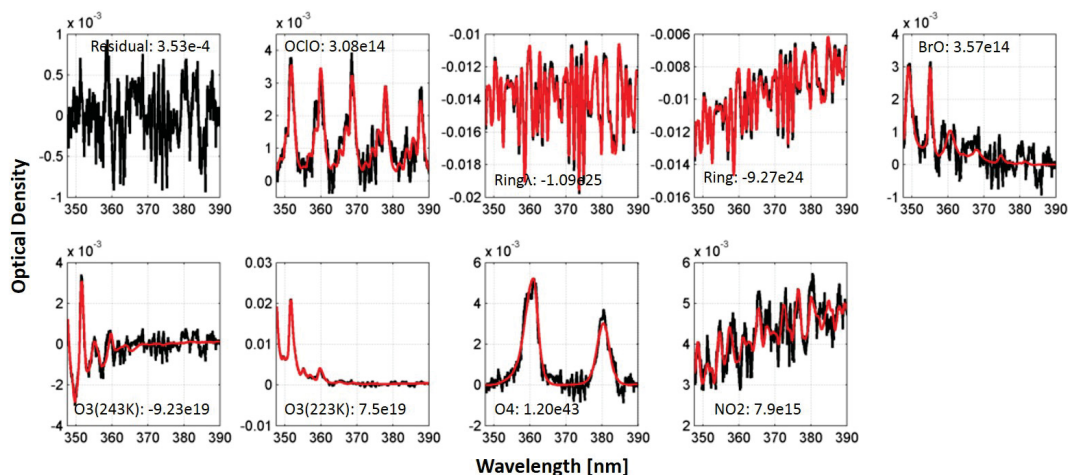


Figure 5.20: Example of the OCIO analysis of a spectrum measured on 2016 Jan. 10, 09:14 UTC (SZA at 91.42°). The red lines indicate the trace gas cross sections scaled to the respective absorptions in the measured spectrum (black lines).

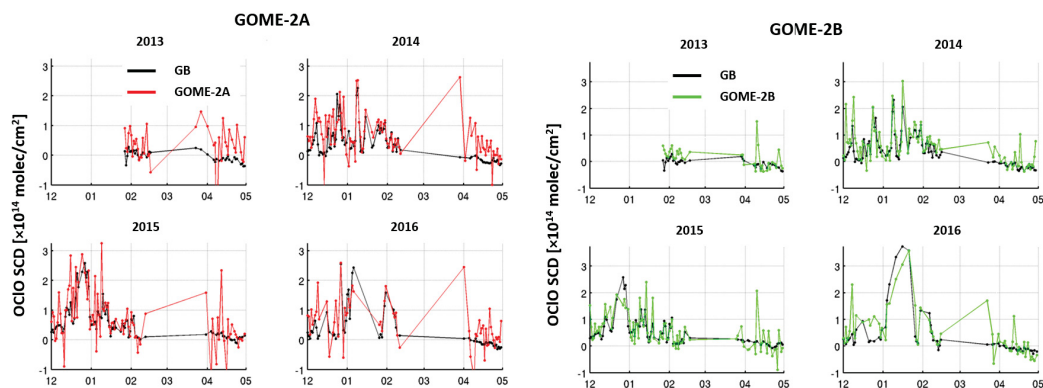


Figure 5.21: Comparison of daily OCIO SCD measured over Kiruna by GOME-2A/B (GDP-4.8) and the ground based measurements (GB). The x -axis represents the period from November to March of the next year. Here, red and green lines indicate GOME-2A and GOME-2B results, respectively. Each panel indicates different years. *Data and figure obtained from Pinardi et al. [2017], SAF/O₃M/IASB/VR/OCIO/TN-IASB-GOME2-O₃MSAF-OCIO-2017 Validation Report pp.14 – 15.)*

shows similar results. In the upper panel time series of daily average of GOME-2A (red), GOME-2B (green) and ground-based zenith sky DOAS (black) measurements are presented. Here, the error bars of GOME2 are calculated from the 1σ range of all daily data included in one month. In the lower panel of Fig. 5.22 scatterplots of the monthly and daily mean values of OCIO are shown. The time series of monthly mean OCIO SCD indicate that satellite and ground based data agree well, both with respect to the seasonal and inter-annual variability. Both data sets well capture periods of enhanced OCIO SCDs in 2013/14, 2014/15, and 2015/16. The correlation between satellite data and DOAS data is quite high for both satellite products, with R values from 0.62 to 0.77. For the comparison of monthly means, the correlation coefficients reach even 0.9. The slopes of the daily comparisons range from 0.83 to 0.86 indicating a slight underestimation of the OCIO SCDs by the satellite observations.

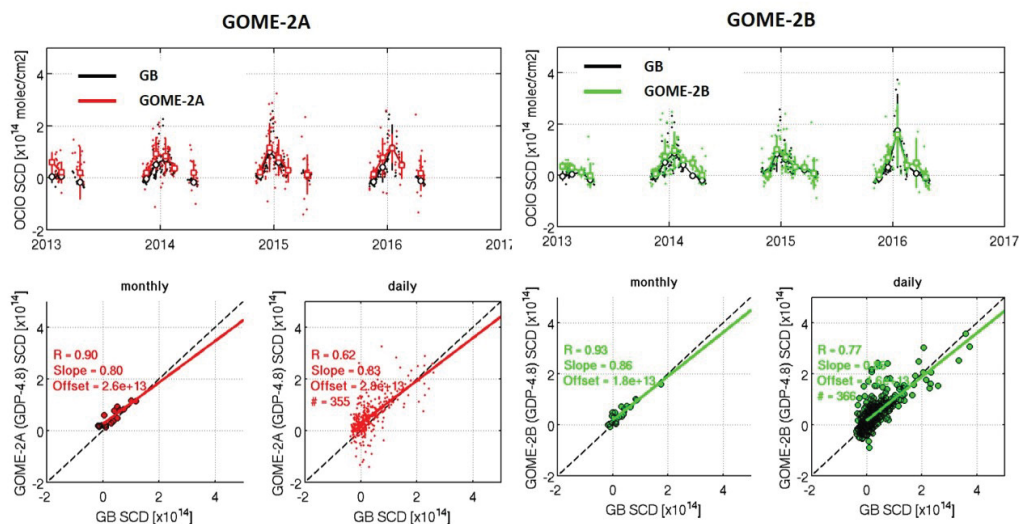


Figure 5.22: Comparison of OCIO SCDs obtained from Zenith Sky DOAS and satellite observations. Red and green lines indicate GOME-2A and GOME-2B results, respectively. Time series of daily average of Zenith Sky DOAS (GB) and satellite observation are shown in the upper panel. In the lower panel scatter plots of monthly and daily results are presented. *Data and figure from Pinardi et al. [2017], SAF/O₃M/IASB/VR/OCIO/TN-IASB-GOME2-O₃MSAF-OCIO-2017 Validation Report pp.14 – 15.*

This underestimation might be related to the effect of aerosols on the atmospheric light paths, which is slightly different for ground based and satellite observations.

5.3 SUMMARY OF THE GROUND-BASED OCLO MEASUREMENTS

In this chapter, the long-term time series of OCIO DSCDs above Kiruna, Sweden which is located inside the Arctic Circle, are investigated by using ground-based zenith sky DOAS measurements. Since these measurements are performed at a fixed site, the relative position of the polar vortex has to be considered for their interpretation. Here, long-term data obtained during about 15 years (1997 – 2016 except 2007, 2008, 2010, and 2011) allows to classify the dependence of the OCIO amount on various meteorological conditions. The following general points summarise the main findings derived from the OCIO data set:

- Measured data are categorised depending on the meteorological conditions such as a long continuous cold winter, enhanced OCIO lasting until late spring, warm winter, and a sudden temperature increases in the middle of the winter. The strong temperature dependence of the measured OCIO DSCDs is confirmed by comparison to the minimum temperatures on the 475K level.
- Three extreme winters with either high or low stratospheric temperatures or winters with a sudden stratospheric warming are chosen to study the relation of the OCIO results with temperature and other trace gases. As mentioned above, a significant anti-correlation of the OCIO DSCDs with temperature is observed as expected from the dependence of the PSC formation on temperature. Highest OCIO DSCDs are also observed when the NO₂ DSCDs are smallest. Interestingly it is found that the BrO DSCDs are decreased during periods of strongly enhanced OCIO DSCDs. This finding

indicates that part of the BrO is consumed during the formation reaction of OCIO. An anti-correlation of O₃ and OCIO (and also BrO) is detected at the end of the winter indicating the effective mixing of air masses after the end of the polar vortex.

- The OCIO SCDs obtained from ground-based zenith DOAS are compared to GOME-2 satellite observations. This comparison focuses only on the late winter periods, from January to March, for which usually the strongest chlorine activation occurs. Time series of daily and monthly mean OCIO SCDs show that GOME-2 and ground-based zenith DOAS observations agree well. Correlation coefficients, R , for monthly averages of OCIO SCDs derived from ground-based and GOME-2 observation are about 0.9 for GOME-2A and 0.92 for GOME-2B. However, the satellite observations show slightly smaller OCIO SCDs than the ground-based observations.

Part III

RESULTS: TROPOSPHERIC TRACE GAS

VOLCANIC TRACE GASES

One of the advantages of a long-term stationary measurement is the possibility of detecting rare events including the plumes of an occasional volcanic eruption. Although a stationary measurement is spatially much more restricted than satellite observations, such measurements could provide better temporal coverage and resolution, and the detected trace gas plumes can often be directly interpreted [Carn and Lopez, 2011].

In this chapter the volcanic plume which erupted from Iceland (from the end of August 2014 to February 2015) spreading across the Norwegian Sea and the northern part of Europe is analysed. In particular it could be shown that enhanced SO_2 signals observed after the eruption at Kiruna are caused by the volcanic eruption. Moreover, an enhancement of BrO higher than the stratospheric background is observed in this period.

Volcanic eruptions are one of the largest SO_2 sources in the atmosphere and can play a very important role in air pollution and climate. For example, SO_2 is oxidised to produce sulphate aerosols which destroy ozone in the stratosphere. Such aerosols can also act as a cloud nucleus and thus influencing the radiative budget on the earth surface. In recent years large efforts have been made to monitor volcanic emissions including the Network for Observation of Volcanic and Atmospheric Change (NOVAC) [Galle et al., 2010] which is composed of more than 80 ground-based DOAS instruments at about 30 volcanoes. More recently, SO_2 from volcanic eruptions and degassing is also monitored using satellite observations. For example, SACS (Support to Aviation Control Service) has offered a near-real-time satellite monitoring of volcanic plumes of SO_2 and ash [Brenot et al., 2014].

The Bárðarbunga volcano had been active from the end of August 2014 to February 2015. It was the strongest eruption in Iceland for more than the last 200 years. The activity comprises lava eruptions without a significant amount of volcanic ash, but there has been continuous SO_2 emissions. The volcano emitted 35,000 tons of SO_2 during the last month of the eruption, which is two times larger than the whole amount of the SO_2 emission from the industry in Europe [Witze, 2014]. And Schmidt et al. [2015] showed that the SO_2 emitting altitude was in the middle troposphere around 4 – 5 km using retrievals from the Ozone Monitoring Instrument (OMI) and the Infrared Atmospheric Sounding Interferometer (IASI). It was also shown that volcanic SO_2 was transported over long distances despite the rather low altitude of the volcanic plume. Figure 6.1 shows SO_2 vertical column densities as seen from GOME-2 measurements offered from SACS.

This chapter describes ground based measurements of enhanced SO_2 and BrO related to the volcanic eruption. First the analysis settings for the retrieval of tropospheric volcanic SO_2 and BrO are presented. Then observations of enhanced SO_2 originated from the volcanic plume are interpreted using satellite images. In addition, a sensitivity study on the effect of the sky condition is presented.

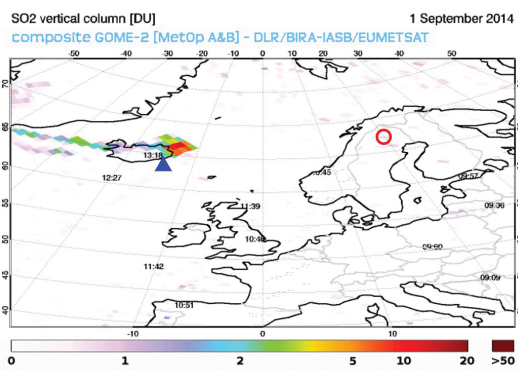


Figure 6.1: SO_2 vertical column densities derived from GOME-2 measurements in September 1, 2014. In the map, a blue-triangle and a red dot indicate the locations of the Bárðarbunga volcanic system and the Kiruna measurement site, respectively. The map is obtained freely from the SACS website. (<http://sacs.aeronomie.be>).

6.1 ANALYSIS

In this section, the determination of analysis settings for volcanic SO_2 and BrO are described in detail. For the analysis the spectral ranges of 315 – 325 nm and 336 – 360 nm are chosen. Further details of the DOAS analysis are summarised in Tab.6.1. Here, a fixed reference spectrum taken at noon on Sep. 01.2014 is used for the whole measurement period. As shown in Fig. 6.1 no enhancement of SO_2 above the measurement site is detected on that day.

Table 6.1: Specification for the ground-based zenith sky DOAS spectrum evaluation settings for SO_2 and BrO.

Gas	Fit range	Fitted Spectra	Reference
SO_2	315–325	SO_2	Bogumil et al. [2003] 273K
		O_3	Bogumil et al. [2003] 223K and 243K
		Ring	Kraus [2006]; Wagner et al. [2009]
		Polynomial order	3rd
BrO	336–360	BrO	Wilmouth et al. [1999] 228K
		SO_2	Bogumil et al. [2003] 273K
		O_3	Bogumil et al. [2003] 223K and 243K
		Ring	Kraus [2006]; Wagner et al. [2009]
		O_4	Thalman and Volkamer [2013] 293K
		NO_2	Vandaele et al. [1998] 294K
Polynomial order	4th		

Background correction

In this study, for the retrieval of SO_2 the wavelength range 315 – 325 nm is used in which not only SO_2 absorptions occur but also strong O_3 absorptions. As was shown in many other studies an interference of O_3 and SO_2 absorptions can take place, especially at high

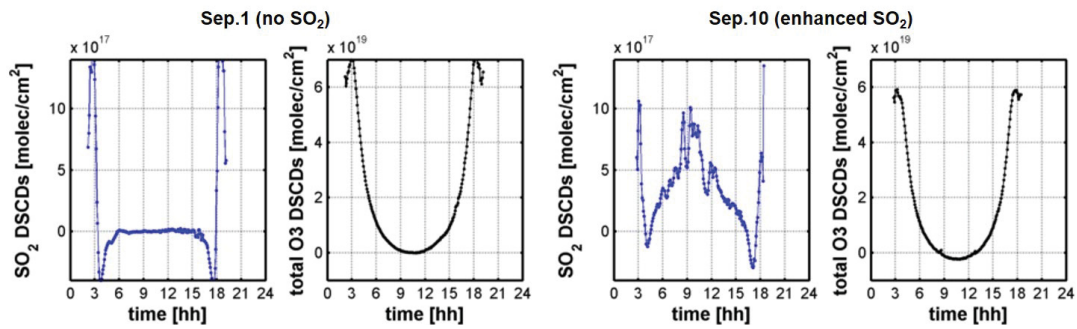


Figure 6.2: DSCDs of SO_2 and O_3 obtained from ground-based zenith sky DOAS measurements. The two left figures represent results for a day without a volcanic plume above Kiruna (Sep.1) and the two right figures for a day with the volcanic plume above Kiruna (Sep. 10).

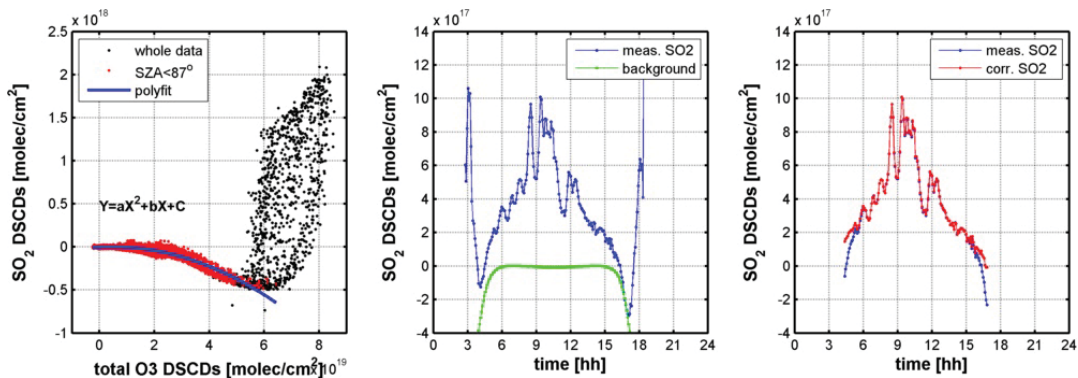


Figure 6.3: Scheme of the SO_2 background correction. Left: the black dots represent the measured SO_2 dSCDs on the day without enhanced SO_2 , the red dots indicate the data points below $\text{SA} < 87^\circ$, which are used for the polynomial fit (solid blue curve). Middle: blue line indicates the SO_2 DSCD retrieved from the DOAS fit on Sep.10, the green line represents the background amount calculated from the polynomial fit. Right: blue and red lines represent the measured and corrected SO_2 dSCDs, respectively.

SA. Due to this interference, the SO_2 results at high SA have to be interpreted with care. Figure 6.2 shows the diurnal variation of the DSCDs of SO_2 and O_3 on a day without the volcanic plume above Kiruna (Sep.01.2014) and on a day with the volcanic plume above Kiruna (Sep.10.2014). On both days ‘unrealistic’ SO_2 DSCDs at high SA are found. With increasing SA, first negative SO_2 DSCDs are found, and for higher SA strongly positive SO_2 DSCDs are found (see also Fig. 6.3). Based on these findings, this study applies a simple background correction, which is described in Fig. 6.3. The first step of the correction procedure is the quantification of the interference between SO_2 and O_3 . For that purpose, one can relate the SO_2 DSCDs with the O_3 DSCDs for a day without the volcanic plume above Kiruna (without SO_2 enhancement). Data points for SA above 87° are skipped and a polynomial fit is carried out to the remaining data (left in Fig. 6.3). It should be noted here that measurements for SA $> 87^\circ$ are skipped, because the rather high values of the ‘artificial’ SO_2 , for which a meaningful correction is impossible. The ‘artificial’ SO_2 values (green lines in the middle of Fig. 6.3) are obtained using the polynomial fit parameters. Finally the background values obtained by the polynomial are subtracted from the SO_2 dSCDs retrieved from the DOAS fit (right in Fig.6.3).

To convert the measured SO₂ and BrO SCDs to the vertical column densities (VCDs), an air mass factor (AMF) which is defined as the ratio of the SCD to the VCD is needed. However, calculating the SO₂ AMF is not straightforward because the SO₂ AMF strongly depends on the SO₂ vertical distribution, which is largely unknown. It also depends on the surface albedo, clouds and aerosol loading. Moreover, for the case of BrO, the calculation of AMFs is further complicated by the fact that the BrO concentration is rapidly changing due to photochemical reactions. As a result, this study focuses on retrieving only SO₂ and BrO SCDs. While this complicates the quantitative interpretation of the results, it still allows to study the basic effect of the volcanic emissions at the measurement site of the instrument.

6.2 RESULTS

Since Aug. 31, 2014 there has been a continuous effusive eruption without an explosive activity from the Bárðharbunga volcano. Figure A.18 in Appendix shows time series of corrected SO₂ DSCDs from Sep.1 to Oct.4, 2014, which can be directly compared to the satellite SO₂ images. The reason of the selection of that period is that from late autumn to early spring the observation geometry of the satellite and ground-based measurements are extreme at high latitudes (high SZA), which strongly affects the data quality. Therefore, this study focuses on eight days when strong SO₂ enhancements are observed as well as a BrO enhancement.

6.2.1 Enhanced SO₂ during the volcanic episode

Figure 6.4 shows the time series of SO₂ VCDs derived from GOME-2 observations during the selected days after the volcanic eruptions (1st and 2nd columns), and MODIS RGB images for the corresponding days. From the MODIS observations information on the sky conditions, especially the cloud cover, can be derived. As already shown above, after the satellite first detects an enhanced SO₂ signal on Sep.1, the SO₂ plume moves towards Scandinavia. According to the ground-based observations, the plume starts to be detected on Sep.5 in Fig.6.5, and further SO₂ enhancements are observed on Sep.6 and 8. After that, a high SO₂ enhancement is observed on Sep. 10, which is consistent with the volcanic plume passing over the Scandinavia peninsula in Fig. 6.4. Further enhancements are observed on 21, 27 and 29 of September. Figure 6.5 shows DSCDs of SO₂ and BrO on selected days observed from ground-based zenith sky DOAS. Especially, on Sep.11, 26, 27, and 29, BrO is enhanced above the stratospheric background during some periods (marked by the red-shading).

Interestingly, both the satellite and the ground-based observations simultaneously detect SO₂ above Kiruna only on Sep. 6, 10, 27, and 29. From the MODIS RGB images, those days are also mostly cloudy. Therefore, it is concluded that the volcanic plumes on these days is very probably located above the clouds. The comparison between both data sets indicates important advantages of ground based observations: they provide continuous time series, and can also detect volcanic plumes on days, which show no enhancement in the satellite observations.

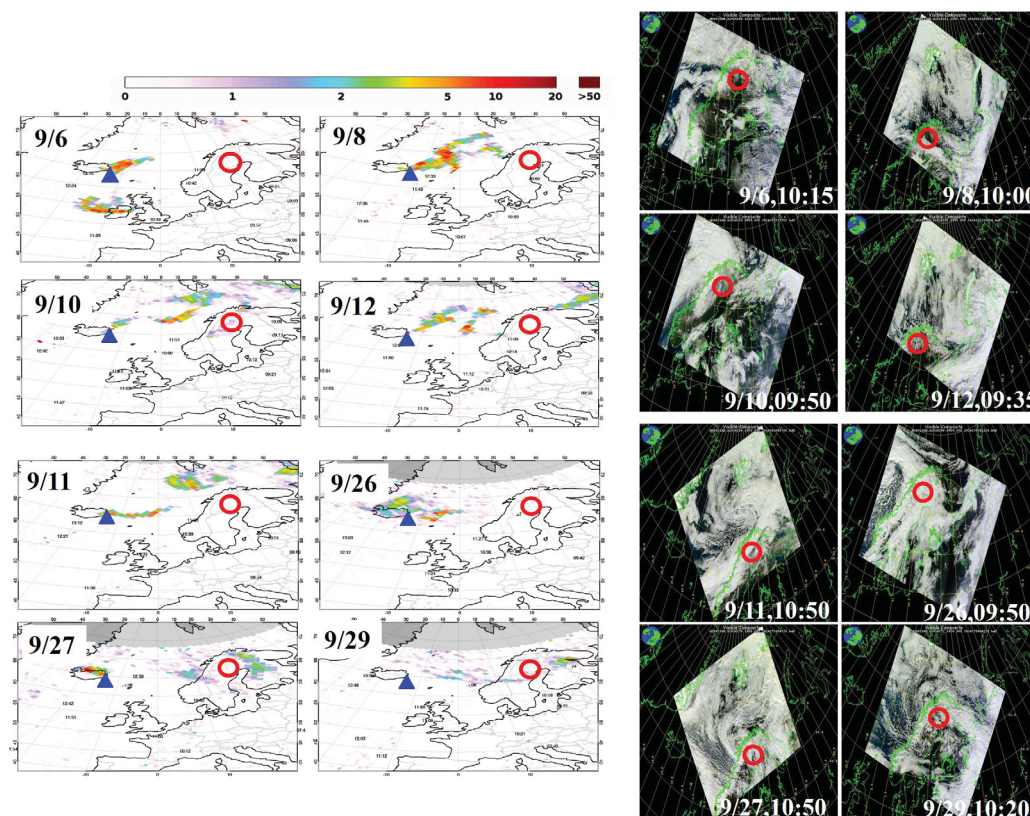


Figure 6.4: SO₂ vertical column density (values are given in DU) derived from GOME-2 on MetOp A & B (1st and 2nd columns) for the selected eight days during the fissure eruption. Here, the blue triangles and red dots indicate the volcano and the ground-based measurement site, respectively. The 3rd and 4th columns show MODIS RGB images of the same days, where the red dot indicates Kiruna.

6.2.2 Enhanced BrO correlation with sky condition

As already mentioned above, also the BrO DSCDs (Fig.6.5) are enhanced above the stratospheric background on some of the selected days. The patterns of BrO enhancements can be classified into two categories. The first is that BrO DSCDs and the SO₂ SCDs are simultaneously enhanced (e.g. Sep.27 and 29), and the second category contains days on which only enhanced BrO signals are showing up (e.g. Sep.11 and 26). The enhanced BrO might be either directly contained in the volcanic plume or caused by a small and possibly uniform tropospheric background BrO which is strongly enhanced by multiple scattering. Because a slant column density of a trace gas is determined by the light path through the atmosphere as mentioned in Frieß et al. [2004], multiple scattering on cloud particles could strongly enhance the atmospheric light path and thus the observed dSCDs. Most of the days with BrO enhancements are cloudy days. (See Fig. 6.4 with MODIS RGB images and Tab. 6.2 about the cloud classification results using the scheme described in Sec.3.2.3).

Figure 6.6 shows the diurnal variations of BrO DSCDs, cloud classification results, O₄ DSCDs, Ring effect, normalised intensity (at 350 nm), and colour index (330/390 nm) derived from the spectral analysis for the four selected days with enhanced BrO. From this figure the relation between the cloud conditions and the BrO can be investigated. Here, the color index (CI) is used to identify clear and cloudy sky conditions. Rayleigh scattering increases

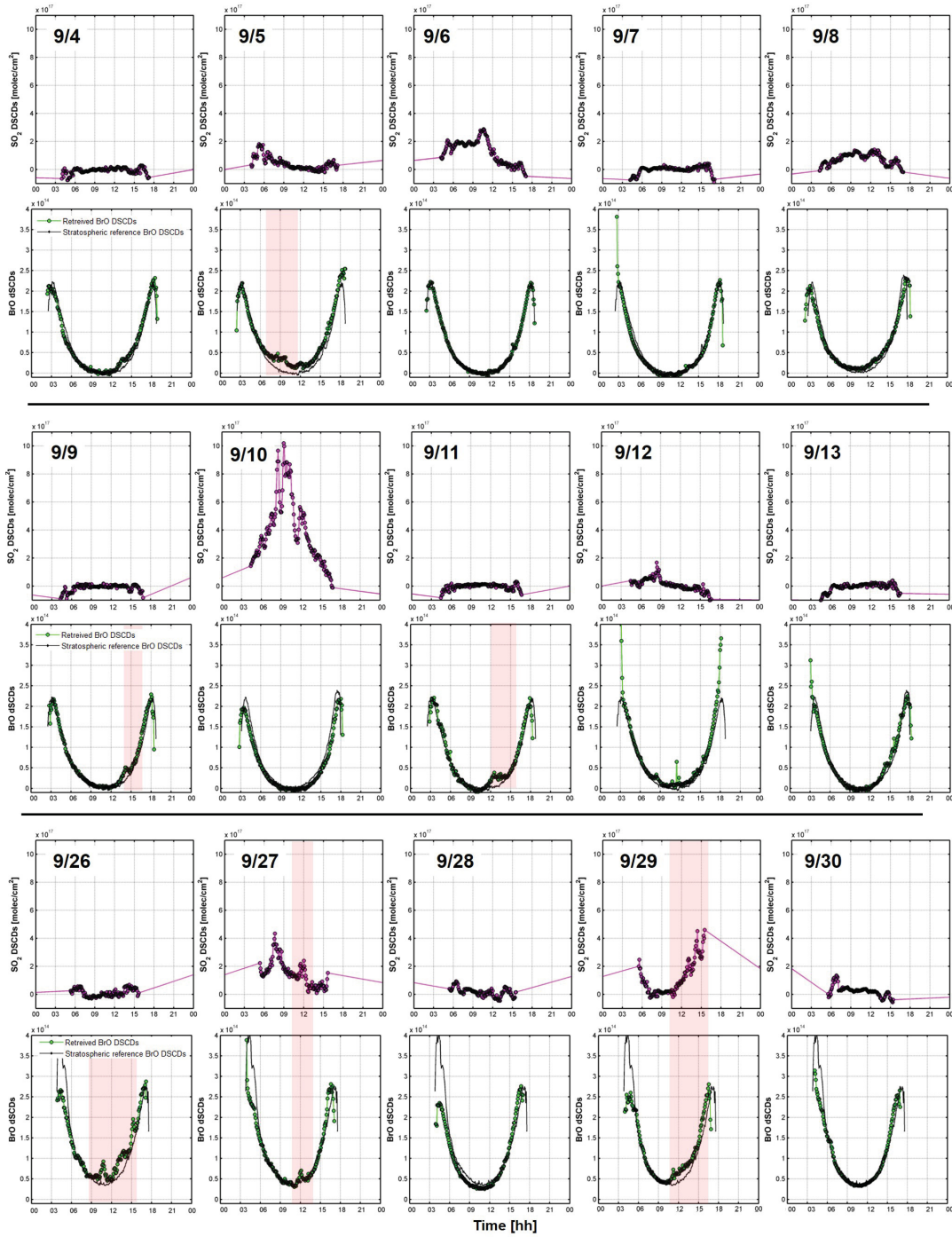


Figure 6.5: SO₂ (odd number rows) and BrO (even number rows) dSCDs from Sep.4 to Sep.30 measured from ground-based zenith sky DOAS. The period 14 to 25 September, for while no SO₂ enhancement was found is excluded. In the figure, the red-shaded area indicates the period of enhanced BrO which has the value above the stratospheric background.

towards the UV spectral range while scattering on cloud particles is roughly independent of wavelength. To verify that the BrO signal is larger than the stratospheric background amount, the typical stratospheric BrO DSCDs are indicated by a black line as a reference in the 1st row of Fig.6.6. This reference value is determined from the BrO DSCDs measured during clear sky conditions within 10 days. In the 3rd row, O₄ is analysed for three different wavelength ranges e.g 350 – 370 nm, 335 – 385 nm, and 336 – 360 nm to verify that the

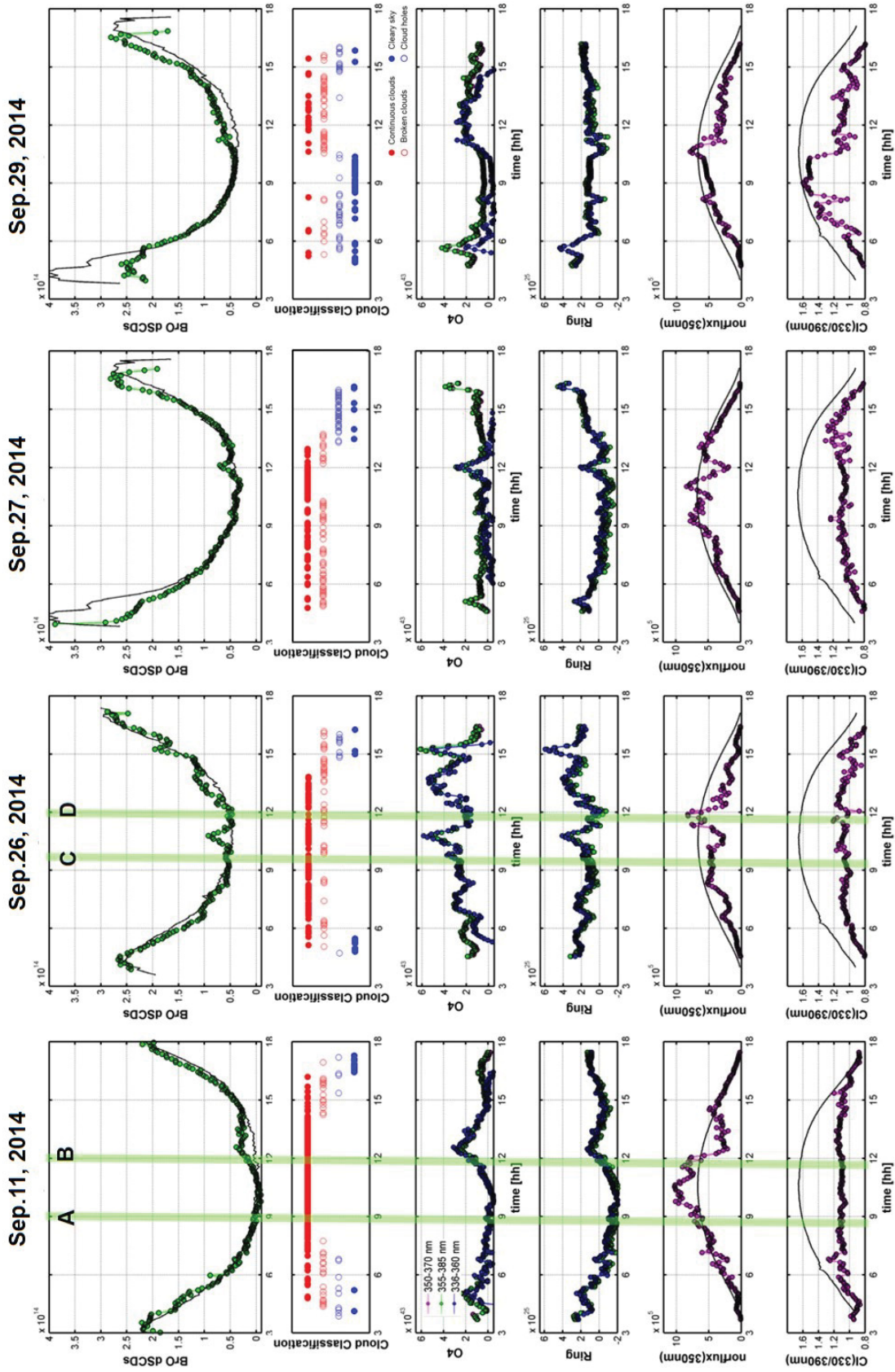


Figure 6.6: BrO DSCDs measured by the ground-based zenith sky DOAS on Sep.11, Sep.26, Sep.27, and Sep.29, 2014. On each day, the diurnal variation of BrO DSCDs, cloud classification, O₄ DSCD, Ring effect, normalised intensity (at 350 nm), and colour index (330/390 nm) derived from the spectral analysis are provided. Cloud classification results include 4 different cases: red-open and red-closed symbols represent broken clouds and continuous clouds, respectively. Blue-open and blue-closed symbols indicate cloud holes and clear sky conditions, respectively.

Table 6.2: Cloud classification results for four days in September.

Date (Sep. 2014)	11	26	27	29
clear sky	2.1%	8.1%	-	38.6%
cloud holes	9.6%	1.2%	-	25.3%
broken clouds	18.1%	25.6%	44.7%	24.1%
continuous clouds	70.2%	65.1%	55.3 %	12.0%

enhanced values are not an artifact caused by spectral interference. (See Fig.6.6, O_4 graph). In the 5th and 6th rows, the normalised intensity and CI are shown as magenta dots and the clear sky reference values are also plotted (black line) for the comparison. In these graphs, a clear enhancement of BrO larger than the stratospheric background can be found on all selected days. At the same time all cloud indicators and light path proxies including O_4 , and Ring effect show a strong enhancement due to multiple scattering caused by clouds.

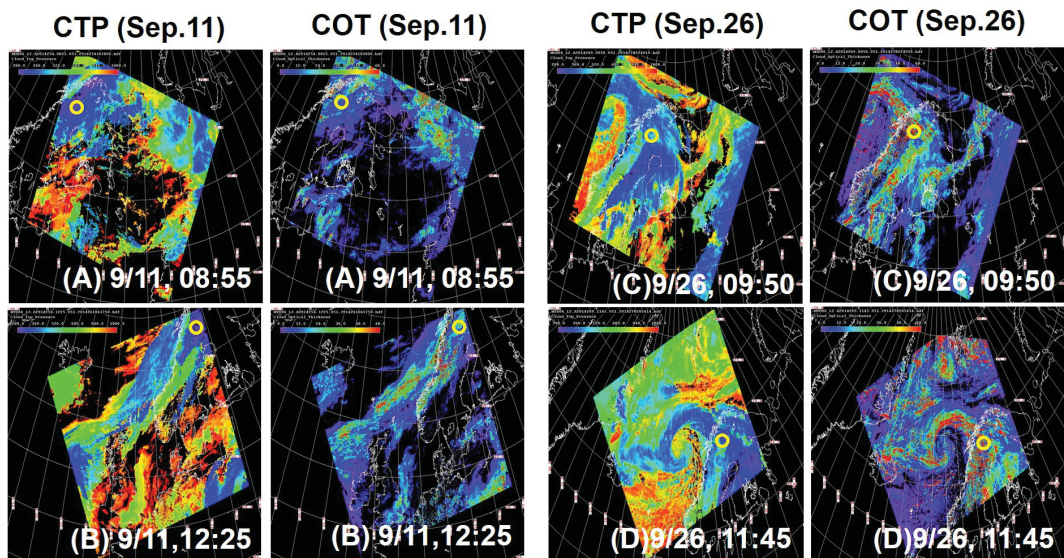


Figure 6.7: MODIS-Terra & Aqua cloud top pressure and cloud optical thickness images on Sep.11 (1st and 2nd column) and Sep.26 (3rd and 4th column). Upper and lower rows represent morning and afternoon images, respectively. (A),(B),(C), and (D) indicate time frames also described by the green lines in Fig.6.6.

Figure 6.7 shows MODIS-Terra and Aqua cloud top pressure (CTP) and cloud optical thickness (COT) images on Sep.11 and Sep.26, which allows to directly compare the BrO to the sky conditions. Sep.11 is cloudy with continuous clouds which are also indicated by the low and stable CI values during the whole day. It can be expected that there are optically thick clouds in the afternoon, because the measured radiance is very low (see a normalised intensity graph of Fig. 6.6). According to MODIS cloud top pressure and cloud optical thickness, there is no big change from morning to afternoon and the height of the cloud top is around 9 km. The increase of the cloud optical thickness in the afternoon fits well to the increase of the O_4 and Ring measurements (see Fig. 6.6).

On Sep.26 continuous and broken clouds are dominant. On that day, the difference between morning and afternoon is noticeable, which can be understood by the MODIS cloud top pressure. In the morning the cloud top height is around 4 km and then it increases

up to around 8 km. The increased COT indicates that the clouds in the afternoon have a higher top pressure in the afternoon.

On Sep.27 and 29, both enhanced BrO and SO₂ signals are observed. Because in the BrO fit range, the BrO OD (6×10^{-4}) is much larger than the SO₂ OD (1×10^{-6}) it can be concluded that the BrO signal can not be caused by a spectral interference of SO₂. As shown in Fig. 6.5 on Sep. 27, a strong enhancement of SO₂ is detected in the morning but weak enhancements of both gases are observed around noon. The sky condition does not significantly vary from the morning to the afternoon, but there are O₄ and Ring peaks observed around noon as well. As a result, it can be concluded that multiple scattering has probably led to the increased BrO DSCDs on those four days. Here it is also important to note that the enhancements of BrO and SO₂ do not occur at exactly the same times. However, the possibility of volcanic BrO cannot be completely ruled out, especially for Sep.27, when a peak of both species occurs simultaneously (around 12:00). However, at exactly that time also the Ring effect and O₄ absorption show a peak indicating that multiple scattering takes place. The most probable explanation for the enhanced SO₂ value at that time is that there exists a slightly enhanced SO₂ concentration. Due to the multiple scattering the SO₂ absorption is further increased.

In order to more carefully look at the effect of multiple scattering, an additional case study is carried out (fig.6.8). The same analysis as for 2014 is performed for the same time of the year in September 2013, when no volcanic plume was observed above Kiruna. Nevertheless, enhanced BrO DSCDs are still found on these days like in September 2014. At the same time all cloud indicators and light path proxies show a strong enhancement. On these days, continuous and broken clouds are dominant. In the afternoon of Sep.6, the CI strongly decreases according to the MODIS cloud top pressure (CTP) and cloud optical thickness (COT). The MODIS cloud top pressure and cloud optical thickness images are attached in Appendix A.19. The increased COT in the afternoon is well consistent with the increase of the O₄ and Ring measurements indicating thick clouds. On Sep.11, 13, and 14, the sky conditions do not significantly change, but peaks of O₄ and the Ring signal are observed simultaneously with the BrO enhancement. In general, the fact that the Ring effect and the O₄ absorption show a peak at the same time indicates that multiple scattering takes place.

Although this chapter only shows a small number of cases, interesting findings about the connection between multiple scattering and enhanced BrO DSCDs could be identified. Future work should make use of the whole data set by comparing BrO and O₄ together with the cloud classification. Here one important question is whether the same correlation (indicating a tropospheric BrO background) will be found for all seasons.

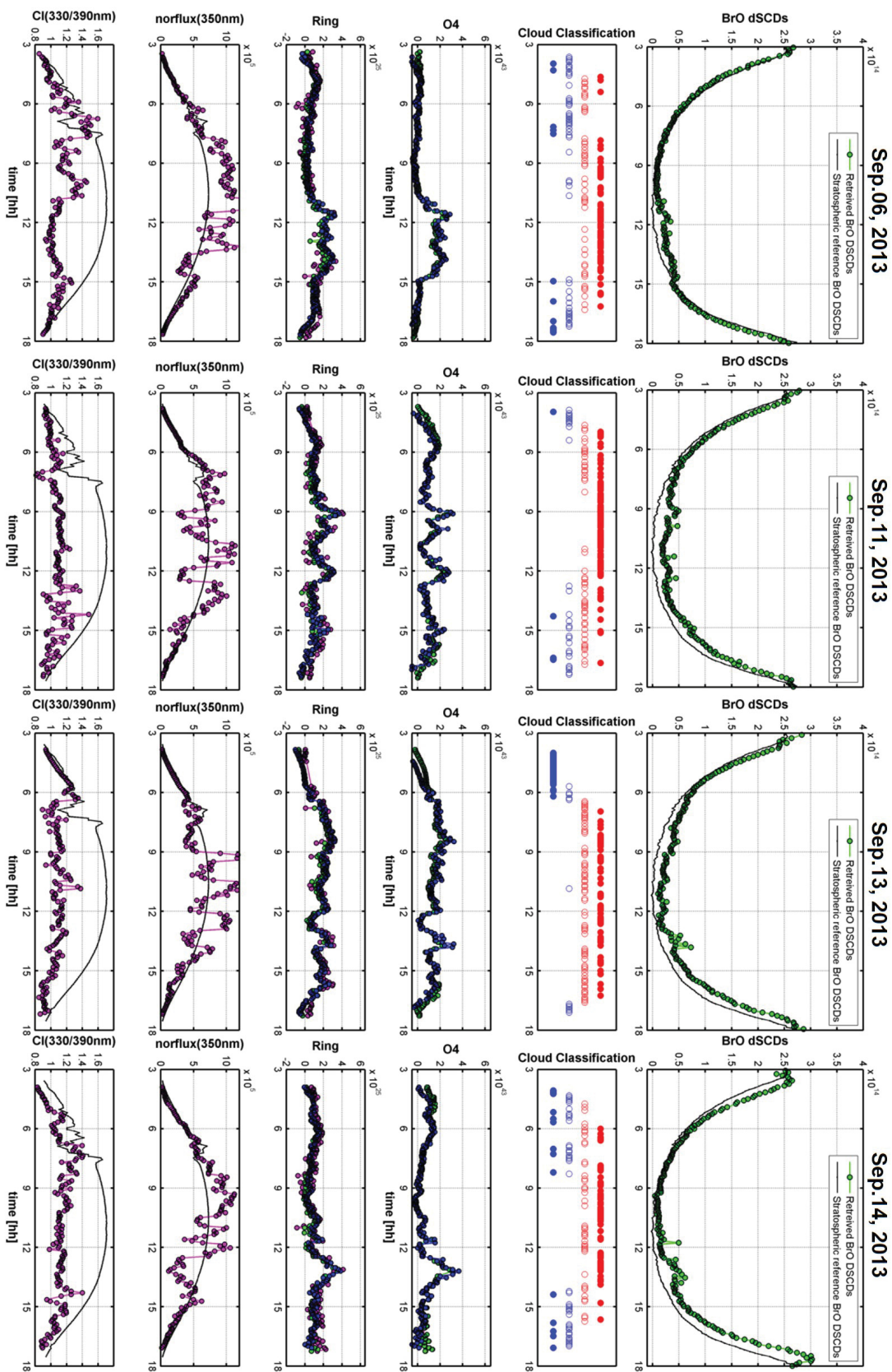


Figure 6.8: BrO DSCDs measured by the ground-based zenith sky DOAS on Sep.06, Sep.11, Sep.13, and Sep.14, 2013. On each day, the diurnal variation of BrO dSCDs, cloud classification, O₄ dSCD, Ring effect, normalised intensity (at 350 nm), and colour index (330/390 nm) derived from the spectral analysis are provided. Cloud classification results include 4 different cases: red-open and red-closed symbols represent broken clouds and continuous clouds, respectively. Blue-open and blue-closed symbols indicate cloud holes and clear sky conditions, respectively.

Part IV

CONCLUSION AND OUTLOOK

CONCLUSION

This thesis showed measurements of stratospheric NO₂, BrO and OCIO obtained from ground-based zenith sky DOAS observations at Kiruna, Sweden. The ground-based zenith sky DOAS observation system has been monitoring since December 1996 until now (almost continuously). It is one of the sites in the Northern hemisphere with the longest record of stratospheric trace gas measurements.

An important aspect of the thesis was the consistent data analysis and quality control using improved analysis settings and various sensitivity tests. In addition, the obtained data sets were compared with results from other remote sensing instruments to validate the quality of retrieved results. The obtained long term dataset (1997 – 2016) can be used to address several scientific questions mentioned also in Introduction that have been frequently emerged in the field of atmospheric chemistry:

- What are the concentrations (or column densities) of BrO, NO₂, and OCIO above Kiruna?
- How well do those agree with other remote sensing measurements?
- How are the diurnal, seasonal, and year-to-year variations of these trace gases related to the dynamic variability and the temperature variations of the stratosphere?
- What are the long-term trends of stratospheric NO₂ and BrO? How do they agree with other trend studies and the trends of the precursor species?
- How can this work contribute to the estimation of the total stratospheric inorganic bromine budget, which is in general hard to determine because of the large uncertainties of the contribution of brominated very short-lived substances (VSLs)?

These questions are addressed individually for the different trace gases in the following sub-sections.

C.1 NO₂

The mean annual stratospheric NO₂ VCDs are 3.2×10^{15} and 3.8×10^{15} molec/cm² for sunrise and sunset, respectively. The diurnal variation is strongest in spring and autumn, while in winter and summer the differences between morning and evening are small because of polar night and polar day, respectively. The stratospheric NO₂ VCDs also show a strong seasonal variation due to the variation of the day length and stratospheric temperature. The retrieved NO₂ vertical profiles using the optimal estimation method indicate that the strong annual cycle and in general the highest variability occurs below 30 km.

Several sensitivity tests have been performed about the influence of different analysis parameters. For the profile inversion, especially the effect of clouds is investigated. Hendrick et al. [2007] mentioned that clouds might influence the profile inversion, but several studies presenting profile inversion data did not consider this effect. This study quantified the

cloud effect on the profile inversion for the first time to our best knowledge. Applying a cloud classification scheme, the observation data were separated according to different sky conditions (clear sky, cloud holes, broken clouds, and continuous clouds). By comparing the profiles for the different sky conditions it was found that cloud effects are in general small but in some cases systematic discrepancies were found. For example, profile shapes between clear sky and cloud sky below 28 km were found to be different, especially in spring. This effect should be investigated in more detail in future studies, e.g. by including clouds in the radiative transfer simulations.

Another interesting finding is that the shape of the sunset profiles is systematically different from the sunrise profiles. Part of these differences might be related to an artifact of the photochemical modeling tool which should be improved for future applications.

The results from the ground based ZS-DOAS measurements have been compared against several other remote sensing technique instruments: Satellites (Limb mode observations: SCIAMACHY, Nadir mode observations: GOME, SCIAMACHY, and GOME2) and SAOZ-Balloon borne measurements to confirm (validate) the data.

- Balloon borne (SAOZ, 7 coincidence events): Generally, the retrieved profiles and partial columns show good agreement with SAOZ. However, most of the ZS-DOAS NO₂ profiles show lower NO₂ number densities than SAOZ, while the magnitude and peak altitudes show in general good agreement. The relative differences are within about 20% at around 25 km. They are probably partly related to the different measurement and retrieval techniques.
- Satellite nadir observations (from 1997 to 2016): Three satellite data in different periods are used for the comparison (GOME: 1997 – 2002, SCIAMACHY: 2002 – 2009, and GOME2-A: 2009 – 2016). All data sets show generally a similar seasonality with minima in winter and maxima in summer. The correlation coefficients are higher than 0.8 but the summer and autumn. The differences can be explained with the difference of the time of the ground based measurements and the satellite overpass, and differences of the applied stratospheric air mass factors.
- SCIAMACHY limb observations (2005 and 2006): The seasonal mean profiles show good agreement with relative differences around $\pm 20\%$ at sunrise and -40 to 20% at sunset. The comparison of partial columns (19 – 37 km) shows different results for the different ZS-DOAS NO₂ data: the relative differences for the Langley plot method are up to 50%, while they are around 20% for the profile inversion results. These differences are expected and can be explained by the effects of photochemistry and/or the fact that the total VCDs (Langley-plot method) also include altitudes above and below the 19 – 37 km range of the SCIA limb observations.

Above Kiruna, the year-to-year meteorological conditions show large variations and a few studies have performed detailed comparisons of stratosphere NO₂ in different winter conditions. This thesis examined the vertical and temporal distribution of stratospheric NO₂ for the whole measurement period (1997 – 2016). In particular it was investigated how the daily position of the polar vortex and temperature variations influence the NO₂ concentrations. For examples, in very cold winters 1996/97, 2005/06, 2013/14, 2015/16 relatively large ozone loss was found. In those years very low NO₂ amounts were found

until the middle of spring while in warm winters the NO₂ reformation has already begun earlier.

To see the long-term variability of stratospheric NO₂, a trend analysis was performed using a nonlinear least squares algorithm. For the trend analysis, two different stratospheric NO₂ data sets, NO₂ VCDs derived from the Langley plot method, and from the integration of the retrieved stratospheric profiles are used. It was found that the relative trends of stratospheric NO₂ are 1.38 ± 2.29 (0.66 ± 2.07)/decade in a.m and 2.23 ± 1.63 (3.36 ± 1.63)/decade in p.m for 1996 – 2015 (values in brackets denote the trends derived from the retrieved profiles).

Overall, the stratospheric NO₂ over Kiruna has not strongly changed within the last two decades (a slight positive, but non-significant change of about $1.5 \pm 2\%$ /decade was found). This trend is reasonably consistent with the positive trend of N₂O (2.3%/decade) observed between 1991 and 2010 (taking into account the age of stratospheric air above Kiruna of about 5.7 years). However, it is an interesting finding that NO₂ trends derived by former studies show rather inconsistent results. Besides possible measurement errors, this finding indicates that stratospheric NO₂ trends strongly depend on the measurement site and the selected period. We expect that this work contributes to better understand the more recent NO₂ variations at high latitude and the relationship of NO₂ with stratospheric O₃ and temperature variations.

C.2 BRO

The mean annual stratospheric BrO partial columns (15 – 27 km) are 2.1×10^{13} and 1.5×10^{13} molec/cm² at SZA 80° for sunrise and sunset, respectively. The vertical distribution of BrO derived from the optimal estimation method shows a strong seasonal variation like NO₂, and a high variability below 20 km. The maxima are found in early spring with values around 2.5×10^7 molec/cm³ around 19 km and the minima are observed in summer. The variation of BrO profiles is a result of photochemical reactions and it depends in particular on the concentration of NO₂.

The retrieved BrO stratospheric profiles and partial columns were compared with SCIAMACHY limb observations and SAOZ-balloon borne measurements.

- Four coincidences with SAOZ-balloon borne measurements were found. Generally both measurements are consistent with each other. The relative differences of the vertical distributions are typically around 20 % at 15 – 20 km, and the partial BrO columns deviate by less than 10 %. Interestingly, those four events represent different meteorological conditions (inside and outside the polar vortex, winter or summer) and thus clearly different BrO profiles are found with higher values inside the polar vortex, and smaller values in summer (due to high NO₂ concentrations and high actinic flux).
- For the comparison with SCIAMACHY limb observations, the altitude range was chosen from 15 to 27 km. The comparison shows a good agreement in most seasons except in winter (below 20 km, up to 60 % difference). The BrO column densities obtained from both measurements show a clear seasonal variation with high values in winter and low values in summer. The agreement also depends on the SZA: a remarkably good agreement is found for ZS-DOAS results for SZA of 80 and 85°.

To understand the connection of the stratospheric halogen chemistry to atmospheric dynamics, the day-to-day variation of the stratospheric BrO vertical distribution during

spring for individual years was investigated. The BrO concentrations increase after polar night and decrease starting from the beginning of March until May. The main BrO layer develops at around 20 km, and an anti-correlation with NO₂ is found. During cold winters (1997, 2000, 2005, and 2016), a strong BrO enhancement inside the polar vortex is found. Most cases of high BrO concentrations are found when temperatures drop below or near the threshold for the formation of polar stratospheric clouds.

Also for the results of the BrO profile retrieval, the potential influence of clouds was investigated. While the NO₂ concentrations under continuous clouds are slightly higher than under clear sky, the BrO results have an opposite tendency but with only small deviations. Compared to the sunrise (a.m) mean profiles, the BrO sunset mean profiles show larger discrepancies depending on the sky conditions. In particular, the maximum peak height of the profile changes under cloudy conditions. The cloud effect on the BrO profiles is larger than for NO₂, mainly because in the stratosphere the BrO layer is usually lower than the NO₂ layer.

Also the long term trends for BrO were investigated. The relative trend of stratospheric BrO derived from the integrated retrieved profiles is 0.15 ± 3.69 (4.15 ± 3.27) %/year for 1997 – 2001 and -1.38 ± 0.79 (-1.07 ± 0.61) %/year for 2005 – 2015 (Values in brackets indicate the trends for sunset data). A strong increasing trend before 2001 was found but a slightly negative (or an insignificant trend) was found after 2001. For the whole period (1997 – 2015) a slightly positive trend (0.25 ± 0.36 %/year in sunrise, and 0.46 ± 0.25 %/year in sunset) was found.

The stratospheric bromine budget is hard to determine because of the large uncertainties of the contribution of brominated VSLs. From this study, the total stratospheric inorganic bromine budget (Br_y) was derived from the retrieved BrO to about 20.6 ± 1.2 ppt at sunrise and 20.8 ± 1.9 ppt at sunset, respectively. Considering the mean age of air, 5.7 years, it seems that the stratospheric BrO load has increased until 2001 and after 1997 it has slightly declined and/or rather stayed constant. Such a tendency is consistent with the decrease in total tropospheric Halons and CH₃Br. From the comparison of the derived total stratospheric inorganic bromine load and the expected contribution of long lived bromine precursor gases, the contribution of VSLs to the total stratospheric inorganic bromine (Br_y) is estimated as 4.9 – 5.5 ppt at sunrise and 4.7–5.7 ppt at sunset, respectively.

C.3 OCLO

The dependence of the OCIO amount on various meteorological conditions for 15 years was investigated. The results obtained are well consistent with findings in former studies. In particular, the measured data are categorised depending on the meteorological conditions of the individual winters. For example, in long continuous cold winters, enhanced OCIO has lasted until late spring indicating strong chlorine activation. In such winters, a 4–5 times larger ozone destruction was found than in warmer winters. In contrast, in warm winters, no or only a very weak enhancement of the OCIO concentrations was found. In such winters, often sudden temperature increases in the middle of the winter were found. A systematic comparison of OCIO DSCDs to the minimum temperature on 475 K level confirmed the strong temperature dependence of the stratospheric chlorine activation.

The temporal evolution of OCIO was compared to those of other trace gases (NO₂, BrO, and O₃) and meteorological conditions. OCIO is clearly anti-correlated with O₃ and NO₂.

Another interesting finding is that the BrO DSCDs decreased during periods of strongly enhanced OCIO DSCDs. Also a clear anti-correlation of the OCIO DSCDs with temperature was observed as expected from the dependence of the PSCs formation on temperature.

The OCIO data shows good agreement with GOME-2 satellite OCIO SCDs. The correlation coefficients for monthly averages are about 0.9 for GOME-2A and 0.92 for GOME-2B.

C.4 VOLCANIC TRACE GASES

Although this study mainly focuses on the retrieval of stratospheric trace gases, I also investigated the variation of tropospheric trace gases during specific events such as occasional volcanic eruptions. From Sep. 1st to Oct. 4th, 2014, enhanced SO₂ absorptions were observed after the Bárðarbunga volcano eruption. During these episodes, also enhancements of BrO above the stratospheric background were observed. The reason of the enhanced BrO is not fully clear. It might be e.g. caused by the direct emission of bromine compounds from the volcanic eruption. Another more probable explanation might be that the absorption by a uniform tropospheric BrO background was strongly enhanced by multiple scattering since enhancements of O₄ and the Ring effect are observed simultaneously with the BrO enhancements. Further studies should investigate the effect of multiple scattering on the possible tropospheric BrO background in more detail.

C.5 OUTLOOK

The biggest achievement of this study is the consistent analysis of the long-term ground-based observation at a high latitude site. The ground-based dataset at Kiruna of 19 years (with some data gaps) allows to study the variability of the atmospheric composition in the past, and should be extended into the future. Already up to know the temporal trends of important trace gases (in particular NO₂ and BrO) were determined. In the case of NO₂, they are reasonably consistent with existing theories of the formation of stratospheric NO₂. Also for BrO, the time series allowed to check whether the expected reduction of the emission of brominated precursor gases was actually observed in the stratosphere. The continuation of the long term measurements is therefore of utmost importance. In addition, the continuation of the measurements will allow the validation of new space-borne sensors.

This work presented the diurnal, seasonal and year to year variation of the stratospheric NO₂ and BrO vertical distributions and OCIO DSCDs. An important future work would therefore be the comparison of the obtained results with results from atmospheric chemistry models like e.g. ECHAM5/MESy Atmospheric Chemistry (EMAC) [Jöckel et al., 2006, 2010]. From such a comparison, the underlying mechanisms like e.g. the formation of polar stratospheric clouds, the effects of sudden warmings, the effects of mountain lee waves, or the mixing of air from inside and outside the polar vortex, might be better understood. Finally, regarding the calculation of the Br_y-VSL contribution, the model calculations of the partitioning of BrO to Br_y should be refined to be better determine the exact contribution of VSL to the stratospheric bromine budget.

Part V

APPENDIX

APPENDIX

A.1 APPENDIX: STRATOSPHERIC NO₂

A.1.1 *Vertical distribution of stratospheric NO₂*

In this section the temporal and vertical variability of stratospheric NO₂ from 1997 to 2016 is given.

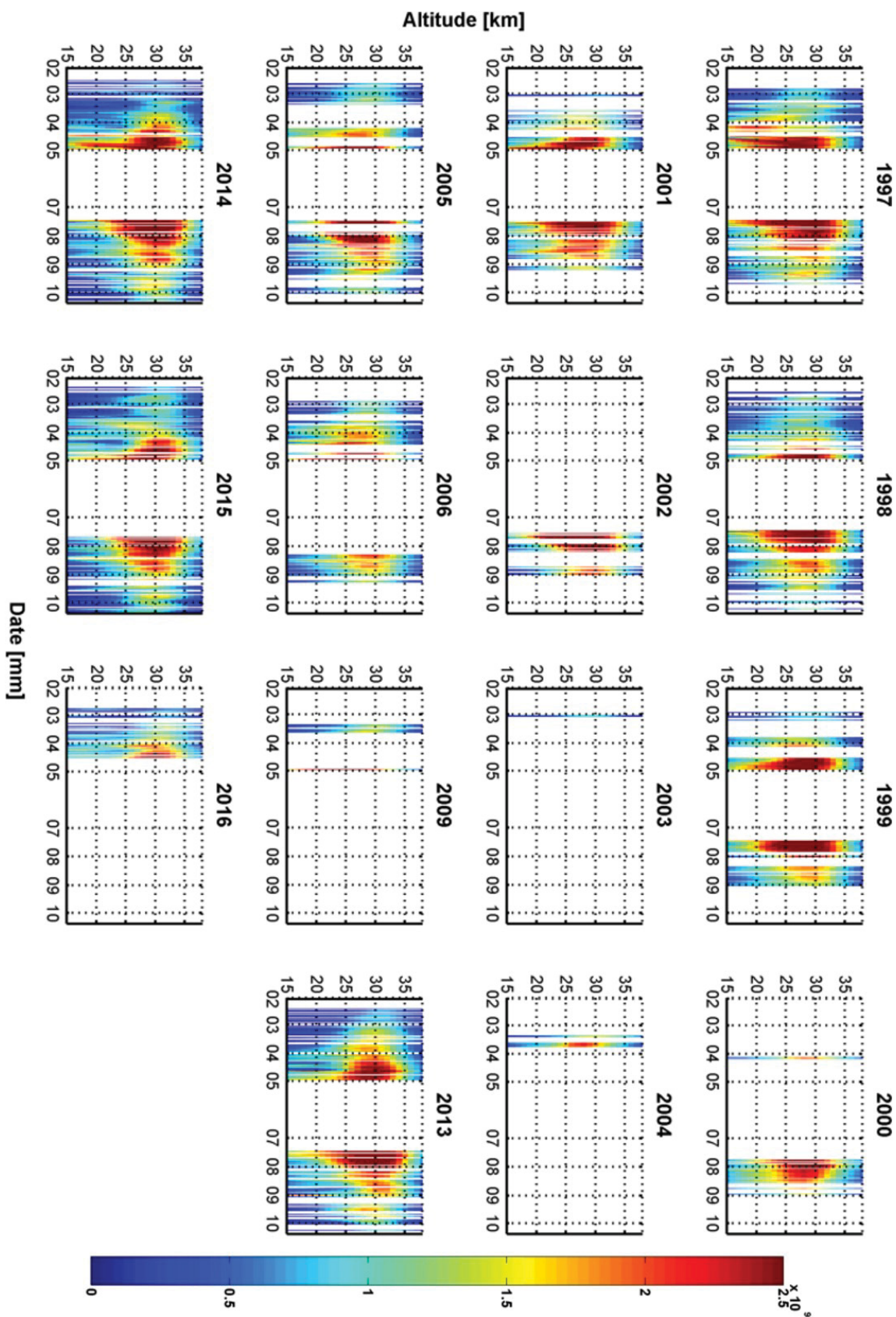


Figure A.1: Curtain plots of the time series of a stratospheric NO₂ vertical distribution measured in a.m from 1997 to 2016. As mentioned before in Fig. 3-2, during the periods before middle of February, middle of May to end of July and after the end of October data are ignored due to the limited SZA ranges.

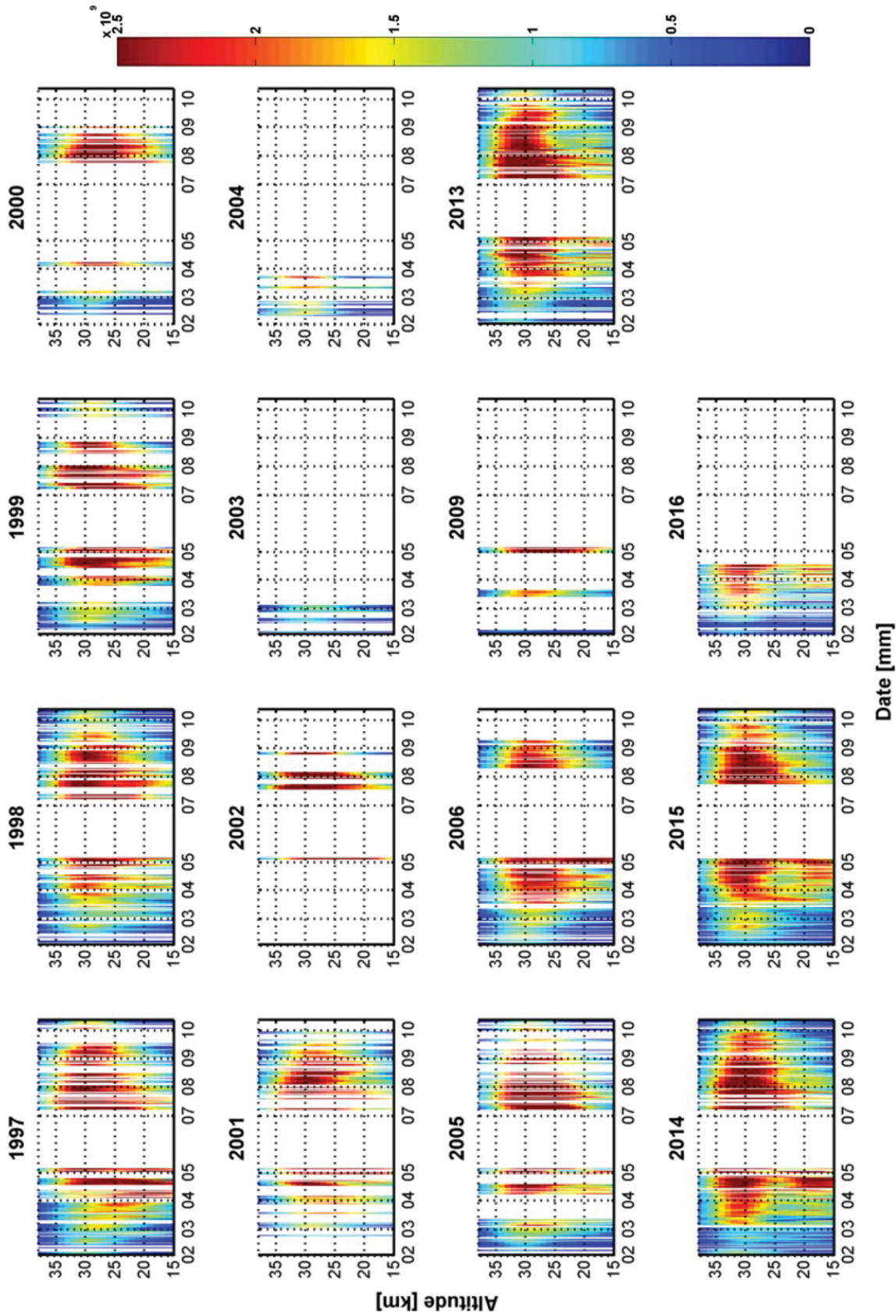


Figure A.2: Curtain plots of the time series of a stratospheric NO₂ vertical distribution measured in p.p.m from 1997 to 2016. As mentioned before in Fig. 3-2, during the periods before middle of February, middle of May to end of July and after the end of October data are ignored due to the limited SZA ranges.

A.1.2 Trend analysis

In this section the results of the trend analysis without the semi-annual term are shown.

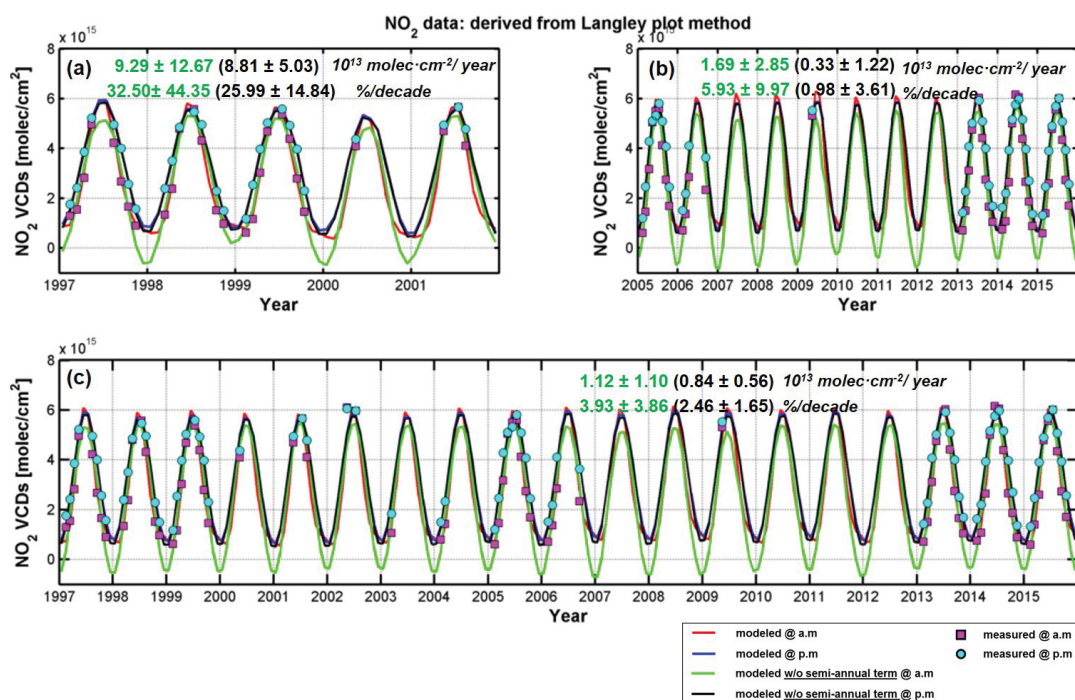


Figure A.3: Trend analysis of NO₂ VCDs determined by the Langley plot method. In each figure, magenta squares and cyan dots represent measured data at a.m and p.m, respectively. The continuous lines and the dashed lines indicate the corresponding modeled NO₂ VCDs at a.m and p.m, respectively. The green and black lines represent results for which the semi-annual term is excluded from the fit. Figures (a) to (c) show the results for the different time periods. The absolute and relative trends at a.m (green) and p.m (black) are represented in each figure.

Table A.1: Derived absolute trends of the stratospheric NO₂ VCDs (molec·cm²/year) and relative trends (%/decade) performed without semi-annual terms.

Method	Period	molec·cm ² /year		%/decade	
		a.m (×10 ¹³)	p.m (×10 ¹³)	a.m	p.m
Langly Method	(a) 1997-2001	9.29±12.67	8.81±5.03	32.50±44.35	25.99±14.84
	(b) 2005-2015	1.69±2.85	0.33±1.22	5.93±9.97	0.98±3.61
	(c) 1997-2015	1.12±1.10	0.84±0.56	3.93±3.86	2.46±1.65
Integrated	(a) 1997-2001	4.44±12.02	6.03±5.73	15.07±40.81	17.33±16.47
	(b) 2005-2015	2.56±3.18	2.00±1.71	8.68±10.80	5.75±4.91
	(c) 1997-2015	0.29±1.09	1.30±0.62	1.00±3.69	3.71±1.77

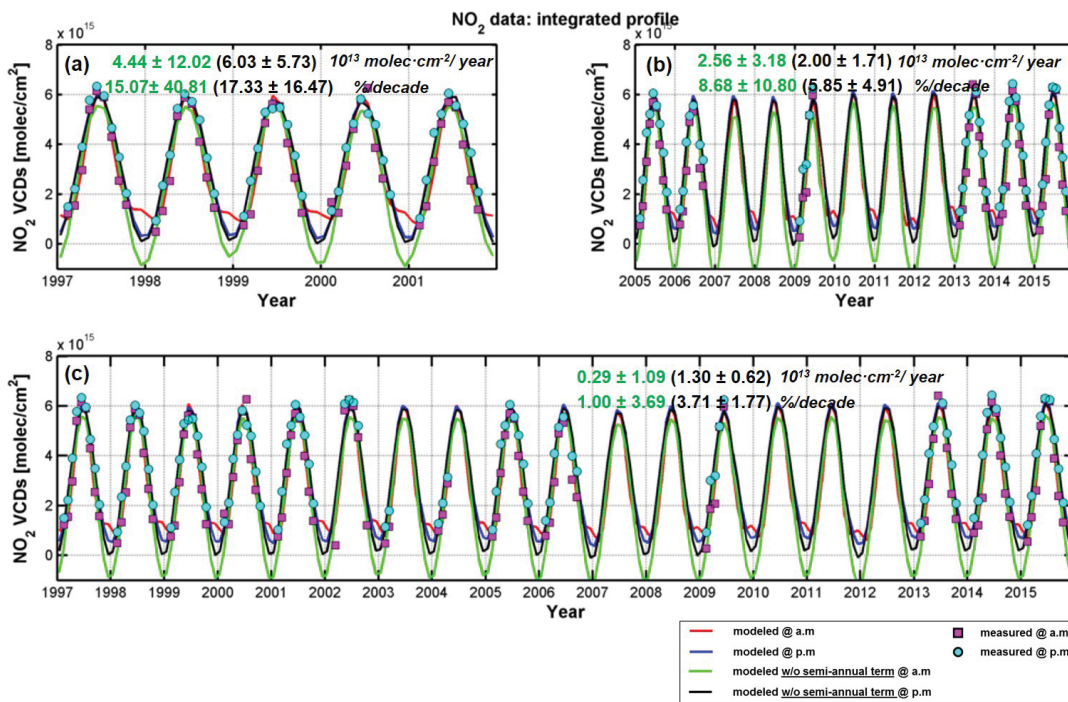


Figure A.4: Trend analysis of NO₂ VCDs determined by the integrated profiles. In each figure, magenta squares and cyan dots represent measured data at a.m and p.m, respectively. The continuous lines and the dashed lines indicate the corresponding modeled NO₂ VCDs at a.m and p.m, respectively. The green and black lines represent the results for which semi-annual term is excluded from the fit. Figures (a) to (c) show the results for the different time periods. The absolute and relative trends at a.m (green) and p.m (black) are represented in each figure.

A.2 APPENDIX: STRATOSPHERIC BRO

A.2.1 Analysis

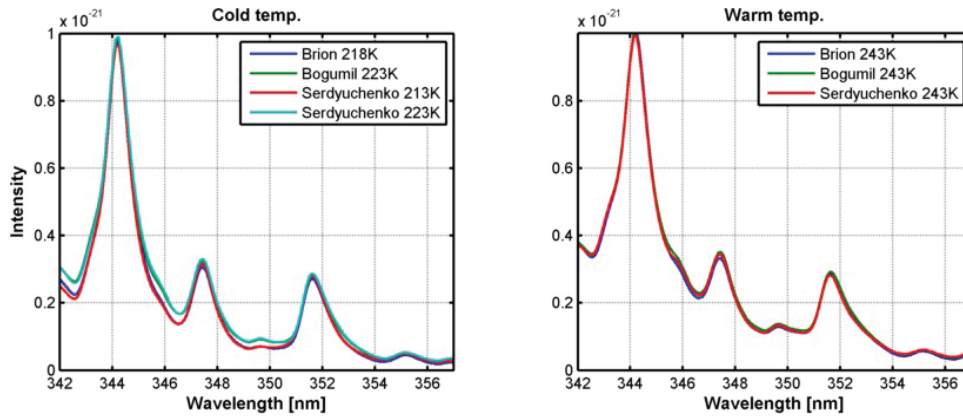


Figure A.5: Comparison for the different ozone cross sections

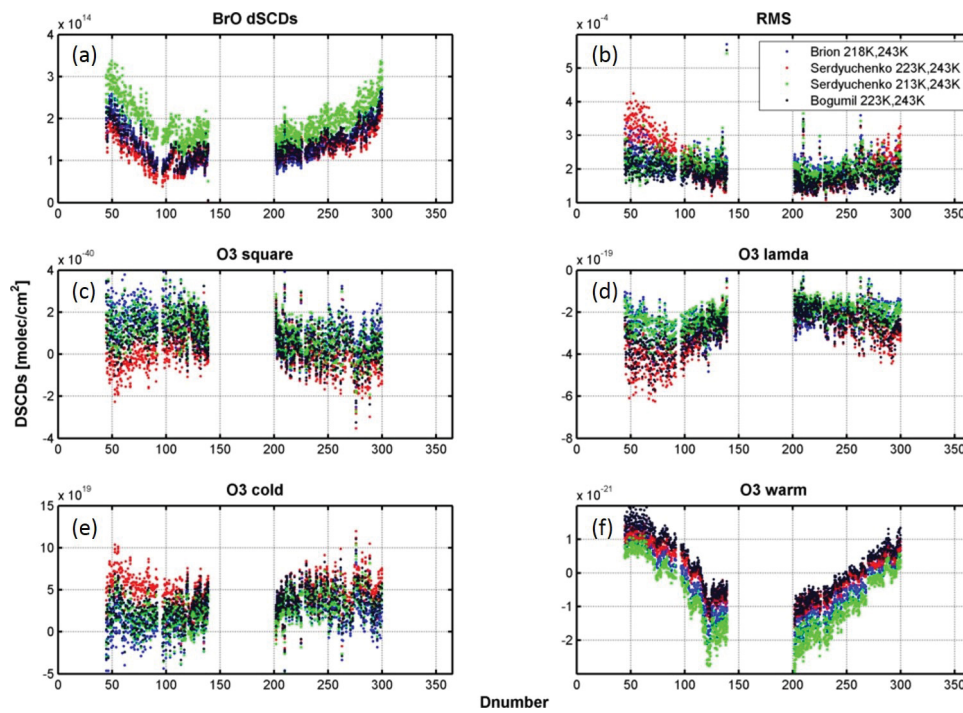


Figure A.6: Time series of BrO of the residuals, and Taylor series O₃ dSCDs measured on 2013, p.m. Each subplot includes four different colored dots indicating results by using different O₃ cross sections.

A.2.2 Temporal and vertical distribution of stratospheric BrO at different SZA condition

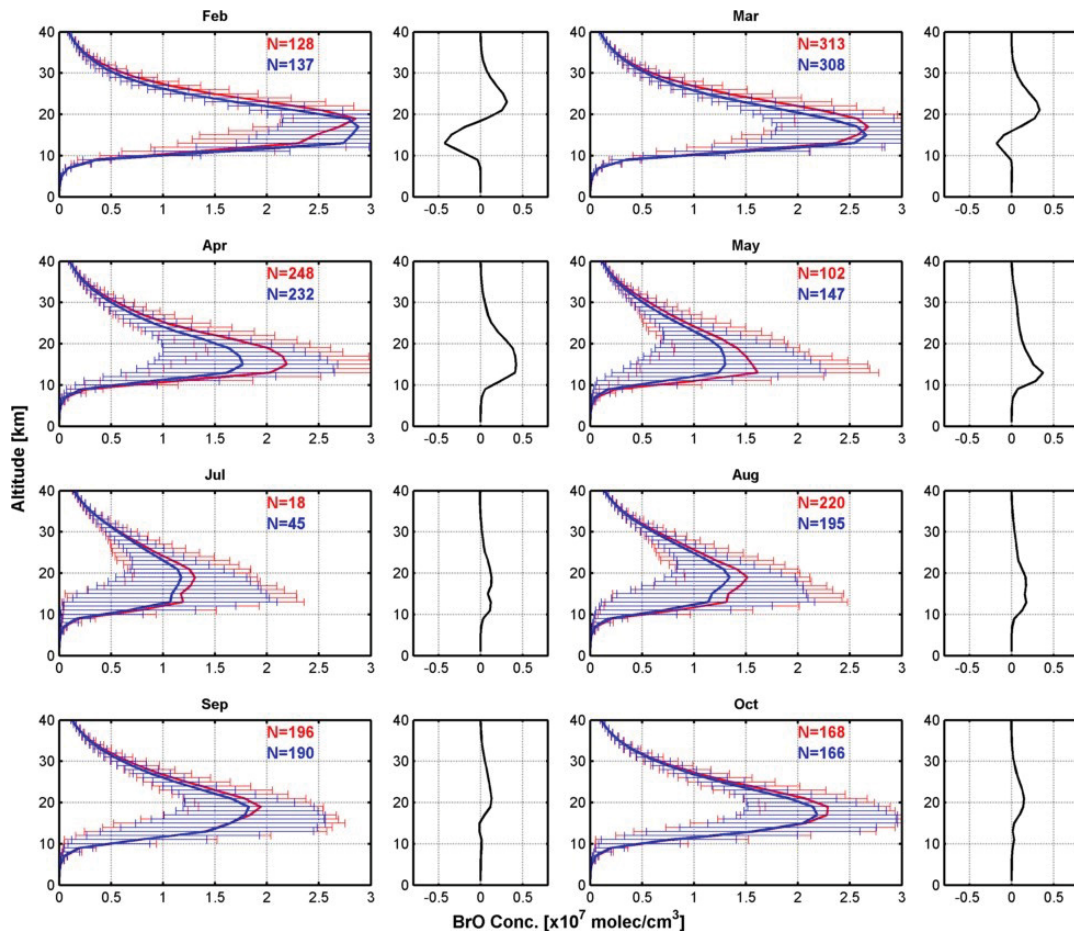


Figure A.7: Monthly mean BrO profiles from ZS-DOAS observations from 1997 to 2016. Odd number-columns represent monthly means and the number of occurrences; the error bars indicate the 1-sigma standard deviation. In these graphs, red and blue lines indicate mean profiles measured during a.m and p.m, respectively. All retrieval results are shown for a SZA of 80° . Also the mean differences between profiles in a.m and p.m are shown. The x -axis and y -axis represent the number concentration and altitude from ground to 40 km, respectively.

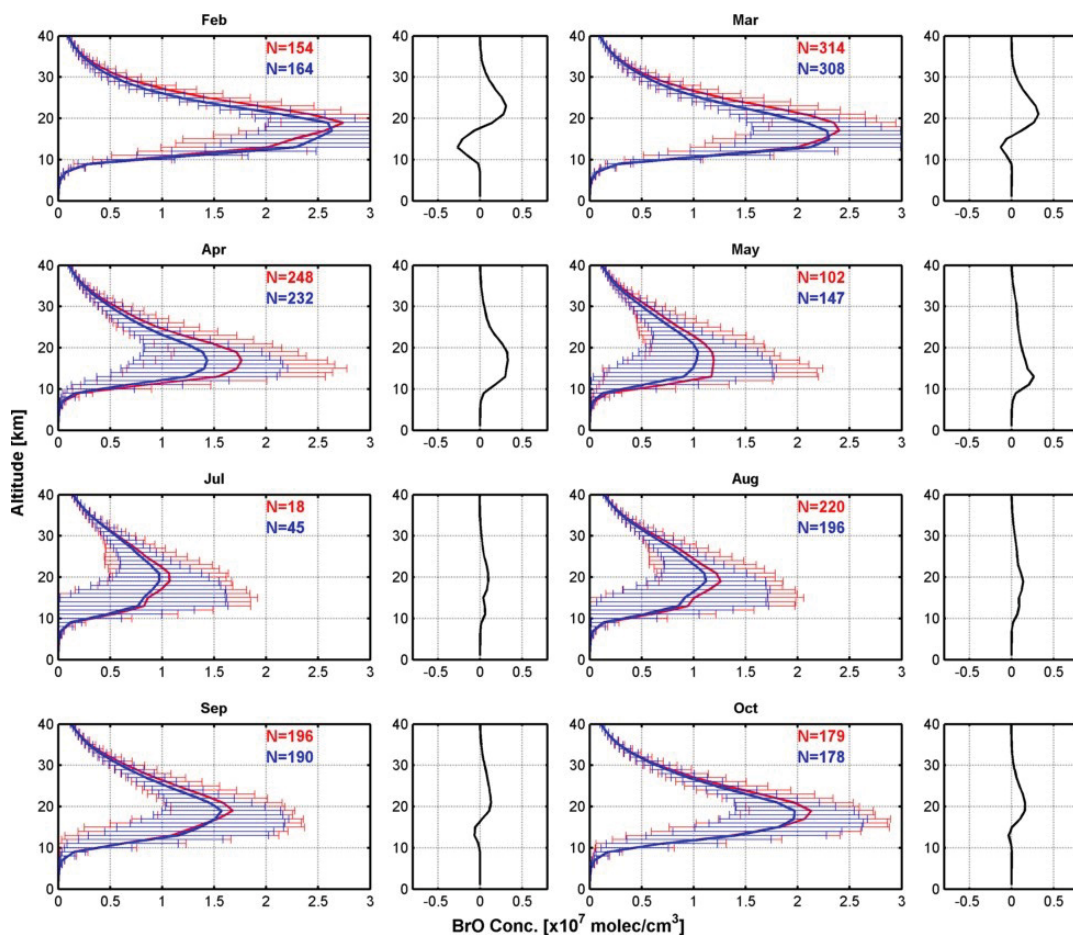


Figure A.8: Monthly mean BrO profile from ZS-DOAS observations from 1997 to 2016. Odd number-columns represent monthly means and the number of occurrences; the error bars indicate the 1-sigma standard deviation. In these graphs, red and blue lines indicate mean profiles measured during a.m and p.m, respectively. All retrieval results are shown for a SZA of 85°. Also the mean differences between profiles in a.m and p.m are shown. The x-axis and y-axis represent the number concentration and altitude from ground to 40 km, respectively.

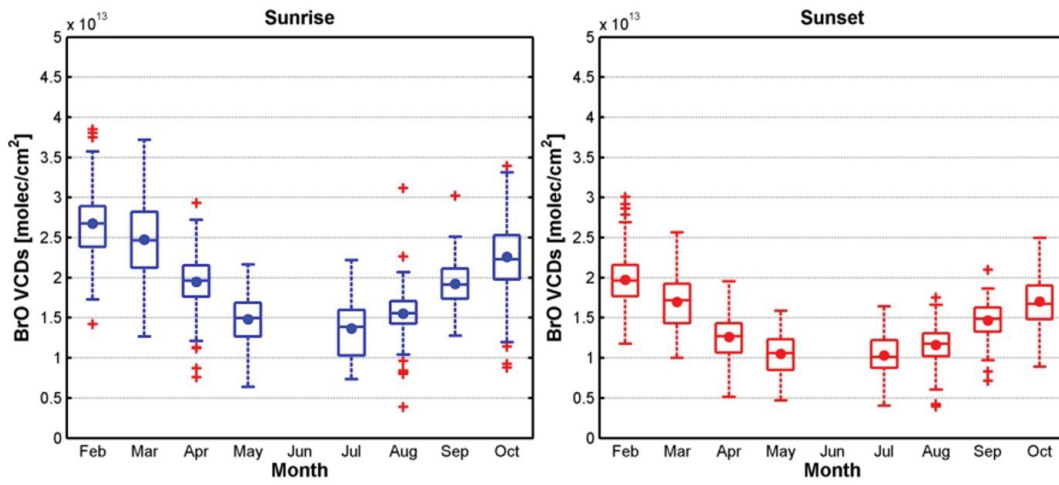


Figure A.9: Box and whisker plots of time series of stratospheric BrO partial columns (15 – 27 km) from 1997 to 2016 derived from integrating retrieved profile by the OEM method at SZA 80°. Left and right panels represent measurements during sunrise and sunset, respectively. The box edges denote 25 and 75 % of the BrO partial columns and the center lines and dots indicate the median and mean, respectively. Red cross indicates an outliers.

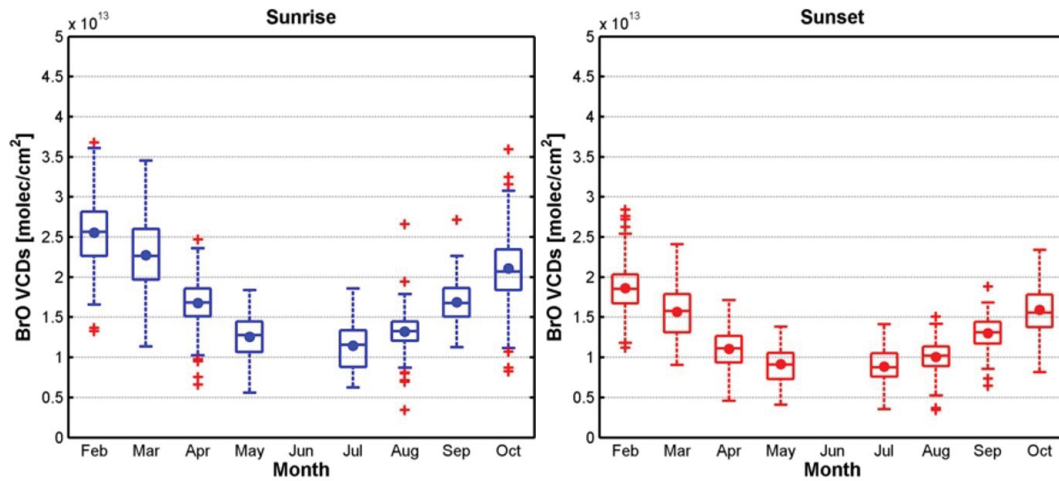


Figure A.10: Box and whisker plots of time series of stratospheric BrO partial columns (15 – 27 km) from 1997 to 2016 derived from integrating profiles by the OEM method at SZA 85°. Left and right panels represent measurements during sunrise and sunset, respectively. The box edges denote 25 and 75 % of the BrO partial columns and the center lines and dots indicate the median and mean, respectively. Red cross indicates an outliers.

A.2.3 Meteorology of polar winter periods

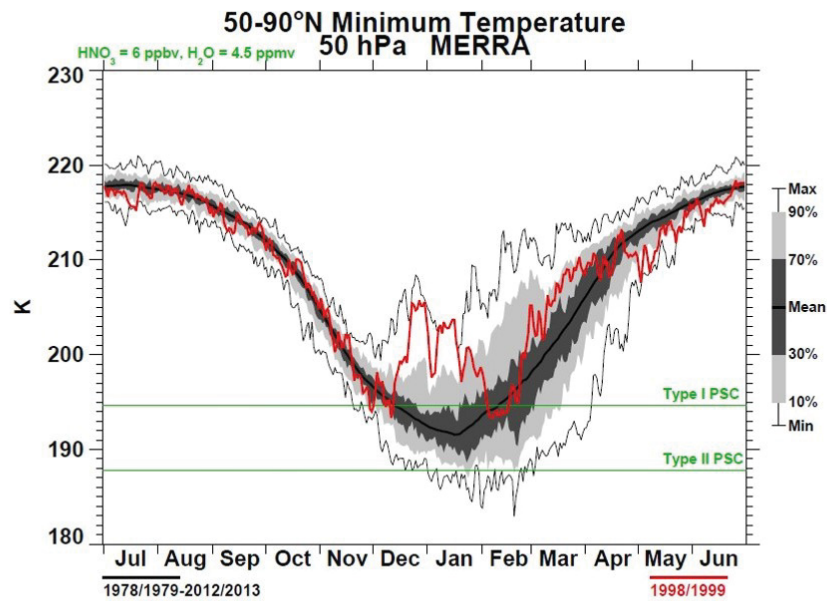


Figure A.11: The minimum temperature for the Arctic polar region on the 50hPa surface between 50°N and 90°N during the winter of 1998/1999 in comparison to the climatological mean of the years between 1978 and 2017. Also shown are the threshold temperatures for the formation of PSCs of type1 and type2 calculated with constant mixing ratios for HNO₃(6ppb) and H₂O(4.5ppm).[Rienecker et al., 2011]

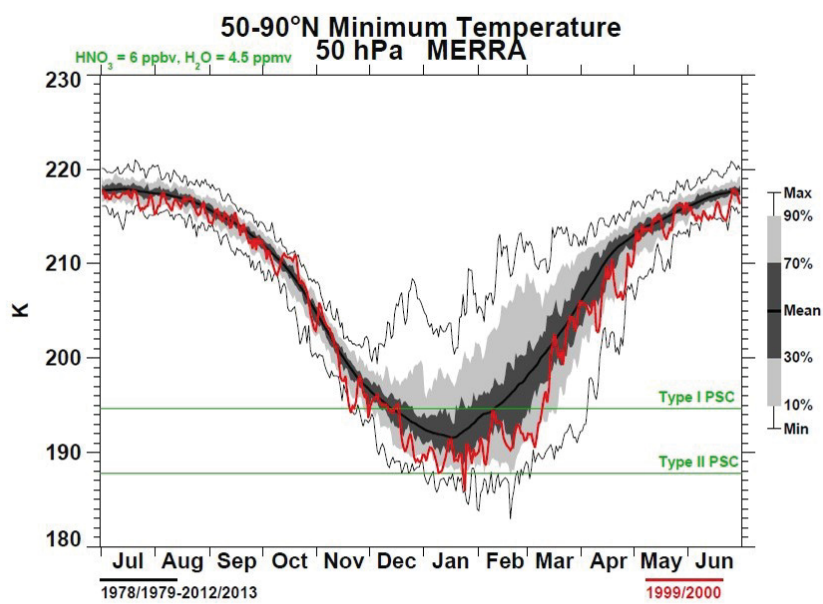


Figure A.12: The minimum temperature for the Arctic polar region on the 50hPa surface between 50°N and 90°N during the winter of 1999/2000 in comparison to the climatological mean of the years between 1978 and 2017. Also shown are the threshold temperatures for the formation of PSCs of type1 and type2 calculated with constant mixing ratios for HNO₃(6ppb) and H₂O(4.5ppm).[Rienecker et al., 2011]

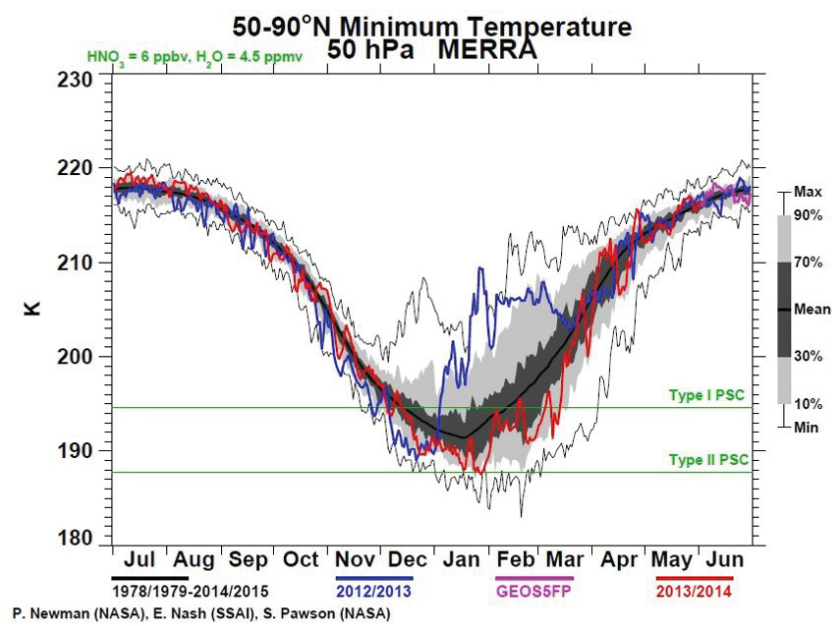


Figure A.13: The minimum temperature for the Arctic polar region on the 50hPa surface between 50°N and 90°N during the winter of 2013/2014 in comparison to the climatological mean of the years between 1978 and 2017. Also shown are the threshold temperatures for the formation of PSCs of type1 and type2 calculated with constant mixing ratios for HNO_3 (6ppb) and H_2O (4.5ppm).

A.2.4 *Vertical distribution of stratospheric BrO*

In this section the temporal and vertical variability of stratospheric BrO from 1997 to 2016 are given.

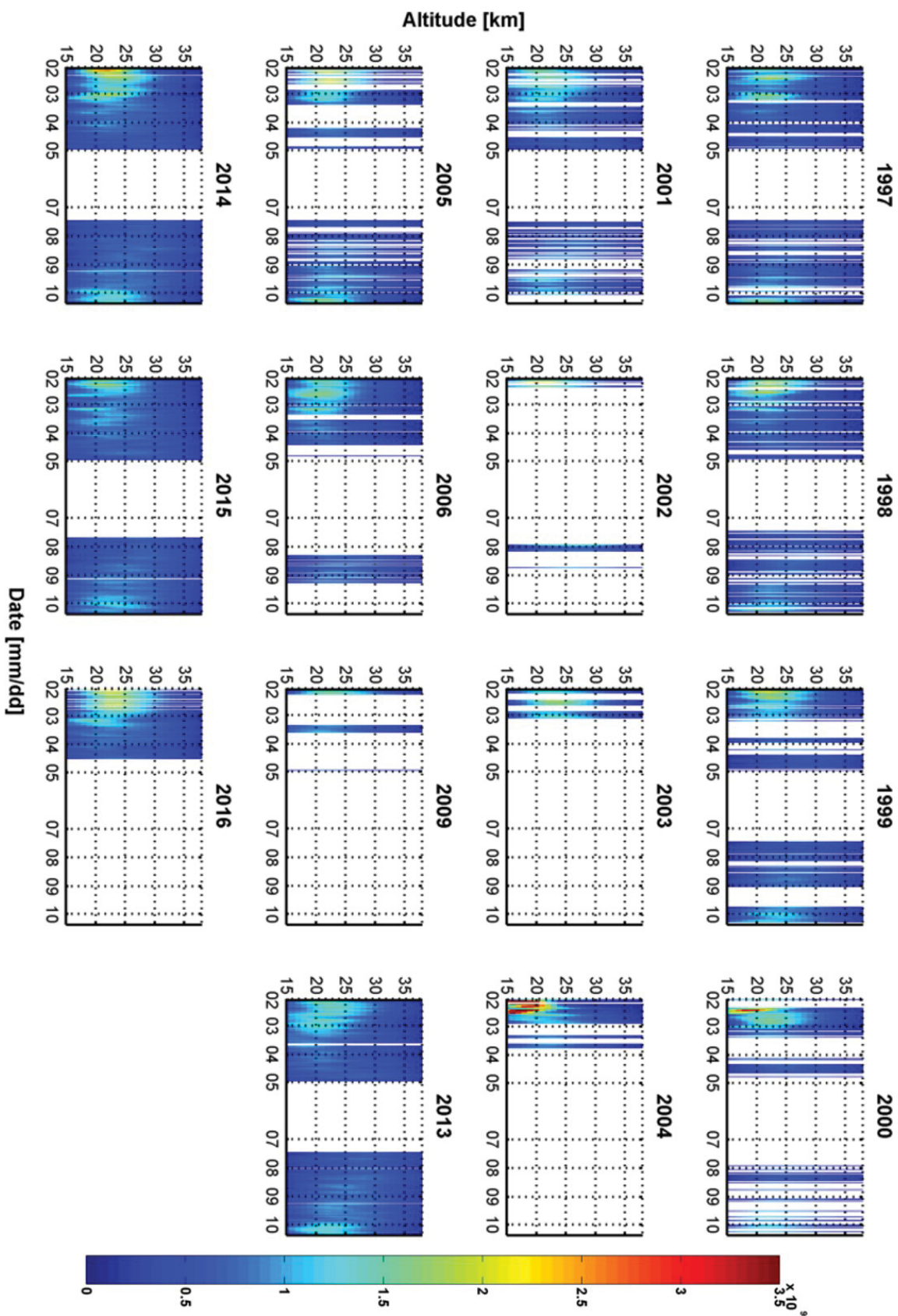


Figure A.14: Curtain plots of the time series of a stratospheric BrO vertical distribution measured in a.m from 1997 to 2016. As mentioned before in Fig. 3-2, during the periods before middle of February, middle of May to end of July and after the end of October data are ignored due to the limited SZA ranges.

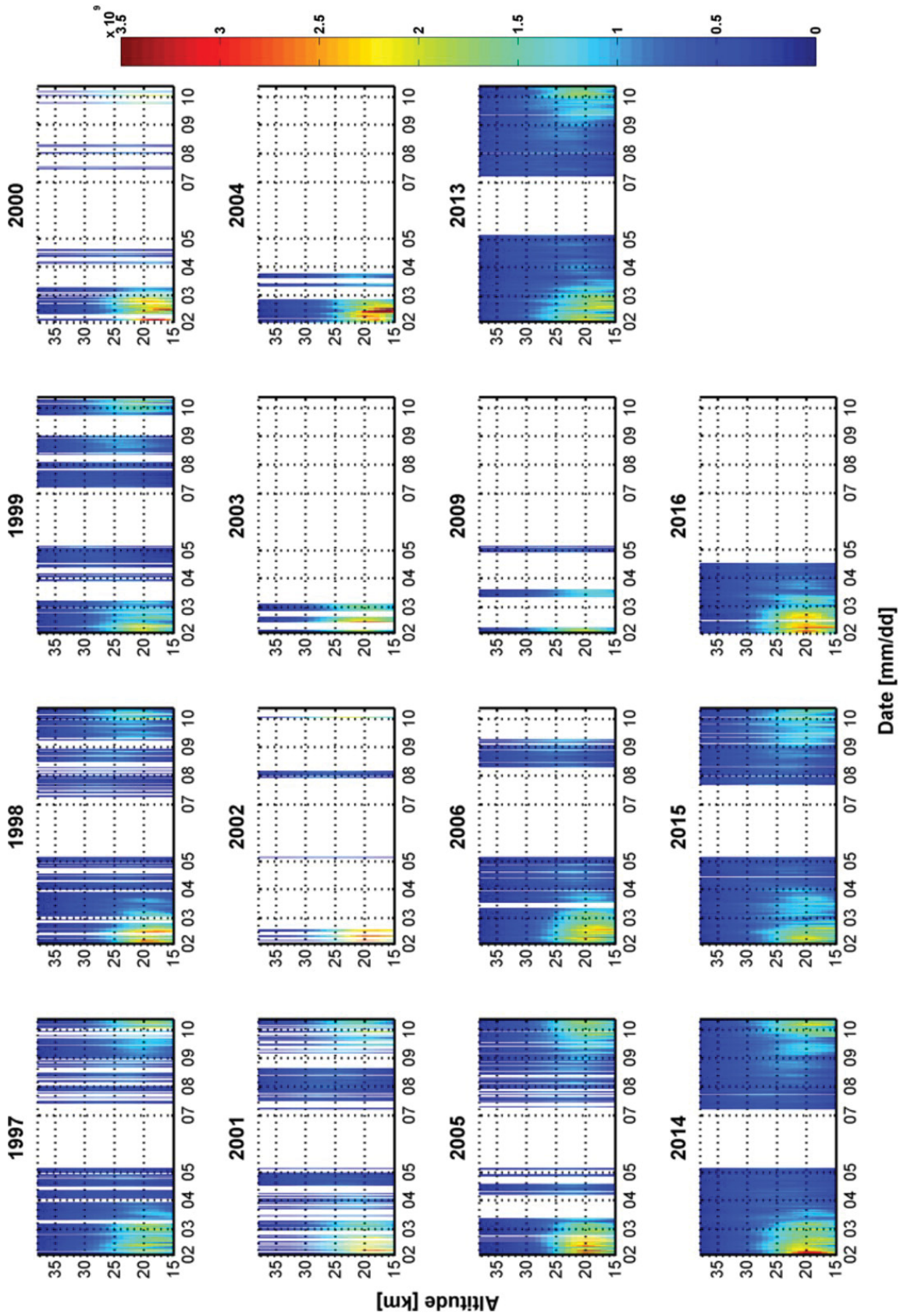


Figure A.15: Curtain plots of the time series of a stratospheric BrO vertical distribution measured in p.m from 1997 to 2016. As mentioned before in Fig. 3-2, during the periods before middle of February, middle of July and after the end of October data are ignored due to the limited SZA ranges.

A.2.5 Trend analysis

In this section the summary of the trend analysis without the semi-annual term is shown.

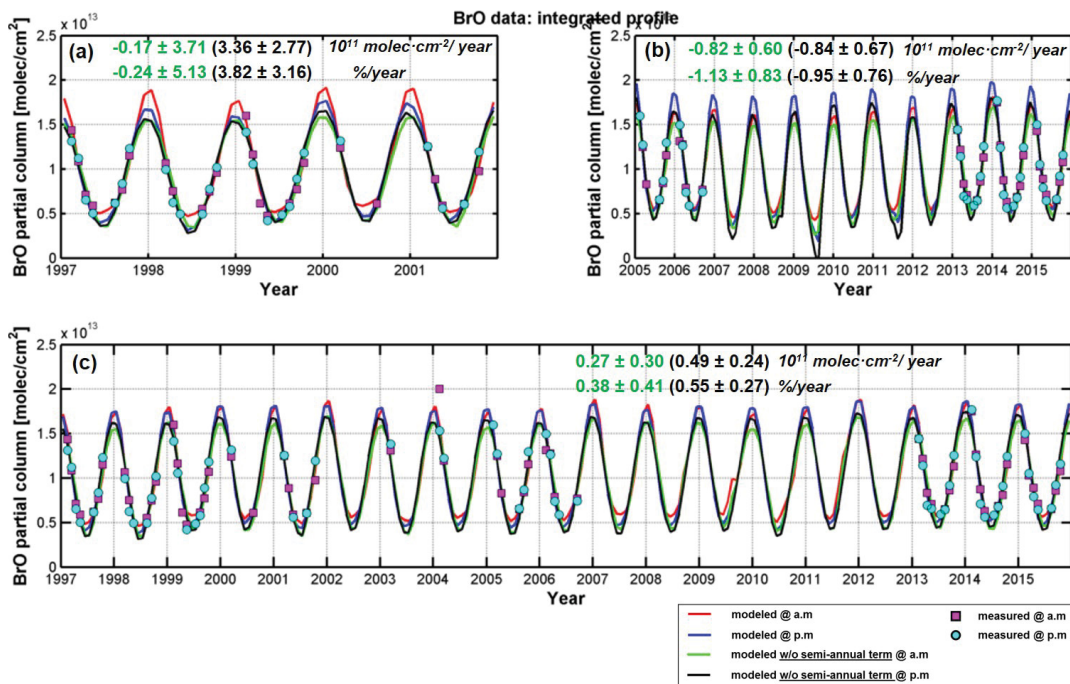


Figure A.16: Trend analysis of BrO VCDs determined from the integrated profiles. In each figure, magenta squares and cyan dots represent measured data at a.m and p.m, respectively. The continuous lines and the dashed lines indicate the corresponding modeled BrO columns at a.m and p.m, respectively. The green and black lines represent the results when the semi-annual term is excluded from the fit. Figures (a) to (c) show the results for the different time periods. The absolute and relative trends at a.m (green) and p.m (black) are represented in each figure.

Table A.2: Derived absolute trends of the stratospheric BrO VCDs (molec· cm²/year) and relative trends (%/year) performed without semi-annual terms.

Period	molec· cm ² /year		%/year	
	a.m (×10 ¹¹)	p.m (×10 ¹¹)	a.m	p.m
(a)1997–2001	-0.17 ± 3.71	3.36 ± 2.77	-0.24 ± 5.13	3.82 ± 3.16
(b)2005–2015	-0.82 ± 0.60	-0.84 ± 0.67	-1.13 ± 0.83	-0.95 ± 0.76
(c)1997–2015	0.27 ± 0.30	0.49 ± 0.24	0.38 ± 0.41	0.55 ± 0.27

A.3 APPENDIX: STRATOSPHERIC OCLO

A.3.1 Analysis

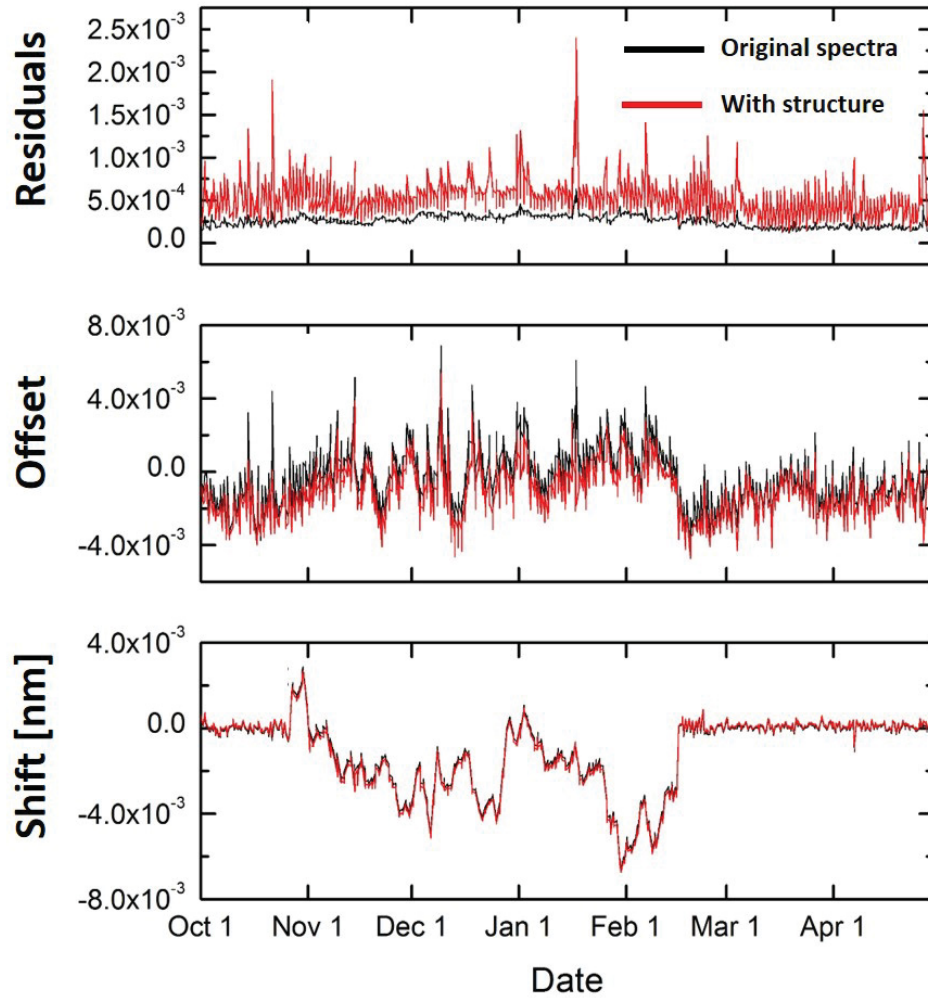


Figure A.17: Times series of (A) the RMS of the residuals, (B) intensity offsets, and (C) spectral shift using the original or modified spectra (see also Fig. 5.7.)

A.4 APPENDIX: TROPOSPHERIC VOLCANIC GAS

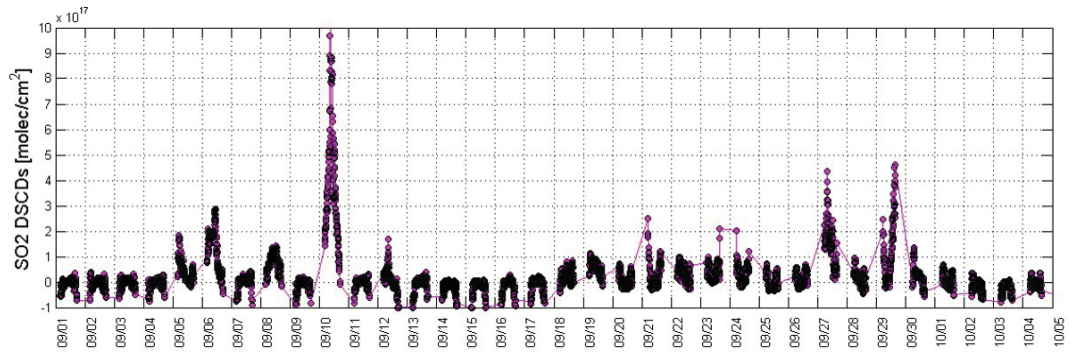


Figure A.18: Time series of SO₂ dSCDs from Sep.1, 2014 to Oct.5, 2014.

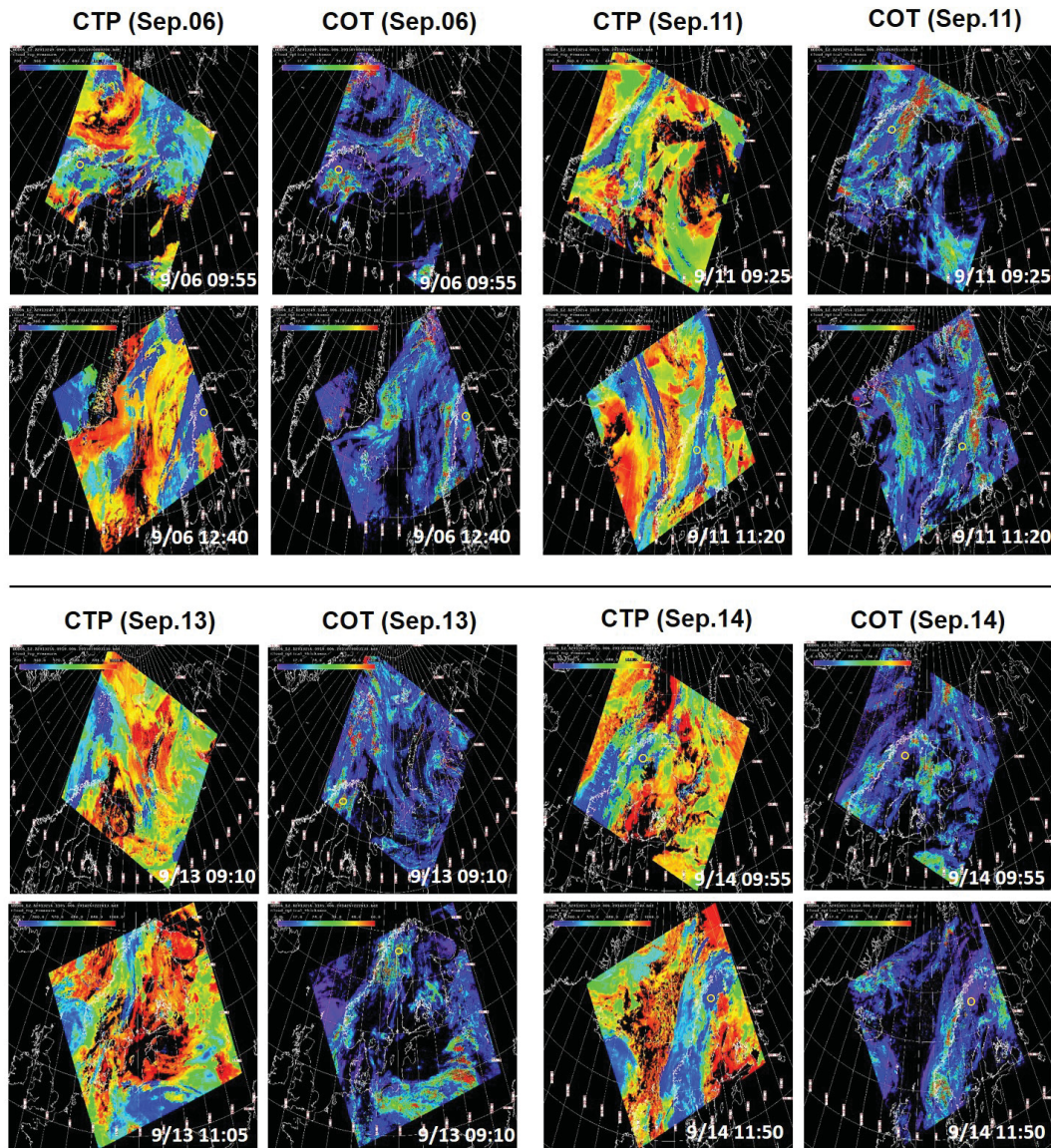


Figure A.19: MODIS-Terra & Aqua cloud top pressure and cloud optical thickness images on Sep.06 and Sep.11,(1st and 2nd rows), Sep.13 and Sep.14 (3rd and 4th rows). Odd and even number rows represent morning and afternoon images, respectively. In the figure, the yellow dot indicates the ground-based measurement site, Kiruna.

BIBLIOGRAPHY

- Baldwin, M., Gray, L., Dunkerton, T., Hamilton, K., Haynes, P., Randel, W., Holton, J., Alexander, M., Hirota, I., Horinouchi, T., Jones, D., Kinnarsley, J., Marquardt, C., Sato, K., and Takahashi, M.: The quasi-biennial oscillation, *Reviews of Geophysics*, 39, 179–229, doi:10.1029/1999RG000073, 2001.
- Bates, D. R. and Nicolet, M.: The photochemistry of atmospheric water vapor, *Journal of Geophysical Research*, 55, 301–327, 1950.
- Beirle, S., Sihler, H., and Wagner, T.: Linearisation of the effects of spectral shift and stretch in DOAS analysis, *Atmospheric Measurement Techniques*, 6, 661–675, doi:10.5194/amt-6-661-2013, 2013.
- Beyer, K., Seago, S., Chang, H., and Molina, M.: Composition and freezing of aqueous H₂SO₄/HNO₃ solutions under polar stratospheric conditions, *Geophysical research letters*, 21, 871–874, 1994.
- Bogumil, K., Orphal, J., Homann, T., Voigt, S., Spietz, P., Fleischmann, O., Vogel, A., Hartmann, M., Kromminga, H., Bovensmann, H., Frerick, J., and Burrows, J.: Measurements of molecular absorption spectra with the SCIAMACHY pre-flight model: Instrument characterization and reference data for atmospheric remote-sensing in the 230–2380 nm region, *Journal of Photochemistry and Photobiology A: Chemistry*, 157, 167–184, doi:10.1016/S1010-6030(03)00062-5, 2003.
- Brenot, H., Theys, N., Clarisse, L., Van Geffen, J., Van Gent, J., Van Roozendaal, M., Van Der A, R., Hurtmans, D., Coheur, P.-F., Clerbaux, C., Valks, P., Hedelt, P., Prata, F., Rason, O., Sievers, K., and Zehner, C.: Support to aviation control service (SACS): An online service for near-real-time satellite monitoring of volcanic plumes, *Natural Hazards and Earth System Sciences*, 14, 1099–1123, doi:10.5194/nhess-14-1099-2014, 2014.
- Brewer, A., Mcelroy, C., and Kerr, J.: Nitrogen dioxide concentrations in the atmosphere, *Nature*, 246, 129–133, doi:10.1038/246129a0, 1973.
- Bugarski, S.: Spektroskopische Messungen der stratosphärischen Spurengase BrO und OCIO in Kiruna (Schweden), Diploma thesis, Institute for Applied Physics of the Technical University of Darmstadt, 2003.
- Butler, J., Battle, M., Bender, M., Montzka, S., Clarke, A., Saltzman, E., Sucher, C., Severinghaus, J., and Elkins, J.: A record of atmospheric halocarbons during the twentieth century from polar firn air, *Nature*, 399, 749–755, doi:10.1038/21586, 1999.
- Butz, A., Bösch, H., Camy-Peyret, C., Chipperfield, M., Dorf, M., Dufour, G., Grunow, K., Jeseck, P., Köhl, S., Payan, S., Pepin, I., Pukite, J., Rozanov, A., Von Savigny, C., Sioris, C., Wagner, T., Weidner, F., and Pfeilsticker, K.: Inter-comparison of stratospheric O₃ and NO₂ abundances retrieved from balloon borne direct sun observations and Envisat/SCIAMACHY limb measurements, *Atmospheric Chemistry and Physics*, 6, 1293–1314, 2006.

- Callis, L. and Lambeth, J.: NO_y formed by precipitating electron events in 1991 and 1992: Descent into the stratosphere as observed by ISAMS, *Geophysical Research Letters*, 25, 1875–1878, 1998.
- Carn, S. and Lopez, T.: Opportunistic validation of sulfur dioxide in the Sarychev Peak volcanic eruption cloud, *Atmospheric Measurement Techniques*, 4, 1705–1712, doi:10.5194/amt-4-1705-2011, 2011.
- Carslaw, K., Luo, B., Clegg, S., Peter, T., Brimblecombe, P., and Crutzen, P.: Stratospheric aerosol growth and HNO₃ gas phase depletion from coupled HNO₃ and water uptake by liquid particles, *Geophysical Research Letters*, 21, 2479–2482, 1994.
- Carslaw, K. S., Peter, T., and Clegg, S. L.: Modeling the composition of liquid stratospheric aerosols, *Reviews of Geophysics*, 35, 125–154, 1997.
- Chapman, S.: XXXV. On ozone and atomic oxygen in the upper atmosphere, *The London, Edinburgh, and Dublin Philosophical Magazine and Journal of Science*, 10, 369–383, 1930.
- Chipperfield, M.: New version of the TOMCAT/SLIMCAT off-line chemical transport model: Intercomparison of stratospheric tracer experiments, *Quarterly Journal of the Royal Meteorological Society: A journal of the atmospheric sciences, applied meteorology and physical oceanography*, 132, 1179–1203, 2006.
- Coffey, M.: Observations of the impact of volcanic activity on stratospheric chemistry, *Journal of Geophysical Research Atmospheres*, 101, 6767–6780, 1996.
- Coffey, M., Mankin, W., and Goldman, A.: Airborne measurements of stratospheric constituents over Antarctica in the austral spring, 1987. 2. Halogen and nitrogen trace gases, *Journal of Geophysical Research*, 94, 1989.
- Connor, B., Siskind, D., Tsou, J., Parrish, A., and Remsberg, E.: Ground-based microwave observations of ozone in the upper stratosphere and mesosphere, *Journal of Geophysical Research*, 99, 16,757–16,770, 1994.
- Cook, P. and Roscoe, H.: Variability and trends in stratospheric NO₂ in Antarctic summer, and implications for stratospheric NO_y, *Atmospheric Chemistry and Physics*, 9, 3601–3612, 2009.
- Crutzen, P.: The influence of nitrogen oxides on the atmospheric ozone content, *Quarterly Journal of the Royal Meteorological Society*, 96, 320–325, doi:10.1002/qj.49709640815, 1970.
- Daumont, D., Brion, J., Charbonnier, J., and Malicet, J.: Ozone UV spectroscopy I: Absorption cross-sections at room temperature, *Journal of Atmospheric Chemistry*, 15, 145–155, doi:10.1007/BF00053756, 1992.
- Dee, D., Uppala, S., Simmons, A., Berrisford, P., Poli, P., Kobayashi, S., Andrae, U., Balmaseda, M., Balsamo, G., Bauer, P., Bechtold, P., Beljaars, A., van de Berg, L., Bidlot, J., Bormann, N., Delsol, C., Dragani, R., Fuentes, M., Geer, A., Haimberger, L., Healy, S., Hersbach, H., Hólm, E., Isaksen, I., Kållberg, P., Köhler, M., Matricardi, M., McNally, A., Monge-Sanz, B., Morcrette, J.-J., Park, B.-K., Peubey, C., de Rosnay, P., Tavolato, C., Thépaut, J.-N., and Vitart, F.: The ERA-Interim reanalysis: Configuration and performance of the data assimilation system, *Quarterly Journal of the Royal Meteorological Society*, 137, 553–597, doi:10.1002/qj.828, 2011.

- Dirksen, R., Boersma, K., Eskes, H., Ionov, D., Bucsele, E., Levelt, P., and Kelder, H.: Evaluation of stratospheric NO₂ retrieved from the Ozone Monitoring Instrument: Intercomparison, diurnal cycle, and trending, *Journal of Geophysical Research Atmospheres*, 116, doi:10.1029/2010JD014943, 2011.
- Dorf, M., Bösch, H., Butz, A., Camy-Peyret, C., Chipperfield, M., Engel, A., Goutail, F., Grunow, K., Hendrick, F., Hrechanyy, S., Naujokat, B., Pommereau, J.-P., Van Roozendaal, M., Sioris, C., Strohm, F., Weidner, F., and Pfeilsticker, K.: Balloon-borne stratospheric BrO measurements: Comparison with Envisat/SCIAMACHY BrO limb profiles, *Atmospheric Chemistry and Physics*, 6, 2483–2501, 2006a.
- Dorf, M., Butler, J., Butz, A., Camy-Peyret, C., Chipperfield, M., Kritten, L., Montzka, S., Simmes, B., Weidner, F., and Pfeilsticker, K.: Long-term observations of stratospheric bromine reveal slow down in growth, *Geophysical Research Letters*, 33, doi:10.1029/2006GL027714, 2006b.
- Dorf, M., Butz, A., Camy-Peyret, C., Chipperfield, M., Kritten, L., and Pfeilsticker, K.: Bromine in the tropical troposphere and stratosphere as derived from balloon-borne BrO observations, *Atmospheric Chemistry and Physics*, 8, 7265–7271, 2008.
- Engel, A., Strunk, M., Müller, M., Haase, H.-P., Poss, C., Levin, I., and Schmidt, U.: Temporal development of total chlorine in the high-latitude stratosphere based on reference distributions of mean age derived from CO₂ and SF₆, *Journal of Geophysical Research: Atmospheres*, 107, 2002.
- Errera, Q. and Fonteyn, D.: Four-dimensional variational chemical assimilation of CRISTA stratospheric measurements, *Journal of Geophysical Research Atmospheres*, 106, 12 253–12 265, 2001.
- Farman, J. C., Gardiner, B. G., and Shanklin, J. D.: Large losses of total ozone in Antarctica reveal seasonal ClO_x/NO_x interaction, *Nature*, 315, 207, 1985.
- Feng, W., Chipperfield, M., Dorf, M., Pfeilsticker, K., and Ricaud, P.: Mid-latitude ozone changes: studies with a 3-D CTM forced by ERA-40 analyses, *Atmospheric Chemistry and Physics*, 7, 2357–2369, 2007.
- Fiedler, M., Frank, H., Gomer, T., Hausmann, M., Pfeilsticker, K., and Platt, U.: Groundbased spectroscopic measurements of stratospheric NO₂ and OClO in Arctic winter 1989/90, *Geophysical Research Letters*, 20, 963–966, doi:10.1029/92GL00088, 1993.
- Fraser, P., Oram, D., Reeves, C., Penkett, S., and McCulloch, A.: Southern Hemispheric halon trends (1978–1998) and global halon emissions, *Journal of Geophysical Research: Atmospheres*, 104, 15 985–15 999, 1999.
- Frieß, U., Hollwedel, J., König-Langlo, G., Wagner, T., and Platt, U.: Dynamics and chemistry of tropospheric bromine explosion events in the Antarctic coastal region, *Journal of Geophysical Research D: Atmospheres*, 109, 2004.
- Frieß, U., Kreher, K., Johnston, P., and Platt, U.: Ground-based DOAS measurements of stratospheric trace gases at two Antarctic stations during the 2002 ozone hole period, *Journal of the Atmospheric Sciences*, 62, 765–777, doi:10.1175/JAS-3319.1, 2005.

- Galle, B., Johansson, M., Rivera, C., Zhang, Y., Kihlman, M., Kern, C., Lehmann, T., Platt, U., Arellano, S., and Hidalgo, S.: Network for Observation of Volcanic and Atmospheric Change (NOVAC) - A global network for volcanic gas monitoring: Network layout and instrument description, *Journal of Geophysical Research Atmospheres*, 115, doi:10.1029/2009JD011823, 2010.
- Gil, M., Puertedura, O., Yela, M., Parrondo, C., Jadhav, D., and Thorkelsson, B.: OClO, NO₂ and O₃ total column observations over Iceland during the winter 1993/94, *Geophysical Research Letters*, 23, 3337–3340, 1996.
- Gil, M., Yela, M., Gunn, L., Richter, A., Alonso, I., Chipperfield, M., Cuevas, E., Iglesias, J., Navarro, M., Puertedura, O., and Rodríguez, S.: NO₂ climatology in the northern subtropical region: Diurnal, seasonal and interannual variability, *Atmospheric Chemistry and Physics*, 8, 1635–1648, 2008.
- Gottschalk, M.: Characterisation of a new CCD-Detector for the Zenith-DOAS in Kiruna, Sweden, Bachelor thesis, Johannes Gutenberg-University of Mainz, 2013.
- Goutail, F., Pommereau, J.-P., Pazmino, A., Lefevre, F., Chipperfield, M., Feng, W., Van Roozendaal, M., Eriksen, P., Stebel, K., Kivi, R., Bogner, K., Strong, K., and Walker, K.: Total ozone loss during the 2016/17 Arctic winter and comparison to previous years, vol. 19, European Geosciences Union General Assembly, European Geosciences Union General Assembly, 2017.
- Greenblatt, G., Orlando, J., Burkholder, J., and Ravishankara, A.: Absorption measurements of oxygen between 330 and 1140 nm, *Journal of Geophysical Research*, 95, 18,577–"18,582", 1990.
- Gruzdev, A.: Latitudinal structure of variations and trends in stratospheric NO₂, *International Journal of Remote Sensing*, 30, 4227–4246, doi:10.1080/01431160902822815, 2009.
- Hanson, D. and Ravishankara, A.: Heterogeneous chemistry of bromine species in sulfuric acid under stratospheric conditions, *Geophysical research letters*, 22, 385–388, 1995.
- Hanson, D., Ravishankara, A., and Lovejoy, E.: Reaction of BrONO₂ with H₂O on sub-micron sulfuric acid aerosol and the implications for the lower stratosphere, *Journal of Geophysical Research: Atmospheres*, 101, 9063–9069, 1996.
- Harrison, A.: Midsummer stratospheric NO₂ at latitude 45°S, *Canadian Journal of Physics*, 57, 1110–1117, doi:10.1139/p79-155, 1979.
- Hegglin, Michaela Land Fahey, D., McFarland, M., Montzka, S. A., and Nash, E. R.: Twenty Questions and Answers About the Ozone Layer: 2014 Update, Scientific Assessment of Ozone Depletion: 2014, World Meteorological Organization, Geneva, Switzerland, 2015.
- Hendrick, F., Barret, B., Van Roozendaal, M., Boesch, H., Butz, A., De Mazière, M., Goutail, F., Hermans, C., Lambert, J.-C., Pfeilsticker, K., and Pommereau, J.-P.: Retrieval of nitrogen dioxide stratospheric profiles from ground-based zenith-sky UV-visible observations: Validation of the technique through correlative comparisons, *Atmospheric Chemistry and Physics*, 4, 2091–2106, 2004.

- Hendrick, F., Van Roozendael, M., Chipperfield, M., Dorf, M., Goutail, F., Yang, X., Fayt, C., Hermans, C., Pfeilsticker, K., Pommereau, J.-P., Pyle, J., Theys, N., and De Mazière, M.: Retrieval of stratospheric and tropospheric BrO profiles and columns using ground-based zenith-sky DOAS observations at Harestua, 60° N, *Atmospheric Chemistry and Physics*, 7, 4869–4885, 2007.
- Hendrick, F., Johnston, P., De Mazière, M., Fayt, C., Hermans, C., Kreher, K., Theys, N., Thomas, A., and Van Roozendael, M.: One-decade trend analysis of stratospheric BrO over Harestua (60°N) and Lauder (45°S) reveals a decline, *Geophysical Research Letters*, 35, doi:10.1029/2008GL034154, 2008.
- Hendrick, F., Rozanov, A., Johnston, P., Bovensmann, H., De Mazière, M., Fayt, C., Hermans, C., Kreher, K., Lotz, W., Sinnhuber, B.-M., Theys, N., Thomas, A., Burrows, J., and Van Roozendael, M.: Multi-year comparison of stratospheric BrO vertical profiles retrieved from SCIAMACHY limb and ground-based UV-visible measurements, *Atmospheric Measurement Techniques*, 2, 273–285, 2009a.
- Hendrick, F., Rozanov, A., Johnston, P., Puentedura, O., Bovensmann, H., Burrows, J., Mazière, D., Gil, M., Kreher, K., Sinnhuber, B.-M., Theys, N., and Van Roozendael, M.: Trend analysis of stratospheric BrO: Comparison between SCIAMACHY limb and ground-based UV-visible observations, European Space Agency, Atmospheric Science Conference, 2009b.
- Hendrick, F., Mahieu, E., Bodeker, G., Boersma, K., Chipperfield, M., De Mazière, M., De Smedt, I., Demoulin, P., Fayt, C., Hermans, C., Kreher, K., Lejeune, B., Pinardi, G., Servais, C., Stübi, R., Van Der A, R., Vernier, J.-P., and Van Roozendael, M.: Analysis of stratospheric NO₂ trends above Jungfraujoch using ground-based UV-visible, FTIR, and satellite nadir observations, *Atmospheric Chemistry and Physics*, 12, 8851–8864, doi:10.5194/acp-12-8851-2012, 2012.
- Hönninger, G., von Friedeburg, C., and Platt, U.: Multi axis differential optical absorption spectroscopy (MAX-DOAS), *Atmospheric Chemistry and Physics*, 4, 231–254, 2004.
- Hood, L., Soukharev, B., and McCormack, J.: Decadal variability of the tropical stratosphere: Secondary influence of the El Niño/Southern Oscillation, *Journal of Geophysical Research Atmospheres*, 115, doi:10.1029/2009JD012291, 2010.
- Höpfner, M., Orphal, J., Von Clarmann, T., Stiller, G., and Fischer, H.: Stratospheric BrONO₂ observed by MIPAS, *Atmospheric Chemistry and Physics*, 9, 1735–1746, 2009.
- Humphreys, W. J.: *Physics of the air, Meteorology, Atmosphere, Climatology*, Philadelphia, Pub. for the Franklin Institute of the state of Pennsylvania by J.B. Lippincott Company, URL <https://archive.org/details/physicsofair00hump>, 1940.
- Jöckel, P., Tost, H., Pozzer, A., Brühl, C., Buchholz, J., Ganzeveld, L., Hoor, P., Kerkweg, A., Lawrence, M., Sander, R., Steil, B., Stiller, G., Tanarhte, M., Taraborrelli, D., Van Aardenne, J., and Lelieveld, J.: The atmospheric chemistry general circulation model ECHAM5/MESy1: Consistent simulation of ozone from the surface to the mesosphere, *Atmospheric Chemistry and Physics*, 6, 5067–5104, 2006.

- Jöckel, P., Kerkweg, A., Pozzer, A., Sander, R., Tost, H., Riede, H., Baumgaertner, A., Gromov, S., and Kern, B.: Development cycle 2 of the Modular Earth Submodel System (MESSy2), *Geoscientific Model Development*, 3, 717–752, doi:10.5194/gmd-3-717-2010, 2010.
- Johnston, H.: Reduction of stratospheric ozone by nitrogen oxide catalysts from supersonic transport exhaust, *Science*, 173, 517–522, 1971.
- Khaykin, S., Godin-Beekmann, S., Keckhut, P., Hauchecorne, A., Jumelet, J., Vernier, J.-P., Bourassa, A., Degenstein, D., Rieger, L., Bingen, C., Vanhellemont, F., Robert, C., DeLand, M., and Bhartia, P.: Variability and evolution of the midlatitude stratospheric aerosol budget from 22 years of ground-based lidar and satellite observations, *Atmospheric Chemistry and Physics*, 17, 1829–1845, doi:10.5194/acp-17-1829-2017, 2017.
- Koike, M., Kondo, Y., Matthews, W., Johnston, P., and Yamazaki, K.: Decrease of stratospheric NO₂ at 44°N caused by Pinatubo volcanic aerosols, *Geophysical Research Letters*, 20, 1975–1978, doi:10.1029/93GL01800, 1993.
- Kovalenko, L., Livesey, N., Salawitch, R., Camy-Peyret, C., Chipperfield, M., Cofield, R., Dorf, M., Drouin, B., Froidevaux, L., Fuller, R., et al.: Validation of aura microwave limb sounder BrO observations in the stratosphere, *Journal of Geophysical Research: Atmospheres*, 112, 2007.
- Kraus, S.: DOASIS a framework design for DOAS, Doctoral dissertation, Technische Informatik, Univ. Mannheim, 2006.
- Kreher, K., Keys, J., Johnston, P., Platt, U., and Liu, X.: Ground-based measurements of OC₁O and HCl in austral spring 1993 at Arrival Heights, Antarctica, *Geophysical Research Letters*, 23, 1545–1548, 1996.
- Kreher, K., Johnston, P., Wood, S., Nardi, B., and Platt, U.: Ground-based measurements of tropospheric and stratospheric BrO at Arrival Heights, Antarctica, *Geophysical Research Letters*, 24, 3021–3024, 1997.
- Kromminga, H., Orphal, J., Spietz, P., Voigt, S., and Burrows, J.: New measurements of OCIO absorption cross-sections in the 325–435 nm region and their temperature dependence between 213 and 293 K, *Journal of Photochemistry and Photobiology A: Chemistry*, 157, 149–160, doi:10.1016/S1010-6030(03)00071-6, 2003.
- Kühl, S.: Quantifying Stratospheric chlorine chemistry by the satellite spectrometers GOME and SCIAMACHY, Doctoral dissertation, University of Heidelberg, Heidelberg, Germany, 2005.
- Kühl, S., Wilms-Grabe, W., Frankenberg, C., Grzegorski, M., Platt, U., and Wagner, T.: Comparison of OCIO nadir measurements from SCIAMACHY and GOME, *Advances in Space Research*, 37, 2247–2253, doi:10.1016/j.asr.2005.06.061, 2006.
- Kühl, S., Pukite, J., Deutschmann, T., Platt, U., and Wagner, T.: SCIAMACHY limb measurements of NO₂, BrO and OCIO. Retrieval of vertical profiles: Algorithm, first results, sensitivity and comparison studies, *Advances in Space Research*, 42, 1747–1764, doi:10.1016/j.asr.2007.10.022, 2008.

- Lampel, J., Pöhler, D., Polyansky, O., Kyuberis, A., Zobov, N., Tennyson, J., Lodi, L., Frieß, U., Wang, Y., Beirle, S., Platt, U., and Wagner, T.: Detection of water vapour absorption around 363 nm in measured atmospheric absorption spectra and its effect on DOAS evaluations, *Atmospheric Chemistry and Physics*, 17, 1271–1295, doi:10.5194/acp-17-1271-2017, 2017.
- Lary, D.: Gas phase atmospheric bromine photochemistry, *Journal of Geophysical Research Atmospheres*, 101, 1505–1516, 1996.
- Lary, D., Chipperfield, M., Toumi, R., and Lenton, T.: Heterogeneous atmospheric bromine chemistry, *Journal of Geophysical Research: Atmospheres*, 101, 1489–1504, 1996.
- Liley, J., Johnston, P., McKenzie, R., Thomas, A., and Boyd, I.: Stratospheric NO₂ variations from a long time series at Lauder, New Zealand, *Journal of Geophysical Research Atmospheres*, 105, 11 633–11 640, 2000.
- Luo, B., Carslaw, K. S., Peter, T., and Clegg, S. L.: Vapour pressures of H₂SO₄/HNO₃/HCl/HBr/H₂O solutions to low stratospheric temperatures, *Geophysical research letters*, 22, 247–250, 1995.
- Malicet, J., Daumont, D., Charbonnier, J., Parisse, C., Chakir, A., and Brion, J.: Ozone UV spectroscopy. II. Absorption cross-sections and temperature dependence, *Journal of Atmospheric Chemistry*, 21, 263–273, doi:10.1007/BF00696758, 1995.
- Mankin, W., Coffey, M., Goldman, A., Schoeberl, M., Lait, L., and Newman, P.: Airborne measurements of stratospheric constituents over the Arctic in the winter of 1989, *Geophysical Research Letters*, 17, 473–476, doi:10.1029/GL017i004p00473, 1990.
- Marquardt, D. W.: An Algorithm for Least-Squares Estimation of Nonlinear Parameters, *Journal of the Society for Industrial and Applied Mathematics*, 11, 431–441, doi:10.1137/0111030, 1963.
- Mayer, B. and Kylling, A.: Technical note: The libRadtran software package for radiative transfer calculations - description and examples of use, *Atmospheric Chemistry and Physics*, 5, 1855–1877, doi:10.5194/acp-5-1855-2005, 2005.
- McElroy, M. B., Salawitch, R. J., and Wofsy, S. C.: Antarctic O₃: Chemical mechanisms for the spring decrease, *Geophysical research letters*, 13, 1296–1299, 1986.
- McKenzie, R. and Johnston, P.: Seasonal variations in stratospheric NO₂ at 45°S, *Geophysical Research Letters*, 9, 1255–1258, doi:10.1029/GL009i011p01255, 1982.
- McLinden, C., Haley, C., Lloyd, N., Hendrick, F., Rozanov, A., Sinnhuber, B.-M., Goutail, F., Degenstein, D., Llewellyn, E., Sioris, C., et al.: Odin/OSIRIS observations of stratospheric BrO: Retrieval methodology, climatology, and inferred Bry, *Journal of Geophysical Research: Atmospheres*, 115, 2010.
- Millán, L., Livesey, N., Read, W., Froidevaux, L., Kinnison, D., Harwood, R., MacKenzie, I., and Chipperfield, M.: New Aura Microwave Limb Sounder observations of BrO and implications for Bry, *Atmospheric Measurement Techniques*, 5, 1741–1751, doi:10.5194/amt-5-1741-2012, 2012.
- Miller Jr, H., Sanders, R., and Solomon, S.: Observations and interpretation of column OClO seasonal cycles at two polar sites, *Journal of Geophysical Research Atmospheres*, 104, 18 769–18 783, 1999.

- Molina, L. and Molina, M.: Production of chlorine oxide (Cl_2O_2) from the self-reaction of the chlorine oxide (ClO) radical, *Journal of Physical Chemistry*, 91, 433–436, 1987.
- Molina, M. and Rowland, F.: Stratospheric sink for chlorofluoromethanes: Chlorine atomcatalysed destruction of ozone, *Nature*, 249, 810–812, doi:10.1038/249810a0, 1974.
- Montzka, S., Butler, J., Hall, B., Mondeel, D., and Elkins, J.: A decline in tropospheric organic bromine, *Geophysical Research Letters*, 30, 2003a.
- Montzka, S., Fraser, P. L. A., Butler, J. H., Connell, P. S., Cunnold, D. M. and Daniel, J. S., Derwent, R. G., Lal, S., McCulloch, A., Oram, D. E., Reeves, C. E., Sanhueza, E., Steele, L. P., Velders, G. J. M., Weiss, R. F., and Zander, R. J.: Chapter 1 Controlled substances and other source gases, in: *Scientific Assessment of Ozone Depletion: 2002*, Global Ozone Research and Monitoring Project, vol. Report No. 47, World Meteorological Organization Global Ozone Research and Monitoring Project, 2003b.
- Murphy, D. and Thomson, D.: Halogen ions and NO^+ in the mass spectra of aerosols in the upper troposphere and lower stratosphere, *Geophysical Research Letters*, 27, 3217–3220, 2000.
- Newville, M., Stensitzki, T., Allen, D. B., and Ingargiola, A.: LMFIT: Non-Linear Least-Square Minimization and Curve-Fitting for Python, doi:10.5281/zenodo.11813, URL <https://doi.org/10.5281/zenodo.11813>, 2014.
- Noxon, J.: Nitrogen dioxide in the stratosphere and troposphere measured by ground based absorption spectroscopy, *Science*, 189, 547–549, 1975.
- Noxon, J., Whipple Jr., E., and Hyde, R.: STRATOSPHERIC NO_2 - 1. OBSERVATIONAL METHOD AND BEHAVIOR AT MID-LATITUDE., *Journal of Geophysical Research*, 84, 5047–5065, 1979.
- Oetjen, H., Wittrock, F., Richter, A., Chipperfield, M., Medeke, T., Sheode, N., Sinnhuber, B.-M., Sinnhuber, M., and Burrows, J.: Evaluation of stratospheric chlorine chemistry for the Arctic spring 2005 using modelled and measured OClO column densities, *Atmospheric Chemistry and Physics*, 11, 689–703, doi:10.5194/acp-11-689-2011, 2011.
- Oram, D., Ashfold, M., Laube, J., Gooch, L., Humphrey, S., Sturges, W., Leedham-Elvidge, E., Forster, G., Harris, N., Iqbal Mead, M., Samah, A., Phang, S., Ou-Yang, C.-F., Lin, N.-H., Wang, J.-L., Baker, A., Brenninkmeijer, C., and Sherry, D.: A growing threat to the ozone layer from short-lived anthropogenic chlorocarbons, *Atmospheric Chemistry and Physics*, 17, 11 929–11 941, doi:10.5194/acp-17-11929-2017, 2017.
- Otten, C.: Messung stratosphärischer Spurenstoffe in den Wintern 1992/93 bis 1994/95 über Kiruna in Nordschweden, Doctoral dissertation, Institute for Environmental Physics of the Ruprecht-Karls-University Heidelberg, 1997.
- Otten, C., Ferlemann, F., Platt, U., Wagner, T., and Pfeilsticker, K.: Groundbased Doas UV/visible measurements at Kiruna (Sweden) during the sesame winters 1993/94 and 1994/95., *Journal of Atmospheric Chemistry*, 30, 141–162, doi:10.1023/A:1005810732347, URL <http://dx.doi.org/10.1023/A:1005810732347>, 1998.

- Perner, D., Ehhalt, D., Pätz, H., Platt, U., Röth, E., and Volz, A.: OH Radicals in the lower troposphere, *Geophysical Research Letters*, 3, 466–468, doi:10.1029/GL0031008p00466, 1976.
- Pfeilsticker, K., Sturges, W., Bösch, H., Camy-Peyret, C., Chipperfield, M., Engel, A., Fitzenberger, R., Müller, M., Payan, S., and Sinnhuber, B.-M.: Lower stratospheric organic and inorganic bromine budget for the Arctic winter 1998/99, *Geophysical Research Letters*, 27, 3305–3308, 2000.
- Pinardi, G., Van Roozendaal, M., Hendrick, F., and Valks, P.: Validation report of GOME-2 GDP 4.8 OCIO slant column data record for MetOp-A and -B DRR, http://acsaf.org/docs/vr/Validation_Report_DR_OCIO_GDP48_May_2017.pdf, 2017.
- Platt, U. and Stutz, J.: *Differential Optical Absorption Spectroscopy, Physics of Earth and Space Environments*, Springer-Verlag Berlin Heidelberg, URL <http://www.springer.com/us/book/9783540211938>, 2008.
- Platt, U., Marquard, L., Wagner, T., and Perner, D.: Corrections for zenith scattered light DOAS, *Geophysical research letters*, 24, 1759–1762, 1997.
- Pommereau, J.-P. and Piquard, J.: Ozone and nitrogen dioxide vertical distributions by UV-visible solar occultation from balloons, *Geophysical Research Letters*, 21, 1227–1230, doi:10.1029/94GL00389, 1994.
- Pommereau, J. P., Goutail, F., Pundt, I., Pyle, J., Danis, F., Hansford, G., Freshwater, R., Robinson, A., Jones, R., Harris, N., Adriani, A., Cairo, F., Pulvurenti, L., Difrancesco, G., Kirkwood, S., Nilson, H., Arvelius, J., Woods, P., Swann, N., Howison, I., Garcelon, S., Gardiner, T., Dëshler, T., and Buivan, A.: Small Balloons for Stratospheric Ozone Research and Satellite Validation, *European Rocket and Balloon Programs and Related Research, Proceedings of the 14th ESA Symposium held 31 May-3 June, 1999 in Potsdam, Germany*, 437, 609–614, 1990.
- Portmann, R., Daniel, J., and Ravishankara, A.: Stratospheric ozone depletion due to nitrous oxide: Influences of other gases, *Philosophical Transactions of the Royal Society B: Biological Sciences*, 367, 1256–1264, doi:10.1098/rstb.2011.0377, 2012.
- Preston, K., Jones, R., and Roscoe, H.: Retrieval of NO₂ vertical profiles from ground-based UV-visible measurements: Method and validation, *Journal of Geophysical Research Atmospheres*, 102, 19 089–19 097, 1997.
- Preston, K., Fish, D., Roscoe, H., and Jones, R.: Accurate derivation of total and stratospheric vertical columns of NO₂ from ground-based zenith-sky measurements, *Journal of Atmospheric Chemistry*, 30, 163–172, doi:10.1023/A:1006019628406, 1998.
- Pukite, J., Kühl, S., Deutschmann, T., Wilms-Grabe, W., Friedeburg, C., Platt, U., and Wagner, T.: Retrieval of stratospheric trace gases from SCIAMACHY limb measurements, *European Space Agency, Atmospheric Science Conference*, 2006.
- Pukite, J., Kühl, S., Deutschmann, T., Platt, U., and Wagner, T.: Accounting for the effect of horizontal gradients in limb measurements of scattered sunlight, *Atmospheric Chemistry and Physics*, 8, 3045–3060, 2008.

- Pukite, J., Kühl, S., Deutschmann, T., Platt, U., and Wagner, T.: Extending differential optical absorption spectroscopy for limb measurements in the UV, *Atmospheric Measurement Techniques*, 3, 631–653, doi:10.5194/amt-3-631-2010, 2010.
- Pundt, I., Pommereau, J.-P., Chipperfield, M., Van Roozendaal, M., and Goutail, F.: Climatology of the stratospheric BrO vertical distribution by balloon-borne UV-visible spectrometry, *Journal of Geophysical Research Atmospheres*, 107, doi:10.1029/2002JD002230, 2002.
- Raffalski, U., Hochschild, G., Kopp, G., and Urban, J.: Evolution of stratospheric ozone during winter 2002/2003 as observed by a ground-based millimetre wave radiometer at Kiruna, Sweden, *Atmospheric Chemistry and Physics*, 5, 1399–1407, 2005.
- Randall, C., Harvey, V., Manney, G., Orsolini, Y., Codrescu, M., Sioris, C., Brohede, S., Haley, C., Gordley, L., Zawodny, J., and Russell, J.: Stratospheric effects of energetic particle precipitation in 2003–2004, *Geophysical Research Letters*, 32, 1–4, doi:10.1029/2004GL022003, 2005.
- Richter, A.: The MAXDOAS instrument and measurements, http://http://iup.uni-bremen.de/doas/maxdoas_instrument.htm, 2018.
- Richter, A., Wittrock, F., Weber, M., Beirle, S., Kühl, S., Platt, U., Wagner, T., Wilms-Grabe, W., and Burrows, J.: GOME observations of stratospheric trace gas distributions during the splitting vortex event in the Antarctic winter of 2002. Part I: Measurements, *Journal of the Atmospheric Sciences*, 62, 778–785, 2005.
- Richter, A., Begoin, M., Hilboll, A., and Burrows, J.: An improved NO₂ retrieval for the GOME-2 satellite instrument, *Atmospheric Measurement Techniques*, 4, 1147–1159, doi:10.5194/amt-4-1147-2011, 2011.
- Rienecker, M., Suarez, M., Gelaro, R., Todling, R., Bacmeister, J., Liu, E., Bosilovich, M., Schubert, S., Takacs, L., Kim, G.-K., Bloom, S., Chen, J., Collins, D., Conaty, A., Da Silva, A., Gu, W., Joiner, J., Koster, R., Lucchesi, R., Molod, A., Owens, T., Pawson, S., Pegion, P., Redder, C., Reichle, R., Robertson, F., Ruddick, A., Sienkiewicz, M., and Woollen, J.: MERRA: NASA's modern-era retrospective analysis for research and applications, *Journal of Climate*, 24, 3624–3648, doi:10.1175/JCLI-D-11-00015.1, 2011.
- Robles-Gonzalez, C., Navarro-Comas, M., Puentedura, O., Schneider, M., Hase, F., Garcia, O., Blumenstock, T., and Gil-Ojeda, M.: Intercomparison of stratospheric nitrogen dioxide columns retrieved from ground-based DOAS and FTIR and satellite DOAS instruments over the subtropical Izana station, *Atmospheric Measurement Techniques*, 9, 4471–4485, doi:10.5194/amt-9-4471-2016, 2016.
- Rodgers, C.: Characterization and error analysis of profiles retrieved from remote sounding measurements, *Journal of Geophysical Research*, 95, 5587–5595, 1990.
- Rodgers, C.: *Inverse Methods for Atmospheric Sounding: Theory and Practice*, Series on atmospheric, oceanic and planetary physics, World Scientific, URL <https://books.google.de/books?id=p3b3ngEACAAJ>, 2000.
- Rodgers, C. and Connor, B.: Intercomparison of remote sounding instruments, *Journal of Geophysical Research D: Atmospheres*, 108, ACH 13–1 – ACH 13–14, 2003.

- Ryan, N., Walker, K., Raffalski, U., Kivi, R., Gross, J., and Manney, G.: Ozone profiles above Kiruna from two ground-based radiometers, *Atmospheric Measurement Techniques*, 9, 4503–4519, doi:10.5194/amt-9-4503-2016, 2016.
- Salawitch, R., Canty, T., Kurosu, T., Chance, K., Liang, Q., da Silva, A., Pawson, S., Nielsen, J., Rodriguez, J., Bhartia, P., et al.: A new interpretation of total column BrO during Arctic spring, *Geophysical Research Letters*, 37, 2010.
- Salawitch, R. J., Weisenstein, D. K., Kovalenko, L. J., Sioris, C. E., Wennberg, P. O., Chance, K., Ko, M. K., and McLinden, C. A.: Sensitivity of ozone to bromine in the lower stratosphere, *Geophysical research letters*, 32, 2005.
- Schiller, C., Wahner, A., Platt, U., Dorn, H., Callies, J., and Ehhalt, D.: Near UV atmospheric absorption measurements of column abundances during Airborne Arctic Stratospheric Expedition, January – February 1989: 2. OClO observations, *Geophysical Research Letters*, 17, 501–504, doi:10.1029/GL017i004p00501, 1990.
- Schmidt, A., Leadbetter, S., Theys, N., Carboni, E., Witham, C., Stevenson, J., Birch, C., Thordarson, T., Turnock, S., Barsotti, S., Delaney, L., Feng, W., Grainger, R., Hort, M., Höskuldsson, Á., Ialongo, I., Ilyinskaya, E., Jóhannsson, T., Kenny, P., Mather, T., Richards, N., and Shepherd, J.: Satellite detection, long-range transport, and air quality impacts of volcanic sulfur dioxide from the 2014-2015 flood lava eruption at Bárarbunga (Iceland), *Journal of Geophysical Research: Atmospheres*, 120, 9739–9757, doi:10.1002/2015JD023638, 2015.
- Schofield, R., Connor, B., Kreher, K., Johnston, P., and Rodgers, C.: The retrieval of profile and chemical information from ground-based UV-visible spectroscopic measurements, *Journal of Quantitative Spectroscopy and Radiative Transfer*, 86, 115–131, doi:10.1016/S0022-4073(03)00278-4, 2004.
- Schofield, R., Johnston, P., Thomas, A., Kreher, K., Connor, B., Wood, S., Shooter, D., Chipperfield, M., Richter, A., Von Glasow, R., et al.: Tropospheric and stratospheric BrO columns over Arrival Heights, Antarctica, 2002, *Journal of Geophysical Research: Atmospheres*, 111, 2006.
- Seidel, D., Li, J., Mears, C., Moradi, I., Nash, J., Randel, W., Saunders, R., Thompson, D., and Zou, C.-Z.: Stratospheric temperature changes during the satellite era, *Journal of Geophysical Research: Atmospheres*, 121, 664–681, doi:10.1002/2015JD024039, 2016.
- Serdychenko, A., Gorshelev, V., Weber, M., Chehade, W., and Burrows, J.: High spectral resolution ozone absorption cross-sections Part 2: Temperature dependence, *Atmospheric Measurement Techniques*, 7, 625–636, doi:10.5194/amt-7-625-2014, 2014.
- Sessler, J., Chipperfield, M., Pyle, J., and Toumi, R.: Stratospheric OClO measurements as a poor quantitative indicator of chlorine activation, *Geophysical Research Letters*, 22, 687–690, doi:10.1029/95GL00202, 1995.
- Shindell, D.: Solar cycle variability, ozone, and climate, *Science*, 284, 305–308, 1999.
- Sinnhuber, B.-M., Arlander, D., Bovensmann, H., Burrows, J., Chipperfield, M., Enell, C.-F., Frieß, U., Hendrick, F., Johnston, P., Jones, R., et al.: Comparison of measurements and model calculations of stratospheric bromine monoxide, *Journal of Geophysical Research: Atmospheres*, 107, 2002.

- Sinnhuber, B.-M., Rozanov, A., Sheode, N., Afe, O., Richter, A., Sinnhuber, M., Wittrock, F., Burrows, J., Stiller, G., Von Clarmann, T., et al.: Global observations of stratospheric bromine monoxide from SCIAMACHY, *Geophysical research letters*, 32, 2005.
- Sinnhuber, B.-M., Von Der Gathen, P., Sinnhuber, M., Rex, M., König-Langlo, G., and Oltmans, S.: Large decadal scale changes of polar ozone suggest solar influence, *Atmospheric Chemistry and Physics*, 6, 1835–1841, 2006.
- Sioris, C., Kovalenko, L., McLinden, C., Salawitch, R., Van Roozendaal, M., Goutail, F., Dorf, M., Pfeilsticker, K., Chance, K., Von Savigny, C., et al.: Latitudinal and vertical distribution of bromine monoxide in the lower stratosphere from Scanning Imaging Absorption Spectrometer for Atmospheric Cartography limb scattering measurements, *Journal of Geophysical Research: Atmospheres*, 111, 2006.
- Sissenwine, N., Dubin, M., and Wexler, H.: The US standard atmosphere, 1962, *Journal of Geophysical Research*, 67, 3627–3630, 1962.
- Solomon, S.: The mystery of the Antarctic Ozone “Hole”, *Reviews of Geophysics*, 26, 131–148, doi:10.1029/RG026i001p00131, 1988.
- Solomon, S., Schmeltekopf, A., and Sanders, R.: On the interpretation of zenith sky absorption measurements, *Journal of Geophysical Research*, 92, 8311–8319, 1987.
- Solomon, S., Ivy, D., Kinnison, D., Mills, M., Neely, R., and Schmidt, A.: Emergence of healing in the Antarctic ozone layer, *Science*, 353, 269–274, doi:10.1126/science.aae0061, 2016.
- Stachnik, R., Millán, L., Jarnot, R., Monroe, R., McLinden, C., Kühl, S., Pukite, J., Shiotani, M., Suzuki, M., Kasai, Y., Goutail, F., Pommereau, J., Dorf, M., and Pfeilsticker, K.: Stratospheric BrO abundance measured by a balloon-borne submillimeterwave radiometer, *Atmospheric Chemistry and Physics*, 13, 3307–3319, doi:10.5194/acp-13-3307-2013, 2013.
- Stutz, J. and Platt, U.: Numerical analysis and estimation of the statistical error of differential optical absorption spectroscopy measurements with least-squares methods, *Applied Optics*, 35, 6041–6053, 1996.
- Tapping, K.: The 10.7 cm solar radio flux (F_{10.7}), *Space Weather*, 11, 394–406, 2013.
- Thalman, R. and Volkamer, R.: Temperature dependent absorption cross-sections of O₂-O₂ collision pairs between 340 and 630 nm and at atmospherically relevant pressure, *Physical Chemistry Chemical Physics*, 15, 15 371–15 381, doi:10.1039/c3cp50968k, 2013.
- Theys, N., Van Roozendaal, M., Errera, Q., Chabrilat, S., Daerden, F., Hendrick, F., Loyola, D., and Valks, P.: A stratospheric BrO climatology based on the bascoe 3D chemical transport model, SP-636, 2007a.
- Theys, N., Van Roozendaal, M., Hendrick, F., Fayt, C., Hermans, C., Baray, J.-L., Goutail, F., Pommereau, J.-P., and De Mazière, M.: Retrieval of stratospheric and tropospheric BrO columns from multi-axis DOAS measurements at Reunion Island (21°S, 56°E), *Atmospheric Chemistry and Physics*, 7, 4733–4749, 2007b.
- Tørnkvist, K., Arlander, D., and Sinnhuber, B.-M.: Ground-based UV measurements of BrO and OCIO over Ny-Ålesund during winter 1996 and 1997 and Andøya during winter

- 1998/99, *Journal of Atmospheric Chemistry*, 43, 75–106, doi:10.1023/A:1019905006390, 2002.
- Van Roozendael, M. and Hendrick, F.: Recommendations for NO₂ column retrieval from NDACC zenith-sky UV-VIS spectrometer, http://ndacc-uvvis-wg.aeronomie.be/tools/NDACC_UVVIS-WG_NO2settings_v4.pdf, 2012.
- Van Roozendael, M., Hermans, C., De Mazière, M., and Simon, P.: Stratospheric NO₂ observations at the Jungfraujoch Station between June 1990 and May 1992, *Geophysical Research Letters*, 21, 1383–1386, doi:10.1029/93GL02432, 1994.
- Van Roozendael, M., De Mazière, M., Hermans, C., Simon, P., Pommereau, J.-P., Goutail, F., Tie, X., Brasseur, G., and Granier, C.: Ground-based observations of stratospheric NO₂ at high and midlatitudes in Europe after the Mount Pinatubo eruption, *Journal of Geophysical Research Atmospheres*, 102, 19 171–19 176, 1997.
- Vandaele, A., Hermans, C., Simon, P., Carleer, M., Colin, R., Fally, S., Mérienne, M., Jenouvrier, A., and Coquart, B.: Measurements of the NO₂ absorption cross-section from 42,000 cm⁻¹ to 10,000 cm⁻¹ (238–1000 nm) at 220 K and 294 K, *Journal of Quantitative Spectroscopy and Radiative Transfer*, 59, 171–184, 1998.
- Veefkind, J., De Haan, J., Brinksma, E., Kroon, M., and Levelt, P.: Total ozone from the Ozone Monitoring Instrument (OMI) using the DOAS technique, *IEEE Transactions on Geoscience and Remote Sensing*, 44, 1239–1244, doi:10.1109/TGRS.2006.871204, 2006.
- Wagner, T., Erle, F., Marquard, L., Otten, C., Pfeilsticker, K., Senne, T., Stutz, J., and Platt, U.: Cloudy sky optical paths as derived from differential optical absorption spectroscopy observations, *Journal of Geophysical Research Atmospheres*, 103, 25 307–25 321, 1998.
- Wagner, T., Leue, C., Pfeilsticker, K., and Platt, U.: Monitoring of the stratospheric chlorine activation by Global Ozone Monitoring Experiment (GOME) OCIO measurements in the austral and boreal winters 1995 through 1999, *Journal of Geophysical Research Atmospheres*, 106, 4971–4986, 2001.
- Wagner, T., Beirle, S., and Deutschmann, T.: Three-dimensional simulation of the Ring effect in observations of scattered sun light using Monte Carlo radiative transfer models, *Atmospheric Measurement Techniques*, 2, 113–124, 2009.
- Wagner, T., Apituley, A., Beirle, S., Dörner, S., Friess, U., Remmers, J., and Shaiganfar, R.: Cloud detection and classification based on MAX-DOAS observations, *Atmospheric Measurement Techniques*, 7, 1289–1320, doi:10.5194/amt-7-1289-2014, 2014.
- Wagner, T., Beirle, S., Remmers, J., Shaiganfar, R., and Wang, Y.: Absolute calibration of the colour index and O₄ absorption derived from Multi AXis (MAX-)DOAS measurements and their application to a standardised cloud classification algorithm, *Atmospheric Measurement Techniques*, 9, 4803–4823, doi:10.5194/amt-9-4803-2016, 2016.
- Wamsley, P., Elkins, J., Fahey, D., Dutton, G., Volk, C., Myers, R., Montzka, S., Butler, J., Clarke, A., Fraser, P., et al.: Distribution of halon-1211 in the upper troposphere and lower stratosphere and the 1994 total bromine budget, *Journal of Geophysical Research: Atmospheres*, 103, 1513–1526, 1998.

- Wang, Y., Penning De Vries, M., Xie, P., Beirle, S., Dörner, S., Remmers, J., Li, A., and Wagner, T.: Cloud and aerosol classification for 2.5 years of MAX-DOAS observations in Wuxi (China) and comparison to independent data sets, *Atmospheric Measurement Techniques*, 8, 5133–5156, doi:10.5194/amt-8-5133-2015, 2015.
- Wilmouth, D., Hanisco, T., Donahue, N., and Anderson, J.: Fourier transform ultraviolet spectroscopy of the $A^2\Pi_{3/2} \leftarrow X^2\Pi_{3/2}$ Transition of BrO, *Journal of Physical Chemistry A*, 103, 8935–8945, 1999.
- Witze, A.: Geology: Icelandic volcano stuns scientists, *Nature*, 514, 543–544, doi:10.1038/514543a, 2014.
- WMO: Scientific Assessment of Ozone Depletion: 2002, vol. Report No. 47, World Meteorological Organization Global Ozone Research and Monitoring Project, 2002.
- WMO: Scientific Assessment of Ozone Depletion: 2010, vol. Report No. 52, World Meteorological Organization Global Ozone Research and Monitoring Project, 2010.
- WMO: Scientific Assessment of Ozone Depletion: 2014, vol. Report No. 55, World Meteorological Organization Global Ozone Research and Monitoring Project, 2014.
- WMO: WMO Greenhouse Gas Bulletin: The State of Greenhouse Gases in the Atmosphere Based on Global Observations through 2015, vol. Report No.12, World Meteorological Organization, 2016.
- Wofsy, S. C., McElroy, M. B., and Yung, Y. L.: The chemistry of atmospheric bromine, *Geophysical Research Letters*, 2, 215–218, 1975.
- Woyke, T.: In-situ-Messung von Halogenoxiden in der polaren Stratosphäre: Untersuchungen zur Ozonchemie im Winter 1994/95, *Berichte des Forschungszentrums Jülich, Forschungszentrum, Zentralbibliothek*, URL <https://books.google.de/books?id=uqMwPwAACAAJ>, 1998.
- Yang, X., Abraham, N., Archibald, A., Braesicke, P., Keeble, J., Telford, P., Warwick, N., and Pyle, J.: How sensitive is the recovery of stratospheric ozone to changes in concentrations of very short-lived bromocarbons?, *Atmospheric Chemistry and Physics*, 14, 10 431–10 438, 2014.